The University Of Sheffield.

Hydrodynamics in a Minimal Nanocomposite System: Theoretical Description and Computational Simulation

N. Gibbions

Thesis submitted in partial fulfilment of the requirements for the degree of Doctor of Philosophy

2022

Hydrodynamics in a Minimal Nanocomposite System: Theoretical Description and Computational Simulation

Nigel Gibbions

Thesis submitted in partial fulfilment of the requirements for the degree of Doctor of Philosophy

The University of Sheffield
Faculty of Science
Department of Physics and Astronomy

October 2022

Dedication

To Joe Gibbions, 1931-2015. He was right.

Acknowledgements

This research was made possible by funding from the EPSRC and Solvay (grant number ST/N504282/1). I am grateful to both, for their financial support.

I would like to thank my supervisor, Nigel Clarke for his calming presence and encouragement throughout this project, especially when I wondered if I would ever see it through to the end. Without his constant support and feedback, this would be a poorer piece of work.

I also wish to express my gratitude to my second supervisor, Didier Long, for his work on the theoretical framework, described in chapter 2 of this thesis, and for many other invaluable insights. I also thank him for his hospitality during my stay in Lyon at the end of 2019.

I am grateful to the University of Sheffield's Centre for Doctoral Training in Polymers, Soft Matter and Colloids, which provided me with a solid foundation in the fundamentals of polymer science, and the ideal environment to pursue my research.

I would also like to thank staff and students in the University of Sheffield's Physics and Astronomy Department for welcoming me back to the physics community, as a mature student. Truly, it felt like coming home.

I am grateful to the graduate students and staff at Laboratoire Polymères et Matériaux Avancés, CNRS/Solvay, in Lyon, for making an Englishman, far from home, feel at home, and for humouring my attempts to speak their language. I will always remember their kindness.

I thank my mum, Lillie Gibbions, for the selfless love she has given me, all my life.

My deepest thanks go to my partner, Anna. I don't think she realised what she was letting herself in for when, ten years ago, she casually asked me if I had ever thought of revisiting the physics degree I had left behind in my youth. I offer her my heartfelt gratitude for her understanding, and for standing by me. My greatest hope is that, one day, she will be able to pursue her own intellectual adventure, with me by her side.

Declaration

I, Nigel Gibbions, confirm that the thesis is my own work. I am aware of the University's Guidance on the Use of Unfair Means (www.sheffield.ac.uk/ssid/unfair-means). This work has not been previously been presented for an award at this, or any other, university.

Chapters 2 and 3 of the thesis are based on papers previously published in the journal *Soft Matter* (references [1] and [2], respectively).

The ideas described in chapter 2 were developed by Didier Long, during the early stages of this project.

Abstract

In this thesis, we introduce the concept of a minimal nanocomposite system and use it to explore the wetting and dewetting behaviour that is observed during the fabrication of nanocomposite materials, and the shear-induced migration of a nanoparticle across the interface between two liquid polymer phases. Having described the relevant equilibrium thermodynamics of polymer blends, and the dynamics of phase separation when a polymer blend is near its critical point, we present a theoretical framework for understanding the motion of out-of-equilibrium, inhomogeneous liquids in the presence of a solid surface. This framework is consistent with known results in colloidal science, and with Onsager's formalism for non-equilibrium thermodynamics, and is derived by applying variational principles to a generic Gibbs free energy functional for a system in which there is a composition gradient, and an interaction potential between the inhomogeneous liquid and the solid surface.

Within this framework, we construct a physical model of the minimal nanocomposite system. The model is grounded in continuum fluid dynamics, and uses the fluid particle dynamics method to manage the boundary conditions in a multi-phase system. One benefit of this approach is that a non-zero slip length, of monomer length scale, naturally emerges when the system is described in the correct physical terms. The result is a pair of coupled equations for the velocity field and the order parameter (concentration) field, which we solve numerically. Thus, our model can represent the effects of both hydrodynamic flows and diffusion in the minimal nanocomposite system.

We apply our model to systems with various degrees of entanglement, and various degrees of segregation between the two liquid polymer phases. At higher degrees of entanglement, we observe slower wetting and dewetting dynamics, and greater difficulty in inducing the particle to migrate from one liquid phase to the other when the system is sheared. With weaker segregation between the liquid polymer phases, we observe a wider range of steady

states when the system is sheared, and less predictability in the final steady state. A simple geometrical model of dewetting under shear, combined with a small dose of physical realism, is found to predict the dewetting simulation results with fair accuracy.

Our model is grounded in the physics of continuum fluid dynamics and non-equilibrium thermodynamics and, suitably adapted, has the potential to describe the behaviour of more complex systems, including those that contain many nanoparticles.

Contents

List of Figures

List of Tables

List of Symbols

Where a symbol is used more than once, alternative interpretations are listed in the order in which they appear in the thesis.

A	Entropic term in the Flory-Huggins parameter
a	Monomer length scale
B	Enthalpic term coefficient in the Flory-Huggins parameter
b	Slipping length in fluid flow
D	Effective diffusion coefficient
d	Distance of particle from the interface between the liquid phases
d_c	Critical film thickness
E	Electric field strength
e	Width of the solid particle interface
e	Length scale at which dewetting is almost instantaneous ($e < d_c$)
e'	Effective interface width in a weakly segregated system
F	Free energy
F_{FH}	Flory-Huggins free energy of mixing per lattice site
F_{FHdG}	Flory-Huggins-de Gennes total free energy
F_{GL}	Ginzburg-Landau total free energy
F_i	Free energy of component i
F_{ij}	Free energy of a mixture of components i and j
F_{mix}	Free energy of mixing
f	Free energy density
$\mathbf{f}_{ext}$	External driving force in a fluid system
G	Gibbs free energy
g	Gibbs free energy density
$g^{(0)}$	Gibbs free energy density in the bulk phase
$g^{(1)}$	Gibbs free energy density at the interface between phases
k_B	Boltzmann's constant
L	Size of the system in lattice cell units

l_i	Kuhn length of polymer species i
M	Mobility (taken to be a scalar constant)
N	Degree of polymerisation in a symmetric polymer blend
N_e	Entanglement limit (assumed to be 100 monomers)
N_i	Degree of polymerisation of chemical species i
n	Number of simulation steps
P	Pressure
P	Dissipated power in a system relaxing towards equilibrium
p	Pressure field in a multi-phase system
p_0	Equilibrium pressure (e.g. atmospheric pressure)
p_i	Probability of configuration i
q_c	Characteristic wave number in spinodal decomposition
R	Radius of a spreading, out-of-equilibrium liquid droplet
r	Particle radius
$\mathbf{r}$	Position vector
S	Entropy
S	Spreading parameter of a droplet in Young's equation
S_i	Entropy of component i
S_{ij}	Entropy of a mixture of components i and j
S_{mix}	Entropy of mixing
T	Temperature
t	Time
t_2	Second dewetting time
U	Internal energy
U_i	Internal energy of component i
U_{ij}	Internal energy of a mixture of components i and j
U_{mix}	Internal energy of mixing
u_{ij}	Interaction energy between molecules of species i and j
V	Volume
V	Spreading velocity of an out-of-equilibrium liquid droplet
V_i	Volume of phase i in a binary system
$\mathbf{v}$	Velocity field in a multi-phase system
W	Wetting parameter
X_i	General thermodynamic force i
x_i	General coarse-grained thermodynamic variable i
z	Coordination number of a lattice
α_i	Volume fraction of phase i in a binary system
Γ	Gibbs free energy due to solid-liquid interactions
γ	Shear strain
$\dot{\gamma}$	Shear rate
$\gamma_{a,b}$	Matrix of Onsager coefficients

γ_{dewet}	Shear strain at the first dewetting point
γ_{ij}	Surface tension between phase i and phase j
ζ	Energy barrier at the surface of the particle
η	Viscosity
θ	Thermal noise term in the Cahn-Hilliard-Cook equation
θ_d	Dynamic contact angle of liquid droplet with solid substrate
θ_e	Equilibrium contact angle of liquid droplet with solid substrate
κ	Strength of the interfacial tension between two phases
λ	Effective interaction distance between monomers
λ	Length scale of interaction between solid and liquid phases
λ_c	Characteristic length scale in spinodal decomposition
λ_s	Length scale in the later stages of spinodal decomposition
μ	Total chemical potential
$\mu^{(0)}$	Chemical potential in a bulk phase
$\mu^{(1)}$	Chemical potential at an interface between phases
ρ	Electric charge density
ρ	Number density of monomers
$\boldsymbol{\sigma}$	Local stress tensor
τ	Characteristic time scale
τ_0	Monomer time scale
τ_{rept}	Reptation time scale
τ_{rouse}	Rouse time scale
Φ	Interaction potential between a solid substrate and a liquid
ϕ	Order parameter for the solid particle field
χ	Flory-Huggins interaction parameter
χ_C	Critical value of the Flory-Huggins interaction parameter
χ_{co}	Flory-Huggins interaction parameter on the coexistence curve
χ_{sp}	Flory-Huggins interaction parameter on the spinodal line
Ψ	Partial derivative of $\Gamma(\psi, z)$ with respect to ψ
ψ	Volume fraction, or order parameter of the polymer field
ψ_{eq}	Equilibrium value of the order parameter in a binary system
ψ_i	Volume fraction of component i in a mixture (i = A, B)
ψ_i	Polymer concentration in phase i of binary system (i = 1, 2)
ψ_i	Limiting polymer volume fractions in binary system (i = a, b)

Chapter 1

Introduction and Background

1.1 A Minimal Nanocomposite System

It is sometimes said that we live in the information age; but it might be said, with equal justice, that we live in the age of the synthetic polymer. It is hard to think of any object we use in daily life that does not depend, to some degree, on the ingenuity of chemists and material scientists, and on their ability to develop materials with the properties - be they mechanical, thermal, electrical, or optical - necessary for their intended application. A cursory glance around a typical office or living space suffices to confirm this important fact of modern life.

Yet the development of materials suitable for a given application is a process fraught with difficulty, and subject to trial and error, with all the costs that brings with it. For this reason, material scientists will often seek to fabricate composite materials, from two or more materials with known properties. The idea is that, if one material, A, is, for example, hard but brittle, while another, B, is resilient but easily deformed, some composite of the two might combine the best of both worlds, and have the perfect mechanical properties for the application concerned. Finding the right pair of materials, combining them in the correct proportions, and processing them appropriately, still involves much trial and error, but the search is considerably narrowed.

The difficulty with this approach, at least as far as polymers are concerned, is that the two components of a potential composite material are often reluctant to mix. Instead, the two polymers in the blend tend to separate into

distinct phases, with large domains, relative to the desired microstructure. The end result is a a composite material that is not fit for purpose because, for example, it lacks the desired mechanical properties. Later in this chapter, we describe the basis of this difficulty, in the equilibrium thermodynamics of polymer blends.

The introduction of nanoparticles (of carbon or silica, for example) into the polymer blend can, under the right circumstances, arrest the growth of these phase domains, and thereby enhance the mechanical integrity of the composite material. The use of nanoparticles to fine tune the properties of a composite material is an area of active and growing research, a key aim of which is to predict the macroscopic properties of a composite material from knowledge of its microstructure [3]. Later in this chapter we describe some of the experimental work on nanocomposite systems, and how such systems might be modelled, computationally. However, the difficulties - practical and theoretical - involved in the study of these complex multi-phase systems are already apparent. For this reason, the approach taken in this thesis is to radically simplify the problem and to focus on what we call a minimal nanocomposite system (figure 1.1).

A minimal nanocomposite system consists of just three elements: two liquid polymer phases, separated by a central interface, and a single naonparticle, located at, or close to, this central interface. Once we have a model of this system, it will be possible to vary parameters such as the degree of entanglement in the polymer phases, and the Flory-Huggins interaction parameter, which is introduced in the next section. We will also apply shear to this minimal system, to explore whether the particle can be induced to migrate across the boundary between the two liquid phases. Despite the simplicity of this system, it exhibits a surprisingly rich variety of behaviour as these model parameters are varied.

Therefore, this chapter introduces the background science we need to develop a mathematical model of this minimal nanocomposite system. Firstly, we describe the equilibrium thermodynamics, and introduce the Flory-Huggins theory of the free energy density, of a polymer blend, which forms the foundation of our model. Secondly, we introduce the Cahn-Hilliard equation, which is essential to understanding the dynamics of phase separation of a polymer blend in the unstable (or meta-stable) region of its phase diagram. Although we do not explicitly focus on phase separation in this thesis, the Cahn-Hilliard equation may be applied to any system in which there are interfaces between two or more phases, including the minimal nanocomposite

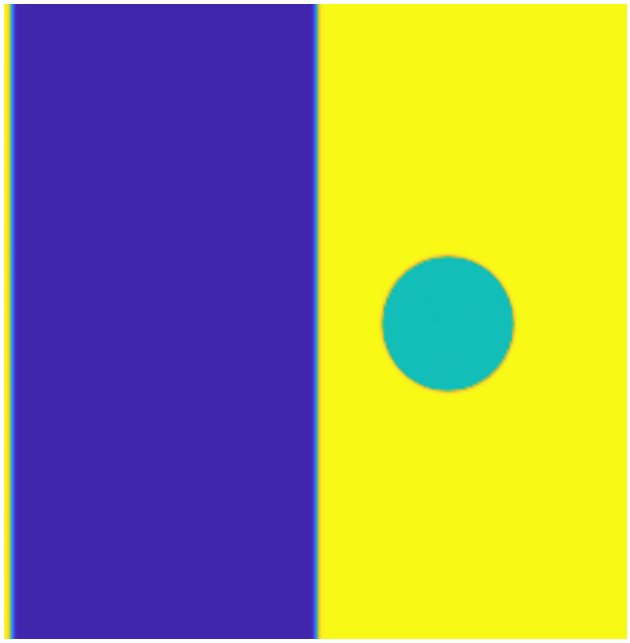

Figure 1.1: A minimal nanocomposite system, consisting of two liquid polymer phases, separated by a central interface, and a single nanoparticle. The nanoparticle may be located at the interface, or close to it, and various parameters of the model, such as the degree of entanglement of the polymer phases, and the Flory-Huggins interaction parameter may be varied.

system described above. Thirdly, we review some key concepts in the theory of wetting and dewetting. Although our mathematical model automatically reproduces the wetting and dewetting behaviour of the minimal nanocomposite system, it is useful to appreciate the underlying physical processes involved, and the vocabulary that is used to describe them.

In the last two sections, we survey some of the milestones in the experimental and theoretical study of nanocomposite systems. Most of these systems are more complex than the minimal system that is the object of this thesis: for example, they usually include many nanoparticles, instead of just one, and some exhibit viscoelastic effects. Nevertheless, it is useful to review this work on relatively complex systems, because it highlights the range of behaviour in real systems that our model might be used to explore in future, while situating our model in its broader practical and theoretical context.

We believe that the minimal nanocomposite system that is the subject of this thesis is of significant theoretical interest in its own right, while also providing some insight into the practical difficulties involved in the fabrication of

nanocomposite materials that are fit for their intended purposes.

1.2 Equilibrium Thermodynamics of Polymer Blends

The thermodynamics of polymer blends is dominated by their low entropy of mixing. This arises because the long, chain-like nature of the molecules severely constrains the number of configurations they may adopt in the presence of other chains. As a result, polymers are usually reluctant to mix, and tend to phase-separate when they are forced to do so. In this section we set out the essential background theory to understand this behaviour, culminating in the phase diagram of a typical two polymer blend. This is one of the building blocks we will need when we develop our mathematical model of a minimal nanocomposite system in later chapters.

Flory and Huggins [4, 5] assume a lattice model, and use a mean field approximation to derive an expression for the free energy of mixing per lattice site for polymer solutions. The former assumption is taken to mean that each individual segment in a polymer chain, and each solvent molecule, fully occupies one site in the lattice, so all segments and solvent molecules effectively have the same volume. Depending on the polymers concerned, a segment may be either an individual monomer, or a number of monomers with a combined length equal to the Kuhn length [6]. The mean field approximation amounts to the claim that the average concentration of either component, in the neighbourhood of any given lattice site is equal to that component's global mean value (thus, it ignores the effect of local correlations on the free energy of mixing). In addition to these two key assumptions, Flory-Huggins' theory also assumes that polymer chains do not cross themselves, and that all polymer chains of the same chemical species have the same length (an idealisation, since any real polymer sample will have a distribution of chain lengths).

Here, we present the derivation of the free energy of mixing of a *polymer blend*, based on the Flory-Huggins theory. The derivation is best approached by first considering a lattice model of of a simple binary fluid (figure 1.2a).

We define the free energy of mixing as:

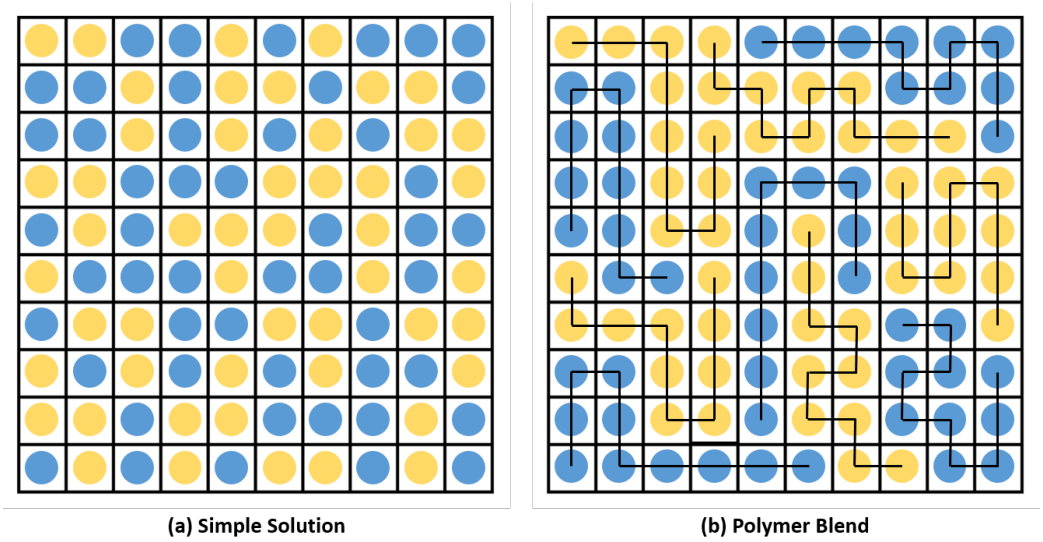

Figure 1.2: Lattice model of a simple solution, and of a polymer blend. The simple solution in (a) consists of 50 molecules each of the solute and the solvent and, for simplicity, we assume that each molecule occupies the same volume, equivalent to that of one lattice cell. The polymer blend in (b) consists of five chains each of two different polymers, with ten monomers in each chain. Again, for simplicity, we assume that each monomer occupies a single lattice cell.

$$F_{mix} = F_{AB} - (F_A + F_B) \tag{1.1}$$

Where F_{AB} is the free energy of the mixture, and F_i is the free energy of the pure fluid sample, of chemical species i. Here, we take F to be the Helmholtz free energy, $F = U - TS$, where U is the internal energy of the system, S is its entropy, and T its temperature. Elsewhere in the thesis, we refer to the Gibbs free energy, $G = U - TS + PV$ (where P and V are the pressure and the volume of the system), as is common in the literature on polymer blends. This distinction is not critical because we assume incompressibility of the polymer blend throughout, so the condition that the volume of the system is constant, implied in the use of the Helmholtz free energy, is automatically satisfied. This is an illustration of the general point that, in thermodynamics, we are usually only interested in *changes* to thermodynamic potentials, not in their absolute values.

Returning to equation 1.1, let us consider the entropy of mixing first:

$$S_{mix} = S_{AB} - (S_A + S_B) \tag{1.2}$$

Where each entropy term is defined analogously to the free energy terms in equation 1.1. We may now use the Boltzmann formula to determine the entropy of mixing per site:

$$S = -k_B \sum_i p_i \, ln(p_i) \tag{1.3}$$

Where the sum is to be taken over all possible configurations of the system, and p_i is the probability of configuration i. Let us suppose that our simple binary fluid consists of a volume fraction ψ_A of chemical species A, and volume fraction ψ_B of chemical species B, and that the volume of the system is constant and independent of its composition, so that $\psi_A + \psi_B = 1$. The mean field approximation implies that the probability of finding a molecule of species i at any given lattice site is ψ_i, and since there are only two chemical species in the mixture, we obtain the entropy of mixing per lattice site:

$$S_{mix} = -k_B(\psi_A \, ln \, \psi_A + \psi_B \, ln \, \psi_B) \tag{1.4}$$

Note that $S_A = S_B = 0$, since the entropy of a pure fluid is zero, so the second term on the right hand side of equation 1.2 vanishes.

Turning now to the internal energy term in equation 1.1, we have:

$$U_{mix} = U_{AB} - (U_A + U_B) \tag{1.5}$$

Let the interaction energy between a molecule of species i and a molecule of species j be u_{ij}. Suppose, also, that each lattice site has z nearest neighbours, where z is known as the coordination number, and that only interactions between nearest neighbours need to be taken into account, when calculating the average interaction energy per lattice site. Then, the average *pairwise* energy of interaction of a molecule of A, with a neighbouring molecule is:

$$U_A = u_{AA}\psi_A + u_{AB}\psi_B \tag{1.6}$$

And similarly, for the average pairwise energy of interaction of a molecule of B:

$$U_A = u_{BB}\psi_B + u_{AB}\psi_A \tag{1.7}$$

So, the average interaction energy per lattice site in the mixture is given by:

$$U_{AB} = \frac{z}{2}(U_A\psi_A + U_B\psi_B) \tag{1.8}$$

Where the factor of one half is introduced to prevent double counting. Using equations 1.6 and 1.7, and after some simplification, this becomes:

$$U_{AB} = \frac{z}{2}(u_{AA}{\psi_A}^2 + 2u_{AB}\psi_A\psi_B + u_{BB}{\psi_B}^2) \tag{1.9}$$

Finally, unlike the entropy, the internal energy of a pure fluid is non-zero, so we must remember the second term on the right hand side of equation 1.5. Similar reasoning to that used above gives the average interaction per lattice site before mixing takes place:

$$U_A + U_B = \frac{z}{2}(u_{AA}\psi_A + u_{BB}\psi_B) \tag{1.10}$$

Substituting equations 1.9 and 1.10 into equation 1.5 gives the desired expression for the energy of mixing per lattice site:

$$U_{mix} = \frac{z}{2}\psi_A\psi_B(2u_{AB} - u_{AA} - u_{BB}) \tag{1.11}$$

However, it is usual to introduce the Flory-Huggins interaction parameter, χ, which is dimensionless, and defined as:

$$\chi = \frac{z}{2}\,\frac{2u_{AB} - u_{AA} - u_{BB}}{k_BT} \tag{1.12}$$

The parameter χ represents the difference between the interaction energy of two unlike molecules, and the mean of the interaction energies of two like molecules (of either chemical species A, or chemical species B). When $\chi < 0$ molecules of one chemical species are preferentially attracted to molecules of the other species, and there is a tendency to form stable mixtures. When

$\chi > 0$, a stable mixture may or may not form, depending on the value of χ, and how the free energy of mixing, per lattice site, varies with the volume fractions, ψ_A and ψ_B. We return to this question of the stability of a mixture (or polymer blend) shortly.

Meanwhile, having defined the Flory-Huggins interaction parameter, we can write down the final version of our expression for the energy of mixing, per lattice site, in a simple binary fluid:

$$U_{mix} = \chi \psi_A \psi_B k_B T \tag{1.13}$$

The free energy of mixing is then obtained by substituting equations 1.4 and 1.13 into equation 1.1. As is common, we also let $\psi = \psi_A$ so that, given incompressibility, $\psi_B = 1 - \psi$. Thus, the free energy of mixing, per lattice site, in a binary fluid is:

$$F_{mix} = k_B T[\psi \, ln \, \psi + (1 - \psi) \, ln \, (1 - \psi) + \chi \psi (1 - \psi)] \tag{1.14}$$

Extension to the case of the polymer blend, represented in figure 1.2b is quite straightforward. The logic of the mean field approximation implies that the interaction energy term in equation 1.14 is unchanged. However, the entropy terms need to be adjusted, to take into account the fact that a segment of a given chemical species is more likely to have segments of the same species as its nearest neighbours, than is the case in a simple binary fluid. This is because polymer molecules exist as long chains of identical segments, so it is more difficult to place segments of different chemical species next to each other on the lattice (this is obvious, if we imagine placing long polymer chains on a one-dimensional lattice, and contrast it with placing individual molecules of two different chemical species). The effect of this constraint is that the entropic terms in equation 1.14 are significantly reduced, and the Flory-Huggins free energy of mixing, per lattice site, of a polymer blend is:

$$F_{FH} = k_B T \left[\frac{\psi}{N_A} \, ln \, \psi + \frac{(1 - \psi)}{N_B} \, ln \, (1 - \psi) + \chi \psi (1 - \psi) \right] \tag{1.15}$$

Where N_i is the degree of polymerisation of species i. Given that, for typical polymer molecules, $N_i >> 1$, it is evident that the entropy of mixing of a polymer blend is much less than that of a simple binary fluid. However, note

also that the entropic terms in equation 1.15 always favour mixing, while the energetic term may or may not favour mixing, depending on the balance of the interaction energies between like and unlike segments at the molecular level, as represented by the parameter χ. Finally, it is worth pointing out that the free energy of mixing for a polymer solution may be obtained from equation 1.15 by setting either $N_A = 1$ or $N_B = 1$ while, if $N_A = N_B = 1$, we recover equation 1.14, the expression for the free energy of mixing of a simple binary fluid, just as we would expect.

The easiest way to appreciate the nature of the Flory-Huggins free energy is to plot it against the volume fraction, ψ, for various values of the parameter, χ (figure 1.3).

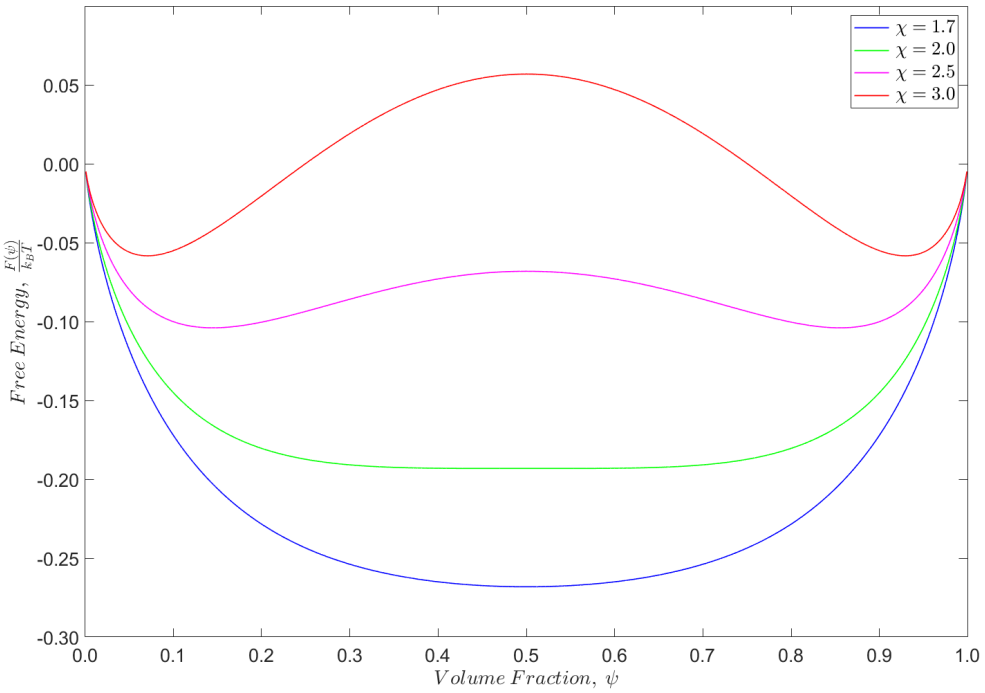

Figure 1.3: The Flory-Huggins free energy of mixing, per lattice site, in a simple binary fluid, for various values of the interaction parameter, χ. Note that when $\chi \leq 2$, the free energy curve is concave in the entire interval $0 \leq \psi \leq 1$. When $\chi > 2$, the free energy curve is convex in an interval between the upper and lower bounds of the volume fraction, ψ, with a local maximum at $\psi = 0.5$. The critical value of the Flory-Huggins interaction parameter, $\chi_C = 2$ marks the transition between these two regimes.

For simplicity, we have plotted the Flory-Huggins free energy curves for a simple binary fluid. In the case of a *symmetric* polymer blend, defined by $N_A = N_B = N$, the free energy has an identical shape but the magnitude of the free energy scales according to the value of N. The effect of relaxing

this last assumption, so that $N_A \neq N_B$ would be to make the free energy curves asymmetrical about the line $\psi = 0.5$ which, as we will note later, has implications for determining the volume fraction(s) at thermodynamic equilibrium. The key point highlighted by figure 1.3 is that there exists a critical value of the Flory-Huggins interaction parameter, $\chi = \chi_C = 2$. When $\chi < \chi_C$, the free energy is concave for all values of ψ. In contrast, when $\chi > \chi_C$, there is a range of values of ψ, at which the free energy curve is convex.

We now show that the dependence of the shape of the free energy curve on the value of the Flory-Huggins interaction parameter has important implications for the thermodynamic equilibrium of the mixture, or polymer blend. Suppose we have a fixed volume of a homogeneous mixture of two chemical species, A and B, and that the initial volume fraction of A is ψ_0, so that the initial volume fraction of B is $1 - \psi_0$. Further, let the free energy of the original mixture be F_0. If this mixture separates into two distinct phases, of volume fractions ψ_1 and ψ_2, we must have:

$$\psi_0 = \alpha_1\psi_1 + \alpha_2\psi_2 \tag{1.16}$$

Where $\alpha_i = \frac{V_i}{V}$, with V_i being the volume of phase i, and V the total volume, such that $V_1 + V_2 = V$, and $\alpha_1 + \alpha_2 = 1$. The free energy of the phase-separated system is then given by:

$$F_{12} = \alpha_1 F(\psi_1) + \alpha_2 F(\psi_2) \tag{1.17}$$

Where $F(\psi_i)$ is the free energy of a *mixture*, in which the volume fraction of species i is ψ_i.

Combining equation 1.17 with equation 1.16, and remembering that $\alpha_1 + \alpha_2 = 1$, we obtain the following expression for the free energy of the phase separated system:

$$F_{12} = \frac{\psi_0 - \psi_2}{\psi_1 - \psi_2}F(\psi_1) + \frac{\psi_1 - \psi_0}{\psi_1 - \psi_2}F(\psi_2) \tag{1.18}$$

This situation is represented graphically in figure 1.4, for two cases, one in which the free energy curve is concave in the interval $0 \leq \psi \leq 1$, and one in

which there is a convex region between the upper and lower bounds of this interval.

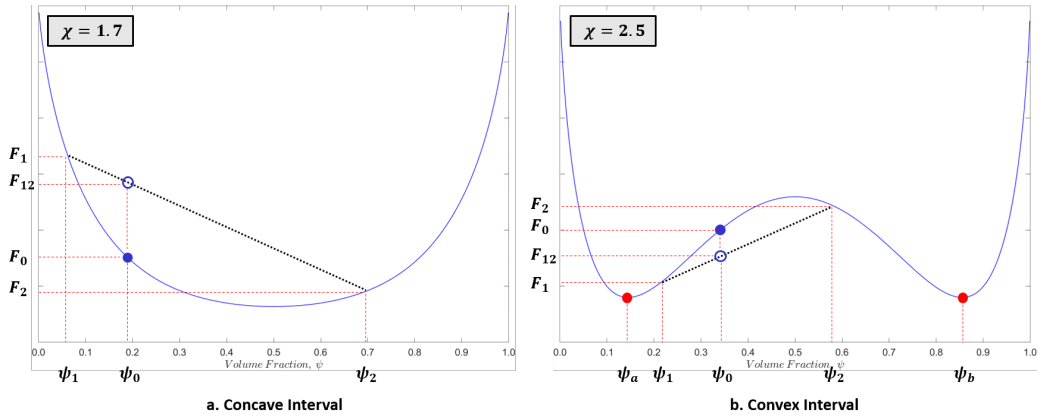

Figure 1.4: Stability and instability in mixtures and polymer blends. For intervals in which the free energy curve is concave (figure 1.4a), the system is locally stable: any combination of two distinct phases has greater free energy than the single phase. Thus, $F_{12} > F_0$, where F_{12} is the free energy of a system that contains distinct phases, with volume fractions, ψ_1 and ψ_2, and F_0 is the free energy of the original blend, with a volume fraction of ψ_0. For intervals in which the free energy curve is convex (figure 1.4b), the system is unstable ($F_{12} < F_0$), and separates into two distinct phases. This region of phase separation is bounded by the limiting volume fractions, ψ_a and ψ_b, where local minima in the free energy occur.

In both cases, the filled blue point represents the original mixed state of the system, and the unfilled blue point represents the potential state of the system, if phase separation occurs. In figure 1.4a, the energy of the two-phase system is greater than that of the original mixture ($F_{12} > F_0$), and a little thought shows that this must be the case for a mixture with any initial volume fraction, ψ_0, no matter what values of ψ_1 and ψ_2 we choose. Thus, for this value of χ, and for any value of $\chi < 2$, a mixture is stable, whatever the volume fractions of species A and B.

Contrast this case with that shown in figure 1.4b, in which $\chi > 2$. Here, there is a region of the curve where the free energy of the two-phase system is less than that of the original mixture ($F_{12} > F_0$). Again, a little thought shows that this region must be bounded by the volume fractions marked as ψ_a and ψ_b. These are known as coexisting compositions, and the locus of all such points, as we vary the Flory-Huggins parameter, χ (and thus the temperature, T), defines what is known as the coexistence curve, or the binodal.

Note that, for simplicity, figure 1.4, assumes that $N_A = N_B = N$ (taking the curves to represent the free energy of mixing of a polymer blend). Thus both curves are symmetrical about the line $\psi = 0.5$, and at the coexisting compositions, ψ_a and ψ_b in figure 1.4b, the partial derivative of the free energy with respect to ψ is zero. So, by differentiating equation 1.15 with respect to ψ, equating the derivative to zero, and rearranging the result, we obtain the following equation for the coexistence curve of a symmetrical polymer blend:

$$\chi_{co} = \frac{1}{N} \frac{1}{2\psi - 1} \ln\left(\frac{\psi}{1-\psi}\right) \tag{1.19}$$

Dropping the assumption that $N_A = N_B = N$ in the case of a polymer blend results in asymmetrical free energy curves. As in the symmetric case, the coexisting compositions are determined by the points at which it is possible to draw a common tangent to the free energy curve, but now it is no longer the case that $\frac{\partial F}{\partial \psi} = 0$. However, recognising that this partial derivative is equivalent to the chemical potential, μ, we can say that, in the general case, at the coexisting compositions, ψ_a and ψ_b, we have $\mu_a = \mu_b$, where the symbols either side have the equality have the natural interpretation.

Before we present the phase diagram of our binary system, we must note one last nuance (figure 1.5). The argument is similar to the one just presented about the *global* stability of a mixture, but here, we focus on small fluctuations about the original volume fraction, ψ_0, which lies in the interval $\psi_a < \psi_0 < \psi_b$. If the curvature of the free energy curve is negative at ψ_0, the free energy of the two phase system with volume fractions $\psi_0 - \delta\psi$ and $\psi_0 + \delta\psi$ is less than the free energy of the original state of the system ($F_{12} < F_0$), and small local fluctuations in the volume fraction will be amplified, leading to phase separation. This system is unstable, both locally and globally. In contrast, if the curvature of the free energy curve is positive at ψ_0, the free energy of the two phase system with volume fractions $\psi_0 - \delta\psi$ and $\psi_0 + \delta\psi$ is greater than the free energy of the original state of the system ($F_{12} > F_0$), and small local fluctuations in the volume fraction will be damped. A system in such a state is said to be *metastable*: although it is globally unstable, and will separate into two distinct phases, if it is sufficiently perturbed, it is locally stable to small fluctuations in the volume fraction, ψ.

Clearly the boundary between the unstable and metastable regions of the free energy curve is marked by the point at which its curvature, $\frac{\partial^2 \chi}{\partial \psi^2} = 0$. The locus of all such points, as we vary the Flory-Huggins parameter, χ, defines

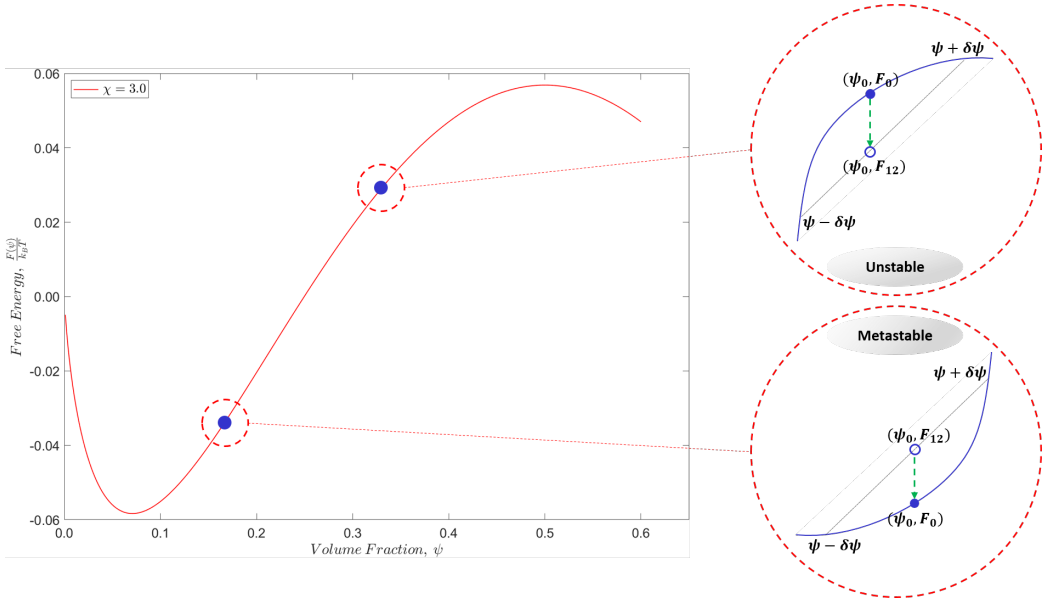

Figure 1.5: Unstable and metastable mixtures and polymer blends. In the unstable region of the free energy curve, small fluctuations in the local volume fraction lower the free energy of the system. Thus $F_{12} < F_0$, where F_{12} is the free energy of a two-phase system with volume fraction $\psi+\delta\psi$ and $\psi-\delta\psi$, and F_0 is the free energy of the original blend, and phase separation occurs spontaneously. In the metastable region of the curve, $F_{12} > F_0$, and the single phase system remains stable, as long as the fluctuations remain small. The transition between the unstable and the metastable regions occurs at the inflection point of the free energy curve, where $\frac{\partial^2 F}{\partial \psi^2} = 0$.

what is known as the spinodal line, which marks the boundary between the unstable and metastable regions of the phase diagram. We may obtain the equation of the spinodal line, for a symmetric polymer blend, by setting the second derivative of equation 1.15 with respect to ψ equal to zero, and rearranging the result:

$$\chi_{sp} = \frac{1}{2N} \frac{1}{\psi(1-\psi)} \tag{1.20}$$

Knowing the equations of both the coexistence curve, and the spinodal line, we are now in a position to construct the phase diagram for the symmetrical binary system that has been the main focus of this section (figure 1.6).

The phase diagram is characterised by a region of instability, where phase separation spontaneously occurs due to thermally induced concentration fluctuations. This region is bounded by the spinodal line, and the process of

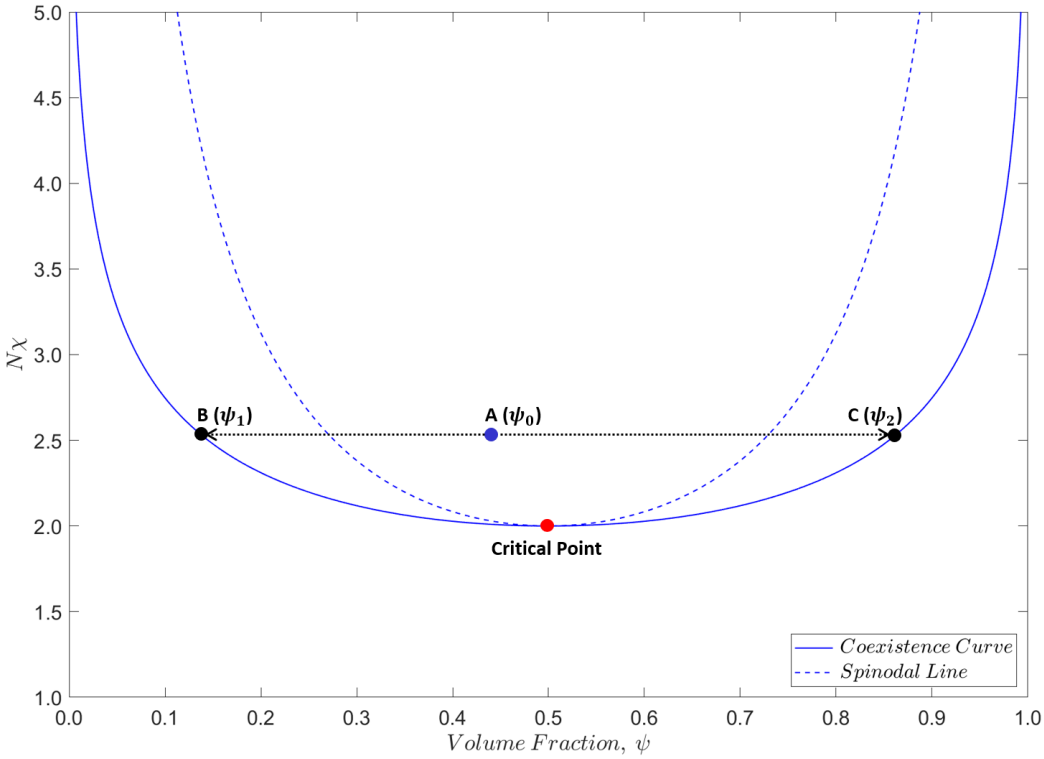

Figure 1.6: Phase diagram in $\chi - \psi$ space for a polymer blend in which $N_A = N_B = N$. In the region below the coexistence curve, the free energy of mixing is less than the free energy of separation into two phases, so the blend is stable. In the region above the spinodal line, the blend is unstable and will spontaneously separate into distinct phases. Thus, a system at point A, with volume fraction ψ_0 will separate into two phases of volume fractions ψ_1 and ψ_2. Between the coexistence curve and the spinodal line, the blend is metastable: phase separation may occur if fluctuations in the local volume fraction are large (or if impurities in the sample act as sites for nucleation and growth). Note that it is possible to construct a similar phase diagram in $T - \psi$ space, but the coexistence curve and the spinodal line will then be inverted since, in the simplest case, the temperature, $T \propto \frac{1}{\chi}$.

phase separation associated with it is known as spinodal decomposition. As we shall see in the next section, the resulting phase-separated microstructure takes a complex bicontinuous form, with a single characteristic length scale. The phase diagram also includes a coexistence curve (or binodal line), which marks the boundary between globally stable and globally unstable blends. The region between the coexistence curve and the spinodal line defines the meta-stable regime where phase separation occurs due to nucleation and growth or, rarely, due to large spontaneous fluctuations in a homogeneous blend. We have plotted the phase diagram in $\chi - \psi$ space, but we could just as easily have plotted it in $T - \psi$ space. Since $\chi \propto \frac{1}{T}$, such a phase diagram

would appear inverted, with respect to figure 1.6. Thus, the critical point shown in figure 1.6 represents the highest possible temperature, T_C (or the lowest possible value of the interaction parameter, χ_C) at which two distinct phases can coexist.

Before moving on to consider the dynamics of phase separation, a brief remark about the behaviour of real polymer blends is in order. The experimental evidence [7] is that the interaction parameter, χ has a more complex dependence on T, than equation 1.12 would lead us to believe. As a result, the relationship between χ and T is commonly taken to be of the form:

$$\chi(T) = A + \frac{B}{T} \tag{1.21}$$

Where A and B are constants, with appropriate dimensions. A is known as the entropic term and reflects the effect of mixing on the conformational entropy of a polymer chain, as opposed to the translational entropy, as represented in figure 1.2. Such effects might arise, for example, from the fact that certain pairs of polymers pack more easily together than other pairs, contrary to the assumptions of Flory-Huggins theory, which treats all monomers (or segments of a polymer chain) as essentially alike. In reality, $\chi(T)$ may be more complex still, involving higher order terms due to additional packing effects, chain stiffness and other factors [8, 9, 10]. These factors will influence the miscibility of real polymer blends, and therefore the nature of their phase diagram but, for the rest of this thesis, we take the simple phase diagram of figure 1.6 as our model.

1.3 Dynamics of Phase Separation

So far, we have focused on the equilibrium thermodynamics of simple binary fluids and polymer blends. Flory-Huggins theory describes how the free energy of such a system varies with its composition, represented by the volume fraction, ψ, and with changes to the interaction parameter, χ. From this, it is possible to construct a phase diagram of a typical binary system, with the coexistence curve, and the spinodal line, marking the boundaries of global stability and metastability, respectively. It is important to realise that this description relates to a homogeneous, bulk, system, characterised by a single variable, ψ, and a single parameter, χ.

Towards the end of the last section, we saw how a homogeneous system could separate into two distinct phases, when the interaction parameter takes certain values ($\chi > \chi_C = 2$), and the volume fraction, ψ, lies within the interval determined by the coexistence curve. Practically, speaking, in many polymer blends, phase separation is initiated by rapidly decreasing the temperature ("quenching"), equivalent to a sudden increase in the Flory-Huggins interaction parameter, so the point representing the system moves from the stable to the unstable region of the phase diagram. As soon as the system is quenched, phase separation begins to occur, regions of inhomogeneity appear, and the equilibrium thermodynamics appropriate to the bulk system cannot be applied without modification. Furthermore, the composition at any given point in the system changes, as spinodal decomposition proceeds, so we need an account of the dynamics of phase separation.

This section presents one such account, based on the work of Cahn and Hilliard, and developed by many other researchers since. The presentation is brief because the development of our own model, introduced in the next chapter, recapitulates most of the relevant content, while tailoring it to the minimal nanocomposite system that is the focus of this thesis. In particular, our aim in this thesis is not to model the process of spinodal decomposition. However, any system consisting of distinct phases, with diffuse interfaces between them - such as our minimal nanocomposite system - may be modelled using some variant of Cahn and Hilliard's approach. Therefore, it is useful to see the Cahn-Hilliard theory of phase separation in its basic form, before presenting our model in detail.

Before introducing Cahn-Hilliard's theory, a clarification is needed. In the previous section we sometimes refer, somewhat loosely, to the free energy of the system. However, as is clear in the derivation of equation 1.15, this is, strictly speaking, the free energy of mixing *per lattice site* and, in a continuous system, a similar expression would describe the free energy *density* at a point in the system. To mark this distinction we will use the notation $f(\psi, \mathbf{r})$ to denote the free energy density at a point with position vector $\mathbf{r}$ in the system, at which the volume fraction is ψ. And, from now on, a capital letter, F, will be used to represent the total free energy of the system.

It might be thought that the total free energy, F, is the integral of the free energy density, $f(\psi, \mathbf{r})$, over the region occupied by the system, but this ignores one of the fundamental effects of phase separation: as the blend separates into distinct phases, boundaries form between them, and these boundaries incur an energy cost. This energy cost must be taken into account,

when calculating the total free energy of the system. The simplest way to do this is to introduce a term that is proportional to the square of the gradient of the free energy density, at any point in the system. This term will be greatest when the interface between the two phases is sharpest, and will decrease as the interface becomes more diffuse, vanishing entirely in single phase regions of the system, where the gradient of the free energy density is zero.

With this clarification, we can now write down the expression for the total free energy of an inhomogeneous system used by Cahn and Hilliard [11, 12, 13, 14, 15, 16, 17], to develop their theory of the dynamics of spinodal decomposition:

$$\frac{F_{GL}\{\psi(\mathbf{r})\}}{k_B T} = \int \left\{ s\psi^2 + t\psi^4 + \frac{\kappa}{2}|\boldsymbol{\nabla}\psi|^2 \right\} d^3\mathbf{r} \tag{1.22}$$

Where the total free energy is now expressed as a dimensionless quantity, as is common, and is now a *functional*, which takes the composition field as its input, and outputs a scalar quantity. In the integrand, on the right hand side, s and t are parameters, and κ measures the strength of the interfacial tension between the two phases. As discussed above, the square gradient term in the integrand reflects the energy cost incurred when interfaces form during spinodal decomposition. Taken together, the first two terms of the integrand represent what is known as the Ginzburg-Landau bulk free energy. The reason for this is that, Cahn and Hilliard's work concerns spinodal decomposition in metallic alloys, where diffusion within a fixed lattice is the sole mechanism by which phase separation occurs. However, their approach is easy to generalise to other two component systems, including systems of magnetic spins [18] and, as in the present case, polymer blends. Thus, De Gennes [19] adapts Cahn-Hilliard's theory to obtain the following (Flory-Huggins-de Gennes) form for the total free energy of a polymer blend:

$$\frac{F_{FHdG}\{\psi(\mathbf{r})\}}{k_B T} = \int \left\{ \frac{f_{FH}\{\psi(\mathbf{r})\}}{k_B T} + \kappa\{\psi(\mathbf{r})\}|\boldsymbol{\nabla}\psi|^2 \right\} d^3\mathbf{r} \tag{1.23}$$

Where $f_{FH}\{\psi(\mathbf{r})\}$ is the Flory-Huggins free energy density, expressed as a dimensionless quantity, and there is now a potential dependence of κ on $\psi(\mathbf{r})$, the volume fraction at a given point in the system. This dependence might arise due to restrictions imposed on chain conformations at phase boundaries and the consequent reduction in entropy, and hence the interfacial energy. Although we assume no such composition dependence in our model, we note

that, using a combination of mean field arguments and the random phase approximation, De Gennes [19] derives the following expression for $\kappa\{\psi(\mathbf{r})\}$:

$$\kappa\{\psi(\mathbf{r})\} = \frac{1}{36}\left[\frac{{l_A}^2}{\psi(\mathbf{r})} + \frac{{l_B}^2}{1-\psi(\mathbf{r})}\right] + \chi\lambda^2 \tag{1.24}$$

Where l_i is the Kuhn segment length of polymer species i and λ is the effective interaction distance between monomers. In practice, the smaller enthalpic term, $\chi\lambda^2$ is commonly omitted.

Returning to the dynamics of phase separation, it is natural to begin by writing down a diffusion equation of the form:

$$\frac{\partial\psi}{\partial t} = D\boldsymbol{\nabla}^2\psi \tag{1.25}$$

Where D is a diffusion coefficient. However, this assumes that diffusion transports material from regions of the system with a high concentration (of polymer species A, say) to regions of low concentration. A moment's reflection is enough to conclude that this does not happen during spinodal decomposition: as the system phase separates, we observe the formation of regions with *increasing* concentration of polymer A (or polymer B). The reason for this apparent reversal is that the quantity of fundamental thermodynamic significance is the chemical potential, not the concentration of any particular chemical species. In a system that is out of equilibrium, the thermodynamic forces act so as to equalise the chemical potential.

The chemical potential may be obtained by taking the *functional* derivative of the total free energy of the system (equation 1.23, for polymer blends) with respect to ψ. Locally, it is the gradient of the chemical potential, that determines the flow from one region of the system to another. This is equivalent to the second derivative of the free energy, with respect to ψ which, as figure 1.5 shows may be either positive or negative, depending on whether we are in the metastable or unstable region of the curve. The former case, of positive curvature, corresponds with our everyday of experience that material flows from regions of high concentration to regions of low concentration. However, in the spinodal region of the curve, the curvature is negative, so material can flow from regions of low concentration to regions of high concentration, as happens during phase separation.

Putting this together with equation 1.25 we obtain the most general form of the Cahn-Hilliard equation for the dynamics of phase separation in a two-component system:

$$\frac{\partial \psi(\mathbf{r},t)}{\partial t} = M\boldsymbol{\nabla}^2 \frac{\delta F\{\psi(\mathbf{r},t)\}}{\delta \psi} \tag{1.26}$$

Here, the δ notation used in the derivative signifies that it is the functional derivative that is taken, and F is now a generic free energy. In the most general case, M is a mobility tensor but, since we neglect viscoelastic effects, and assume isotropy throughout this thesis, we take it to be a scalar constant. Equation 1.26 may be modified by the addition of a thermal noise term, to obtain what is known as the Cahn-Hilliard-Cook equation [20]:

$$\frac{\partial \psi(\mathbf{r},t)}{\partial t} = M\boldsymbol{\nabla}^2 \frac{\delta F\{\psi(\mathbf{r},t)\}}{\delta \psi} + \theta(\mathbf{r},t) \tag{1.27}$$

Where $\theta(\mathbf{r},t)$ is a thermal noise term with a time-averaged value of zero, and other useful statistical properties. Broadly speaking, the effect of this thermal noise term is to increase the sensitivity of the system to the small fluctuations that lead to phase separation, since even random thermal fluctuations will be amplified if the system is within the region of the phase diagram bounded by the spinodal line. Intuitively, the spinodal line itself becomes a more diffuse boundary as a result of the thermal noise in the system. However, the magnitude of this effect is subject to some dispute [21, 22, 23] and, in this thesis, we do not include a thermal noise term in our model. Therefore, we will take equation 1.26 as our reference point, when we build a model of the minimal nanocomposite system in the following chapters.

Before closing this section, it will be useful to briefly describe the solutions to equation 1.26 that pertain to spinodal decomposition. The key insight is that, although all fluctuations in the composition of the blend are amplified in spinodal decomposition, not all fluctuations are amplified equally. Reasoning qualitatively, the driving force of spinodal decomposition is diffusion along gradients of chemical potential, which implies that long wavelength fluctuations will take longer to grow. Conversely, short wavelength fluctuations, unchecked, increase the area of the interface between the two phases and incur a higher energy cost than longer wavelength fluctuations. The result of the competition between these two factors is that there is a favoured length scale that emerges in the early stages of spinodal decomposition.

Quantitatively, this favoured length scale may be determined by a suitable linearisation, valid for short time scales, of the Cahn-Hilliard equation, and solving the resulting equation. It is customary to express the result in terms of a characteristic wave number $q_c = \frac{2\pi}{\lambda_c}$, where λ_c is the fluctuation wavelength favoured by the balance of competing forces during spinodal decomposition. Further, it is possible to show that $q_c \propto \sqrt{\frac{1}{\kappa}}$, where κ is the coefficient of the square gradient term in the free energy functional (equations 1.22 and 1.23). Thus, the characteristic length scale will vary with the polymers in the blend, and the strength of the interfacial tension between them, but values of $\sim 1\,\mu m$ are not uncommon.

When the volume fraction, ψ, is close to 0.5, spinodal decomposition gives rise to co-continuous regions of each phase, randomly orientated, but with a uniform width, dictated by the favoured length scale [12, 17, 19]. In contrast, a blend with unequal volumes of the two polymers will phase separate by spinodal decomposition into a droplet-matrix morphology. Figure 1.7 shows the results of three computer simulations of spinodal decomposition, illustrating the various possibilities. Images of spinodal decomposition in real polymer blends may be seen in Voit et. al. [24], and many other papers in this field.

Figure 1.7: Computer simulation of spinodal decomposition in three polymer blends with volume fractions $\psi = 0.3$, $\psi = 0.5$, and $\psi = 0.7$. Spinodal decomposition of the $50:50$ blend results in an intricate morphoogy in which the two phases are co-continuous, and the width of the phase domains is the characteristic length scale, λ_c. Significant deviations from a $50:50$ blend result in a droplet-matrix morphology. In all simulations, spinodal decomposition was initiated by introducing random fluctuations of $\delta\psi = \pm 0.05$ into a uniform blend.

Although we do not consider it in this thesis, viscoelasticity further complicates the dynamics of phase separation. For example, Tanaka [25] describes a novel viscoelastic mechanism for phase separation in some polymer

blends, when there is a high degree of dynamic asymmetry between components. This may be due either to a large difference in chain size, or to a large difference in the glass transition temperature of the components. In viscoelastic phase separation, the *minority* phase, in a volume-asymmetric blend, can form a network structure. This contrasts with the droplet-matrix morphology observed in dynamically symmetric blends far from the critical composition (figure 1.7a and 1.7c). The network structure develops as a result of self-generated stresses in the more elastic phase, and coarsens with time, eventually breaking up into separate domains.

The later stages of spinodal decomposition are characterised by the slow growth of the phase separated domains, further reducing the interfacial area, and thus the total free energy of the system. This process is known as coarsening, and is driven by non-linear mechanisms. It leads to an increase in the characteristic length scale of the system that typically follows a scaling law of the form $\lambda_s(t) \sim t^a$ [26, 27], the value of a being dependent on the precise mechanism responsible for coarsening at that stage in the evolution of the system. For intermediate time scales, the mechanism of evaporation and condensation at phase interfaces is expected to result in Lifshitz-Slyozov scaling, in which a is of the order $1/3$ [28, 21, 29, 22]. At longer time scales, hydrodynamic coarsening mechanisms are expected to dominate the dynamics, and coarsening is both theoretically predicted [30, 31], and observed in numerical simulations [32, 33, 34, 35, 36] and experiments [26, 37, 38, 39] to scale linearly with time ($a = 1$). However, it has been suggested that the high viscosity of polymers tends to damp hydrodynamic effects, resulting in slower scaling, even in the later stages of phase separation [29].

These considerations highlight an important limitation of Cahn-Hilliard-Cook theory: the only phase separation mechanism it attempts to model is diffusion. This is understandable, given the theory's origin in the study of binary alloys, but it is unlikely to be the whole story in binary fluid systems, including polymer blends, where interfacial tension between phases will become salient at longer time scales, as the efficiency of the diffusive mechanism diminishes. This interfacial tension gives rise to hydrodynamic effects, as the interface between the two phases changes shape over time, generating convection currents as it does so.

Therefore, any complete description of the dynamics of a polymer blend ought to take into account the bulk flow of fluid within the system, as well as the diffusive effects, that dominate the early stages of spinodal decomposition. For this reason, our model of a minimal nanocomposite system incorporates

both diffusive and hydrodynamic mechanisms.

1.4 Wetting and Dewetting

The behaviour of liquids in contact with solid surfaces is a field rich in theoretical interest and practical applications. These applications include the formulation of paints, the design of car windscreens, and the manufacture of contact lens solutions [40, 41]. Theoretical, computational, and experimental studies have explored the static equilibrium properties of droplets on solid substrates, and the dynamics of both wetting and dewetting. Such studies have examined the effects of physical defects or chemical impurities in the substrate on wetting behaviour [42, 43], and the wetting properties of thin rubber films where dissipation due to viscoelastic effects may significantly modify the dynamics [44].

In this thesis, we are interested in wetting and dewetting because we expect to see both in our simulations of a minimal nanocomposite system. Therefore, this section gives a brief overview of the theory of both wetting and dewetting and introduces the concepts we will need to describe some of the effects we aim to observe in our simulations.

The starting point for any discussion of wetting is the equilibrium state of a liquid droplet on an ideal solid substrate, as depicted in figure 1.8. At equilibrium, the balance of forces in the x-direction leads to Young's equation:

$$\gamma_S = \gamma_{SL} + \gamma_L \cos\theta_e \tag{1.28}$$

Where γ_S, γ_L, and γ_{SL} are the surface tensions of the solid, liquid and the solid-liquid interface respectively, and θ_e is the equilibrium contact angle. It is common to categorise solid-liquid interfaces according to their *spreading parameter*, S, defined as:

$$S = \gamma_S - (\gamma_{SL} + \gamma_L) \tag{1.29}$$

Physically, the spreading parameter represents the surface energy difference, per unit area, between a dry substrate and the same substrate covered with a thin film of liquid. If $S > 0$, the liquid spreads without limit (in principle)

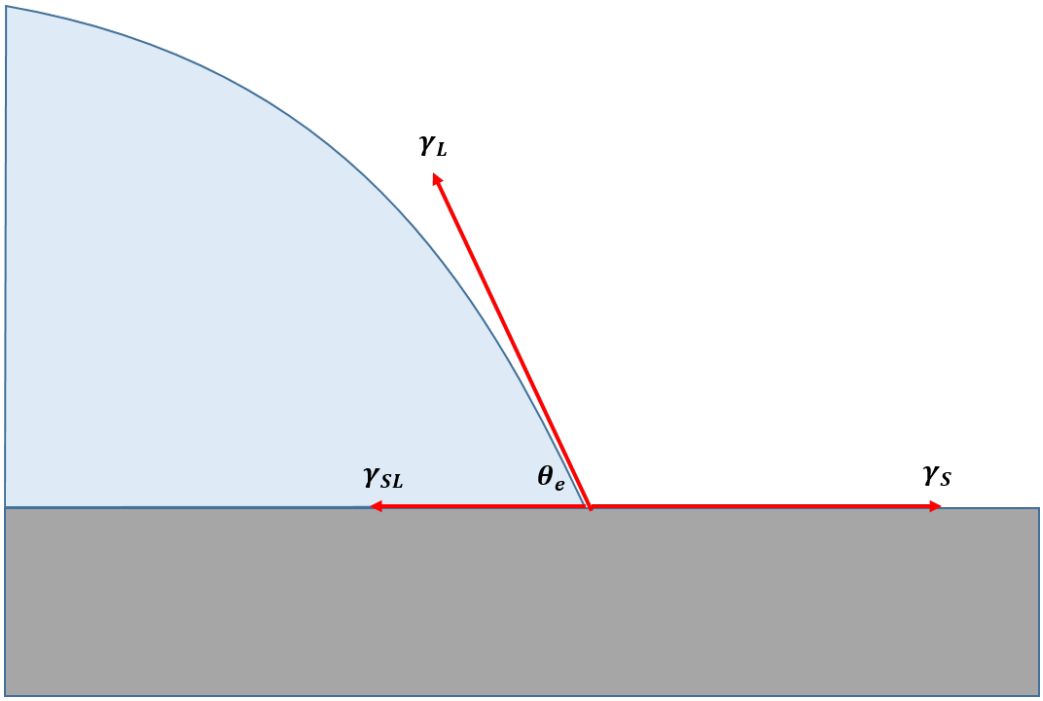

Figure 1.8: The balance of forces at the triple line of a liquid droplet on an ideal, solid substrate, showing the equilibrium contact angle θ_e.

forming a thin film of microscopic thickness, and total wetting is said to occur. In reality, as the thickness of the film approaches the molecular length scale, the balance of intermolecular forces between the three phases often inhibits further thinning of the film, due to the so-called disjoining pressure [41, 45]. If, on the other hand, $S < 0$ partial wetting occurs, and the liquid takes the form of a droplet on the solid, with an equilibrium contact angle determined by:

$$S = \gamma_L(\cos\theta_e - 1) \tag{1.30}$$

Figure 1.9 illustrates the various regimes, from total wetting, through partial wetting, to no wetting, which may occur, for example, when a droplet of water is placed on a highly hydrophobic surface. On scales smaller than what is known as the capillary length, the effect of gravity is negligible. This length scale is typically of the order of a few millimetres [41].

Equation 1.28 may also be derived from the physical picture represented by figure 1.8 using a virtual work principle. In this approach, we imagine the

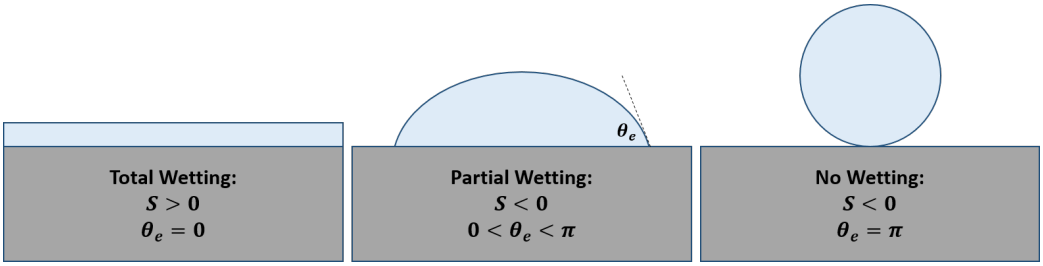

Figure 1.9: Wetting regimes, from total wetting, to no wetting, characterised by the spreading parameter, S, and the equilibrium contact angle θ_e.

work involved in moving the contact line a small distance (δx, say) along the solid substrate, and equate this to the resulting variation of the total interfacial energy. The limitation of both of these approaches is that they are based on a coarse-grained description of the surface tension (or surface energy), so they ignore the effect of non-localised forces (e.g. the van der Waals force) in the vicinity of the interface. Although the range of these forces is small (up to tens of nanometres), they give rise to novel physical effects such as a thin (nanometre scale) precursor film that extends far beyond the macroscopic droplet's boundary [43, 46, 47], and are essential to a full description of wetting dynamics, and other effects, such as diffusio-osmosis [1]. We return to this point when we begin to develop our physical model, in the next chapter.

When a liquid droplet is placed on a solid substrate, it is usually far from thermodynamic and mechanical equilibrium, and will relax towards equilibrium by wetting the surface, either totally or partially. Instead of an equilibrium contact angle, we observe a dynamic contact angle, $\theta_d > \theta_e$, and the radius of the droplet increases, potentially without limit (but see the above comment about the disjoining pressure) when total wetting occurs, leaving a molecular scale film on the substrate.

The dynamics of wetting is governed by the balance between capillary and viscous forces. For small contact angles, and low Reynolds number, the lubrication approximation applies, implying Poiseuille flow within the droplet, and the spreading velocity V is given by [40]:

$$V = \frac{\theta_d \gamma_L (\cos\theta_e - \cos\theta_d)}{3\eta \ln r} \tag{1.31}$$

where η is the viscosity of the liquid, and r is the ratio of the droplet radius,

R, to a characteristic microscopic length scale (so, typically, $|\ln r| \sim 10$). The dynamics of spreading resulting from interfacial tension effects has been the subject of intense research for many years [48, 46]. For now, we note that, again, the above description does not take into account non-localised forces in the vicinity of the substrate, which modify wetting dynamics, just as they modify the equilibrium properties of the droplet. We return to this point in the next chapter.

In contrast *dewetting* refers to the *retraction* of a droplet, far from equilibrium, to its equilibrium state, exposing a dry region of the solid substrate as it retreats. Dewetting is also observed when a thin liquid film on a solid substrate *ruptures* (creating, in effect, a droplet of semi-infinite extent), exposing a dry region, which then expands as the fluid retreats. In both cases, a fluid ridge forms at the solid-liquid boundary, due to conservation of matter and, in the early stages of dewetting, grows in volume (figure 1.10). At longer time scales, following the rupture of a thin film, the fluid ridge itself may break into droplets, due to the Rayleigh-Plateau instability [41], which then continue to dewet by retracting to form smaller droplets. Note that when the liquid interface is between two different liquids, liquid A and liquid B, wetting for one liquid is dewetting for the other. There is no fundamental difference between wetting and dewetting in this respect. It is essentially a matter of initial conditions seen from the point of view of liquid A or liquid B.

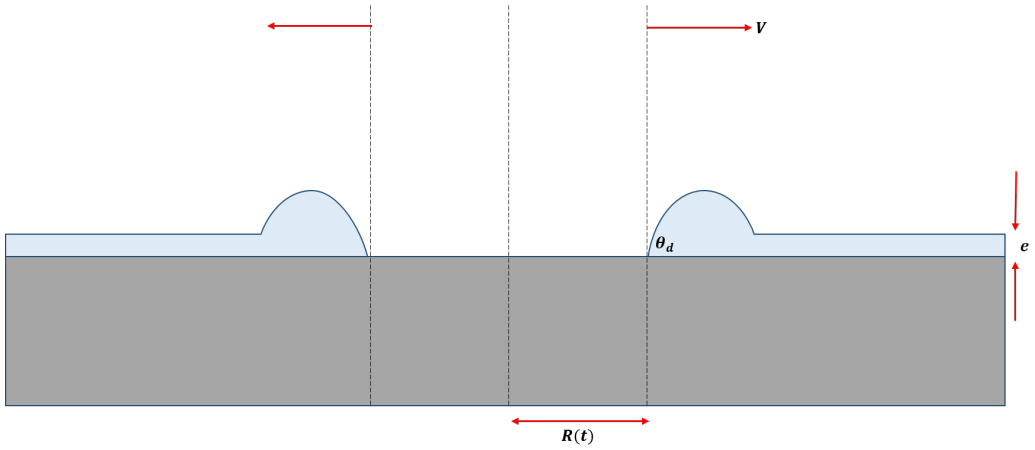

Figure 1.10: Dewetting following the rupture of a thin fluid film of thickness e on a solid substrate. The fluid retracts with a velocity of magnitude V, leaving behind a circular region in its interior, of radius $R(t)$. Conservation of mass implies that a fluid ridge forms at the retracting boundary of the film, with a dynamic contact angle of θ_d, relative to the substrate.

Despite the similarity of the terms, dewetting does not resemble a time-reversed version of wetting: while some of the physical mechanisms involved are the same, the dynamics they give rise to are fundamentally different [49]. For example, an ultra-thin polymer film, subject to viscoelastic effects, can rupture and dewet at speeds high enough to generate a shockwave [41] whereas, as noted previously, the spreading of a droplet is a relatively slow process.

A better point of comparison for dewetting is the spinodal decomposition of a binary system quenched below its critical point, as described in the previous section. Just as small fluctuations in a polymer blend may be amplified and grow rapidly, if the system is in the unstable region of its phase diagram, local fluctuations in the height of a thin film may be amplified, and cause the film to rupture. This instability may be induced by local chemical impurities, physical irregularities in the substrate or, as is the case in spinodal decomposition, by thermal fluctuations, if the film is below a certain critical thickness [50, 51]. In the first two cases, the film is in a metastable state, and dewetting occurs by nucleation and growth, in contrast to spinodal dewetting, which is driven by thermally induced local fluctuations in the height of the film. The analogy with binary systems in metastable and unstable regions of the phase diagram is apparent.

Like spinodal decomposition, spinodal dewetting has a characteristic length scale, related to the critical film thickness, and this often results in patterns of small droplets, or other structures, with long range order. These patterns may be fine-tuned by varying the thickness of the initial film. This ability to fine tune the droplet pattern, following spinodal dewetting, opens up the possibility of a range of applications in, for example, the surface treatment of materials, metallic film manufacturing, and the development of organic semiconductors [52].

In the simulation results, presented in later chapters, we observe both wetting and dewetting in a minimal nanocomposite system, and the existence of a critical film thickness, below which spinodal dewetting occurs.

1.5 Nanoparticles in Polymer Blends: Experimental Perspectives

So far, we have focused on systems consisting of just two components, be they simple fluids of low molecular weight, or polymers, with much greater molecular weight. We have described both the equilibrium thermodynamics of such systems, and the dynamics of phase separation, when the system is quenched below its critical point. In this section, we consider the effect of adding a third component: small, solid particles. Throughout this thesis, we refer to these particles as nanoparticles (or, for brevity, simply as particles) although, in reality, they can range in size from a few nanometres to a few microns in diameter. In terms of the previous section, these are the surfaces that wet, or dewet, as an out of equilibrium system relaxes to a new equilibrium or steady state.

The aim of this section is to identify some of the main themes and questions that emerge in systems with two liquid, and one solid phase, thereby situating the results presented in this thesis within the broader context of the study of nanocomposite materials. Specifically, we highlight studies that consider the *stability* of the structures that result when nanoparticles are added to binary liquids, the effect of varying the *geometry* of those particles, and the effect of varying other properties of those particles, notably their *spreading parameter* with respect to the two liquids in the system. The study of nanocomposite materials is is a large field, so we will be selective in the results we discuss.

Historically, one of the main reasons for adding nanoparticles to a binary liquid system is to improve its stability. For example, nanoparticles may be used as an alternative to such traditional methods as chemical emulsifiers, electrostatic repulsion and steric repulsion to stabilise an emulsion. In the resulting system, known as a Pickering emulsion [53, 54], small droplets of one liquid are surrounded by nanoparticles, shielding them from the other liquid, with which they would not ordinarily mix.

Of more relevance to this thesis are the interpenetrating, bicontinuous microphase structures that emerges in volume symmetric mixtures (and in some volume asymmetric blends), commonly referred to as bijels. As well as enhancing mechanical properties, the continuous nature of the phase domains opens up the possibility of exploiting the electrical properties of composite materials in organic semiconductors with novel applications in photovoltaic films and fuel cells. These novel structures were first predicted in computer

simulations, using the Lattice Boltzmann method, of the de-mixing of binary fluids containing neutrally wetting nanoparticles (i.e. particles with equal affinity for both liquid components in the mixture) [55]. Although the simulations could not be run for long enough to confirm the long-term stability of the bijel structure, the energy threshold for ejecting a nanoparticle from the interface between the two liquid phases was thought to be high enough to prevent depercolation and collapse of the bijel.

Herzig et. al. [56] were the first researchers to observe this new class of material in the laboratory in a mixture of low-molecular weight fluids (2,6-lutidine and water), with added neutrally wetting fluorescent silica nanoparticles. After spinodal decomposition induced by a rapid quench into the two-phase region, it was found that the silica particles migrated to the phase boundaries where, after sufficient numbers accumulated, jamming occurred and arrested further phase domain growth. The result was a bicontinuous structure akin to that predicted by Stratford et. al. [55] that was stable on experimental timescales. Further work, conducted by Lu, Zaccarelli, and their associates [57, 58], and using a different model system found that, for weakly interacting nanoparticles, in a critical binary fluid, bijel formation depends on the concentration of particles added to the binary liquid, the strength of the inter-particle interaction (in thermal units), and the range of the interactions (in units of the particle radius).

The important theoretical and practical question of the stability of bijels is explored further by Reeves et. al. [59, 60]. The stability of a water-lutidine bijel containing fluorescent silica nanoparticles is monitored by measuring the mean interfacial curvature of phase boundaries using confocal microscopy and x-ray computer tomography. The results indicate that smaller nanoparticles, and more rapid quenching, result in "optimally hyperbolic" bicontinuous structures that are more likely to remain stable beyond experimental timescales. For larger particles, with a radius of the order of microns, the bijels formed tend to diverge from this optimal structure over longer timescales of around one hour.

As noted earlier, the geometry of the nanoparticles used might be expected to play a role in the properties of the bijel produced, so rod-like particles, or nano-rods, have also been the subject of experimental and theoretical work. For example, one study by Hijnen et. al. [61], of the stabilisation of bijels from a nitromethane and ethylene glycol mixture, using rod-like silica NPs with an aspect ratio of approximately 10:1, finds that the kinetic arrest of domain growth through the jamming mechanism leads to lower

interfacial separation, and thus a smaller domain size, for any given particle concentration than is the case using spherical nanoparticles, while leaving the overall morphology broadly unchanged. Interestingly, the packing fraction of nano-rods at the phase boundary exceeded theoretical predictions due to the existence of "flippers" – rods that orient themselves perpendicular to the interface, rather than parallel to it.

Polymer blends exhibit much of the same behaviour as mixtures of low molecular weight liquids when nanoparticles are added to them. For example, Chung et. al. [62] describe the formation of a three-dimensional bicontinuous structure in a dPMMA/SAN blend in a thin film geometry when surface-modified, neutrally-wetting silica NPs were added and the blend was allowed to phase separate. The final morphology of the phase-separated system may be tuned by varying the volume fraction of nanoparticles, their radius and the film thickness. A similar study [63] of PMMA/SAN, phase-separating in a thin-film of varying thickness, with silica nanoparticles (1-10% by weight) produced a "jamming map", similar to a phase diagram, of bicontinuous versus discrete morphologies for the polymer blend concerned. The resulting map is compatible with a simple geometrical model of hexagonal close packing of nanoparticles at the phase interfaces.

The neutral-wetting requirement, needed for the production of most bijels using liquids of low molecular weight, becomes onerous when trying to reproduce such structures using polymer blends. Fortunately, Li et. al. [64, 65] show that it is not always necessary, especially if interactions between the nanoparticles are favourable. These studies use a phase-separating blend of PS/PVME and Cadmium Selenide (CdSe) nanoparticles (spheres and rods) to observe the formation of bijels. The nanoparticles are preferentially wetted by the PVME phase, but they are also mutually attractive. The study finds that the critical volume fraction of nano-rods necessary to achieve kinetic arrest of the bicontinuous structure is lower than that for spherical nanoparticles. Although bijel formation is achieved, even without neutral wetting, this comes at a price: the evolution of the system's morphology becomes sensitive to aggregation of the nanoparticles, due to their mutual attraction, so good initial dispersion in the blend is required to achieve the desired final state.

It is possible that the burden of finding neutrally wetting nanoparticles, for a given polymer blend might be alleviated by the use of so-called Janus particles. These are particles with differentiated (usually contrasting) chemical or physical properties, depending on the aspect. For example, a spherical

nanoparticle may be treated chemically so that one half of it is hydrophobic, while the other is hydrophilic. The development of such particles opens up further theoretical and practical avenues, and Walther, Mueller, and their collaborators [66, 67] review their synthesis, self-assembly, properties and potential applications. Although the authors do not specifically refer to applications in phase separating polymer blends, it is clear that the additional functionality provided by Janus particles might support efforts to fine tune the dynamics and microstructure of these systems. Some of these possibilities are explored by Walther et. al. in an earlier paper [68].

An alternative approach is to add two different types of nanoparticle, with contrasting properties, to the polymer blend. In Elias et. al. [69], for example, the stabilisation of an immiscible PP/EVA blend (80/20 by weight) with chemically treated silica nanoparticles is achieved by using both hydrophilic and hydrophobic particles. In the droplet/matrix morphology in which EVA is the minority phase, the droplet size was reduced by the presence of both types of nanoparticles. Similar results were obtained for an immiscible polymer blend of PP/PS (70/30 by weight) with both hydrophilic and hydrophobic nanoparticles.

The precise nature of the mechanism responsible for the stabilisation of morphology by nanoparticles is open to some debate. Du et. al. [70] study a phase separating PMMA/SAN blend, with fumed silica NPs, using a combination of time-resolved small angle light scattering and dynamic rheology. The blends considered range from 30/70 to 60/40, by volume, and the resultant morphologies tend to be matrix/droplet in form but still show stabilisation effects in the presence of nanoparticles, similar to those observed in Pickering emulsions. A two stage process is proposed to account for the final distribution of nanoparticles in the system, and for the size of phase domains: firstly, spinodal decomposition transports particles to phase interfaces where, secondly, they act as nuclei promoting phase separation due to nucleation and growth within the matrix of the majority phase.

Among studies of the *viscoelastic* phase separation of polymer blends with nanoparticles, Zhong et. al. [71] consider the effect of silica particles in several dynamically asymmetric blends (PES/PS, for example) undergoing phase separation. Li et. al. [64, 65] find that the nanoparticles are preferentially immersed in the slow phase of the system due, they surmise, to chain entanglements. Similarly, Yeganeh et. al. [72] explore how nanoparticles introduced into a dynamically asymmetric PS/PVME blend might be used to fine tune the dynamics of phase separation and the resulting morphology.

In this study, both hydrophobic fumed silica particles, which self-assemble in the slow PS-rich phase, and hydrophilic fumed silica particles, which favour self-assembly in the fast PVME-rich phase, are used. Transitions are observed between thermodynamically controlled phase behaviour (i.e. spinodal decomposition) and viscoelastic phase separation, depending on the concentration and type of nanoparticle used.

The significance of these studies of viscoelastic phase separation is that the minority phase is able to form a continuous network structure if it is more elastic (slower) than the majority phase. This opens up the possibility of novel applications. For example, if a conducting polymer is used as the minority component in a blend which undergoes viscoelastic phase separation, it becomes feasible to fabricate a conductive polymer network using very low volume fractions of the polymer concerned.

Finally, a review of the relevant research by Fenouillot et. al. [73] compares the distribution of nanoparticles in a phase-separated polymer blend, with their distribution in a phase separated system of liquids of low molecular weight. The conclusion is that, other things being equal, nanoparticles in a polymer blend tend to be more unevenly distributed after phase separation than they are in systems of binary liquids of low molecular weight. This difference is accounted for in terms of the competition between thermodynamic wetting effects and the dynamics of the mixing process in the polymer blend. In any event, the tendency of nanoparticles to be distributed more unevenly, following the phase separation of a polymer blend, is likely to complicate the fabrication of composite materials with the desired electrical, thermal or mechanical properties.

1.6 Nanoparticles in Polymer Blends: Computational Perspectives

Complex three-phase systems that include many nanoparticles do not lend themselves to analytical treatment, although there are some notable exceptions [74]. Therefore, in this section, we focus on computational approaches to the modelling of such systems. The approach is similar to that of the previous section, in that we highlight some key themes, such as the stability of the phase-separated structure, and the effect of varying the nanoparticle geometry, with a view to situating our research in its broader context. The

section concludes with some general reflections about alternative approaches to modelling these complex systems, and the motivation for the approach we will take in the remainder of the thesis.

On the question of stability, Cates and Clegg [75] return to the simulation work of Stratford et. al. [55] that first predicted the existence of bijels due to the migration of nanoparticles to the interface between the two liquid phases, and subsequent jamming at the interface. One concern arising from this work is that the results of the computer simulations (which used the Lattice-Boltzmann method) do not match the performance of bijels produced experimentally. In particular, the simulations suggest that bijels can form even when the interaction between nanoparticles is purely repulsive, but experimental attempts to produce bijels using mutually repelling particles do not support this prediction.

Similarly Kim and co-authors, including Stratford [76], note that, since the original simulations [55], experiments have shown that bijels may be produced, after quenching, even when there is volume asymmetry between the phases [56]. The Lattice-Boltzmann method is used to simulate the behaviour of a binary solvent with neutrally wetting spherical nanoparticles. The simulations focus on the volume asymmetric case and are able to identify the transition from a bicontinuous structure to the arrested droplet phase (depercolation) as the volume asymmetry of the mixture increases.

In Hore and Laradji [77], large-scale simulations, using dissipative particle dynamics, of spherical nanoparticles in immiscible simple fluids show preferential segregation of neutrally wetting particles at the phase interfaces when $\chi_{AB} \geq |\chi_{AN} - \chi_{BN}|$, where χ is an interaction parameter and the subscripts A, B and N denote the liquid components A and B, and the nanoparticles, respectively. In this regime, at long time scales, the average domain size approaches $\frac{r}{\phi}$ where r is the radius of the nanoparticles and ϕ is their volume fraction.

Hore and Laradji also explore the effect of introducing rod-like nanoparticles into a binary system of immiscible fluids [78]. The parameters of the model are set so that the nano-rods favour dispersion in one of the liquid components. As expected, phase separation is retarded with the addition of nanoparticles, due to them jamming in the preferred component, leading to microphase-separated structures, given a sufficient volume fraction of nano-rods and/or nano-rods of sufficient length. The characteristic length scale of the phase-separated structure is found to decrease as the length and volume

fraction of the nano-rods increases.

In addition to these specific studies, a number of review articles are of note. For example, Allegra et. al. [79] review nanocomposite materials from the perspective of theoretical and computational materials science, taking into account recent experimental results, while Zeng et. al. [80] review the modelling and simulation of polymer nanocomposites at multiple length scales. While the latter contains little about the microstructures that arise when polymer blends containing nanoparticles phase separate, the review contains much helpful background theory. Finally, Yan and Xie [81] offer a wide-ranging survey of how the self-assembly of nanoparticles in a variety of systems, including homopolymer blends and block copolymers, may be modelled. Particles of various geometries are considered, as are potential applications that could exploit the mechanical, optical or electrical properties of the novel materials that might be fabricated. In the final section, Yan and Xie review attempts to simulate the influence of external fields, including shear, electrical and magnetic fields, and how they might be used to further tailor the microscopic structure - and therefore the macroscopic properties - of nanocomposite materials.

Stepping away from the detail, we note the prevalence in computational studies of nanocomposite systems of what might be called *mesoscale* approaches: that is, approaches based on length scales intermediate between the nanometre scale that is characteristic of the molecular dynamics approach, and the macro scale, that is the focus of continuum fluid mechanics. In some ways, molecular dynamics is the natural candidate for modelling nanocomposite systems, since the mechanisms responsible for the dynamics of phase separation, and the resulting microstructures, operate at the nanometre scale. Molecular dynamics, arguably, promises a rigour, grounded in fundamental physical principles, that other computational approaches are unable to match. The drawback is that the reach of simulations based on molecular dynamics is curtailed by the current limits on computational power. Even on very fast supercomputers, it has only been possible to simulate systems of billions of particles for a few hundred nanoseconds [82]. This is not enough to simulate the wetting and dewetting of a single nanoparticle in a two-polymer system, let alone a three-phase system, containing many nanoparticles. Thus, many problems of great interest to interfacial science and the study of soft condensed matter are inaccessible to the molecular dynamics approach.

This accounts for the popularity of more coarse-grained computational approaches to the modelling of nanocomposite systems. Among such methods,

the two main ones, alluded to earlier in this section, are the Lattice Boltzmann Method [83], and dissipative particle dynamics (DPD) [84], both of which are based on the concept of a pseudoparticle. Dissipative particle dynamics, and its refinements, [85, 86, 87] addresses the challenge of modelling a complex, multi-phase, system by coarse graining the system into a collection of point-like particles interacting via both conservative and dissipative forces, in a way that seeks to maintain thermodynamic consistency. While such an approach improves computational efficiency, compared with molecular dynamics based simulations, it does so at the expense of a certain artificiality, and the underlying physics is somewhat obscured. A similar criticism may be made of the Lattice-Boltzmann method. While this criticism might not be unanswerable - and much effort has gone into answering it - we prefer a different approach, grounded in well-understood physical principles.

The more straightforward approach is to apply the familiar methods of continuum fluid mechanics to the problem of simulating the dynamics of our minimal nanocomposite system. It has been known for some time [88] that the continuum approximation remains valid at surprisingly short length scales. Therefore, it becomes feasible to apply continuum fluid mechanics to problems involving the wetting and dewetting of a nanoparticle, and also to the migration of that particle from one liquid phase to another.

One difficulty with applying continuum fluid mechanics at these length scales is that, in principle, the discrete, stochastic nature of the interactions of the nanoparticle surface with molecules in the liquid (and of the interactions between molecules *of* the liquid) ought to be represented. This may be treated quite effectively by adding a stochastic force term to the Navier Stokes equations [89]. The issues that arise here are analogous to those involved when considering the addition of a thermal noise term to the Cahn-Hilliard equation - essentially, the nanocomposite system becomes more sensitive to thermal fluctuations. These effects are of some physical interest, but they are not central to the concerns of this thesis, so we do not include them in our model of the minimal nanocomposite system.

A further persistent difficulty in simulating wetting and dewetting behaviour using fluid mechanical models is the treatment of boundary conditions in multi-phase systems, and the hydrodynamic forces that may act on a particle in the system. These difficulties are not insuperable, but there is a significant computational overhead associated with modelling the complex boundary conditions that arise. Therefore, we adopt a recent approach to overcoming these difficulties, known as fluid particle dynamics, which models

solid particles as fluid particles of extremely high viscosity (typically 50 times greater than that of the surrounding liquid). This method was developed by Araki and Tanaka [90] and applied to a range of physical systems in a series of later papers [91, 92, 93, 94, 95, 96, 97]. As well as computational efficiency, and the ease with which boundary conditions are handled, the fluid particle dynamics approach has other advantages that will become apparent when we develop our model in detail.

1.7 Summary

In this chapter, we have introduced the minimal nanocomposite system that will be the subject of the remainder of the thesis, and presented the essential equilibrium thermodynamics needed to understand it. We have also introduced the Cahn-Hilliard equation, which is used to describe the dynamics of phase separation in two-phase systems, including metallic alloys and polymer blends. Although this equation is usually applied to systems undergoing phase separation, it is relevant to the dynamics of any out of equilibrium system in which two or more phases, separated by phase boundaries, exist. Thus, some version of this equation will be needed to describe our minimal nanocomposite system.

We then explored some of the key concepts needed to understand the phenomena of wetting and dewetting, which we expect to observe in our simulations of a minimal nanocomposite system. In addition to providing the vocabulary to describe the results of our simulations, this also informs the development of our model in the next two chapters, where our central concern is with the behaviour of fluids close to a solid interface.

We then briefly surveyed experimental studies of nanocomposite systems, including bijels, in which the two liquid phases are of low molecular weight, focusing especially on questions of their stability, and the effect of varying the physical and chemical properties of the nanoparticles, and their geometry. The aim was to illustrate the complexity of the field, and to thereby motivate the radical simplification involved in studying a minimal nanocomposite system, while placing this thesis in its wider context.

Finally, we explored some computational approaches to modelling nanocomposite systems, moving rapidly from particular studies, to general reflections about which approaches are most likely to be appropriate for the task of

modelling a minimal nanocomposite system. Our conclusion is that continuum fluid mechanics offers the most straightforward approach, and gives the clearest description of the essential physics of such a system. Further, the difficulties traditionally associated with applying continuum fluid mechanics to multi-phase systems that include solid surfaces, may be mitigated by the adoption of the method, developed by Araki & Tanaka, of fluid particle dynamics.

In the next chapter, we describe the theoretical framework needed to build a model that incorporates both the diffusive effects represented by the Cahn-Hilliard equation, and the hydrodynamic flows that are the subject of continuum fluid mechanics.

Chapter 2

Theoretical Framework

2.1 Introduction

A version of this chapter was previously published in the journal *Soft Matter* (reference [1]). The theoretical framework and the derivations described in that paper are the work of Didier Long, and were developed in the early stages of this project. I contributed to discussions about the theoretical framework, commented on draft versions of the paper and provided the figures used in it. This chapter omits some parts of the paper that are not central to the argument of my thesis, and harmonises the language used in the paper with that used in the rest of this thesis.

Our aim in this chapter is to present a theoretical framework, within which it is possible to describe the motion of an inhomogeneous liquid in the vicinity of a solid interface. We approach the matter indirectly, starting with some general reflections on what we call force-free motions in liquids. We then turn to the phenomenon of diffusio-osmosis, whereby a concentration gradient of a solute, within a solvent, gives rise to a flow, parallel to a solid surface. The usual explanation of this effect, due to Derjaguin [98], posits the existence of an excess pressure, typically confined within a layer of a few nanometres, which arises from the interaction between the liquid and the solid surface. Due to the concentration gradient in the liquid, a confined pressure gradient parallel to the surface emerges, and it is this pressure gradient that drives the diffusio-osmotic flow. However, this picture appears to be in contradiction with the contact theorem of colloidal science, according to which such excess

pressure does not exist.

Therefore, we propose an alternative theoretical approach to calculating the hydrodynamic flow in a inhomogeneous liquid near a solid interface, which is consistent with the contact theorem. This approach is based on a Gibbs free energy and a virtual work principle, introduced by Doi [99], and is used to derive a version of the Stokes equation consistent with the principles of non-equilibrium thermodynamics. Our version of the Stokes equation is similar to that used by Araki and Tanaka [90, 95, 91, 93].

After showing how our formalism may be applied to the simple case of diffusio-osmotic flow in a capillary due to a uniform concentration gradient, we turn to the phenomenon of wetting. Within our approach, it is clear that the same physics is at play in both diffusio-osmosis and wetting, since we can go continuously from the latter to the former, simply by making the concentration gradient sharper. Having established the applicability of our version of the Stokes equation to systems in which wetting occurs, we are then in a position to construct a model of the minimal nanocomposite system that is the subject of this thesis.

2.2 Force-Free Motion and Diffusio-Osmosis

The most simple description of hydrodynamic motion is provided by the Stokes equation, which is valid when inertial effects are negligible, in the so-called low Reynolds number limit [89]. Despite this simplification, the Stokes equation may usefully be applied to a broad range of physical phenomena. For example, it is the relevant equation to describe the dynamics of a polymer undergoing Rouse relaxation, or Zimm relaxation, which takes into account long-range hydrodynamic interactions [99].

The Stokes equation is also used to describe the motion of an electrically charged particle, under the influence of an external electric field, in a liquid [100], a phenomenon known as electrophoresis. The same equation describes the hydrodynamic flow created in a capillary when an electric field is applied [100], which is known as electro-osmosis. The electric field exerts a force in the vicinity of the capillary, where the liquid is electrically charged within the Debye layer. This force pulls the liquid in the vicinity of the capillary and a so-called plug flow is created: velocity gradients are non zero within a few Debye lengths of the capillary wall and, beyond that, the hydrodynamic

flow is uniform.

The Stokes equation is relevant, too, to the description of wetting phenomena [40, 41]. Here, a central issue is accounting for how a droplet spreads on a surface, in order to reduce the interfacial energy, which is the driving force of the effect. As noted in the previous chapter, the reverse process, dewetting, is the retraction of a thin film to form one or more droplets, after it has been spread on a solid surface. Both of these processes are described by Stokes equation in the presence of pulling forces resulting from surface tension imbalances at the triple line between the solid substrate, the liquid, and the atmosphere - or between the substrate and the two liquids, if the droplet is situated within another liquid.

Wetting and dewetting are examples of what have been called force-free motions [101] since, in both cases, motion occurs as a result of internal forces in the system, and in the absence of an external applied field. The contrast is with electrophoresis and electro-osmosis, where the force driving the hydrodynamic flow is the result of an externally applied electric field. Other examples of force-free motions include diffusio-phoresis, in which a solid particle moves in a liquid where there is a concentration gradient, and thermophoresis, in which a particle moves in a liquid with a temperature gradient [100]. A further example of force-free motion occurs when polymer blends undergo the process of spinodal decomposition, described in the previous chapter. As we noted, as well as the diffusive effects described by the Cahn-Hilliard equation, there are also hydrodynamic effects, as the interface between the two liquid phases deforms, pushing liquid from one region of the system to another. The essential point is that this motion occurs in the absence of an applied external field [102, 11].

Usually, each of these phenomena is described in its own specific way. Spinodal decomposition is described by the Cahn-Hilliard equation and its extensions: a gradient of chemical potential results in diffusion and, possibly, also in convection. The wetting dynamics of a droplet is described in terms of the imbalance of capillary forces at the triple line, which induces a Poiseuille-like Stokes flow in the droplet. Diffusio-osmosis and diffusio-phoresis are described by the Derjaguin's model [100, 103, 98, 104, 105, 106], which we consider in the next section. However, given the features that all of these effects have in common, it is desirable to seek a more unified theoretical treatment.

In addition, we believe Derjaguin's treatment of diffusio-osmosis, and the

work on diffusio-phoresis that builds on it, to be problematic. It assumes that the interfacial forces between the solid surface and the liquid, which have a range of a few tens of nanometers, create a local pressure in the vicinity of the interface. A gradient of composition along a capillary results in a gradient of pressure due to the interaction between the liquid and the solid interface. This gradient of pressure in the vicinity of the solid interface creates a diffusio-osmotic flow, which takes the form of a plug flow, if the composition gradient in the vicinity of the interface is constant along the capillary. Calculating the pressure gradient requires a detailed description of forces on a local scale between the liquid and the interface, including any ionized charges in its vicinity when the interface becomes ionized. This description is complex and cannot easily be checked experimentally. In any case, Derjaguin's description of diffusio-osmosis appears to contradict the well established contact theorem of colloidal science [107, 108, 109, 110, 111, 112], according to which the pressure between two plates immersed in a liquid is uniform between the plates. The pressure becomes equal to the atmospheric pressure, assuming that the system is equilibrated under standard conditions, when the distance between the two plates is larger than a few tens of nanometers, depending on the range of the interactions. In particular, the interfacial interactions between a single plate and the liquid do not result in the presence of a pressure in the vicinity of the solid surface. The pressure is uniform and is equal to the pressure under which the system is at thermodynamic equilibrium.

Therefore, there is a need to reconcile what is known in colloidal science about the equilibrium state in the vicinity of solid surfaces, and the description of the physics of diffusio-osmosis. The description of the latter, in its present state, is in contradiction with the former. We solve this problem by introducing a mesoscopic description of Stokes flow in inhomogeneous solutions, and in the presence of solid interfaces, as a relaxation process towards thermodynamic equilibrium in a way that is consistent with the Onsager general formulation. This description is based on a variational principle which relates the Gibbs free energy of the system to the driving forces in the Stokes equation. This variational principle was introduced by Doi and Onuki [113] and is directly linked to the fact that the Stokes equation is an Onsager-like equation [89, 114] which drives the evolution of the system in out-of-equilibrium conditions, and which relate the fluxes to the thermodynamic forces in a linear manner.

Our approach allows for the description of convection in inhomogeneous liquids, and of flow in the presence of solid interfaces in situations corresponding either to wetting, dewetting or diffusio-osmosis. In particular there is no

need for a confined pressure field in the vicinity of solid surfaces for creating diffusio-osmotic flows. Our description allows for a common formalism that encompasses both diffusio-osmosis and wetting as relaxation processes towards thermodynamic equilibrium. In both cases, the essential physics is the same, since one can go continuously from the former to the latter by making the composition gradient sharper.

2.3 Derjaguin's Theory of Diffusio-Osmosis

Derjaguin considers the case of a solution bounded by a solid surface. The volume fraction of the solute is denoted by ψ. In the vicinity of the surface, there is an interaction potential Φ which decays with the distance z from the surface. This interaction potential exerts a body force due to the solute concentration which is given by $\mathbf{f}_{ext} = -\psi\boldsymbol{\nabla}\Phi$ which we assume to be oriented in the direction opposite to the normal to the surface. The Stokes equations read [89]:

$$\begin{aligned} -\boldsymbol{\nabla}p + \boldsymbol{\nabla}.\eta\left(\boldsymbol{\nabla}\mathbf{v} + \boldsymbol{\nabla}\mathbf{v}^{+}\right) - \psi\boldsymbol{\nabla}\Phi = \mathbf{0} \\ \boldsymbol{\nabla}.\mathbf{v} = 0 \end{aligned} \tag{2.1}$$

where η is the viscosity, p is the pressure, $\mathbf{v}$ is the velocity field, and the second equation represents the assumption of incompressibility. The flow velocity is zero in the z-direction and is parallel to the interface. Let us suppose that the gradient of solute volume fraction is in the x-direction, and is a decreasing function of x. By considering equation 2.1 in the z-direction, we obtain:

$$-\frac{\partial p}{\partial z} - \psi\frac{\partial\Phi(z)}{\partial z} = 0 \tag{2.2}$$

Integrating between the current z-position and a point far from the solid surface, we obtain an expression for the pressure term:

$$p(x,z) = -\psi(x)\Phi(z) + p_0 \tag{2.3}$$

where p_0 is, for example, the atmospheric pressure under which the system is equilibrated, in the absence of solute concentration gradient. This pressure field is confined within a layer corresponding to the range of the interaction potential, which may be a few nanometers, or up to a few tens of nanometers, depending on the nature of the interactions, and the the depth of the Debye layer of the solution due to ionic interactions.

We see that this pressure field is present even in the absence of a gradient of solute concentration, provided the solute concentration is not zero. If one considers a high volume fraction of solute, for example 1%, and if the interaction potential is 0.1 eV per molecular volume at the surface, the pressure is of order 10^7 Pa and, beyond the interfacial layer, rapidly decays to the atmospheric pressure, under which the system is equilibrated. If the interface we consider is that of a capillary with diameter a few micrometers or more, which connects two reservoirs, one with a high solute concentration and the other one without solute, a concentration gradient is established along the capillary in the vicinity of its surface. The surface of the latter can be considered as flat if the diameter is much larger than the range of the potential, Φ, as we assume. Then, the pressure gradient is described by equation 2.3 and equation 2.1 becomes:

$$\frac{\partial \psi(x)}{\partial x}\Phi(z) + \eta \frac{\partial^2 v_x}{\partial z^2} = 0 \tag{2.4}$$

Let us assume that Φ is given by:

$$\Phi(z) = \Phi(0) \exp\left(\frac{-z}{\lambda}\right) \tag{2.5}$$

This equation allows us to calculate the flow velocity profile:

$$v_x(z) = \frac{\lambda^2}{\eta}\frac{\partial \psi(x)}{\partial x}\Phi(0)\left(\exp\left(\frac{-z}{\lambda}\right) - 1\right) \tag{2.6}$$

Equation 2.6 represents the so-called plug-flow observed in diffusio-osmosis experiments, and also in electro-osmosis [115]. This is standard behaviour when forces act on the liquid only within a thin layer in the vicinity of a solid surface, as is the case for diffusio-osmotic flow. The driving force in Derjaguin's picture is the pressure field in the vicinity of the capillary wall.

However, the term $p(x, z)$ is difficult to interpret. Even in the absence of a concentration gradient, it corresponds to a local pressure with an order of magnitude between 10^6 Pa and 10^7 Pa. This pressure should be maximal at the interface between the solid and the liquid, and decay towards the atmospheric pressure over the distance represented by the range of the interaction potential, $\Phi(z)$. As mentioned above, this picture contradicts the current understanding of interactions between colloidal particles in solutions, and of the thermodynamic equilibrium of a liquid in the vicinity of a solid surface. For instance, if one considers two parallel plates in an electrolyte solution [109], the Poisson-Boltzmann model predicts that the repulsive pressure between the two plates is homogeneous in the volume bounded by these two plates and is given by :

$$P(z, D) = k_B T \rho_0(D) + p_0 \tag{2.7}$$

where k_B is the Boltzmann constant, T is the temperature, D is the distance between the two plates, $\rho_0(D)$ the counterion density due to the surface charges on the plates and z the coordinate in the direction normal to the plates. In particular the pressure is uniform and decays to zero when the plates are separated by a distance larger than the range of the molecular interactions, which are typically of order a few nanometers, and up to a few tens of nanometers. In a capillary of diameter greate than one micrometer, say, this pressure is uniform and equal to the atmospheric pressure p_0. This result is known as the contact theorem [109, 107, 111, 110], and is considered exact, beyond the Poisson-Boltzmann approach, and regardless of the nature of the interactions.

The presence of a thin layer, with a pressure greater than the atmospheric pressure under which the system is equilibrated, raises a further question about the meaning of the grand-canonical equilibrium under an imposed pressure (*e.g.* atmospheric pressure p_0) if some regions of the system have a higher pressure than the nominal pressure p_0, as a result of the interactions between parts of the system. For instance, the thin layer with a higher pressure in Derjaguin's picture should relax by slightly expanding to decrease the pressure towards p_0, thereby reducing the Gibbs free energy of the system. The very presence of this thin layer with a higher pressure seems to contradict the very concept of thermodynamic equilibrium under an imposed pressure.

Our view is that Derjaguin's calculation only takes into account the part of the stress tensor, corresponding with the long-range molecular interaction

between the solid surface and the solute. However, this is not correct: for instance, when one considers the thermodynamics of dielectric media one does not consider separately the stress associated with intermolecular interactions, and the stress of the electric field itself. One considers only the whole. This is the meaning of the equilibrium condition discussed in Landau and Lifshitz [116], for which the field and the density of the sample relax together towards thermodynamic equilibrium. It is explicitly stated that there is no body force in the dielectric. In contrast, in Derjaguin's picture, the interaction between the solid surface and the liquid are treated as external body forces acting on the liquid. In a dielectric, all forces on an elementary volume are transmitted through the boundaries by the local stress tensor $\boldsymbol{\sigma}$ which therefore satisfies the condition [116]:

$$\boldsymbol{\nabla}.\boldsymbol{\sigma} = 0 \tag{2.8}$$

Derjaguin's approach violates this condition by introducing a body force. Thermodynamic equilibrium is properly described by minimizing the contribution of all the interactions, including that of the field and that of the intermolecular forces, and these cannot be considered separately. This is what makes necessary the introduction of the polarizability of a material. Similarly, the body force in Derjaguin's treatment of diffusio-osmosis is only one component of the interaction. But one cannot suppose that only a part of the local stress tensor acts on an elementary volume within the liquid, without taking into account all the contributions to the stress tensor. And when one does take into account all the contributions, the pressure is that under which the system is equilibrated (in our example, the atmospheric pressure p_0). As a consequence, Derjaguin's picture breaks down for describing diffusio-osmosis.

Therefore, we propose another approach to the explanation of diffusio-osmosis, consistent with what is known about the equilibrium thermodynamics of liquids in the vicinity of colloidal particles, or solid surfaces, in general.

2.4 Hydrodynamics in Out-of-Equilibrium Liquids

In this section, we introduce a formalism for the Stokes equations in out-of-equilibrium liquids, based on a virtual work principle, introduced by Doi and Onuki [113]. This allows us to obtain equations which describe the Stokes flow as a relaxation process towards thermodynamic equilibrium. We use a non-specific Gibbs free energy, in contrast with the Ginzburg-Landau form in equation 1.22 and the Flory-Huggins-de Gennes form in equation 1.23, as we wish our treatment to remain as widely applicable as possible, for now. This free energy is made dimensionless by considering the Gibbs free energy per monomer (or per molecule), and by dividing the physical Gibbs free energy by the thermal energy, while setting the unit length equal to the monomer length, or the molecular radius, in simple liquids. In an out-of-equilibrium situation, one can calculate the stress as a driving force in a liquid according to a principle of virtual work. The total Gibbs free energy is given by:

$$G = \int g(\psi(\mathbf{r}), \boldsymbol{\nabla}\psi(\mathbf{r}))d^3\mathbf{r} \tag{2.9}$$

where g is the density of Gibbs free energy and is a function of ψ and $\boldsymbol{\nabla}\psi$. The dependence of g on $\boldsymbol{\nabla}\psi$ allows us to take into account the finite range of the interactions. Following Doi and Onuki [113], let us consider a virtual displacement in the liquid so that $\mathbf{r}$ is transformed into $\mathbf{r}+\delta\mathbf{r}$. The quantities ψ and $\boldsymbol{\nabla}\psi$ are varied by the amounts:

$$\begin{aligned} \delta\psi &= -\delta\mathbf{r}.\boldsymbol{\nabla}\psi; \\ \delta\boldsymbol{\nabla}\psi &= \boldsymbol{\nabla}\delta\psi \end{aligned} \tag{2.10}$$

Further, let us assume that the density of Gibbs free energy is the sum of two contributions :

$$g(\psi, \boldsymbol{\nabla}\psi) = g^{(0)}(\psi) + g^{(1)}(\boldsymbol{\nabla}\psi) \tag{2.11}$$

Then

$$G = \int g(\mathbf{r})d^3\mathbf{r} = \int \left(g^{(0)}(\psi) + g^{(1)}(\boldsymbol{\nabla}\psi)\right) d^3\mathbf{r} \tag{2.12}$$

and the variation in the Gibbs free energy is given by :

$$\delta G = \int \delta g(\mathbf{r}) d^3\mathbf{r} = \int \left(\frac{dg^{(0)}}{d\psi}\delta\psi + \frac{dg^{(1)}}{d\boldsymbol{\nabla}\psi}.\delta\boldsymbol{\nabla}\psi \right) d^3\mathbf{r} \tag{2.13}$$

By substituting equation 2.11 into equation 2.13, and integrating the second term by parts, we obtain:

$$\delta G = \int -\delta\mathbf{r}.\boldsymbol{\nabla}\psi \left(\frac{dg^{(0)}}{d\psi} - \left(\boldsymbol{\nabla}.\frac{dg^{(1)}}{d\boldsymbol{\nabla}\psi} \right) \right) d^3\mathbf{r} \tag{2.14}$$

We assume that the term

$$\frac{dg^{(1)}}{d\boldsymbol{\nabla}\psi}\delta\mathbf{r}.\boldsymbol{\nabla}\psi \tag{2.15}$$

is zero on the boundaries. This is the case if the flow concerned is zero at the boundaries, or if the fluid is homogeneous at these boundaries. If this is not the case, an additional contribution at the boundaries should be added (equal to $\nabla.\frac{dg^{(1)}}{d\nabla\psi}\delta\mathbf{r}\nabla\psi$).

The stress is related to the variation in the Gibbs free energy by:

$$\delta G = -\int \delta\mathbf{r}.\boldsymbol{\nabla}\boldsymbol{\sigma}_G d^3\mathbf{r} \tag{2.16}$$

Thus, we obtain an expression for the hydrodynamic stress associated with the release of excess Gibbs free energy:

$$\boldsymbol{\nabla}.\boldsymbol{\sigma}_G = \left(\frac{dg^{(0)}}{d\psi} - \boldsymbol{\nabla}.\frac{dg^{(1)}}{d\boldsymbol{\nabla}\psi} \right) \boldsymbol{\nabla}\psi \tag{2.17}$$

This equation may also be written as

$$\boldsymbol{\nabla}.\boldsymbol{\sigma}_G = \frac{dg}{d\psi}\boldsymbol{\nabla}\psi = \mu\boldsymbol{\nabla}\psi \tag{2.18}$$

where $\frac{dg}{d\psi}$ is the generalized chemical potential and is a functional derivative that includes contributions from the gradient of the composition.

We may also introduce the quantities:

$$\begin{aligned} \mu^{(0)} &= \frac{dg^{(0)}}{d\psi} \\ \mu^{(1)} &= \frac{dg^{(1)}}{d\psi} \end{aligned} \tag{2.19}$$

where $\mu^{(0)}$ is the usual bulk chemical potential and $\mu^{(1)}$ reflects the contribution of $\boldsymbol{\nabla}\psi$ to the Gibbs free energy. This is this term which gives rise to surface tension in inhomogeneous liquids. The force term resulting from thermodynamic forces has to be included in the Stokes equation for describing hydrodynamic flow in out of equilibrium conditions.

The stress tensor, $\boldsymbol{\sigma}_G$, introduced above enables us to calculate the free energy release associated with a flow field $\mathbf{v}$, while the Stokes equation allows us to calculate the dissipation due to the flow. When a liquid is subjected to a body force $\mathbf{f}_{ext}$, the dissipated power P is:

$$P = -\int d^3r \boldsymbol{\nabla}.\boldsymbol{\sigma}_{Hydr}.\mathbf{v} = \int \mathbf{f}_{ext}.\mathbf{v} \tag{2.20}$$

When the forces are purely internal, the dissipation is equal to minus the rate of release of free energy, $\boldsymbol{\sigma}_G$, and the equations read:

$$P = -\frac{dG}{dt} = \int \mathbf{v}.\boldsymbol{\nabla}\boldsymbol{\sigma}_G d^3\mathbf{r} \tag{2.21}$$

From which it follows that:

$$\boldsymbol{\nabla}.\boldsymbol{\sigma}_{Hydr} + \boldsymbol{\nabla}.\boldsymbol{\sigma}_G = 0 \tag{2.22}$$

Where we now take the local form of this identity. This equation ensures that the relaxation of the fluid towards equilibrium is consistent with Onsager theory. The fluxes, $(\boldsymbol{\nabla}\mathbf{v})$, are proportional to the thermodynamic forces,

$-\boldsymbol{\sigma}_G$. The free energy release rate is equal to the dissipation rate, and this equality is local. The basic equation regarding the hydrodynamic flow is therefore:

$$\begin{aligned} -\boldsymbol{\nabla} p + \boldsymbol{\nabla}.\eta \left(\boldsymbol{\nabla}\mathbf{v} + \boldsymbol{\nabla}\mathbf{v}^{+} \right) + \mu \boldsymbol{\nabla}\psi = \mathbf{0} \\ \boldsymbol{\nabla}.\mathbf{v} = 0 \end{aligned} \tag{2.23}$$

In addition to the term $\mu\boldsymbol{\nabla}\psi$, we may add an external force $\mathbf{f}_{ext}$ which would drive the system out-of-equilibrium. The Stokes equations then read:

$$\begin{aligned} -\boldsymbol{\nabla} p + \boldsymbol{\nabla}.\eta \left(\boldsymbol{\nabla}\mathbf{v} + \boldsymbol{\nabla}\mathbf{v}^{+} \right) + \mathbf{f}_{ext} + \mu \boldsymbol{\nabla}\psi = \mathbf{0} \\ \boldsymbol{\nabla}.\mathbf{v} = 0 \end{aligned} \tag{2.24}$$

These are Onsager-like equations [89, 117, 114] and describe the relaxation towards equilibrium of a system in a way that is consistent with the general principles of out-of-equilibrium statistical physics [114, 89, 117].

2.5 Hydrodynamics and Non-Equilibrium Statistical Physics

The Navier-Stokes equations are described in Landau and Lifshitz [89] as a branch of out-of-equilibrium statistical physics. Out-of-equilibrium systems are also described by Onsager, through the introduction of an out-of-equilibrium entropy. This entropy is smaller than that at equilibrium, and is expressed as a function of coarse-grained variables x_a, while the derivative of the entropy with respect to each of these variables provides the corresponding thermodynamic forces X_a:

$$X_a = -\frac{\partial S}{\partial x_a} \tag{2.25}$$

Then, the variables x_a relax towards equilibrium according to the Onsager equations:

$$\frac{dx_a}{dt} = -\Sigma\gamma_{a,b}X_b \tag{2.26}$$

where the matrix of Onsager coefficients, $\gamma_{a,b}$, is symmetric positive definite. This equation describes how the entropy increases in order to reach thermodynamic equilibrium, when it is at its maximum. The Navier-Stokes equations can be accommodated within Onsager's formalism by introducing an explicit spatial aspect. The entropy production is then:

$$\frac{dS}{dt} = -\int \Sigma X_a \dot{x_a} dV \tag{2.27}$$

From the expression of the entropy production derived from the Navier-Stokes equations, which express the conservation of momentum, energy, mass, and each component in a mixture, it is then possible to identify the appropriate thermodynamic forces X_a and fluxes $\dot{x_a}$ [89]. The thermodynamic forces, as derived from the Navier-Stokes equations, appear as equal to the thermal gradient and to the chemical potential gradient.

Therefore, the Navier-Stokes equations describe the relaxation processes for Newtonian liquids, when they are out of thermodynamcial equilibrium, as their entropy increases to its maximum possible value. These relaxation processes, as described in Landau and Lifshitz [89] or in De Groot and Mazur [114] are thermal diffusion, and solute diffusion. Note that no coupling between the out-of-equilibrium thermodynamical state and hydrodynamic flow has been introduced, at this point.

Compared to the standard treatment, described above, we make two changes. Firstly, instead of considering an out-of-equilibrium entropy S, we work with an out-of-equilibrium Gibbs free energy, G. In introducing an out-of-equilibrium entropy, the standard treatment treats each small volume elements in the liquid as a closed system. Then, the internal state of the volume elements evolves so that their total entropy is maximised. The Navier-Stokes equations allow for describing the exchange of energy between neighbouring volume elements of the fluid by introducing energy conservation laws. However, when considering the phenomena of wetting or chemo-osmosis problems, the full Navier-Stokes equations are not necessarily required, and the small volume elements may be considered to be thermostated. In that case, the relevant out-of-equilibrium function is the local excess of free energy. Further, if the pressure is reckoned to be imposed, the relevant function is, again,

the local excess of Gibbs free energy. Thus, in contrast with the standard approach, we describe the relaxation processes in an out-of equilibrium fluid in terms of the release of an excess of Gibbs free energy. This is what is done, for example, when considering relaxation processes in polymer rheology where the corresponding function denoted A is called the dynamical free energy in Doi and Edwards [99], and is essentially the excess of Gibbs free energy we have just described.

Secondly, we do not consider solute diffusion, because it is either very fast in the direction normal to the solid surfaces concerned, or too slow in the direction parallel to the solid surfaces that we consider. Nor do we consider thermal diffusion because energy is not conserved in either the canonical ensemble or in the Stokes equation - instead, energy is exchanged rapidly with the thermostat. However, extension of the present theory to describe solute and thermal diffusion, along the lines described in Landau and Lifshitz [89] is possible. In fact, this has been has been done by Julicher and Prost [118], without discussing the effects of convection, or the effect of interfaces, characterised by surface tension gradients, on the flow.

The entropy production function, calculated with reference to the Navier-Stokes equations [89, 114] is important because it relates fluxes to the relevant thermodynamic forces, and allows us to identify them in a way that is consistent with the general formalism of Onsager. Our approach is to do the same for convection, which has not been considered in this way, to the best of our knowledge.

Starting with equation 2.21, which has the required general form, we deduce that $\mathbf{v}$ represents the relevant flux, and that $\boldsymbol{\nabla}\boldsymbol{\sigma}_G = \mu\boldsymbol{\nabla}\psi$ is the thermodynamic force. The general solution is:

$$\mathbf{v} = \mathbf{M}\boldsymbol{\nabla}.\boldsymbol{\sigma}_G \tag{2.28}$$

where $\mathbf{M}$ is a mobility tensor. The only solution for the flow which has the required symmetry (i.e. which is invariant under translation and rotation) is that given by the Stokes equation [89]. Hence the flow is given by the solution of the Stokes equation 2.24.

2.6 Hydrodynamics without Boundary Conditions

Let us consider the Stokes equations in the presence of a chemical composition gradient in unbounded three-dimensional space. In the absence of short-ranged interactions, (i.e. when there is no surface tension term, or gradient term in the free energy), a heterogeneous composition does not create any flow in an unbounded fluid. Indeed, in these conditions, the quantity μ is a function of ψ only and not of $\boldsymbol{\nabla}\psi$. The corresponding driving force in equation 2.24 due to the composition gradient can be written as:

$$\mu(\psi)\boldsymbol{\nabla}\psi = \boldsymbol{\nabla}g^{(0)}(\psi) \tag{2.29}$$

since we have:

$$\frac{dg^{(0)}(\psi)}{d\psi} = \mu(\psi) \tag{2.30}$$

The Stokes equation then reads:

$$\begin{aligned} -\boldsymbol{\nabla}\left(p - g^{(0)}(\psi)\right) + \boldsymbol{\nabla}.\eta\left(\boldsymbol{\nabla}\mathbf{v} + \boldsymbol{\nabla}\mathbf{v}^{+}\right) &= \mathbf{0} \\ \boldsymbol{\nabla}.\mathbf{v} &= 0 \end{aligned} \tag{2.31}$$

where, for simplicity, we now assume there is no external force acting on the liquid.

From these two equations, we obtain the following:

$$\begin{aligned} -\boldsymbol{\nabla}\left(p - g^{(0)}(\psi)\right) + \eta\boldsymbol{\nabla}^2\mathbf{v} &= \mathbf{0} \\ \boldsymbol{\nabla}^2\left(p - g^{(0)}(\psi)\right) &= 0 \end{aligned} \tag{2.32}$$

Given the boundary conditions of uniform pressure and solute concentration at infinity, and of no flow at infinity, we obtain the following solution:

$$p - g^{(0)}(\psi) = p_0;$$
$$\mathbf{v} = \mathbf{0} \tag{2.33}$$

The physical pressure is the entire term $p - g^{(0)}(\psi)$ and is uniform. The quantity p is not the total pressure, it is just the Lagrange multiplier that ensures the incompressibility of the flow. The term $\mu\boldsymbol{\nabla}\psi$, which appears as a body force in the Stokes equation, would result in a longitudinal flow with non zero divergence. This effect must be compensated for to maintain the purely transverse nature of the flow. Without the non-local interactions, as represented by the dependence of the Gibbs free energy on $\boldsymbol{\nabla}\psi$, a non-homogeneous composition cannot create convection in an unbounded fluid, and the relaxation towards equilibrium occurs entirely by diffusion. For example, if we consider a salt gradient concentration in water, if there is no long range interaction, and the chemical potential depends only on the local concentration, ψ, such a gradient cannot create flow. In fact the local Lagrange multiplier, p, adjusts so that $p - g^{(0)}(\psi)$ is uniform, and no flow takes place. This issue has been discussed, with different arguments, by Julicher and Prost [118].

In contrast, the term $g^{(1)}$ *does* contribute to convection flow in the presence of concentration gradients. The corresponding term in the Gibbs free energy is responsible for the surface tension between two phases of a polymer blend (or a simple binary liquid) undergoing spinodal decomposition, [11, 119]. Thus, all the convection in such out-of-equilibrium systems is due to surface tension-like effects; that is, all the contributions to convection come from the dependence on $\boldsymbol{\nabla}\psi$ of the Gibbs free energy.

Finally, another way to see that $g^{(0)}$ contributions cannot give rise to convection is the following. Under an infinitesimal displacement, the new Gibbs free energy is given by:

$$G' = \int g(\mathbf{r})d^3\mathbf{r} = \int g^{(0)}(\psi(\mathbf{r} - \delta\mathbf{r}))d^3\mathbf{r} \tag{2.34}$$

Now, consider the change of variable $\mathbf{r}' = \mathbf{r} - \delta\mathbf{r}$. Since incompressibility is assumed, the allowed displacements preserve the volume, and the corresponding Jacobian of the change of variable is 1. Thus, we have:

$$G' = \int g^{(0)}(\psi(\mathbf{r} - \delta\mathbf{r}))d^3\mathbf{r} = \int g^{(0)}(\psi(\mathbf{r}))d^3\mathbf{r} \tag{2.35}$$

Virtual displacements which preserve the volume cannot change the Gibbs free energy when the latter depends only on local variables. As a consequence, there can be no convection due to purely local contributions to the Gibbs free energy, such as those corresponding to ideal solutions. For convection to occur, we need to introduce short-range interactions and a concentration gradient contribution to the Gibbs free energy.

Therefore, when there are no short-range interactions, the concentration evolves towards equilibrium only by diffusion (or, conceivably, by an imposed convection), but composition gradients do not cause convection. In general, the complete equation for the evolution of the concentration field is a convection-diffusion equation.

2.7 Hydrodynamics in the Presence of an Interface

2.7.1 General Considerations

Having established the hydrodynamic equations in an unbounded liquid, we need to establish the equivalent equations in the presence of a solid surface, be it the wall of a capillary, or the surface of a particle. The boundary conditions must take into account two important physical effects. Firstly, it is important that the interactions between the solid surface and the liquid have a finite range. Though small, this range is not zero and, typically, it is of the order of a few nanometers [100]. This fact is of fundamental importance to the wetting and dewetting dynamics that we expect to observe in our minimal nanocomposite system. The physical origins of these interactions are van der Waals forces between molecules or, potentially, ionic interactions.

The second effect that must be taken into account when describing hydrodynamics in the presence of a solid interface is the so-called slipping length. The macroscopic description of hydrodynamics assumes a no-slip boundary condition for the flow. However, if we wish to understand wetting and dewetting dynamics, we must suppose that there is a non-zero slipping length. In

the case of the wetting dynamics of simple liquids, this slipping length may be assumed to be of order one nanometer [40]. A larger slipping length has been discussed in the literature, up to a few tens of nanometer [105] but the issue is still under debate [120].

To describe the effect of the interface on the hydrodynamic flow, we introduce an additional contribution to the Gibbs free energy density in the vicinity of an interface. We denote this contribution by $\Gamma(\psi, \mathbf{r})$, where ψ is the solute volume fraction in the liquid just beyond the interfacial region. The range of Γ is typically a few nanometers, and up to a few tens of nanometers, depending on the thickness of the interfacial layer. This is the contribution of the solid surface to the free energy of the liquid in its vicinity. The contribution of the interface to the Gibbs free energy is therefore:

$$G_{Int} = \int \Gamma(\psi, \mathbf{r}) d^3\mathbf{r} \tag{2.36}$$

The quantity $\Gamma(\psi, \mathbf{r})$ must be understood in the following way. We assume that, at some distance from the interface, the solute volume fraction ψ is imposed by the flow. Then, the interfacial layer equilibrates locally to assume a certain profile corresponding to the local minimum of Gibbs free energy, given the specific nature of the interactions between the solute, the solvent and the solid surface, and the imposed conditions on ψ, the solute concentration, a few correlation lengths from the solid surface [119]. This decription relies on several assumptions. Firstly, local equilibration in the vicinity of the solid surface is fast, compared to the flow. Secondly, the concentration gradient imposed by the flow, parallel to the solid surface, corresponds to a length scale much larger than the thickness of the interfacial region between the solid and the liquid. Finally, the bulk of the capillary acts as a reservoir for equilibrating the interfacial layer. Thus local equilibration is assured by a diffusion process, which is faster on the scale of the interfacial layer than the disturbance caused by the flow.

We now apply the same principle of virtual work as before to the liquid close to the solid surface, to obtain the appropriate Stokes equation. Consider a virtual displacement in the liquid so that $\mathbf{r}$ is changed into $\mathbf{r} + d\mathbf{r}$. The quantity ψ is varied by an amount:

$$\delta\psi = -\delta\mathbf{r}.\boldsymbol{\nabla}\psi(\mathbf{r}); \tag{2.37}$$

So that:

$$\delta G_{Int} = \int -\delta\mathbf{r}.\boldsymbol{\nabla}\psi(\mathbf{r})\frac{\partial\Gamma(\psi,\mathbf{r})}{\partial\psi} \tag{2.38}$$

where the derivative of Γ is calculated with respect to the imposed solute concentration beyond the interfacial layer, as described above. By adding the corresponding term to the Stokes equation, we obtain the Stokes equation in the presence of an interface:

$$\begin{aligned} -\boldsymbol{\nabla}p(\mathbf{r}) + \boldsymbol{\nabla}.\eta\left(\boldsymbol{\nabla}\mathbf{v}(\mathbf{r}) + \boldsymbol{\nabla}\mathbf{v}^{+}(\mathbf{r})\right) + \mu(\mathbf{r})\boldsymbol{\nabla}\psi(\mathbf{r}) \\ + \frac{\partial\Gamma(\psi,\mathbf{r})}{\partial\psi}\boldsymbol{\nabla}\psi(\mathbf{r}) = \mathbf{0} \\ \boldsymbol{\nabla}.\mathbf{v} = 0 \end{aligned} \tag{2.39}$$

The total chemical potential is given by

$$\mu_{tot} = \mu + \frac{\partial\Gamma(\psi,\mathbf{r})}{\partial\psi} \tag{2.40}$$

The term μ represents the entire contribution from bulk liquid, where the concentration gradient is imposed by the flow. The second term represents the contribution which results from the interaction between the liquid and the solid surface in the thin interfacial layer. Thus, the second term $\frac{d\Gamma(\psi)}{d\psi}$ differs from zero only in the vicinity of the interface.

The variation in the surface tension, $\Delta\gamma(\psi)$, between the solid surface and the liquid with solute concentration ψ and the liquid with solute concentration zero is given by:

$$\Delta\gamma = \int_0^\infty \left(\Gamma(\psi,z) - \Gamma(0,z)\right) dz \tag{2.41}$$

This leads to:

$$\frac{d\gamma}{d\psi} = \int_0^\infty \frac{\partial \Gamma(\psi, z)}{\partial \psi} dz = \int_0^\infty \Psi(\psi, z) dz \tag{2.42}$$

where γ is the surface tension between the liquid and the solid, and we have introduced the quantity:

$$\Psi(\psi, z) = \frac{\partial \Gamma(\psi, z)}{\partial \psi} \tag{2.43}$$

for the sake of brevity.

2.7.2 Diffusio-Osmosis without Slipping Length

Let us apply this thinking to a capillary of sufficiently large diameter that its surface can be considered locally flat. Suppose that the liquid has a uniform gradient of composition which induces a uniform gradient of surface tension between the liquid and the capillary in the x-direction. The normal to the flat surface is the local z-direction. Further, let us suppose that the bulk chemical potential μ in equation 2.40 does not contain contributions from $\mu^{(1)}$, and recall that contributions from $\mu^{(0)}$ cannot give rise to convection, and can therefore be discarded from the flow equations. Then the flow equation, 2.39 reduces to:

$$-\frac{\partial p}{\partial x} + \eta \frac{\partial^2 v_x}{\partial z^2} + \frac{\partial \psi}{\partial x} \frac{\partial \Gamma}{\partial \psi} = 0 \tag{2.44}$$

Finally, let us assume that the gradient of concentration ψ is constant along the capillary as well as Ψ, which is the contribution of the interfacial interactions to the local chemical potential. By taking the derivative of Eq.2.44 with respect to x and by using the incompressibility condition and the invariance by translation of the other terms, we deduce that the pressure p satisfies the following equation:

$$\frac{\partial^2 p}{\partial x^2} = 0 \tag{2.45}$$

If the pressure at both ends of the capillary is identical (e.g. atmospheric pressure), we deduce from this equation that the pressure is uniform within the capillary and equal to the atmospheric pressure.

This equation allows us to calculate the flow velocity profile:

$$\frac{\partial v_x}{\partial z}(z) = \frac{-1}{\eta}\frac{\partial \psi}{\partial x}\left(\int_0^z \Psi(z')dz' - \int_0^\infty \Psi(z')dz'\right) = \frac{1}{\eta}\frac{\partial \psi}{\partial x}\int_z^\infty \Psi(z')dz' \tag{2.46}$$

We observe that the shear rate is a decreasing function of the distance from the capillary wall, and is zero at distances larger than the range of the thermodynamic perturbation of the liquid by the interface. Thus:

$$\frac{\partial v_x}{\partial z}(0) = \frac{1}{\eta}\frac{\partial \psi}{\partial x}\int_0^\infty \Psi(z')dz' \tag{2.47}$$

If we denote the range of Ψ by a, and assume a no slip boundary condition at $z = 0$, we obtain the following approximate expression for the velocity of the flow at a distance $z > a$:

$$v_x(z) \approx \frac{a}{\eta}\frac{\partial \psi}{\partial x}\int_0^\infty \Psi(z')dz' \tag{2.48}$$

The velocity field obtained by solving equation 2.46, and assuming a no slip boundary condition at $z = 0$ is given by:

$$v_x(z) = \frac{1}{\eta}\frac{\partial \psi}{\partial x}\int_0^z \left(\int_{z'}^\infty \Psi(z'')dz''\right)dz' \tag{2.49}$$

Equation 2.49 represents the so-called plug-flow observed in diffusio-osmosis in a capillary, and also in (for example) electro-osmosis. This is the standard behaviour when forces act on the liquid only within a thin layer in the vicinity of a solid surface, as is the case in these examples. We note, from equation 2.48 that the flow velocity depends on the range of the interfacial forces a.

The term $\frac{\partial \psi}{\partial x}\frac{\partial \Gamma}{\partial \psi}$ in equation 2.44 represents a pulling force parallel to the interface. This term is analogous to the term ρE_∞ in electro-osmosis [100,

115] where ρ is the density of charge in the vicinity of a solid surface, and is non zero within the Debye layer, and E_∞ is the applied electric field in the direction parallel to the capillary. In the diffusio-osmosis problem we consider here, the forces are internal and result from the interaction between the liquid and the solid. They appear as parallel to the solid surface: the surface pulls the liquid in order to reduce the Gibbs free energy of the liquid, taking into account the interaction between the solid and the liquid. These forces are tangential and do not result in the appearance of a confined pressure, nor are they the result of a pre-existing confined pressure in the vicinity of the liquid-solid interface. As noted, the diffusio-osmotic flow is a so-called plug flow when the tangential force is constant. When this is not the case, we observe the superposition of local plug flow and a Poiseuille flow at longer length scales. This situation is discussed in the case of electro-osmosis in reference [115], for example.

For specificity, let us assume that $\Psi(z)$ is given by:

$$\Psi(z) = \Psi(0) \exp\left(\frac{-z}{a}\right) \tag{2.50}$$

We then obtain:

$$\frac{d\gamma}{d\psi} = a\Psi(0) \tag{2.51}$$

These equations allow to calculate the flow velocity profile:

$$v_x(z) = \frac{a^2}{\eta}\frac{\partial\psi}{\partial x}\Psi(0)\left(1 - \exp\left(\frac{-z}{a}\right)\right) \tag{2.52}$$

The diffusio-osmotic velocity in the capillary is then given by:

$$V = \frac{a^2}{\eta}\frac{\partial\psi}{\partial x}\Psi(0) = \frac{a}{\eta}\frac{\partial\psi}{\partial x}\frac{d\gamma}{d\psi} \tag{2.53}$$

and is illustrated in figure 2.1, where the reason this motion is known as plug flow is apparent.

The diffusio-osmotic mobility defined by $\mathbf{V} = \mu\boldsymbol{\nabla}\psi$ is then given by:

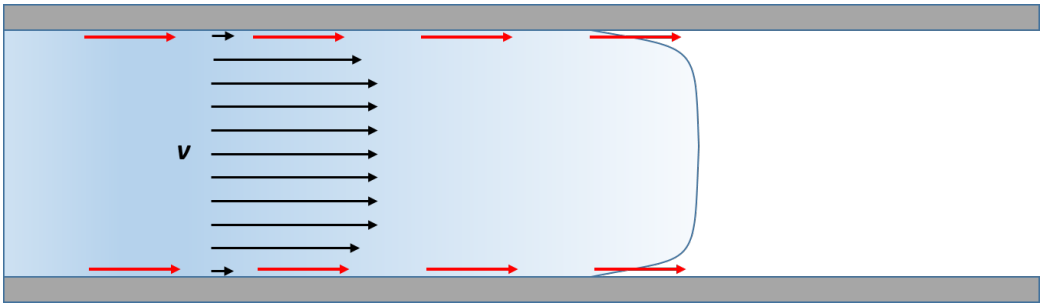

Figure 2.1: Diffusio-osmotic "plug" flow in a capillary. The driving force in equation 2.44 appears as a tangential force in the liquid distributed within a distance a of the solid surface. This force, though purely internal to the system, is analogous to the force in electro-osmosis, due to an external electrical field, which is exerted within the Debye length

$$\mu_{chem}^{osm} = \frac{a}{\eta}\frac{d\gamma}{d\psi} \tag{2.54}$$

We conclude that the diffusio-osmotic mobility is proportional to the range of the interaction, a, and to the derivative of the liquid-solid surface tension with respect to the solute concentration in the bulk. When the gradient of solute concentration is zero, equation 2.39 allows a no-flow and uniform pressure solution (for example, the atmospheric pressure p_0), contrary to the description of diffusio-osmosis in Derjaguin's model [98, 121, 100, 106], as can be seen by referring to equation 2.3. The fact that the diffusio-osmotic mobility is related to the gradient of surface tension has been recognized by many authors [122, 121]. However, the calculations by Ruckenstein, or by Anderson et. al., derive from Derjaguin's picture, and rely on a confined pressure gradient as a driving force. Levich describes the flow as being due to a surface tension gradient, at a liquid-liquid interface, in his study of the Marangoni effect [123]. However, this description cannot be extended to a liquid-solid interface, which must take into account the physics of the thin interfacial layer, which is absent from Levich's description.

More recently, Marbach et. al. [106] and Liu et. al. [124] question the role of the local pressure gradient and conclude that the osmotic flow is more probably related to the chemical potential gradient. Equations 2.39 and 2.49 show an explicit dependence on the chemical potential of the driving forces in the liquid, and of the resulting diffusio-osmotic flow. This driving force in the vicinity of the surface is, apart from a pre-factor, the derivative of the local excess Gibbs free energy density with respect to the imposed solute

concentration beyond the interfacial layer. Our expression makes explicit the detailed nature of the interaction between the surface and the liquid which is responsible for the flow.

It is important to note that the driving force that we obtain is $\mu\boldsymbol{\nabla}\psi$ in equation 2.24. Araki and Tanaka [95] introduce a similar Stokes equation but the driving force in their article is $-\psi\boldsymbol{\nabla}\mu$. With reference to our derivation of the driving force, Araki and Tanaka's equation may be obtained by an additional integration by parts following equation 2.14, using the fact that $\boldsymbol{\nabla}.\delta\mathbf{r} = 0$ due to incompressibility. However, this integration by parts should come with a contribution at the boundaries which is:

$$-\psi\left(\frac{dg^{(0)}}{d\psi} - \left(\boldsymbol{\nabla}.\frac{dg^{(1)}}{d\boldsymbol{\nabla}\psi}\right) + \Psi(\psi(x), z)\right)\delta\mathbf{r} \tag{2.55}$$

The contribution of this term is zero on the boundary corresponding to the solid interface since $\delta\mathbf{r}$ is zero there. But the contribution of this term is non zero in general. This is the case, in particular, if we consider diffusio-osmosis along a capillary which connects two reservoirs, of respective concentrations $\psi_1 > \psi_2$. The quantities related to $g^{(1)}$ in equation 2.55 may be considered as zero at the boundaries because the reservoirs have a homogeneous concentration, but the two quantities $\psi\frac{dg^{(0)}}{d\psi}$ corresponding to the two reservoirs are different. The integration by parts which leads to this different driving force (as compared to $\mu\boldsymbol{\nabla}\psi$) is unwarranted, except in the special case of periodic boundary conditions, relevant to the application considered by Araki and Tanaka [95]. In this case the difference between $\mu\boldsymbol{\nabla}\psi$ and $-\psi\boldsymbol{\nabla}\mu$ is unimportant since the contributions at the boundaries cancel. An analogous term $\psi\boldsymbol{\nabla}\mu$ has also been considered by Marbach et al [106], and by Liu et al [124], but without specifying μ in terms of the interfacial interactions, as we do. If this term is used as a driving force in the Stokes equation, we obtain a description very similar to that of Derjaguin since this term leads to the appearence of a confined pressure in the vicinity of the capillary, as we show in the paper on which this chapter is based [1]. In principle this confined pressure should be cancelled by the effect of the boundary terms just mentioned, but these are absent in all descriptions in the literature [98, 121, 100, 95, 106, 124]. As a consequence, the term $-\psi\boldsymbol{\nabla}\mu$ cannot be considered as the local driving force in the Stokes equation [95], and we therefore propose that the local driving force is $\mu\boldsymbol{\nabla}\psi$.

2.7.3 Diffusio-Osmosis and Slipping Length

We can also describe diffusio-osmosis by taking into account a non-zero slipping length whereby the range of the interaction between the solid surface and the liquid is zero (so the interaction is purely interfacial). The flow equation is given by equation 2.44. We now assume that the interfacial perturbation due to the solid-liquid interface is non-zero only at the interface, and that the flow is characterized by a slipping length b [41]. If the interface is located at $z = 0$, Γ as a three-dimensional function may be written as:

$$\Gamma(\psi(\mathbf{r}), z) = \Gamma(\psi(x, y, 0))\delta(z) \tag{2.56}$$

where $\delta(z)$ is the Dirac function.

Then, equation 2.44 can be solved by describing a virtual velocity profile for $z > -b$. The slipping length, b, is the length at which the flow, extrapolated in the negative z region vanishes [41]. The flow is then described with a no-slip boundary condition at $z = -b$ and with pulling forces located at $z = 0$. We then obtain a plug like velocity profile where the velocity is uniform for $z > 0$ and is given by:

$$v_x(z) = \frac{b}{\eta}\frac{\partial\psi}{\partial x}\frac{d\Gamma}{d\psi} \tag{2.57}$$

The diffusio-osmotic mobility defined by $\mathbf{V} = \mu\boldsymbol{\nabla}\psi$ is then given by

$$\mu_{chem}^{osm} = \frac{b}{\eta}\frac{d\Gamma}{d\psi} \tag{2.58}$$

Thus, we see that the diffusio-osmotic mobility is proportional either to the slipping length, b, or to the range of the interaction, a. The general result involves a combination of these two length scales as discussed by, for example, Ajdari and Bocquet [105], although their interpretation of the origin of the effect is different.

2.7.4 Wetting

Wetting can also be described using the formalism developed in this chapter. Considering equation 2.44, we note that the wetting of a liquid on a solid surface corresponds to a situation in which there is a sharp concentration gradient. We may assume that $\psi = 0$ on the right of the triple line in figure 2.2, and that $\psi = 1$ on the left, corresponding with the spreading droplet. The term $\boldsymbol{\nabla}\psi$ is essentially a Dirac δ function at the interface between the liquid and the surrounding atmosphere, so we may write $\boldsymbol{\nabla}\psi = -\delta(x)$. The quantity $\frac{\partial\Gamma(\psi,z)}{\partial\psi}$ may be integrated in the z-direction, normal to the surface. It yields the quantity $d\gamma/d\psi$ which is equal to $\gamma_S - \gamma_{SL}$, where γ_S is the surface tension of the solid substrate with the atmosphere, and γ_{SL} is the surface tension of the liquid with the solid surface. Note that we assume a linear relationship for γ as a function of ψ, which is consistent with the assumption made when deriving equation 2.44, but this assumption is not critical. In either case, we deduce that the pulling force is $\gamma_S - \gamma_{SL}$.

This net force due to the interaction potential, combined with the $-\gamma_L \cos\theta_d$ term from the surface tension of the liquid, where θ_d is the dynamic contact angle of the droplet with the solid substrate, recovers the net force at the triple line, as represented in Young's equation. The full picture is shown in figure 2.2, which should be contrasted with figure 1.8.

The earlier figure is a macroscopic picture of the surface tension forces acting at the triple line of the three-phase system. Applying a virtual work principle to this picture (or simply considering the balance of forces in the x-direction) recovers the standard description of wetting, as described in Young's equation. Figure 2.2 is the corresponding microscopic picture, which our formalism aims to describe. Since our formalism results in the same standard description of wetting [40, 41], we conclude that it enables us to describe wetting or dewetting phenomena as special cases of diffusio-osmosis, in which the composition gradient approaches a delta function.

2.8 Summary

We have introduced a formalism that enables us to describe the motion of inhomogeneous liquids in the vicinity of a solid surface. This enables us to describe diffusio-osmosis in a way that is consistent with the contact value

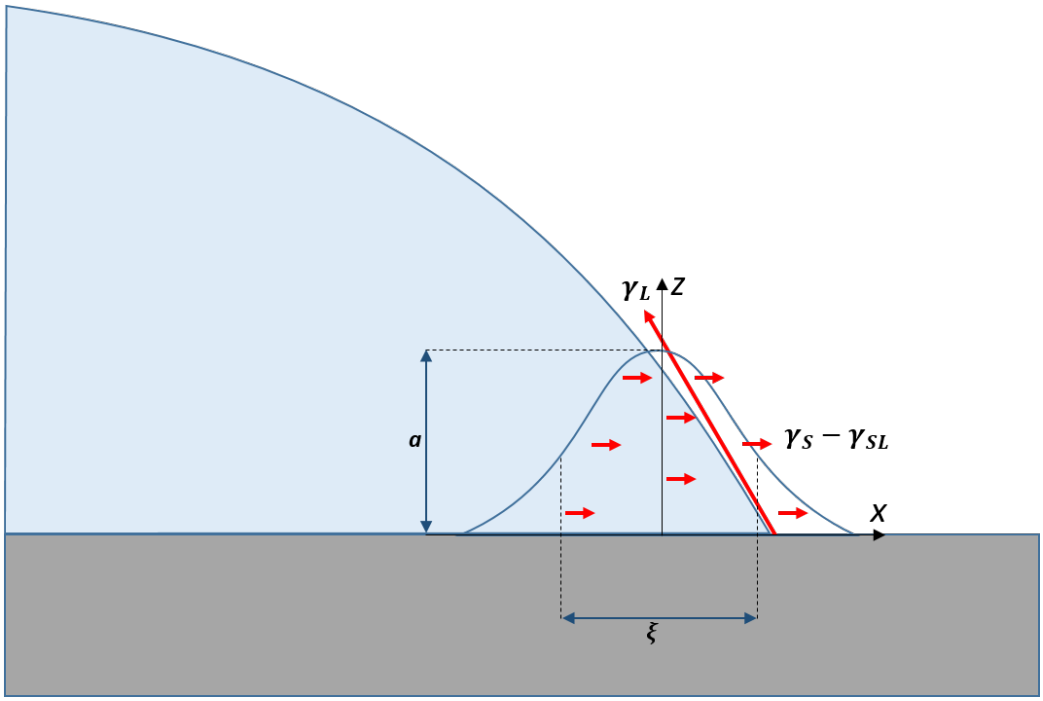

Figure 2.2: The driving force term in equation2.44 is non zero in the vicinity of the liquid-atmosphere interface. The net contribution is a tangential body force in the liquid over a region of spatial extent a in the direction normal to the substrate and ξ in the direction parallel to the substrate. When integrated over this region, it yields $\gamma_S - \gamma_{SL}$.

theorem of colloidal science [107, 109, 110, 111, 112]. Our approach contrasts with a commonly accepted account, due to Derjaguin, in which an excess pressure gradient, close to the solid surface, is used to account for diffusio-osmotic flow. However, this feature of Derjaguin's theory is not consistent with the contact value theorem in colloidal science, according to which there is no excess pressure in the vicinity of a solid surface immersed in a liquid. More recently, the relevance of the assumed pressure gradient as the cause of diffusio-osmotic flow has been questioned by Marbach et. al. [106] and by Liu et. al. [124], both concluding that the chemical potential gradient is the more relevant quantity. Our formalism supports this conclusion and provides an explicit expression for the driving force of the diffusio-osmotic flow.

The formalism is based on a virtual work principle, and makes apparent that the driving force in diffusio-osmosis is the consequence of the release of an excess of Gibbs free energy, in a way that is consistent with Onsager's description of non-equilibrium thermodynamics. This excess of Gibbs free energy, in an out of equilibrium situation, is located in the vicinity of the

solid-liquid interface. In the presence of a gradient of composition of the liquid along the solid surface, it gives rise to tangential body forces within the interfacial layer. In a coarse-grained picture, this excess of free energy may be related to a gradient of surface tension between the liquid and the solid. What is key in this picture is that the driving forces are purely transverse and have a spatial extension. They are not applied only at the point where a no-slip boundary condition holds.

The formalism can also be applied to the description of wetting or dewetting, which now appear as a limiting cases of diffusio-osmotic flow, in which there is a sharp composition gradient between the liquids (or between the liquid and the atmosphere). In wetting situations, our approach is consistent with the driving forces implied by Young's equation, which is the standard macroscopic description. In particular, it makes no reference to a possible region of excess pressure at the interface between the liquid and the solid, as is implied by Derjaguin's account.

Therefore, the principle of virtual work introduced by Doi and Onuki [113] allows us to propose a unified and consistent picture for decribing wetting [40, 41] and diffusio-osmosis [98, 104, 121, 100] which aligns with some key results of colloidal science [107, 108, 110, 111, 112, 109]. In the next chapter we build on this formalism to develop a mathematical model of a minimal nanocomposite system, in which hydrodynamic flows in the context of wetting or dewetting may be calculated.

Chapter 3

Physical Model and First Applications

3.1 Introduction

In the previous chapter, we presented a theoretical description of hydrodynamic flow in inhomogeneous liquids in the vicinity of solid interfaces, consistent with current theoretical descriptions of thermodynamic equilibrium in multi-phase systems, and with the Onsager formalism for linear response theory in out-of-equilibrium liquids. We showed that this theoretical framework enables us to describe diffusio-osmosis along a capillary and also, in the limit, as the concentration gradient approaches a delta function, the dynamics of the wetting and dewetting of a liquid on a solid substrate.

This approach enables us to finesse a persistent difficulty in simulating wetting and dewetting behaviour using continuum fluid mechanical models, namely, the treatment of boundary conditions in multi-phase systems, and how to account for the interfacial forces. Specifically, how can the no-slip boundary condition commonly assumed in fluid mechanics be reconciled with the requirement of relative motion between the liquid and the solid substrate, at their interface, in both wetting and dewetting? An additional issue in such sytems is *where* the interfacial forces in the liquids should be located, and how they should be represented. Finally, the same no-slip condition also leads to a divergence in the energy dissipated by the flow close to the contact line, which forces truncation of the relevant integral at both the lower limit

(of molecular length scale) and the upper limit (the size of the droplet, say) [43].

In order to make progress, it was necessary to correctly describe the thermodynamics of a system consisting of an inhomogeneous liquid phase in contact with a third solid phase, using an appropriate Gibbs free energy functional. This entailed showing how driving forces arise due to concentration gradients in the bulk and in the vicinity of the triple line, and how a non-zero slip-length of $\sim 0.5\,nm$ (the monomer length scale) emerges naturally when the system is described in the appropriate physical terms.

The Stokes equations then describe the convective contribution, in an out-of-equilibrium liquid, to the relaxation towards thermodynamic equilibrium. What is key in this picture is that the driving forces are purely transverse and have a spatial extension. They are not applied exactly where a no-slip boundary condition holds, which allows these forces to give rise to a flow. This feature solves the apparent paradoxes regarding wetting, if the forces are supposed to be applied right at the solid interface.

Thus, our approach is grounded in continuum fluid mechanics, supplemented by a diffuse interface approach, versions of which are also used by Araki and Tanaka [90, 95, 91, 93], and Anderson et. al. [125], among others . It enables coupled equations of motion for the concentration field and the velocity field to be solved numerically, thereby reproducing realistic wetting and dewetting dynamics. In this chapter, we show how it is possible to apply the ideas of the previous chapter to construct a model of our minimal nanocomposite system. Details of the physical model are described in the next section, after which we show how the model may be implemented, with the introduction of dimensionless parameters, and other quantities.

Having built the model, we apply it to the simple case of the wetting of a fixed particle, positioned symmetrically at the central interface between the two liquid phases in the system. We then consider the case of dewetting in a quiescent system, and use the simulation results to determine an approximate value for the critical film thickness, below which spinodal dewetting occurs. Having established that the model realistically simulates the dynamics of wetting and dewetting in a quiescent system, we finally apply it to a system subject to a constant shear rate. The aim is to further explore the dynamics of dewetting, and to determine the conditions under which a particle may be induced to migrate across an interface between two liquid phases, a problem of great practical interest in the manufacture of composite materials.

Anderson et. al. have also addressed this problem in a series of papers [126, 127, 128, 129]. In the first paper, a constant external force, acting on the particle, and perpendicular to the interface, is introduced to promote the migration of the particle from one phase to the other. Without this external force, the particle remains stuck at the interface between the liquid phases. In the later papers, the same effect is achieved by modelling the interface between a viscoelastic fluid and a Newtonian fluid, as shear is applied *parallel* to the interface. In this chapter, we model the effect of shear *perpendicular* to the interface between the liquid phases, and show that no special assumptions about the rheological properties of the liquids are needed to observe the migration of a particle from one liquid phase to the other.

All of the simulations described in this chapter take place in what is known as the Rouse regime, where the effect of entanglement between polymer chains at the microscopic level is small. We also assume strong segregation between the two liquid phases in the minimal nanocomposite system, meaning that the Flory-Huggins interaction parameter is high ($\chi = 4.0$, in fact), and the two polymers present in the system do not readily mix. Simulations in the highly segregated Rouse regime are among the simplest to run, as will become apparent in later chapters, where we relax both of these assumptions, in turn.

3.2 Physical Model

In building our model of a minimal nanocomposite system, we start with the general expression for the total Gibbs free energy in a system in which concentration gradients are present, as presented in the previous chapter:

$$G = \int g(\mathbf{r}) d^3\mathbf{r} = \int \{g^{(0)}(\psi) + g^{(1)}(\boldsymbol{\nabla}\psi)\} d^3\mathbf{r} \tag{3.1}$$

As before, we assume that the density of the Gibbs free energy is the sum of two contributions:

$$g(\psi, \boldsymbol{\nabla}\psi) = g^{(0)}(\psi) + g^{(1)}(\boldsymbol{\nabla}\psi) \tag{3.2}$$

where ψ represents the concentration field and the first term is the Gibbs free energy density of a homogeneous liquid with concentration ψ, while the

second term is the contribution of the spatial gradient in ψ to the free energy density.

In the presence of a solid interface, the Gibbs free energy may be written as:

$$G = \int g(\mathbf{r}) d^3\mathbf{r} = \int \{g^{(0)}(\psi) + g^{(1)}(\boldsymbol{\nabla}\psi) + \Gamma(\psi, \mathbf{r})\} d^3\mathbf{r} \qquad (3.3)$$

where we have introduced a generic interaction potential between the fluid phases in the system and the solid surface of the particle. The properties of this interaction potential are described in the previous chapter, and in the paper upon which it is based [1]. Note that now, the quantity ψ in the potential $\Gamma(\psi, \mathbf{r})$ is the concentration in the liquid just beyond the interfacial layer. It is imposed by the flow whereas the concentration profile within the interfacial layer equilibrates so as to minimize the Gibbs free energy with ψ as an imposed boundary condition just beyond the interfacial layer.

To make progress, we adapt the fluid particle dynamics method developed by Araki and Tanaka [90]. In this approach, hard particles are modelled as highly viscous fluids (typically 50 times more viscous than the surrounding fluid). Thus, it is an example of a diffuse interface method, as discussed in [125, 126], and avoids the difficulties with managing the boundary conditions associated with hard surfaces in fluid flows. The fluid particle dynamics approach has been applied to charged colloidal suspensions [96], colloidal aggregation in liquid crystals [97], and nanoparticles in a phase separating binary mixture [95, 91] but this is the first time it has been used to study the dynamics of wetting and dewetting under shear, and the shear induced migration of a particle from one fluid phase to another.

Taking this approach enables us to specify the form of each term in the generic free energy functional (equation 3.3):

$$G\{\psi, \phi\} = \int \{g(\psi) + \frac{\kappa}{2}|\boldsymbol{\nabla}\psi|^2 + We\psi|\boldsymbol{\nabla}\phi|^2 + \zeta\phi(\psi - \bar{\psi})^2\} d^3\mathbf{r} \qquad (3.4)$$

The first and second terms correspond with the first two terms in equation 3.3. The bulk free energy term, $g(\psi)$, is based on the Flory-Huggins free energy density for a binary polymer mixture [6], which we encountered in the introductory chapter:

$$\frac{g(\psi)}{k_B T} = \psi \ln(\psi) + (1-\psi)\ln(1-\psi) + \chi\psi(1-\psi) \tag{3.5}$$

Here, we assume that both polymers have the same degree of polymerization N. The Flory-Huggins interaction parameter, χ, may be considered as proportional to N. As previously, T is the temperature.

The term that depends upon $|\boldsymbol{\nabla}\psi|$ represents the free energy density at the interface between phases in the system, and the parameter κ is a measure of the strength of the interfacial tension.

The third term in equation 3.4 is new, and represents the free energy density at the particle-polymer interface, replacing the term $\Gamma(\psi, \mathbf{r})$ in the generic free energy functional. In this term, W is a wetting parameter, and represents the degree to which the particle favours one liquid phase over the other, e is the width of the particle interface and is typically of the monomer length scale, and ϕ is an order parameter representing the presence of the particle (that is, $\phi = 1$ within the boundary of the particle, and $\phi = 0$ elsewhere, with a steep gradient at the interface).

The final term in equation 3.4 represents the energy barrier at the surface of the particle and the parameter ζ is tuned to limit ingress of the polymer across the particle boundary during the simulation. The mean value of the concentration field in the system is represented by $\bar{\psi}$, and we take this to be zero in all our simulations - in other words, the two polymer species, A and B, occupy equal volumes in the system.

Note that ϕ varies in value from 0 to 1, over a length scale equal to the width of the particle interface, e. Thus, $|\boldsymbol{\nabla}\phi|$ is of order $\frac{1}{e}$. We assume the width of the interface to be the monomer length scale of approximately $0.5\,nm$, which we equate to 1, in the dimensionless units of the model (see section 3.4).

As in the previous chapter, we now apply variational principles to equation 3.3 to determine the evolution of this three-phase system. Based on the above free energy functional, the relationship between the Gibbs free energy and the chemical potential, and the equations of hydrodynamics, we obtain coupled equations of motion for the velocity field (a modified Stokes equation) and the concentration field (a modified Cahn-Hilliard equation):

$$-\boldsymbol{\nabla}p + \boldsymbol{\nabla}\{\eta[\boldsymbol{\nabla}\mathbf{v} + (\boldsymbol{\nabla}\mathbf{v})^T]\} + \mu\boldsymbol{\nabla}\psi = \mathbf{0} \tag{3.6}$$

$$\frac{\mathrm{d}\psi}{\mathrm{d}t} = -\mathbf{v}.\boldsymbol{\nabla}\psi + D\boldsymbol{\nabla}^2\mu \tag{3.7}$$

The velocity field in the fluid is represented by $\mathbf{v}$ and the concentration field by ψ. As is common, we also assume incompressibility:

$$\boldsymbol{\nabla}.\mathbf{v} = 0 \tag{3.8}$$

In equation 3.7, D is the diffusion coefficient and depends on the degree of polymerisation of the polymer (see section 3.4). In equation 3.6, p is the pressure (which enforces the incompressibility condition), and η is the viscosity of the fluid, while μ represents the chemical potential, defined as the functional derivative with respect to ψ, of the Gibbs free energy in equation 3.4. The expression for μ obtained in this way is:

$$\mu = \frac{dg}{d\psi} - \kappa\boldsymbol{\nabla}^2\psi + We|\boldsymbol{\nabla}\phi|^2 + 2\zeta\phi\psi \tag{3.9}$$

where $\frac{dg}{d\psi}$ is just the ordinary derivative of g, the Flory-Huggins free energy of mixing, with respect to the volume fraction, ψ, and we have used the fact that $\bar{\psi} = 0$.

Due to the presence of a solid interface, this chemical potential has two contributions, one from the liquid phases and the interface between them, and one from the interaction of the liquid phases with the solid surface of the particle. Comparing equation 3.9 with equation 2.40, we may identify the former with the first two terms of equation 3.9, while the latter may be identified with the last two terms (or, physically speaking, with the third term, since the last term is, essentially, an artefact of our model). The contribution to the total chemical potential of the interaction between the liquid phases and the particle is non-zero only in the vicinity of the solid surface. As argued in the previous chapter, this represents the driving force on the liquid in the vicinity of the solid interface due to the interaction potential.

3.3 Implementation and Solution

To implement the model described in the previous section, we use a modified version of the usual expression for the Flory-Huggins free energy of mixing (equation 3.5):

$$\frac{g(\psi)}{k_B T} = \frac{1+\psi}{2}\ln(1+\psi) + \frac{1-\psi}{2}\ln(1-\psi) + \frac{\chi}{4}(1+\psi)(1-\psi) - \frac{\chi}{4} \quad (3.10)$$

where now, ψ is an order parameter with values of $\psi = \pm 1$ corresponding to the two pure polymers in the system, and the constant term is introduced to ensure that the local maximum of free energy density occurs at the origin. The equations of motion, 3.6, 3.7 and 3.8 are unchanged in form, by this transformation of the variable ψ.

To solve the equations of motion, we use an FTCS (Forward-Time, Central-Space) finite difference scheme on a discrete two-dimensional lattice, with periodic boundary conditions. To avoid the numerical instability associated with logarithmic functions, we approximate the Flory-Huggins free energy density, equation 3.10, with a 10^{th} order polynomial in even powers of ψ:

$$g(\psi) = a_1\psi^{10} + a_2\psi^8 + a_3\psi^6 + a_4\psi^4 + a_5\psi^2 \quad (3.11)$$

where the a_i are parameters obtained from fitting equation 3.10 to the polynomial form of 3.11. Note that, as χ varies, only the term in ψ^2 changes in the approximation of the Flory-Huggins free energy density. Thus, changing the coefficient of the ψ^2 term in equation 3.11 enables us to represent the variation of the Flory-Huggins interaction parameter, χ and thereby the concentrations of the equilibrium phases, and the interfacial width (and surface tension) between them. For reference, we note that the critical point occurs when $\chi = \chi_C = 2.0$ and that when $\chi > 4.8$ or $\chi < 2.05$, we consider our numerical approximation to be unreliable. This still leaves a wide range of χ values to explore, with higher values of χ signifying stronger segregation between the phases.

In outline, the numerical solution of the equations of motion proceeds by solving the Stokes equation without the pressure term, in order to calculate an *uncorrected* velocity field. It is then possible to take the divergence of

both sides of the *complete* Stokes equation (3.6), including the pressure term, and to apply the incompressibility condition to calculate the pressure field and thus the corrected velocity field. Having calculated the velocity field, it is straightforward to solve the modified Cahn-Hilliard equation (3.7) to calculate the ψ field. The interior of the particle is the region of the system where the ψ field is near-zero and the ϕ field is unity. The motion of the particle is tracked by integrating the velocity field within this region and averaging over the region's extent. The circularity of the particle boundary is enforced after each step in the simulation, to reflect the physical reality that it is a rigid particle.

Although our theoretical framework naturally allows for the modelling of three dimensional systems, for the sake of computational efficiency, we restrict our simulations to two dimensions. This simplification sacrifices little, if any, of the essential physics, especially when the minimal nature of the system that is the topic of this thesis is taken into account. We choose a default lattice size of 256 x 256 cells. The default particle radius is 25 lattice cells ($\sim 12.5\,nm$) and the particle interface width is of order one lattice cell ($\sim 0.5\,nm$) throughout. The ratio of the particle "fluid" viscosity to the viscosity of the liquid phases is 50:1 in all simulations, and the parameter that represents the energy barrier at the particle surface, $\zeta = 10$ to limit ingress of the liquid phases into the particle's interior. With this value of ζ, the order parameter field in the interior of the particle is typically $\psi \sim 10^{-4}$.

All simulations take place in the Rouse regime, where entanglement effects of polymer chains at the molecular scale may be neglected. In our model and, given the chosen time scale, this implies an effective diffusion coefficient of $D = 1$, and a fluid viscosity of $\eta \sim 1$. In the simulations described in this chapter, we assume strong segregation between the polymers and set the Flory-Huggins interaction parameter, $\chi = 4.0$. For the wetting parameter, we usually assume a high intermediate value of $W = 4.0$; in other words, the particle has a marked preference for one phase over the other.

When the particle starts in the non-favoured liquid phase, its distance from the central interface is specified in lattice cell units. Physically, a lattice cell has dimensions comparable with a typical monomer length of $0.5\,nm$. In the dewetting simulations, the distance of the particle from the interface is varied from $2.5\,nm$ to $10.0\,nm$. Both a quiescent system and a system subject to a shear rate of $\dot{\gamma} = 1.0 \times 10^4\,s^{-1}$ and $\dot{\gamma} = 2.0 \times 10^4\,s^{-1}$ are simulated. The former shear rate implies 100 percent shear in $10^6 \times \Delta t = 100\,\mu s$.

In the next section, we discuss the mapping of dimensionless quantities to physical quantities in greater detail and show that, given the above choices, a single simulation time step equates to a physical time step of $\Delta t = 10^{-10}\, s$. When running simulations, snapshots of the system are taken after each 1000 simulation steps. Thus, the time resolution of the simulations is $10^{-7}\, s$. This strikes a good balance between data storage capacity and computation time, on the one hand, and the ability to observe the system at short time scales, on the other.

3.4 Dimensionless Quantities and Parameter Settings

As alluded to in the previous section, to implement our physical model, we wish to make certain parameters in it dimensionless. We do this by choosing a suitable time scale, τ, length scale, a (which we take to be the monomer length scale, $\sim 0.5\, nm$) and energy scale, T (which we take to be the thermal energy at room temperature, $0.025\, eV \approx 4 \times 10^{-21}\, J$). For the diffusion coefficient and viscosity, we then have:

$$\tilde{D} = \frac{D\tau}{a^2} \tag{3.12}$$

$$\tilde{\eta} = \frac{\eta a^3}{T\tau} \tag{3.13}$$

Here, where there is a need to make the distinction, $\tilde{A}$ signifies a dimensionless quantity corresponding with the physical quantity A. For notational convenience, this convention is sometimes dropped outside of this section. In particular, since we only ever need to refer to the dimensionless value of the effective diffusion coefficient in the rest of this thesis, we use the notation, D, rather than $\tilde{D}$.

Our aim is to determine the value of these quantities in the Rouse and the entangled regimes, along with the physical values of other important dimensionless quantities in our model - specifically, the time step, the shear rate, and the viscosity of the liquid phases.

In the Rouse regime, which is the focus of the current chapter, we have [6]:

$$D = \frac{Na^2}{\tau_{rouse}} \tag{3.14}$$

$$\eta = \frac{T}{Na^3}\tau_{rouse} \tag{3.15}$$

Where N is the degree of polymerisation, and τ_{rouse} is the Rouse time scale, which is related to the monomer time scale τ_0 according to: $\tau_{rouse} = \tau_0 N^2$. We note that $\tau_0 \sim 10^{-9}\, s$ and that, in the Rouse regime, $N \lesssim N_e \approx 100$, with N_e being the entanglement limit. Here, the value of N_e is an order of magnitude estimate, chosen for its arithmetical convenience, and represents the upper limit of the degree of polymerisation in the Rouse regime. In real polymer melts, entanglement can occur when the degree of polymerisation, N, is less than 100, as is the case for polyethylene ($N_e \approx 50$), or when N is greater than 100, as is the case for poly(dimethyl siloxane) ($N_e \approx 160$).

Then, choosing $\tau = \frac{\tau_{rouse}}{N}$ ensures that both $\tilde{D} = 1$ and $\tilde{\eta} = 1$.

We also have:

$$\tau = \frac{\tau_{rouse}}{N} = \frac{\tau_0 N^2}{N} = \tau_0 N \tag{3.16}$$

Thus, physically, $\tau = 10^{-9}\, s \times 100 = 10^{-7}\, s$, where we have taken $N = N_e = 100$ for the sake of being specific. This sets an upper limit on the time scale characteristic of the Rouse regime.

In our computational model, this implies that a dimensionless time of $\tilde{t} = 1$ corresponds to a physical time of $t = 10^{-7}\, s$. Since our Rouse regime simulations use a dimensionless time step of $\tilde{\Delta}t = 0.001$. This implies that each step equates to $\Delta t = 10^{-10}\, s$ in physical time. As noted earlier, we take a snapshot of the system every 1000 steps, during our simulations, so the temporal resolution achieved is $10^{-7}\, s$.

We also need to know the physical shear rate associated with any given dimensionless shear rate used in our simulations. Our model computes the displacement due to shear as follows:

$$\Delta\gamma = n \times L \times \tilde{\dot{\gamma}} \times \tilde{\Delta}t \tag{3.17}$$

Where n is the number of simulation steps, $L = 256$ is the size of the system, in lattice cell units, and $\tilde{\dot{\gamma}}$ is the dimensionless shear rate which, in our Rouse regime simulations, ranges from ~ 0.001 to ~ 0.002. Since $\tilde{\Delta}t = 0.001$ and taking, for example, $\tilde{\dot{\gamma}} = 0.001$, we have:

$$\Delta\gamma = n \times L \times 10^{-6} \tag{3.18}$$

100% shear ($\gamma = 1$) occurs when $\Delta\gamma = L$ which, based on the above, is the case after $n = 10^6$ simulation steps. Thus we may calculate the physical shear rate that corresponds with our dimensionless shear rate of 0.001:

$$\dot{\gamma} = \frac{\gamma}{t} = \frac{1}{10^6 \times 10^{-10}\, s} = 10^4\, s^{-1} \tag{3.19}$$

Other shear rates used in our Rouse regime simulations scale linearly with this result so, for example, a shear rate of $\tilde{\dot{\gamma}} = 0.002$ corresponds with a physical shear rate of $\dot{\gamma} = 2 \times 10^4\, s^{-1}$.

Finally, we return to equation 3.13 to calculate an order of magnitude estimate of the viscosity of our fluid in the Rouse regime. Rearranging, we obtain:

$$\eta = \frac{\tilde{\eta} T \tau}{a^3} \tag{3.20}$$

Substituting the relevant orders of magnitude:

$$\eta \sim \frac{10^0 \times 10^{-21}\, J \times 10^{-7}\, s}{(10^{-9}\, m)^3} = 0.1\, Pa\, s \tag{3.21}$$

This is equivalent to 100 centipoise, which is typical of a light engine oil.

We will need a corresponding set of results for the entanged regime, in which the degree of polymerisation, $N > N_e$, the entanglement limit. Now, we have:

$$D = \frac{Na^2}{\tau_{rept}} \tag{3.22}$$

$$\eta = \frac{T}{N_e a^3}\tau_{rept} \tag{3.23}$$

Where τ_{rept} is the reptation time scale (see chapter 4), given by:

$$\tau_{rept} = \tau_0 {N_e}^2 \left(\frac{N}{N_e}\right)^3 \tag{3.24}$$

This time we choose $\tau = \frac{\tau_{rept}}{N_e}$ to ensure that $\tilde{D} = \frac{N}{N_e}$, while $\tilde{\eta} = 1$, as previously.

We also have:

$$\tau = \frac{\tau_{rept}}{N_e} = \tau_0 N_e \left(\frac{N}{N_e}\right)^3 \tag{3.25}$$

In our entangled regime simulations, we initially use $\tilde{D} = \frac{N}{N_e} = 10$ so, recalling that $N_e = 100$:

$$\tau = \tau_0 \times 100 \times 10^3 \tag{3.26}$$

Since $\tau_0 = 10^{-9}\, s$, this implies that $\tau = 10^{-4}\, s$. Thus, in our model, when $\tilde{D} = 10$, a dimensionless time of $\tilde{t} = 1$ corresponds with a physical time of $t = 10^{-4}\, s$. Our entangled regime simulations use a dimensionless time step of $\tilde{\Delta}t = 0.0001$, which implies that each simulation step equates to $\Delta t = 10^{-8}\, s$ in physical time.

Turning to the shear rate, our model computes the displacement due to shear using equation 3.17, as before. Since $\tilde{\Delta}t = 0.0001$ and again taking $\tilde{\dot{\gamma}} = 0.001$, for the sake of being specific, we have:

$$\Delta\gamma = n \times L \times 10^{-7} \tag{3.27}$$

100% shear ($\gamma = 1$) occurs when $\Delta\gamma = L$ which, based on the above, is the case after 10^7 simulation steps. Thus we may calculate the physical shear rate that corresponds with our dimensionless shear rate of $\tilde{\dot{\gamma}} = 0.001$:

$$\dot{\gamma} = \frac{\gamma}{t} = \frac{1}{10^7 \times 10^{-8}\, s} = 10\, s^{-1} \tag{3.28}$$

As before, other shear rates used in our simulations of the entangled regime, with $\tilde{D} = 10$, scale linearly so, for example, a dimensionless shear rate of $\tilde{\dot{\gamma}} = 0.002$ corresponds with a physical shear rate of $\dot{\gamma} = 20\, s^{-1}$.

Finally, turning to equation 3.13, we calculate an order of magnitude estimate of the viscosity of our fluid in the entangled regime, with $\tilde{D} = 10$. Rearranging as before, and substituting the relevant orders of magnitude, we obtain:

$$\eta \sim \frac{10^0 \times 10^{-21}\, J \times 10^{-4}\, s}{(10^{-9}\, m)^3} = 100\, Pa\, s \tag{3.29}$$

This is equivalent to 10^5 centipoise, which is comparable with the viscosity of polypropolene melt or, in more familiar terms, peanut butter.

For ease of reference, we summarise the physical values corresponding with the main dimensionless quantities used in our simulations, for all values of $\tilde{D}$, in table 3.1.

$\tilde{D}$	$\tilde{\Delta}t$	Physical Value Corresponding with:		
		$\tilde{t} = 1$ $[s]$	$\tilde{\dot{\gamma}} = 0.001$ $[s^{-1}]$	$\tilde{\eta} = 1$ $[Pa\, s]$
1	0.0010	1.00×10^{-7}	10000	0.10
2	0.0005	8.00×10^{-7}	1250	0.80
5	0.0002	1.25×10^{-5}	80	12.5
10	0.0001	1.00×10^{-4}	10	100

Table 3.1: Mapping physical values to dimensionless quantities, for various values of the effective diffusion coefficient, $\tilde{D}$. The second column is the dimensionless time step associated with the value of $\tilde{D}$ in the first column. Note that $\tilde{D} \times \tilde{\Delta}t$ is constant; this ensures the stability of our simulations. The *physical* time step used in a given simulation may be found by multiplying the dimensionless time step, $\tilde{\Delta}t$, by the physical time corresponding with a dimensionless time of $\tilde{t} = 1$, for the value of $\tilde{D}$ used in the simulation.

We make two final observations about the use of dimensionless quantities in the model. Firstly, inspecting table 3.1, we see that, as $\tilde{D}$ varies from the value of unity, characteristic of the Rouse regime, the physical time scales according to $\tilde{D}^3$, as does the physical viscosity, while the physical shear rate scales according to $\frac{1}{\tilde{D}^3}$. Since, in the entangled regime, the dimensionless diffusion coefficient, $\tilde{D} = \frac{N}{N_e}$, this implies that the physical viscosity also scales with N^3. Thus, our model reproduces the result, familiar from the rheological study of polymer melts, that $\eta \propto N^{3.4}$ [6], but with the value of the exponent changed from 3.4 to 3, for simplicity.

Secondly, note that the degree of polymerisation, N partly determines the value of the dimensionless diffusion coefficient, $\tilde{D}$. This accounts for the counter-intuitive feature of our model that, as the effective diffusion coefficient increases, the dynamics of the minimal nanocomposite system become slower. The easiest way to see this is to express the dimensionless diffusion coefficient in terms of the physical diffusion coefficient. In the Rouse regime, we have $\tilde{D} = \frac{\tau_0 N}{a^2} D$, while the equivalent expression in the entangled regime is $\tilde{D} = \frac{\tau_0 N^3}{a^2 {N_e}^2} D$. In both regimes, the physical diffusion coefficient, D is multiplied by a factor involving N, the degree of polymerisation, to obtain the dimensionless diffusion coefficient. It is this additional factor (N in the Rouse regime, N^3 in the entangled regime) that is responsible for the slowing of the dynamics of the system when $\tilde{D}$ increases. Recalling that, in the entangled regime, we also have $\tilde{D} = \frac{N}{N_e}$, it may be observed that the transition between the Rouse regime and the entangled regime occurs when $N = N_e$, since the two expressions for $\tilde{D}$ are the same, if this condition is satisfied. Therefore, by varying the dimensionless diffusion coefficient, $\tilde{D}$ (which, in the rest of the thesis, is referred to as D, for notational convenience) we may study the behaviour of a representative polymer, in which entanglement effects are observed when the degree of polymerisation, $N = N_e = 100$, at the edge of the Rouse regime ($\tilde{D} = 1$), and in the entangled regime ($\tilde{D} > 1$).

3.5 Wetting of a Fixed Particle

Our focus in this chapter is on spinodal dewetting, which occurs when the film thickness is of the order of a few nanometres, and which we therefore expect to observe in our simulations of a particle close to the interface between the two liquid phases. The effect of shear on such a system, and in particular on whether shear promotes the migration of the particle from one liquid phase

to the other, is also of great theoretical and practical interest. Additionally, we may also use our model to explore the dynamics of wetting. To do this, the particle is initially located symmetrically with respect to the central interface between the two liquid phases, and its position is fixed. This is an artificial constraint since a particle in a real system moves under the influence of hydrodynamic forces, but it enables us to treat the surface of the particle as analogous to the solid substrate in our earlier discussions of wetting statics and dynamics. We vary the wetting parameter, W, from 1.0 to 8.0, and observe the evolution of the system in each case. The Flory-Huggins interaction parameter is $\chi = 4.0$ in all simulations, implying strong segregation between the two phases, with an equilibrium value of the order parameter of $\psi_{eq} = \pm 0.9562$. Denoting the favoured phase as A and the non-favoured phase as B, Young's equation becomes:

$$\gamma_{SB} = \gamma_{SA} + \gamma_{AB} \cos\theta_e \tag{3.30}$$

Where the subscripts refer to the particle/phase B, particle/phase A, and the phase A/phase B interfaces respectively. The spreading parameter, S is defined in a similar fashion:

$$S = \gamma_{SB} - (\gamma_{SA} + \gamma_{AB}) \tag{3.31}$$

Moreover, if we assume that the deformation of the interface between phase A and phase B, as wetting proceeds, is relatively small, and that the thickness of any film formed due to total wetting is also small, it remains the case that total wetting occurs when $S > 0$. In fact, as we shall see, wetting does distort the interface when the W parameter is high, but we can still make valid deductions, based on our simpler approach.

To make further progress, we recall that the wetting parameter, $W = 2(\gamma_{SB} - \gamma_{SA})$, so the condition for total wetting becomes:

$$W > 2\gamma_{AB} \tag{3.32}$$

It is possible to derive various approximate expressions relating the surface tension between the liquid phases to the Flory-Huggins parameter. For example, a simple argument based on the energy of a polymer chain at the interface [130] may be used to show that:

$$\gamma_{AB} \sim \rho a \sqrt{\chi} \tag{3.33}$$

Where γ_{AB} is measured in units of $k_B T$, ρ is the number density of monomers, and a is the monomer length scale. In Helfand's model of the polymer-polymer interface [131] the latter two parameters are replaced by a pre-factor of order unity. This is consistent with our model in which both ρ and a have dimensionless values of order unity, and equation 3.33 reduces to $\gamma_{AB} \sim \sqrt{\chi}$. To be specific, if $\chi = 4.0$, as it is in our Rouse regime simulations, $\gamma_{AB} \sim 2$. Therefore, from equations 3.32 and 3.33, we predict that total wetting will occur when $W \gtrsim 4$.

We turn now to the results of our wetting simulations. Figure 3.1 shows typical dynamics for the $W = 4.0$ case.

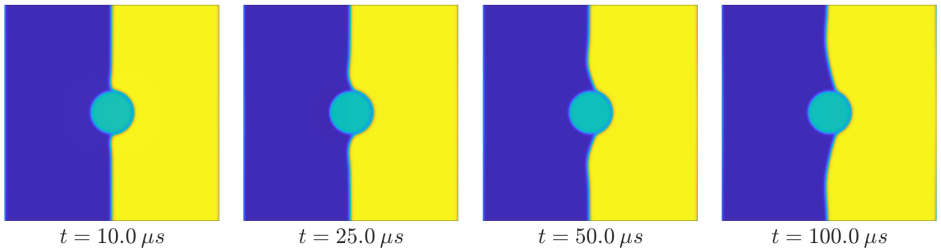

Figure 3.1: Stages of wetting, with wetting parameter $W = 4.0$. The particle is initially located symmetrically at the interface and immobilised, allowing the preferred phase to wet its surface.

We also show the state of system after $1.0 \times 10^7\,\Delta t$ (equivalent to $1.0\,ms$), for values of W from 1.0 to 8.0 (figure 3.2).

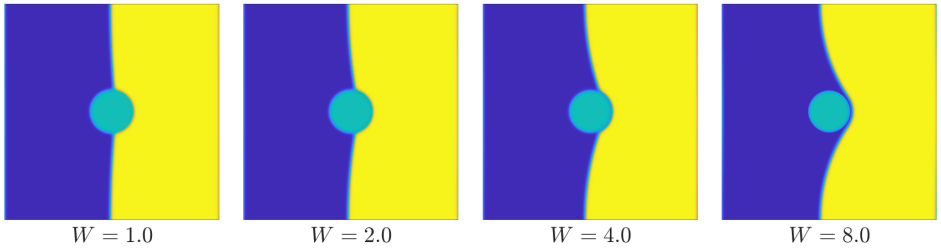

Figure 3.2: Long term wetting behaviour for $W = 1.0$ to $W = 8.0$. We show the state of the system after $1.0\,ms$; further relaxation of the interface is very slow, and beyond the reach of our simulation time scales.

Finally, we show the evolution of the mean free energy density of the system as the favoured phase wets the particle, for values of W from 1.0 to 8.0. (figure 3.3).

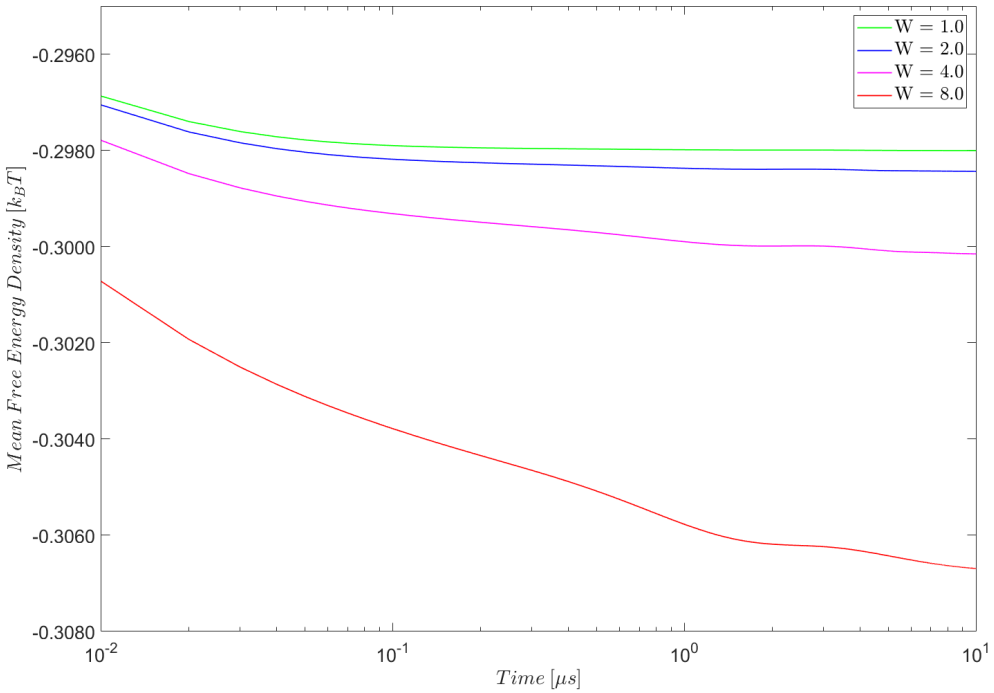

Figure 3.3: Evolution of the mean free energy density with time during wetting, for $W = 1.0$ to $W = 8.0$. In each case, the particle is positioned symmetrically, with respect to the interface, where it is pinned, allowing the preferred phase to wet its surface.

Note that in the early stages of the simulation $(0.1 - 0.2\,\mu s)$ the interface between the liquid phases rapidly equilibrates, and this effect is superimposed on the wetting dynamics. This is unavoidable, but occurs rapidly enough not to obscure the wetting dynamics. Thus our model is consistent with assumptions made in the previous chapter, and in our paper [1], about the relative time scales associated with local equilibration close to the solid surface and with the hydrodynamic flow itself.

From these results, we note that, qualitatively, the wetting behaviour appears physically realistic for all values of W. As W increases, the degree of wetting by the favoured polymer is greater, and the contact angle decreases.

Total wetting clearly occurs when $W = 8.0$. This appears to correspond to a kink in the free energy density plot at $t \approx 0.7\,\mu s$. From a video of the early stages of wetting when $W = 8.0$, we estimate that complete wetting occurs at $t \sim 0.9\,\mu s$, supporting this hypothesis. Although not so obvious in

the snapshots of the system's evolution, it is possible that total wetting also occurs when $W = 4.0$, as marked by a similar kink in the free energy density plot, also at $t \approx 0.7\,\mu s$. The occurrence of total wetting at $W = 8.0$ and $W = 4.0$ is consistent with the condition for total wetting: $W \gtrsim 4$ derived above.

The characteristic time scale for wetting is $\sim 1.0\,\mu s$ for all values of W considered. There is some evidence that higher values of W result in faster wetting: $\frac{d\bar{g}}{dt}$ is greater at low values of t, for higher values of W), although this is accompanied by greater relaxation time scales.

3.6 Dewetting without Shear

To observe the qualitative dynamics of dewetting at a higher spatial resolution, we choose a system size of 1024 x 1024 cells, and a particle of radius 100 lattice cells ($\sim 50\,nm$). In this simulation, the particle is initially positioned at $d = 4.0\,nm$ from the central interface. Figure 3.4 shows the state of the system in the early stages of its evolution, up to $t = 80.0\,\mu s$.

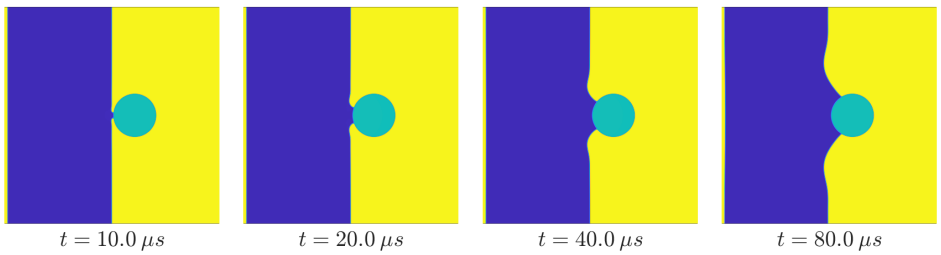

Figure 3.4: Qualitative dewetting dynamics in a larger system of 1024×1024 cells. The particle starts at a distance $d = 4.0\,nm$ from the central interface, and has radius $r = 50\,nm$, and the wetting parameter is $W = 4.0$.

As expected, we observe the formation of a rim of liquid, characteristic of dewetting at around $t = 20.0\,\mu s$. At later times, the rim continues to grow and moves outwards towards the edge of the system, at constant speed. At longer time scales (not shown), the curvature of the interface becomes more uniform, and the interface is expected to flatten over time scales that are computationally inaccessible.

We also show the magnitude of the velocity field, at various times close to the

dewetting point, in figure 3.5. The maximum speed of fluid flow is observed close to the surface of the particle, just after dewetting occurs, and is of order $1.0\,ms^{-1}$.

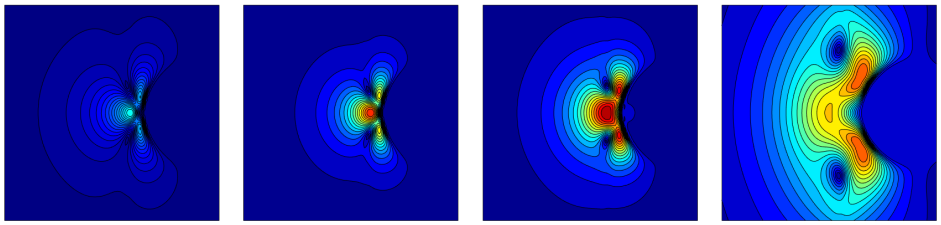

Figure 3.5: Heat map of the magnitude of the fluid velocity field in a quiescent system at the onset of dewetting, and shortly afterwards, when the energy associated with rapid flow begins to dissipate. We focus on a region close to the surface of the particle (visible as a curved dark region on the right of each snapshot), which starts at $d = 4.5\,nm$ from the interface between the two liquid phases. Dark blue shading indicates a quiescent region of the system, while red indicates the highest flow speeds.

To study the *quantitative* dynamics of dewetting, we vary the initial distance of the particle from the central interface and observe the time to the onset of dewetting. In a strongly segregated system ($W = 4.0$), all stages of dewetting occur in rapid succession: the time between the first sign of the interface distorting, and first contact of the favoured phase with the particle service is typically $\lesssim 1.0\,\mu s$. Thus, we take the dewetting point to be when the favoured phase first makes contact with the particle surface. This is quite straightforward to assess by inspection of snapshots of the system close to the dewetting point.

With these parameters, we observe (table 3.2 and figure 3.8) that dewetting occurs in less than $1.0\,\mu s$ when the particle starts at a distance $d = 2.5\,nm$ from the central interface, and the dewetting time increases to $\sim 60\,\mu s$ when $d = 4.5\,nm$. At $d = 5.0\,nm$ dewetting is not observed, indicating a critical film thickness, $d_c \sim 5\,nm$, given our assumptions about the strength and range of the intermolecular forces involved. This is broadly consistent with the literature, where theoretical predictions and measurements of the critical film thickness for spinodal dewetting range from a few nanometres to a few tens of nanometres [130].

We end this section with a note about the dynamics of the polymer-polymer interface long after dewetting has occurred. To observe the behaviour of the interface over longer time scales, we use a smaller particle, of radius $r = 5.0\,nm$, to reduce the computational load. In this simulation, the inter-

face continues to flatten, carrying the particle with it, even after $\sim 2.2\,ms$, indicating that the system has not reached equilibrium. The final equilibrium state of the system, in which the interface is flat and meets the surface of the particle at the true contact angle implied by the a wetting parameter of $W = 4.0$, is inaccessible in the time scale of our simulations.

3.7 Dewetting with Shear

The study of dewetting behaviour under shear has special practical relevance to the manufacture of composite materials, where nanoparticles are often added to polymer blends to enhance the mechanical properties of the end product. During the manufacturing process, particles can migrate to the phase boundaries, where they can retard, or even halt, further phase separation, or remain embedded in one phase or the other. The final distribution of particles in the composite material contributes to its mechanical properties (toughness and elasticity, for example). Since the dispersion of nanoparticles within a blend is commonly achieved by shearing the mixture, there are potential practical benefits to understanding this process in a minimal nanocomposite system.

The ability to model the behaviour of a particle near an interface under shear is an important first step in understanding the behaviour of such systems, and how to achieve the desired distribution of particles in the final product. Anderson et. al. [129] study the behaviour of a single particle close to an interface under shear, building on previous work on the dynamics of a particle, subject to an external force, near the interface between two liquid phases [126, 128]. In the later paper, the shear stress is applied parallel to the interface, which separates a viscoelastic fluid (within which the particle is initially situated), and a Newtonian fluid. Shearing the system induces a gradient in the normal stress close to the interface, and also creates a Laplace pressure as the interface is subtly distorted by the effect of shearing. The motion of the particle is determined by the balance of these forces which, in turn depend on dimensionless parameters in the model - chiefly the Weissenberg number, Wi (shear rate times relaxation time), and the Capillary number, Ca (the ratio of viscous stress and capillary stress). The simulations delineate four possible outcomes: migration of the particle away from the interface; movement towards the interface (which eventually stalls); adhesion to the interface; and migration across the interface into the Newtonian fluid. By varying Wi and Ca, the authors are able to produce morphology plots,

showing the dependence of the final state of the particle on the dimensionless parameters. They also vary other parameters in the model - for example, the equilibrium contact angle (determined by W in our model) and the mobility of the particle (determined by D in our model) - and show how these changes modify the morphology plots.

In a similar vein, Araki and Tanaka [95, 91] considers the movement of multiple particles, under hydrodynamic forces caused by phase separation in a quenched homogeneous polymer blend, and show how the resultant morphology of the system varies as the particle concentration and mobility is varied. In these simulations, there is no external shear on the system.

In contrast, the approach taken in this chapter is to apply a shear force that is perpendicular to the interface between the two liquid phases, and to observe the behaviour of the particle at different shear rates: in particular, can the particle be induced to migrate to its preferred phase, or does it adhere to the interface and remain stuck there? We begin by studying the dewetting of a thin film of the preferred phase at the surface of the particle, before considering later stages of the process by which the particle might migrate across the interface between the liquid phases.

As before, we use a wetting parameter of $W = 4.0$ in all simulations. The particle is initially located in the non-favoured phase, $4.5\,nm$ from the interface between the liquid phases, just less than the critical film thickness of $d_c \sim 5\,nm$. We vary this distance up to $d = 10\,nm$, and observe the dynamics of dewetting.

Initially, we consider the effect of two different shear rates on the dewetting behaviour of the system: $\dot{\gamma} = 1.0 \times 10^4\,s^{-1}$ and $\dot{\gamma} = 2.0 \times 10^4\,s^{-1}$. The former shear rate corresponds to a strain of 100% at $10^6 \times \Delta t = 100\,\mu s$. In all cases, the time at which dewetting occurs is estimated from snapshots of the system.

First, we illustrate the qualitative dynamics of dewetting at the chosen shear rates, compared with the dynamics of the quiescent system. Figure 3.6 shows snapshots of the system near the point of dewetting, after dewetting, and at a later stage, for the two shear rates considered, and at zero shear.

We also show the magnitude of the fluid velocity field, close to the surface of the particle, at the dewetting point, and shortly afterwards (figure 3.7). As in the quiescent system, the maximum speed of fluid flow is observed close to the surface of the particle, just after dewetting occurs, and is $\sim 1.0\,ms^{-1}$.

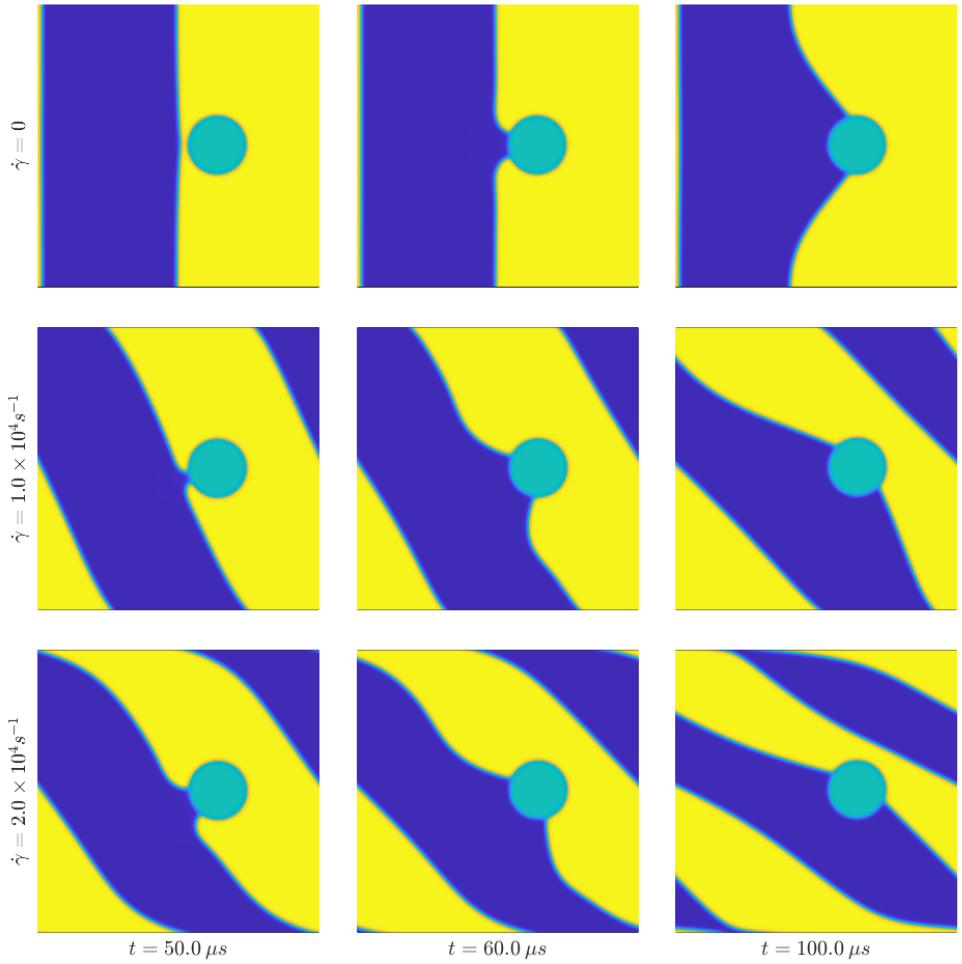

Figure 3.6: Stages of dewetting in a quiescent system, and at two different shear rates. In each case, the particle starts at a distance $d = 4.5\,nm$) from the interface between the liquid phases, and we show the system at or near the dewetting point, after dewetting, and at a later stage, as shearing continues.

To quantify these observations, we plot the dewetting time, against the initial distance of the particle from the interface, which ranges from $d = 2.5\,nm$ to $d = 10.0\,nm$, for the quiescent system and for the two shear rates used. Table 3.2 summarises the results, which are plotted in figure 3.8.

Again, we note a critical film thickness of $d_c \sim 5\,nm$. When $d \gtrsim d_c$, dewetting only occurs under shear, as the externally imposed flow deforms the interface between the liquid phases, bringing it closer to the surface of the particle. This is consistent with the assumed range of the intermolecular

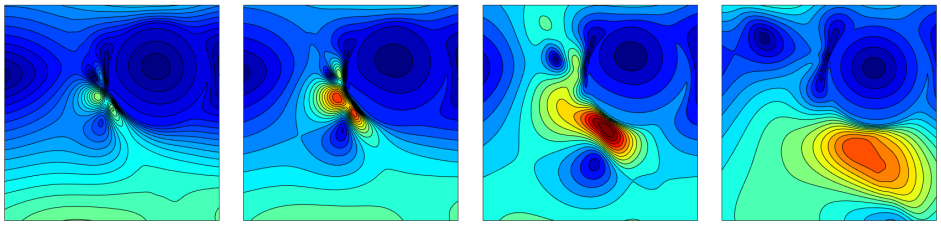

Figure 3.7: Heat map of the magnitude of the fluid velocity field in a sheared system ($\dot{\gamma} = 2.0 \times 10^4\, s^{-1}$) at the onset of dewetting, and shortly afterwards. We focus on a region close to the surface of the particle (visible as a circular region at the top-right of each snapshot), which starts at a distance $d = 4.5\,nm$) from the interface between the liquid phases. Dark blue shading indicates a quiescent region of the system, while red indicates the highest flow speeds.

	Dewetting Time $[\mu s]$		
Distance [nm]	$\dot{\gamma} = 0$ $[\times 10^4\, s^{-1}]$	$\dot{\gamma} = 1.0$ $[\times 10^4\, s^{-1}]$	$\dot{\gamma} = 2.0$ $[\times 10^4\, s^{-1}]$
2.5	1.2	1.2	1.2
4.0	10.4	10.6	10.8
4.5	57.4	49.7	46.8
5.0	-	64.2	54.5
6.0	-	76.5	61.1
7.0	-	86.4	65.9
8.0	-	96.2	70.5
9.0	-	107.0	74.9
10.0	-	118.4	79.0

Table 3.2: Dewetting time in a quiescent system and under a constant shear rate of $\dot{\gamma} = 1.0 \times 10^4\, s^{-1}$ and $\dot{\gamma} = 2.0 \times 10^4\, s^{-1}$ as the distance of the particle from the interface varies from $d = 2.5\,nm$ to $d = 10.0\,nm$.

forces in our model, and with the range of values for the critical film thickness seen in the literature [41]. The dewetting time ranges from $\sim 1\,\mu s$ to $\sim 100\,\mu s$. Again, this is consistent with our assumptions about the range of intermolecular forces, and the characteristic time scale used in our model. Finally, the dewetting curves in figure 3.8 clearly show a transition from the diffusive regime to the hydrodynamic regime, close to the critical film thickness, d_c. When $d \leq d_c \sim 5\,nm$ the dewetting time is almost independent of the shear rate, because the dynamics of the system are dominated by the rapid diffusive mechanism at these length scales. In contrast, when $d \gtrsim 7.0\,nm$, the dewetting time appears to vary almost linearly with d, since

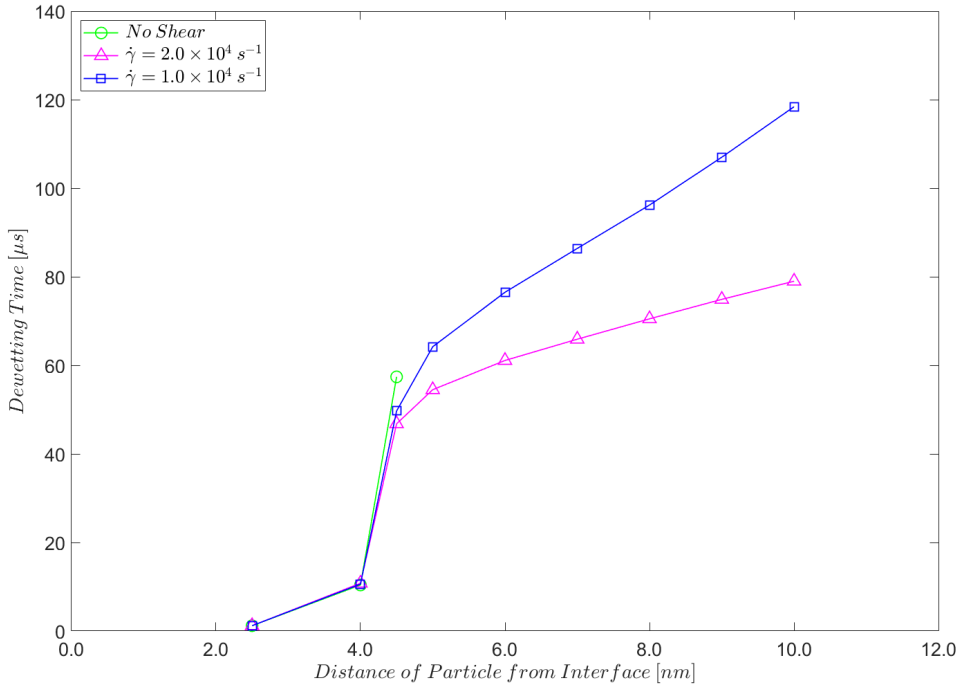

Figure 3.8: Dependence of the dewetting time, in the Rouse regime, on the initial distance of the particle from the interface, with and without shear.

the constant shear applied to the system is now the dominant mechanism in the dewetting process. In the next chapter, we show that these observed dewetting times are consistent with a simple model, in which the interface between the two liquid phases shears linearly with time, and dewetting occurs almost instantaneously when the distance between the particle and the interface is small (less than $\sim 3.0\,nm$, say).

3.8 Shear-Induced Migration across an Interface

Under shear, it is possible that the particle will be fully expelled from its non-preferred phase, after dewetting has occurred. In this section, we consider the steady state of the particle, beyond the dewetting point, at a range of constant shear rates. We take an initial state in which the particle begins $d = 4.5\,nm$ (i.e. just below the critical film thickness, $d_c \sim 5.0\,nm$) from the central interface as our base case, and vary the shear rate from $\dot{\gamma} =$

$1.0 \times 10^4\, s^{-1}$ to $\dot{\gamma} = 2.4 \times 10^4\, s^{-1}$ in steps of $\Delta\dot{\gamma} = 0.2 \times 10^4\, s^{-1}$. In each case, the simulation runs long enough to observe the complete expulsion of the particle from its non-preferred phase or, if expulsion does not occur, any alternative steady state that might arise.

When complete expulsion occurs, it is preceded by initial dewetting, breaking of the central interface under shear-induced stress, a second dewetting, and wetting of the particle by its preferred phase. Expulsion occurs when the non-preferred phase detaches completely from the surface of the particle. Some time after the particle is expelled, the system reaches its steady state. Figure 3.9 illustrates the generic stages in the expulsion process. Note that, in this figure, "interface breaking" refers to the central interface between the two liquid polymer phases, and not to the interface of either liquid phase with the solid particle. Loosely speaking, breaking occurs when the central interface detaches itself from the top edge of the system, under the effect of shear strain. A more precise, operational definition of interface breaking might be desirable for some purposes but we do not pursue this here, as our main interest is in the other stages of the expulsion process.

However, in some cases, after the interface between the two liquid phases breaks, the second dewetting fails to occur because the region of the preferred phase fails to make contact with the surface of the particle, as it retracts. In this scenario, which occurs at the lowest and highest shear rates used in our simulations, an alternative steady state is reached in which the particle adheres to the surface of a droplet of the preferred phase, embedded in the non-preferred phase (figure 3.10).

The motion of the particle as the system is sheared, and dewetting occurs, depends on the steady state reached. Figure 3.11 compares the trajectory of the particle in real space for shear rates of $\dot{\gamma} = 1.2 \times 10^4\, s^{-1}$ and $\dot{\gamma} = 1.6 \times 10^4\, s^{-1}$. At the higher shear rate, the particle is expelled from its non-preferred phase while, at the lower shear rate it reaches the alternative steady state of figure 3.10. The trajectories shown in figure 3.11 are typical of the two cases. Note that the displacement of the expelled particle, relative to its starting position, is primarily in the positive y-direction, while the displacement of the particle in the alternative steady state is primarily in the negative x-direction

It is also instructive to consider the evolution of the mean free energy density at various shear rates up to a point just after dewetting first occurs (figure 3.12).

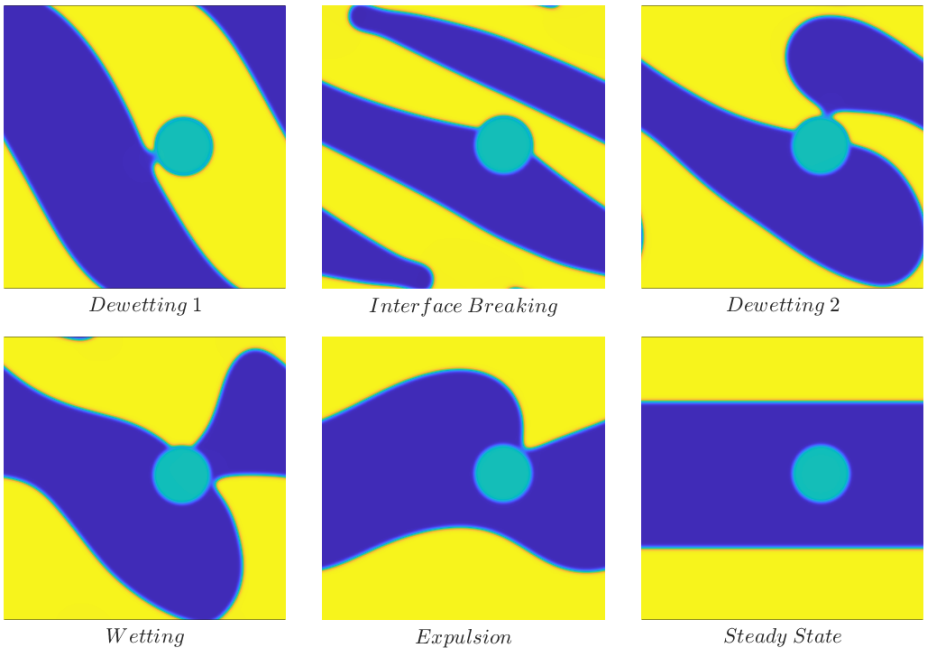

Figure 3.9: Generic stages of the expulsion process, from initial dewetting, via interface breaking, to the point of expulsion, and the steady state at long time scales. In this simulation, the particle starts at a distance $d = 4.5\,nm$ from the central interface, and the shear rate is $\dot{\gamma} = 2.0 \times 10^4\,s^{-1}$. Interface breaking occurs at $\sim 200.0\,\mu s$, and the steady state shown occurs after $\sim 1.0\,ms$.

Figure 3.12 shows a period of very early, rapid equilibration at the interface of duration $\sim 1.0\,\mu s$, during which the mean free energy density decreases slightly. This is followed by a steady increase in the mean free energy density due to the increased strain at the interface as the system is sheared at a constant rate. At all shear rates, dewetting occurs between $40\,\mu s$ and $50\,\mu s$, and is accompanied by a temporary decrease in the mean free energy density, before it resumes its steady increase due to shear-induced strain at the interface between the two liquid phases. The sawtooth pattern superimposed on the mean free energy density curves is an artefact of the discretisation of the lattice.

Finally, we turn to the time scales over which the various stages of the particle's expulsion from its non-preferred phase occur. Table 3.3 summarises the results of simulations in the Rouse regime at shear rates between $\dot{\gamma} = 1.0 \times 10^4\,s^{-1}$ and $\dot{\gamma} = 2.4 \times 10^4\,s^{-1}$. For completeness, we also show the dewetting time in the quiescent system, where the other stages of expulsion do not occur (instead, the particle adheres to the slowly flattening interface).

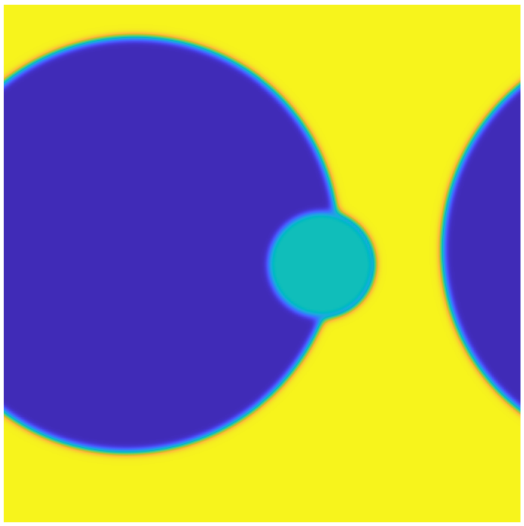

Figure 3.10: Alternative steady state, observed at the lowest and highest shear rates used in our simulations. In this case, $\dot{\gamma} = 1.2 \times 10^4\, s^{-1}$ and the initial distance of the particle from the central interface is $d = 4.5\, nm$. The image shows the state of the system after $600\, \mu s$.

Shear Rate $[\times 10^4\, s^{-1}]$	Dewetting 1 $[\mu s]$	Dewetting 2 $[\mu s]$	Wetting $[\mu s]$	Expulsion $[\mu s]$
No Shear	57.4	-	-	-
1.0	49.7	A	A	A
1.2	48.9	A	A	A
1.4	48.2	225.6	245.8	310.8
1.6	47.7	201.0	220.8	295.4
1.8	47.2	175.9	194.3	270.3
1.9	47.0	159.7	176.7	251.3
2.0	46.8	144.6	159.6	160.3
2.2	46.4	A	A	A
2.4	46.0	A	A	A

Table 3.3: Stages of the expulsion process at constant shear rates from $\dot{\gamma} = 1.0 \times 10^4\, s^{-1}$ to $\dot{\gamma} = 2.0 \times 10^4\, s^{-1}$. In all simulations, the particle starts $4.5\, nm$ from the central interface. A letter 'A' indicates that the alternative steady state in which the particle adheres to a droplet of its preferred phase is reached (i.e. after the initial dewetting, no further stages of the expulsion process are observed).

The expulsion data summarised in table 3.3 is plotted in figure 3.13.

In these simulations, complete expulsion occurs at shear rates of $1.4 \times 10^4\, s^{-1} \leq \dot{\gamma} \leq 2.0 \times 10^4\, s^{-1}$. Outside this range, the system reaches the alternative

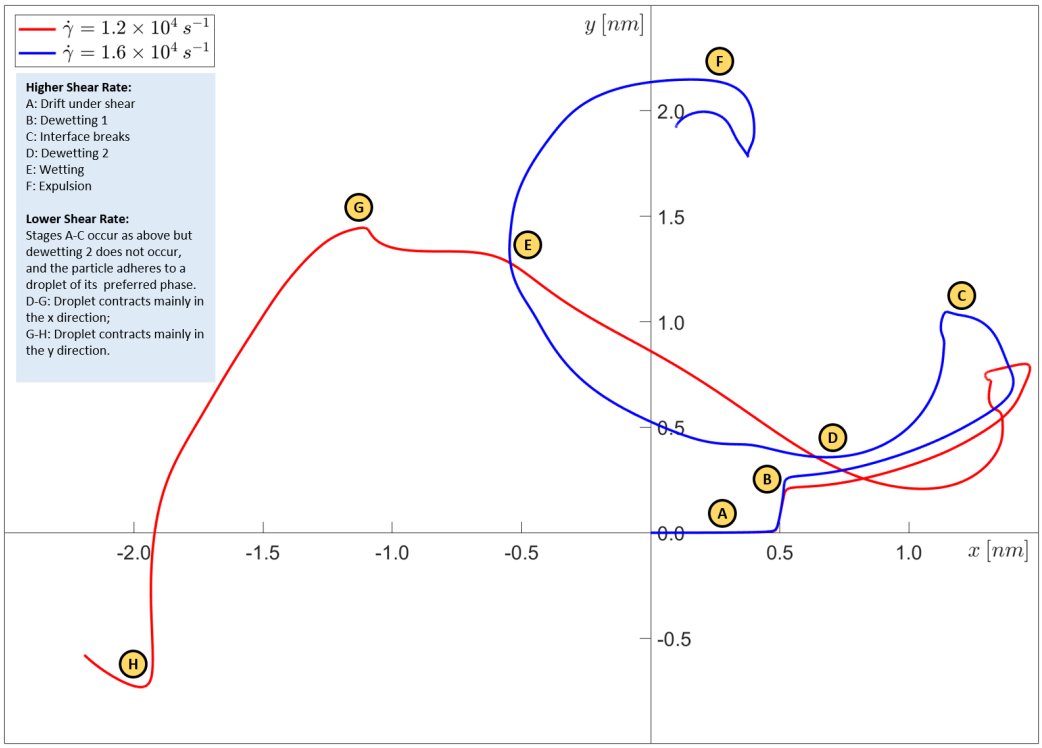

Figure 3.11: Typical particle trajectories at two shear rates, over a physical time period of $400\,ms$. At the higher shear rate of $\dot{\gamma} = 1.6 \times 10^4\ s^{-1}$, the particle is fully expelled from the non-preferred phase. Labels A to F correspond with the stages of expulsion depicted in figure 3.9. At the lower shear rate of $\dot{\gamma} = 1.2 \times 10^4\ s^{-1}$, dewetting 2 does not occur. Instead, a droplet of the preferred phase forms, and the particle adheres to it. From the point corresponding with D to the point G, the droplet contracts mainly in the x-direction. From G to H, the droplet contracts mainly in the y-direction.

steady state in which the particle adheres to a droplet of its preferred phase.

The second dewetting time decreases (approximately) linearly as the shear rate increases. Similarly, the wetting time decreases (approximately) linearly as the shear rate increases, and the time between second dewetting and wetting is roughly constant ($\sim 20\,\mu s$) at all shear rates at which complete expulsion occurs.

The relationship between the expulsion time and the shear rate is more complex. Between $\dot{\gamma} = 1.4 \times 10^4\ s^{-1}$ and $\dot{\gamma} = 1.9 \times 10^4\ s^{-1}$ the expulsion time decreases as the shear rate increases, but the relationship is notably less linear than that between the times of the earlier stages of expulsion, and the shear rate. At $\dot{\gamma} \leq 2.0 \times 10^4\ s^{-1}$, there is a sudden decrease in the expulsion time, and the particle is expelled from its non-preferred phase very soon after

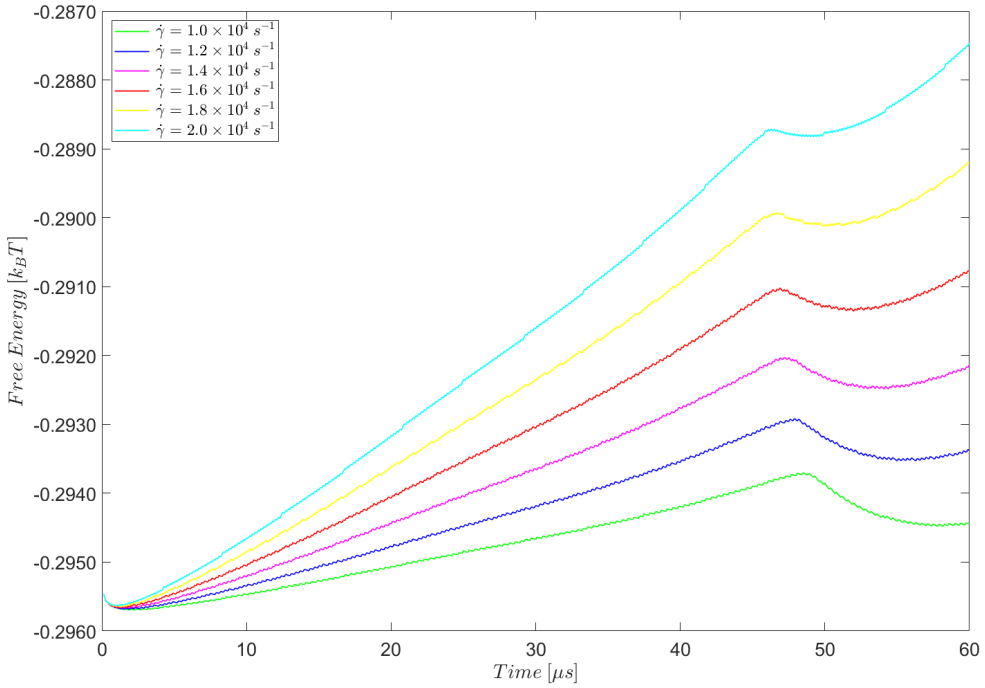

Figure 3.12: Evolution of the mean free energy density under shear up to, and just after, the first dewetting point for $\dot{\gamma} = 1.0 \times 10^4\ s^{-1}$ to $\dot{\gamma} = 2.0 \times 10^4\ s^{-1}$.

wetting occurs, In fact, these two events are almost simultaneous.

Finally, although it is not obvious in figure 3.13, the initial dewetting time decreases as the shear rate increases. To highlight this point, we present the corresponding simulation results and plot as previously, but with an initial distance of the particle from the interface of $d = 9.0\,nm$, double the value used in the earlier simulations (table 3.4 and figure 3.14).

As expected, the decrease in the initial dewetting time as the shear rate increases is now more easily visible, although the relationship is still quite weak due to the short time scales involved, compared with the time scales of the later stages of the expulsion process. In contrast with simulations where the particle starts $d = 4.5\,nm$ from the interface, the particle is now almost always expelled from its non-preferred phase. This indicates that the steady state of the particle is determined by both the initial configuration of the system, and the applied shear rate.

For shear rates between $\dot{\gamma} = 1.0 \times 10^4\ s^{-1}$ and $\dot{\gamma} = 1.4 \times 10^4\ s^{-1}$, figure 3.14 resembles the higher shear rate region of figure 3.13. That is, we observe a somewhat linear relationship between the times of the various stages of

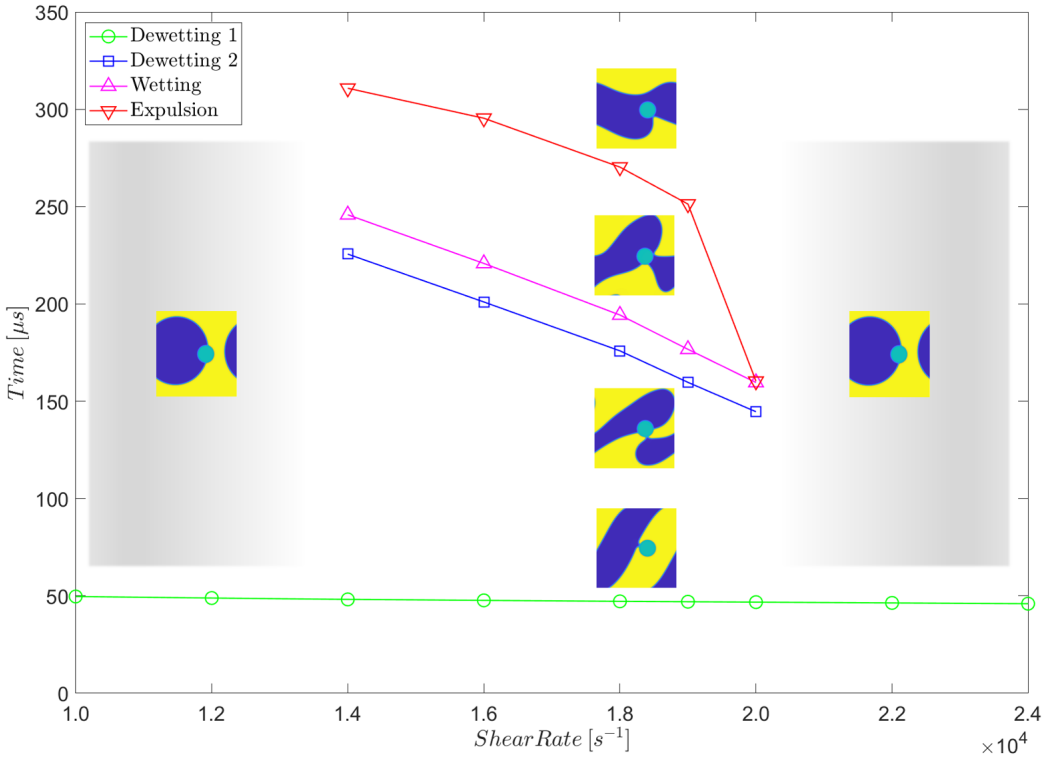

Figure 3.13: Stages of the expulsion process at constant shear rates from $\dot{\gamma} = 1.0 \times 10^4\, s^{-1}$ to $\dot{\gamma} = 2.4 \times 10^4\, s^{-1}$. In all simulations, the particle starts $4.5\, nm$ from the central interface. At shear rates of $\dot{\gamma} \leq 1.2 \times 10^4\, s^{-1}$ and $\dot{\gamma} \geq 2.2 \times 10^4\, s^{-1}$ the alternative steady state, in which the particle adheres to a droplet of its preferred phase, is reached.

Shear Rate $[\times 10^4\, s^{-1}]$	Dewetting 1 $[\mu s]$	Dewetting 2 $[\mu s]$	Wetting $[\mu s]$	Expulsion $[\mu s]$
No Shear	-	-	-	-
1.0	106.9	291.4	315.6	381.0
1.2	92.5	243.9	267.8	329.6
1.4	85.1	214.1	235.0	300.7
1.6	80.5	159.8	189.7	190.7
1.8	77.2	158.5	178.4	180.4
2.0	74.7	162.7	206.0	217.2
2.2	73.0	192.1	267.4	300.2
2.4	71.9	A	A	A

Table 3.4: Stages of the expulsion process at constant shear rates from $\dot{\gamma} = 1.0 \times 10^4\, s^{-1}$ to $\dot{\gamma} = 2.0 \times 10^4\, s^{-1}$. In all simulations, the particle starts $9.0\, nm$ from the central interface.

the expulsion process and the shear rate. Again, the time between second

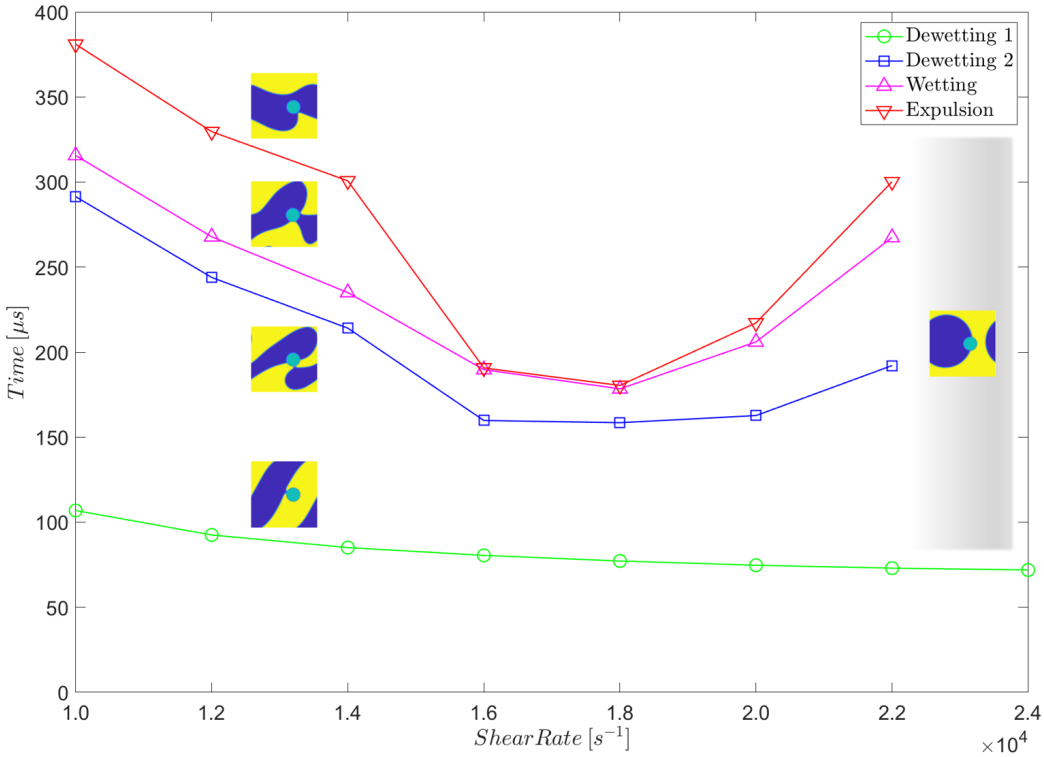

Figure 3.14: Stages of the expulsion process at constant shear rates from $\dot{\gamma} = 1.0 \times 10^4\, s^{-1}$ to $\dot{\gamma} = 2.4 \times 10^4\, s^{-1}$. In all simulations, the particle starts $9.0\, nm$ from the central interface. In contrast with the case when the particle starts $4.5\, nm$ from the central interface, the particle is expelled into its preferred phase, at almost all shear rates.

dewetting and wetting is roughly constant at $\sim 20\, \mu s$ in this range of shear rates.

At $\dot{\gamma} = 1.6 \times 10^4\, s^{-1}$, there is a sudden decrease in the expulsion time, and the particle is expelled from its non-preferred phase very soon after wetting occurs (the two events are virtually simultaneous). This is similar to what we observe in the previous simulations with $d = 4.5\, nm$ at a shear rate of $\dot{\gamma} = 2.0 \times 10^4\, s^{-1}$.

At shear rates of $\dot{\gamma} \geq 1.6 \times 10^4\, s^{-1}$, the times of the later stages of expulsion (second dewetting, wetting, and expulsion) remain relatively constant as the shear rate increases, before beginning to increase when the shear rate is $\dot{\gamma} \sim 2.0 \times 10^4\, s^{-1}$. This rising trend in the times to second dewetting, wetting and expulsion continues up to a shear rate of $\dot{\gamma} \sim 2.4 \times 10^4\, s^{-1}$ when the system abruptly reverts to the alternative steady state illustrated in figure 3.10.

The behaviour of the system when the shear rate is $\dot{\gamma} = 1.8 \times 10^4\, s^{-1}$ is unusual. Although the particle is *initially* expelled from the non-preferred phase at $t = 180.4\,\mu s$ (as plotted in figure 3.14), it then repeatedly adheres to, and detaches from, the interface between the liquid phases, before finally reaching the steady state observed in the other simulations (figure 3.15). The *final* expulsion of the particle from the non-preferred phase occurs at $t \sim 550\,\mu s$, much later than the initial expulsion time plotted in figure 3.14.

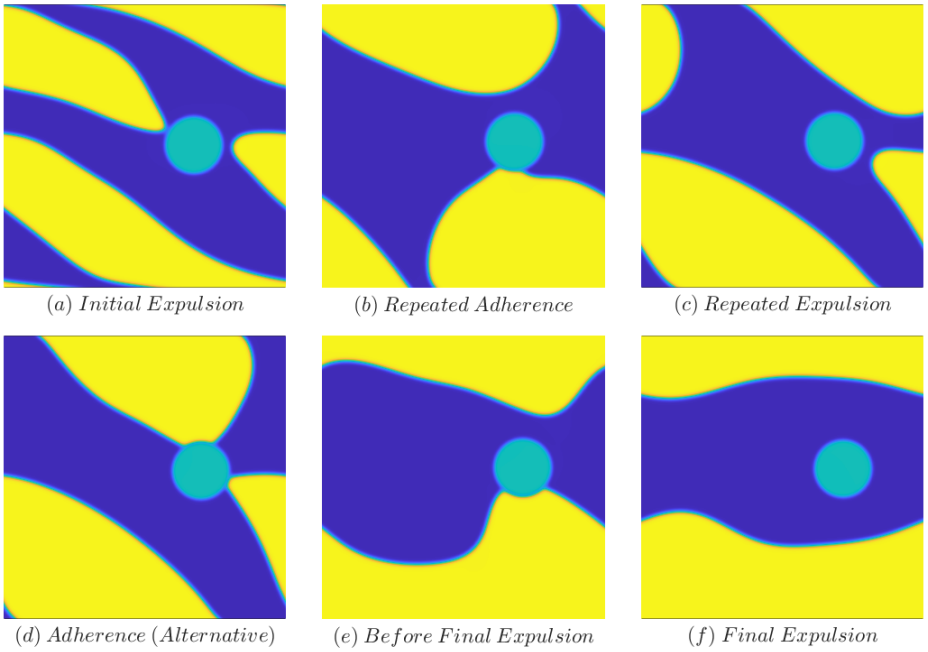

(a) *Initial Expulsion* (b) *Repeated Adherence* (c) *Repeated Expulsion*

(d) *Adherence (Alternative)* (e) *Before Final Expulsion* (f) *Final Expulsion*

Figure 3.15: Stages of the expulsion process at $\dot{\gamma} = 1.8 \times 10^4\, s^{-1}$ when the particle starts $9.0\,nm$ from the central interface. Image (a) shows the initial expulsion of the particle at $t = 180.4\,\mu s$. The system then alternates between states similar to those shown in images (b) and (c), although (d) is also observed at $t \approx 450\,\mu s$. Eventually, the state shown in image (e) is reached, and the particle is finally expelled from it's non-preferred phase at $t \approx 550\,\mu s$; image (f) shows the system shortly afterwards, as it evolves towards its steady state.

Regardless of the starting position of the particle, two steady states are observed: expulsion from the non-preferred phase; and adhesion to the interface of a droplet of the preferred phase, in a matrix of the non-preferred phase. Both of these regimes are seen in [95], where the migration of multiple particles is promoted by hydrodynamic currents in a phase-separating blend. In contrast to [129], we do not observe steady states in which the particle remains in the non-preferred phase. This is to be expected, since the effect of shear in our simulations is to move the interface between the two liquid

phases closer to the surface of the particle, until the the non-localised forces in the vicinity of the particle surface become sufficient to initiate dewetting.

However, it is not necessarily the case that the particle *cannot* remain in the non-preferred phase, when the system is sheared. As figure 3.11 shows, the particle initially moves *away* from the interface, under the influence of shear-induced flow. It is also possible that different parameter choices might lead to a wider variety of steady states, like those observed in [129]. In particular, we hypothesise that the relative strength of the particle's affinity for the two liquid phases, as represented by the W parameter, will partially determine the final steady state of the system under shear.

3.9 Methodological Note

We end this chapter with some methodological remarks about how the dewetting point - and the other stages of the particle's migration across the interface between the two liquid phases - is determined. Earlier, we stated that we take our cue from snapshots of the system, as it approaches the dewetting point, and that we take dewetting to occur when the preferred phase first makes clear contact with the surface of the particle. An alternative approach is to observe the evolution of the mean free energy density of the system as it approaches the dewetting point. As figure 3.12 makes clear, dewetting is accompanied by a spontaneous and rapid decrease in the mean free energy density. Figure 3.16 compares these two approaches for a quiescent system (so, for clarity, the increase in the mean free energy density due to shear is absent), when the initial distance of the particle from the central interface is $d = 4.5\,nm$.

Dewetting occurs rapidly in the strongly segregated regime, in which the Flory-Huggins interaction parameter, $\chi = 4.0$. Nevertheless, there is a difference of more than $1.0\,\mu s$ between the dewetting times, as measured by the two methodologies. It is tempting to insist that the first method, which identifies the dewetting point with the point at which the mean free energy density spontaneously decreases, is the correct one, since it is firmly grounded in the thermodynamics of the system. However, this approach falls foul of a practical difficulty, as illustrated by figure 3.17, which plots the evolution of the mean free energy density of the system over a longer period, up to the point at which it is expelled from its non-preferred phase, or reaches the alternative steady state. Note that the labels in figure 3.17 match the labels

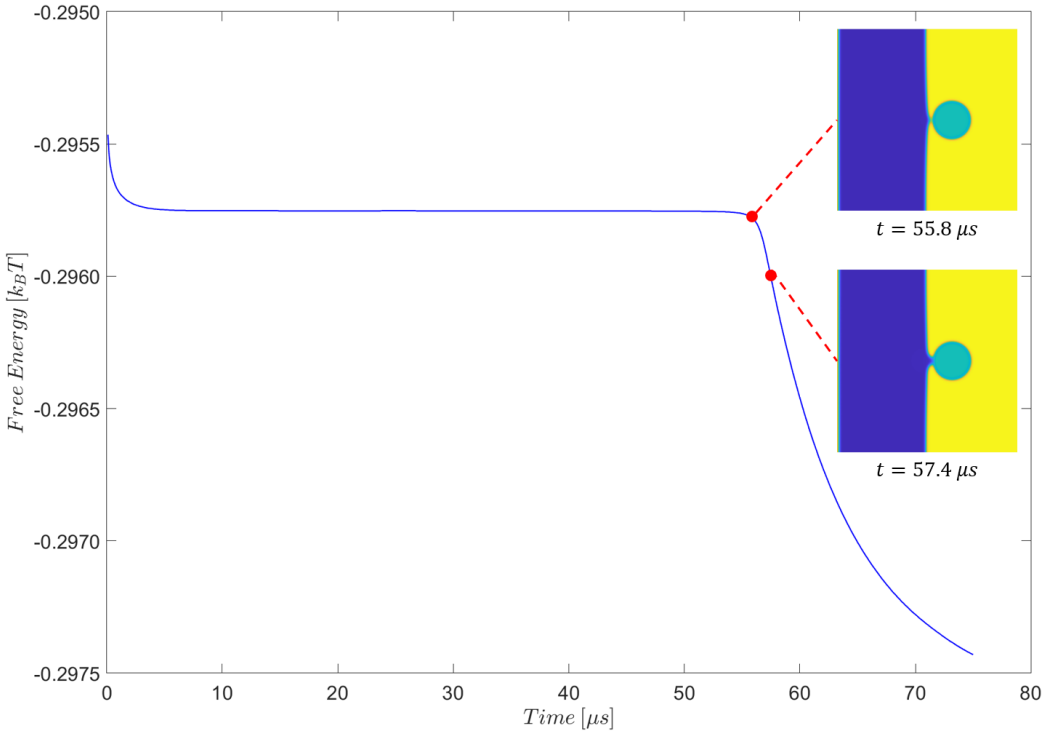

Figure 3.16: Comparison of two methods of determining the dewetting point. The system is quiescent, and the initial distance of the particle from the central interface is $d = 4.5\,nm$. If we take dewetting to occur when there is a spontaneous and rapid decrease in the mean free energy density of the system, the dewetting time is $t = 55.8\,\mu s$. If we take dewetting to occur when the preferred phase first makes clear contact with the surface of the particle, the dewetting time is $t = 57.4\,\mu s$.

in figure 3.11, and mark key stages in the particle's trajectory, as the system is sheared.

In figure 3.17 we observe the first dewetting at both shear rates as a temporary decrease in the mean free energy density, before it continues to rise due to the shear induced strain at the interface between the two liquid phases. When the interface breaks, the mean free energy density rapidly decreases, and the variations in the mean free energy density due to the second dewetting, and later stages of the expulsion process, are very difficult to discern. The later variations in mean free energy density may be attributed to the net effect of shear, which tends to increase the total free energy of the system, and the relaxation of the interface between the two liquid phases, which tends to decrease the free energy. In any case, it is difficult to correlate the key events in the particle's migration across the interface between the two liquid phases, with changes in the evolution of the mean free energy density

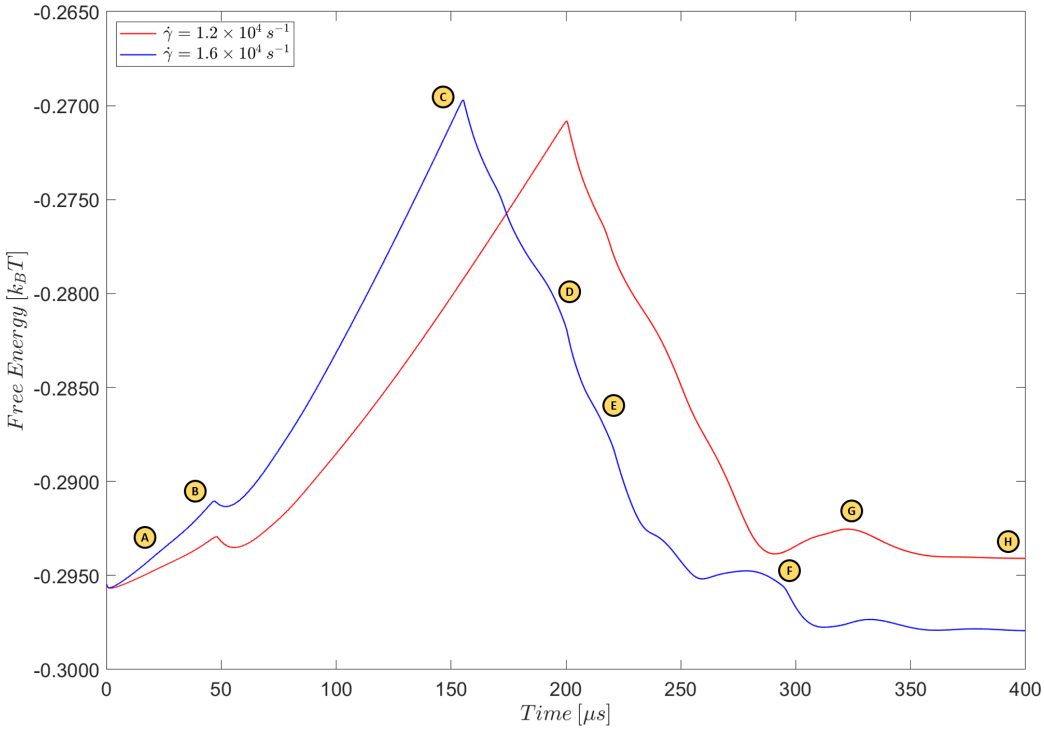

Figure 3.17: Evolution of mean free energy density, at two shear rates, over a physical time period of $400\,ms$. At the higher shear rate of $\dot{\gamma} = 1.6 \times 10^4\ s^{-1}$, the particle is fully expelled from the non-preferred phase, while at the lower shear rate of $\dot{\gamma} = 1.2 \times 10^4\ s^{-1}$, the particle adheres to a droplet of the preferred phase. Labels A to H correspond with the same labels in figure 3.11.

of the system.

Before leaving figure 3.17, it is interesting to note that the mean free energy density in the alternative steady state (figure 3.10) is higher than the mean free energy density when the particle is expelled from the non-preferred phase. This may be due to a combination of two factors. Firstly, there is an energy cost to the particle remaining in contact with the non-preferred phase. Secondly, the droplet of the preferred phase in the alternative steady state remains subject to shear, which prevents it from reaching an energy-minimising shape, and increases the total free energy. In contrast, when the particle is expelled from the non-preferred phase, both interfaces between the liquid phases are parallel to the applied shear field, which therefore performs no work on them.

A further difficulty with using a plot of the mean free energy density to determine the dewetting point, and the timing of other key events in the

particle's migration will become apparent in chapter 5, where we consider weakly segregated systems. The issue here is that dewetting is a much more gradual process in a weakly segregated system, due to the lower energy of the central interface between the two liquid phases. Thus, the determination of the dewetting point, by inspection of the evolution of the mean free energy density, is not straightforward, and determination of the timing of other key events in the particle's migration is even more difficult.

For these reasons, we prefer to determine the timing of key events in the particle's migration across the central interface by inspecting snapshots of the system, as it is sheared. Although this approach is not strictly grounded in the thermodynamics of wetting and dewetting, it is more practical, given the effect of shear on the mean free energy density of the system, and it may be applied consistently to a wide range of systems in which the degree of entanglement, and the strength of the segregation between the two liquid phases is varied.

3.10 Summary

Building on the theoretical work of the previous chapter, we have constructed and solved a physical model for the Stokes equations of a non-homogenous liquid in the presence of solid interfaces, and applied it to a minimal nanocomposite system. Our model is consistent with the contact value theorem regarding thermodynamical equilibrium of liquids in contact with solid interfaces [107, 109, 112, 110] and with the general formalism of Onsager regarding the linear response theory of out-of-equilibrium systems [114, 117, 89]. It allows us to describe how non-homogeneous liquids relax towards equilibrium by diffusion and convection. A key feature of our model is that the interfacial forces on solid interfaces are not located on the interface itself but are distributed in their vicinity and appear as body forces in the Stokes equations.

To solve the physical model, we use a numerical approach introduced by Araki and Tanaka where the particle is described as a highly viscous liquid; this allows us to solve the Stokes equations in the whole system without managing complex boundary conditions. The model enables us to describe wetting and dewetting of particles at, or in the vicinity of, liquid interfaces, at rest or in the presence of an imposed shear. It also enables us to realistically model the migration of a particle from one liquid phase to another, via a process of first dewetting, second dewetting, wetting by the preferred phase,

and expulsion, when shear is applied to the system, while enabling us to explore the factors which determine whether expulsion eventually occurs, or whether an alternative steady state is reached.

All the results described in this chapter refer to systems in the Rouse regime, where $D = 1$, and the effects of the entanglement of polymer chains at the microscopic level are not significant. In addition, the minimal nanocomposite system considered in this chapter is strongly segregated ($\chi = 4.0$). That is, the liquid phases in the system are close to being pure polymers of either species A or species B, and the interfacial energy between the two liquid phases is high. Both of these factors make it relatively straightforward to simulate the behaviour of the minimal nanocomposite system. In the remainder of the thesis, we relax each in turn, and observe how the behaviour of the minimal nanocomposite system changes, while also becoming more difficult to simulate.

Chapter 4

Entangled Systems

4.1 Introduction

In this chapter we consider the behaviour, in the entangled regime, of a particle close to the interface between the two liquid phases in a minimal nanocomposite system. In the terms of our model, this means that the degree of polymerisation, N exceeds the entanglement limit, N_e, which we take to be 100. At the molecular scale, this implies that polymer chain dynamics may be described by the theory of reptation.

In brief, the reptation model treats a single, test polymer chain as if it were moving within a tube defined by topological constraints (entanglements) imposed by other chains in the melt (or solution) [99, 132]. It is a mean field theory in the sense that it abstracts from the detail of local interactions with other chains and, in effect, replaces the potential they create with an average potential represented by the tube, within which the test chain is said to be confined. This means that the tube may only move parallel to the axis of the tube defined by these topological constraints: in other words, it reptates through the tangle of other chains in the system, as a snake slithers through grass. Such entangled systems are defined by a characteristic reptation time, τ_{rept}, which determines what fraction of the test chain, at time t, is still located within the tube that enclosed it at the earlier time t'. The relaxation of an entangled polymer system (as characterised by its plateau modulus) is determined by this characteristic timescale, τ_{rept}.

Further refinement of this model is possible, and the dynamics of entangled

polymer systems remains an active area of research. For example, the double reptation model developed by des Cloiseaux [133] and Tsenoglou [134] recognises that the physical reality of the tube that constrains the test chain in the reptation model lies in the topological constraints imposed by other polymer chains in the melt. To take account of the fact that these other tubes are themselves in motion, the double reptation model treats the tube defined by their entanglements with the test chain as subject to relaxation with its own characteristic timescale.

In our model, we focus on the mesoscale, and abstract from these complications at the molecular level. The degree of entanglement in the system is represented by the parameter D (a dimensionless effective diffusion coefficient), which equates to the ratio of N, the number of monomers in a polymer chain, to the entanglement limit, $N_e = 100$. The use of a single parameter, D to represent the underlying complexity at the molecular scale means that we also neglect viscoelastic effects, and effects attributable to the non-isotropy at the molecular scale, of long polymer chains. Nevertheless, as we will see, varying D gives rise to a rich variety of dewetting behaviour in the minimal nanocomposite system that is the focus of our study.

The chapter is structured as follows. Firstly, we consider the case when $D = 10$. This corresponds with a degree of polymerisation of $N = 1000$ monomers per chain. This is the close to largest value of N accessible, given the computational resources available. Although much larger polymer molecules exist, the case of $N = 1000$ places us well into the entangled regime, and is sufficient to exhibit behaviour that contrasts with the behaviour of our system in the Rouse regime.

Next, we turn to the two intermediate cases of $D = 5$ and $D = 2$, and compare the dewetting behaviour of our system with the behaviour of both the maximally entangled system ($D = 10$) and the system in the Rouse regime.

Finally, we review some of the main results obtained so far, and consider their implications for the mechanisms at work in the dewetting process. In particular, we assess the influence of shear-induced hydrodynamic flow and the forces associated with it on the shear strain of the system at the first dewetting point. A simple geometrical model of dewetting under shear, based on three key assumptions, is used to guide the analysis.

4.2 Parameter Settings

The parameters that define the strength of interactions between polymers and between each polymer and the particle remain unchanged. That is, as in the Rouse regime simulations, we take $\chi = 4.0$ and $W = 4.0$.

The main change is that the effective diffusion coefficient, D, is no longer equal to 1, but is instead set, initially, to the higher value of $D = 10$ to reflect the entanglement of polymer chains at the molecular level. In our model, D equates to $\frac{N}{N_e}$, where N is the degree of polymerisation, and N_e is the entanglement limit. Thus $D = 10$ implies that each polymer chain in our system consists of 1000 monomers, and we are well into the entangled regime.

To maintain computational stability, we decrease the time step in our simulations from $\tilde{\Delta}t = 0.001$ to $\tilde{\Delta}t = 0.0001$. Physically, this means that each time step equates to $10^{-8}\,s$ in our entangled regime simulations, compared with $10^{-10}\,s$ in the Rouse regime.

From our earlier discussion (section 3.4) of dimensionless quantities in the model, we can deduce that varying D will also change some of the other *physical* quantities represented by the model. For example, the increase in the effective diffusion coefficient from $D = 1$ to $D = 10$ *reduces* the physical shear rate. In the entangled regime, with $D = 10$, a dimensionless shear rate of $\tilde{\dot{\gamma}} = 0.001$ implies a physical shear rate of $\dot{\gamma} = 10\,s^{-1}$; in contrast, the same dimensionless shear rate implies a physical shear rate of $\dot{\gamma} = 1.0 \times 10^4\,s^{-1}$ in the Rouse regime. In general, the relationship between the physical shear rate and the effective diffusion coefficient is given by: $\dot{\gamma} \propto \frac{1}{D^3}$.

Similarly, increasing D increases the mean physical viscosity, η, of the system. Consideration of the relationships between the various quantities in the model shows that $\eta \propto D^3$.

4.3 Dewetting in a Highly Entangled System

In this section, we consider the dewetting behaviour of a minimal nanocomposite system when the effective diffusion coefficient, $D = 10$. This is the highest value of D used in our simulations due to computational resource

constraints, and corresponds with a polymer chain length of $N = 1000$. Having already validated our model with simple wetting simulations in the Rouse regime (section 3.5), we proceed directly to an investigation of the dewetting behaviour of our entangled system.

As in the Rouse regime simulations, we first vary the initial distance d of the particle from the central interface and observe the time it takes for spinodal dewetting to occur. In a quiescent system, this enables us to determine the critical film thickness. We then explore dewetting behaviour under two different shear rates ($\dot{\gamma} = 10\,s^{-1}$ and $\dot{\gamma} = 20\,s^{-1}$) for a range of values of d above and below the critical film thickness.

Table 4.1 summarises the results of our simulations, and these are plotted in figure 4.1.

	Dewetting Time $[ms]$		
Distance [nm]	$\dot{\gamma} = 0$	$\dot{\gamma} = 10\,s^{-1}$	$\dot{\gamma} = 20\,s^{-1}$
2.5	0.2	0.1	0.1
4.0	3.6	3.6	3.6
4.5	24.8	24.5	22.9
5.0	-	53.0	45.1
6.0	-	67.1	53.3
7.0	-	78.5	59.1
8.0	-	89.8	64.2
9.0	-	101.6	68.9
10.0	-	113.6	73.2

Table 4.1: Dewetting time in a quiescent system, and at constant shear rates of $\dot{\gamma} = 10\,s^{-1}$ and $\dot{\gamma} = 20\,s^{-1}$. The distance of the particle from the interface is varied from $d = 2.5\,nm$ to $d = 10.0\,nm$. The system is highly entangled, with an effective diffusion coefficient, $D = 10$.

Comparing these results with those in the Rouse regime, we first note the similarity in the overall shape of the dewetting curves at the upper and lower shear rates used in the simulations. A second important observation is that, in both regimes, the critical film thickness, d_c, lies between $4.5\,nm$ and $5.0\,nm$. This is to be expected as the principal effect of increasing D is to slow down the dynamics of the system, while leaving many of its other essential physical properties intact.

The slower dynamics of the highly entangled system is shown by the dewetting times which are of the order of milliseconds, in contrast to dewetting

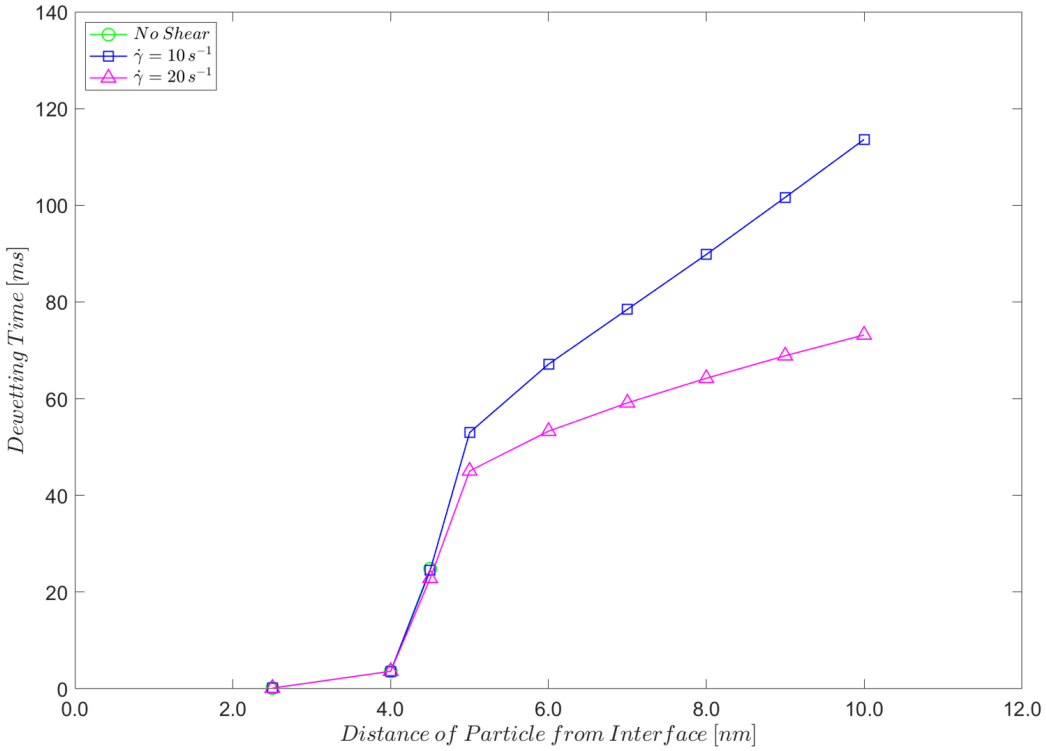

Figure 4.1: Dependence of dewetting time on the distance of the particle from the interface, with and without shear. At rates much greater than $20\,s^{-1}$ shear is not sustainable. The system is highly entangled, with an effective diffusion coefficient, $D = 10$.

times in the Rouse regime, which are of the order of microseconds. For example, when $d = 10.0\,nm$ and the dimensionless shear rate is $\tilde{\dot{\gamma}} = 0.002$, the dewetting time in the Rouse regime is approximately $79\,\mu s$, while in the highly entangled regime, the dewetting time is approximately $73\,ms$. In this example, a factor of roughly 1000 separates the two dewetting times. It is no coincidence that $D^3 = 10^3 = 1000$, since the parameter D determines the dynamics of our system. In particular, as noted in our earlier discussion of parameter settings, the physical shear rate scales with D^3. Since shear is applied to the system at a constant rate, a simple model in which the central interface approaches the particle linearly, with dewetting occurring just before the interface becomes tangential to the surface of the particle predicts that the dewetting time will also vary with D^3.

The comparison of dewetting times in the quiescent system is a little more complicated. Since there is no shear, we cannot appeal to the relationship between the physical shear rate and the parameter D to explain the difference. Instead, we note that dewetting in the quiescent system is governed almost

entirely by a diffusive mechanism, for which the time scale is determined by the physical time associated with each step in the simulation. Referring to our earlier discussion of parameter settings, one simulation step in the highly entangled regime corresponds with a physical time increment of $\Delta t = 10^{-8}\,s$ while in the Rouse regime, the corresponding time increment is $\Delta t = 10^{-10}\,s$, so the two time increments differ by a factor of 100. We might expect this to be reflected in the dewetting times in a quiescent system in the two regimes, but this is not quite what we observe. For example, when $d = 4.5\,nm$, the dewetting time of a quiescent system in the Rouse regime is approximately $57\,\mu s$, while in the highly entangled regime, the dewetting time is approximately $25\,ms$, which is approximately 400 times longer. Similarly, when $d = 2.5\,nm$. the ratio between the dewetting times in the two regimes is approximately 160. The reason for this discrepancy with what might be expected is not clear, but we speculate that it might be related to the fact that the particle is free to move under the influence of hydrodynamic forces. As we saw in sections 3.6 and 3.7, the fluid flows associated with dewetting are not negligible, and tend to push the particle away from the central interface, even as the interface is breached. It is plausible to suppose that this contributes to a small increase in the dewetting time. We consider the influence of hydrodynamic forces on the motion of the particle, and the implications of this for the dewetting time, further in section 5.6.

Turning to the specific shape of the dewetting curves, we see that when $d \leq d_c \sim 4.5\,nm$ the dewetting time is almost independent of the shear rate (and, indeed, of whether shear is applied at all). This is because dewetting at these length scales is dominated by the rapid diffusive mechanism, so there is insufficient time for the effect of shear to become apparent. In contrast, for $d \gtrsim 7.0\,nm$, the dewetting time varies almost linearly with d, consistent with a simple linear model in which shear is uniform and dewetting occurs very rapidly, once the central interface is close ($d < d_c$) to the surface of the particle. It is worth noting that, for any given value of $d \gtrsim 7.0\,nm$, the dewetting time at the higher shear rate is approximately half the dewetting time at the lower shear rate. For example, when $d = 10.0\,nm$, the dewetting times are $73.2\,ms$ and $113.6\,ms$, respectively. The fact that the former is not exactly half of the latter is mostly due to the confounding effect of the diffusive mechanism, which is influential when the central interface nears the surface of the particle.

In the range $d_c \leq d \lesssim 7.0\,nm$, the system transitions from the diffusive regime to the hydrodynamic regime where the dewetting time depends almost linearly on d. There is some evidence that the transition to the hydrodynamic

regime occurs more rapidly at the lower shear rate of $\dot{\gamma} = 10\,s^{-1}$, as indicated by the gradient of the two curves at $d = 4.5\,nm$. Again, we hypothesise that this reflects the differential effect of hydrodynamic flows at the two shear rates.

4.4 Expulsion in a Highly Entangled System

We now explore the behaviour of our highly entangled system under shear over a longer time period - in principle, up to the steady state in which the particle resides in its preferred phase, after being expelled from the non-preferred phase. From the simulations in the Rouse regime, we expect to observe four main stages in the expulsion process: initial dewetting, second dewetting (following the breaking of the central interface at high shear strain), wetting, and expulsion (figure 3.9). However, in practice, lower shear rates in the highly entangled regime, when $D = 10$, tend to result in the alternative steady state previously observed in Rouse regime simulations, in which the particle adheres to a droplet of its preferred phase, within a matrix of the non-preferred phase (figure 3.10)

Furthermore, even at higher shear rates, up to the maximum value used in our simulations in this highly entangled regime, the particle is *never* completely expelled from its non-preferred phase. Instead, it adheres to the interface between the two polymers, which is now horizontal, due to prolonged shear, as the interface continues to relax. Figure 4.2 shows this new alternative steady state.

The state shown in figure 4.2 was achieved after 20 days of simulation time. At this point, the upper interface between the two liquid phases was continuing to relax, so this cannot accurately be described as the final steady state. However, we expect the final steady state to closely resemble this snapshot of the system. In particular, we do not expect the particle to be expelled into its preferred phase since the applied shear is now almost parallel to the interfaces, and is unlikely to be of sufficient magnitude to overcome the forces that bind the particle to the interface. Instead, we expect the upper interface to continue to relax (flatten), taking the particle with it, until it reaches a final steady state. At this point, we would expect to see a contact angle between the interface and the surface of the particle that is consistent with Young's equation.

Figure 4.2: Alternative steady state of a simulation in the entangled regime after 900 ms. In this simulation, the particle begins 9.0 lattice cells ($\sim 4.5\,nm$) from the interface and the system is sheared at $\dot{\gamma} = 20\,s^{-1}$.

In summary, and in contrast with the Rouse regime, simulations in the highly entangled regime, exhibit the stages of the "expulsion" process depicted in figure 4.3.

Having described the typical long term evolution of the system under shear, we now present the quantitative results of our simulations. Table 4.2 shows the times to the various stages in the evolution of the system at shear rates ranging from $\dot{\gamma} = 10\,s^{-1}$ to $\dot{\gamma} = 20\,s^{-1}$. As in the corresponding Rouse regime simulations, the initial distance of the particle from the central interface is $d = 4.5\,nm$ in all cases (i.e. just below the critical film thickness, d_c). These results are then plotted in figure 4.4.

The most striking thing about figure 4.4 is its simplicity compared with the corresponding plots for the Rouse regime (figures 3.13 and 3.14). For a range of shear rates, from $\dot{\gamma} = 10\,s^{-1}$ to $\dot{\gamma} \lesssim 16\,s^{-1}$, only the first dewetting occurs. Following that, interface between the two liquid phases fails to make contact with the surface of the particle after it breaks due to shear-induced strain, and the steady state in which the particle adheres to a droplet of its preferred phase is reached. Furthermore, as previously noted, even when the second dewetting does occur, at shear rates of $\dot{\gamma} \geq 160\,s^{-1}$, the particle is never fully expelled from its non-preferred phase.

In common with the Rouse regime results, there is an approximately linear

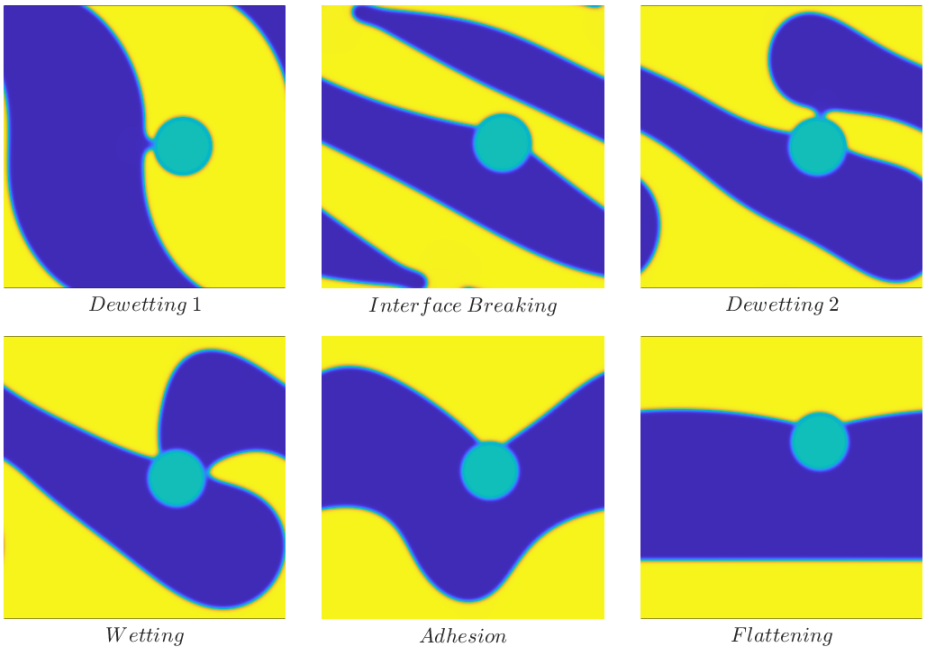

Figure 4.3: Generic stages of the expulsion process in the highly entangled regime ($D = 10$), from initial dewetting to the end state observed at long time scales. In this simulation, the particle starts at $d \sim 4.5\,nm$ from the interface, and the shear rate is $\dot{\gamma} = 18\,s^{-1}$. Interface breaking occurs at approximately $t = 132\,ms$, and the end state shown is at $t = 900\,ms$. An earlier state of the system at $t = 200\,ms$ (Adhesion) is shown for illustrative purposes.

Shear Rate $[s^{-1}]$	Dewetting 1 [ms]	Dewetting 2 [ms]	Wetting [ms]	Expulsion [ms]
10	24.5	A1	A1	A1
12	24.3	A1	A1	A1
14	24.0	A1	A1	A1
16	23.6	189.0	199.4	A2
18	23.2	163.4	174.3	A2
20	22.8	137.7	148.1	A2

Table 4.2: Summary of times to various stages in the long-term evolution of the highly entangled ($D = 10$) system at shear rates $\dot{\gamma} = 10\,s^{-1}$ to $\dot{\gamma} = 20\,s^{-1}$. A1 denotes the alternative steady state in which the particle adheres to a droplet of its preferred phase in a matrix of the non-preferred phase, previously observed at low shear rates in the Rouse regime. A2 denotes an steady state in which the particle remains stuck at one of the horizontal interfaces between the two phases at long physical time scales (of the order of one second).

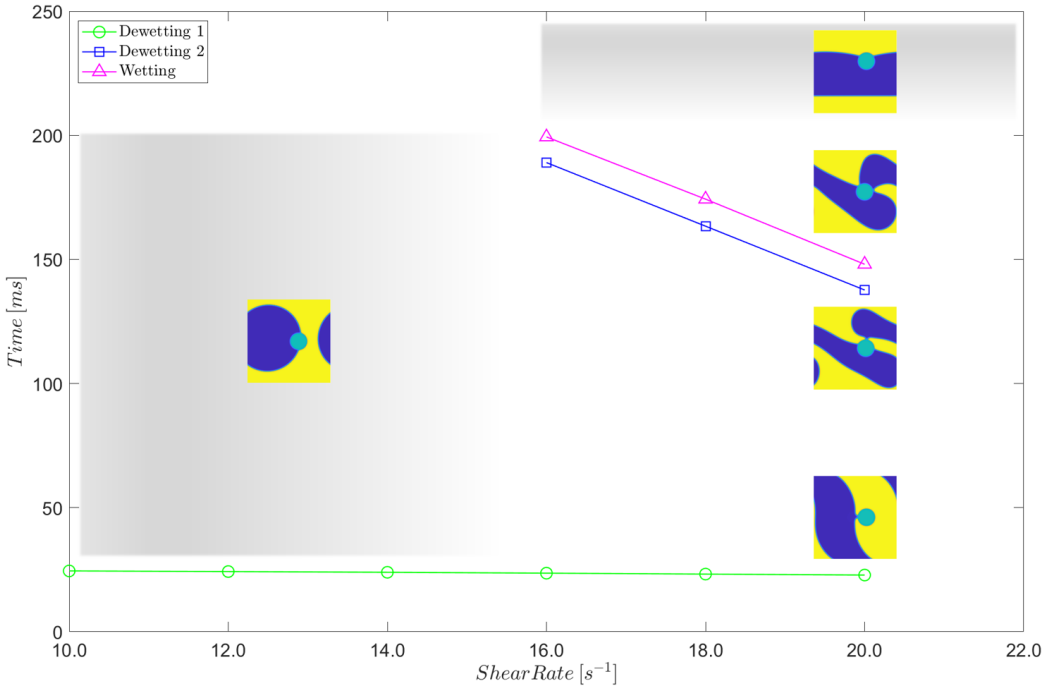

Figure 4.4: Dependence of the evolution of the highly entangled ($D = 10$) system on shear rate. In all simulations, the particle starts at $\sim 4.5\,nm$ from the interface and the system is sheared at various rates. At higher shear rates of $\dot{\gamma} \geq 16\,s^{-1}$ the stages observed are dewetting 1, dewetting 2, wetting, and adhesion/flattening.

relationship between the second dewetting time and the shear rate, with the former decreasing as the latter increases. A similar linear relationship is observed between the wetting time and the shear rate. It is interesting that, amid the apparent unpredictability introduced by the breaking of the central interface under sustained shear, a quite regular linear relationship persists between these two pairs of variables. It is also worth noting that the interval between the second dewetting time and the wetting time, for any given shear rate in the upper end of the range, is approximately constant at $\sim 10\,ms$. Again, this is an example of regularity persisting in the midst of unpredictability. The ultimate source of both of these regularities is almost certainly the uniform shear rate applied to the system.

Finally, as in the Rouse regime, the first dewetting time decreases as the shear rate increases, although this effect is not easy to discern, given the scale used in figure 4.4. In addition, given that the particle starts at $d = 4.5\,nm$ from the central interface in all simulations, the rapid diffusive mechanism dominates the dewetting process, and the dewetting time is largely independent of the shear rate.

It is also useful to show the evolution of the system's mean free energy density under shear up to just after the first dewetting point (figure 4.5). As previously, the sawtooth pattern superimposed on the free energy curves is an artefact of the discrete numerical scheme used in the simulation.

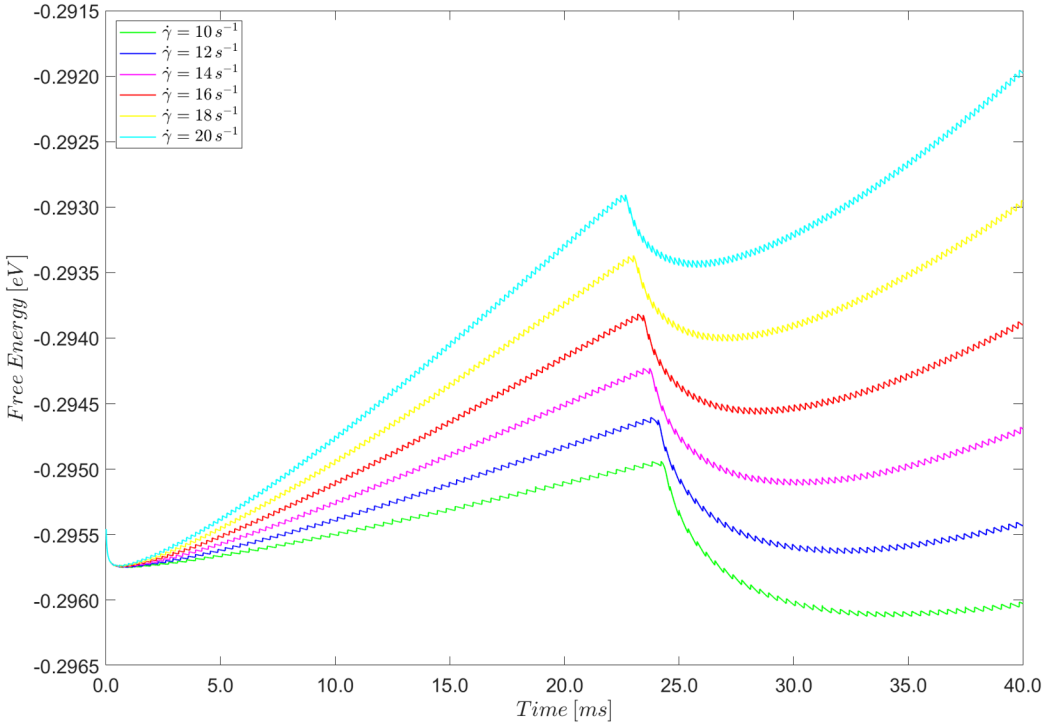

Figure 4.5: Evolution of the mean free energy density of the system under shear up to, and just after, the first dewetting point, for $\dot{\gamma} = 10\,s^{-1}$ to $\dot{\gamma} = 20\,s^{-1}$.

As in the Rouse regime, figure 4.5 shows a period of rapid equilibration at the interface ($\sim 0.5\,ms$), during which the mean free energy density decreases slightly. This is followed by a steady increase in the mean free energy density due to the increase in the length of the interface as the system is sheared at a constant rate. At all shear rates, dewetting occurs between $20.0\,ms$ and $25.0\,ms$, and is accompanied by a temporary drop in the mean free energy density, before it rises again as the system continues to be sheared at a constant rate. In this respect, the timing of the fall in the mean free energy density is consistent with the first dewetting times deduced from inspecting snapshots of the system close to the dewetting point. We note that the value of the mean free energy density in the system is not sensitive to the parameter D. In both the Rouse regime ($D = 1$) and the highly entangled regime ($D = 10$), the initial value of the mean free energy density is approximately $-0.2955\,k_BT$. This is consistent with the fact that the total

free energy of the system, as given by equation 3.4, does not depend on D.

However, the *range* of mean free energy densities at which dewetting occurs does vary between the two regimes. In the Rouse regime, this range extends from roughly $-0.2940\,k_BT$ to $-0.2890\,k_BT$, as the shear rate increases from $\dot{\gamma} = 10\,s^{-1}$ to $\dot{\gamma} = 20\,s^{-1}$. In the highly entangled regime, the corresponding range (allowing for appropriate scaling of the physical shear rates) extends from roughly $-0.2950\,k_BT$ to $-0.2930\,k_BT$. The interpretion of this result is not straightforward but, intuitively, it is likely to reflect the difference in the way the central interface deforms under shear in the two regimes (see section 4.6).

4.5 Dewetting and Expulsion in Moderately Entangled Systems

Having investigated the Rouse regime, and what we have called the highly entangled regime, where the effective diffusion coefficient $D = 10$, we now consider two intermediate cases in which $D = 2$ and $D = 5$. The former implies a polymer chain of double the length of a chain in the Rouse regime, while the latter implies a chain length half of that in the highly entangled regime (200 and 500 monomers, respectively). The aim of the section is to assess how sensitive the behaviour of our system is to changes in the effective diffusion coefficient, and to understand how this behaviour changes between the two limiting values of D considered so far.

Thus, we run the same set of simulations as previously with $D = 2$ and $D = 5$. Now, a dimensionless shear rate of $\tilde{\dot{\gamma}} = 0.001$ equates to a physical shear rate of $\dot{\gamma} = 1.25 \times 10^3\,s^{-1}$ ($D = 2$) and $\dot{\gamma} = 80\,s^{-1}$ ($D = 5$). For each intermediate value of D, we present the two main plots as before: dewetting time versus the initial distance of the particle from the central interface (in a quiescent system and at a lower and higher shear rate); and the times to the various stages of expulsion versus the shear rate. Tables 4.3 and 4.4 show the first dewetting times, as the initial distance of the particle from the central interface is varied for $D = 2$ and $D = 5$ respectively, and these results are plotted in figures 4.6 and 4.7.

In both of these intermediate cases, the dewetting results closely resemble the results in both the Rouse regime and the highly entangled regime. In

Distance [nm]	Dewetting Time $[\mu s]$		
	$\dot{\gamma} = 0$	$\dot{\gamma} = 1.25 \times 10^3\, s^{-1}$	$\dot{\gamma} = 2.50 \times 10^3\, s^{-1}$
2.5	5.6	5.6	5.2
4.0	65.6	65.6	65.2
4.5	376.8	357.6	340.4
5.0	-	492.4	417.6
6.0	-	592.4	471.2
7.0	-	672.8	512.0
8.0	-	752.8	549.6
9.0	-	839.2	584.0
10.0	-	930.8	616.8

Table 4.3: Dewetting time in a quiescent system, and at constant shear rates of $\dot{\gamma} = 1.25 \times 10^3\, s^{-1}$ and $\dot{\gamma} = 2.50 \times 10^3\, s^{-1}$ when $D = 2$. The distance of the particle from the interface is varied from $d = 2.5\, nm$ to $d = 10.0\, nm$.

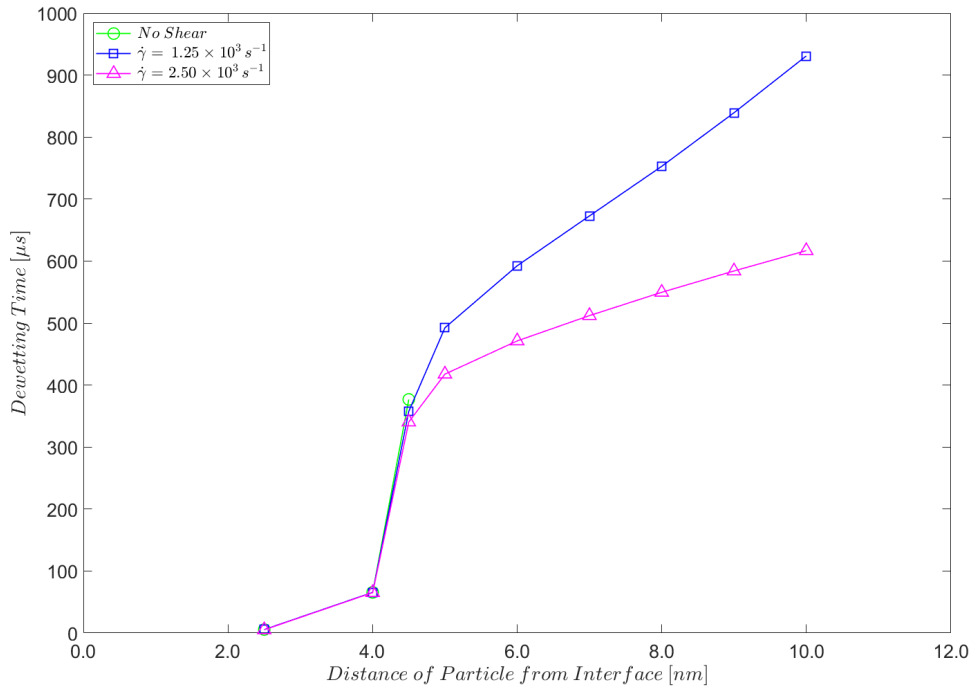

Figure 4.6: Dependence of dewetting time on the initial distance of the particle from the interface, with and without shear when $D = 2$. At shear rates much greater than $2.50 \times 10^3\, s^{-1}$ shear is not sustainable.

particular, all four plots show rapid dewetting as a result of the rapid diffusive mechanism when the particle's initial position is close to the central

Distance [nm]	Dewetting Time $[ms]$		
	$\dot{\gamma} = 0$	$\dot{\gamma} = 80\,s^{-1}$	$\dot{\gamma} = 160\,s^{-1}$
2.5	0.04	0.04	0.04
4.0	0.70	0.70	0.70
4.5	4.27	4.28	3.95
5.0	-	7.15	6.08
6.0	-	8.79	7.01
7.0	-	10.12	7.69
8.0	-	11.45	8.29
9.0	-	12.86	8.85
10.0	-	14.34	9.38

Table 4.4: Dewetting time in a quiescent system, and at constant shear rates of $\dot{\gamma} = 80\,s^{-1}$ and $\dot{\gamma} = 160\,s^{-1}$ when $D = 5$. The distance of the particle from the interface is varied from $d = 2.5\,nm$ to $d = 10.0\,nm$.

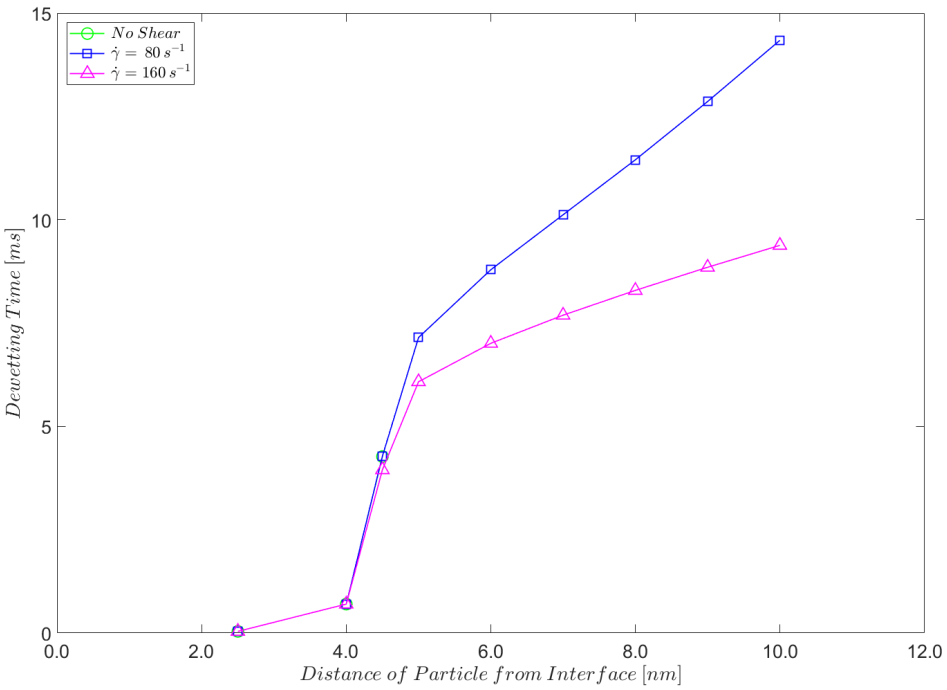

Figure 4.7: Dependence of dewetting time on the distance of the particle from the interface, with and without shear when $D = 5$. At shear rates much greater than $160\,s^{-1}$ shear is not sustainable.

interface, and a critical film thickness, d_c in the range $4.5\,nm < d_c < 5.0\,nm$. This confirms our earlier observation that the critical film thickness does

not depend on the degree of entanglement of the system. Again, in all four cases, the system transitions from the diffusive regime to the hydrodynamic regime, where the effect of shear becomes apparent, from roughly $d = 4.0\,nm$ $d = 7.0\,nm$. In the hydrodynamic regime, the dewetting time varies almost linearly with the initial distance of the particle from the central interface, reflecting the fact that the system is sheared at a constant rate.

As in the highly entangled regime, the main effect of changing D is to dilate the time scales in which dewetting occurs and once again, our results at higher shear rates are consistent with the fact that the physical shear rate scales with $\frac{1}{D^3}$. To take just one example, when $d = 10.0\,nm$ and the dimensionless shear rate is $\tilde{\dot{\gamma}} = 0.002$, the dewetting time when $D = 2$ is $616.8\,\mu s$ compared with a dewetting time in the Rouse regime of $79.0\,\mu s$. These dewetting times differ by a factor of roughly 7.8, which is close to $D^3 = 2^3 = 8$, as we would predict. There is similar dilation of the dewetting time scales at lower values of d, where the diffusive mechanism is dominant but, as in the highly entangled regime, these results are harder to interpret due to the difficulty of isolating the several mechanisms that contribute to ultimate value of the dewetting time.

Turning to the longer term evolution of the system under shear, up to and including the potential expulsion of the particle into its preferred phase, tables 4.5 and 4.6 summarise the relevant results when $D = 2$ and $D = 5$, respectively; these results are then plotted in figures 4.8 and 4.9.

Shear Rate $[\times 10^3\,s^{-1}]$	Dewetting 1 $[\mu s]$	Dewetting 2 $[\mu s]$	Wetting $[\mu s]$	Expulsion $[\mu s]$
1.25	358	A1	A1	A1
1.50	354	A1	A1	A1
1.75	350	1774	1900	2448
2.00	347	1570	1698	2314
2.25	345	1382	1505	2135
2.50	340	1128	1228	1232

Table 4.5: Summary of times to various stages in the long-term evolution of the system when $D = 2$, at shear rates from $\dot{\gamma} = 1.25 \times 10^3\,s^{-1}$ to $\dot{\gamma} = 2.50 \times 10^3\,s^{-1}$. A1 denotes the alternative steady state in which the particle adheres to a droplet of its preferred phase in a matrix of the non-preferred phase, previously observed at low shear rates in the Rouse regime.

Before comparing these results with those in the Rouse and the highly entangled regime, we must note an interesting anomaly in the results when $D = 5$.

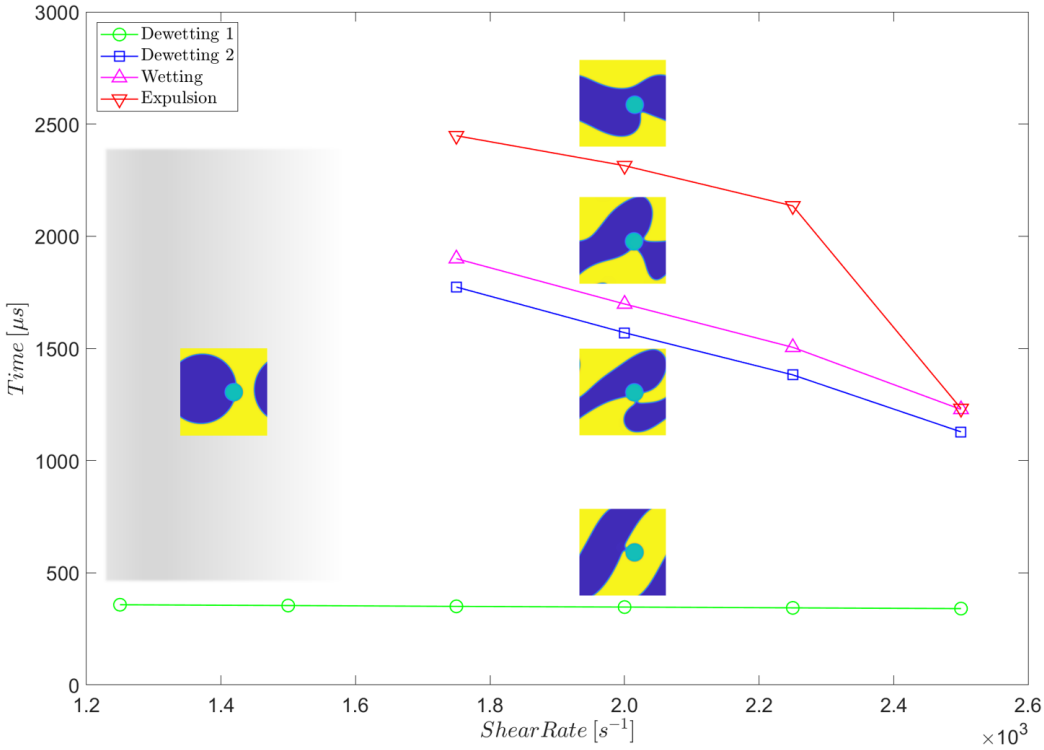

Figure 4.8: Dependence of the expulsion process on shear rate when $D = 2$. The initial distance of the particle from the central interface is $4.5\,nm$ in all simulations, and the system is sheared at various rates. The time to each of the stages of expulsion (dewetting 1, dewetting 2, wetting and expulsion) is determined from snapshots of the system.

Shear Rate $[s^{-1}]$	Dewetting 1 [ms]	Dewetting 2 [ms]	Wetting [ms]	Expulsion [ms]
80	4.28	A1	A1	A1
96	4.27	A1	A1	A1
112	4.24	A1	A1	A1
128	4.17	23.83	25.44	A2
144	4.07	20.80	22.41	A2
160	3.95	17.31	18.76	18.97
176	3.80	13.83	14.90	A2

Table 4.6: Summary of times to various stages in the long-term evolution of the system when $D = 5$, at shear rates from $\dot{\gamma} = 80\,s^{-1}$ to $\dot{\gamma} = 160\,s^{-1}$. A1 denotes the alternative steady state in which the particle adheres to a droplet of its preferred phase in a matrix of the non-preferred phase, previously observed at low shear rates in the Rouse regime. A2 denotes an steady state in which the particle remains stuck at one of the horizontal interfaces between the two phases at long time scales (of the order of one second).

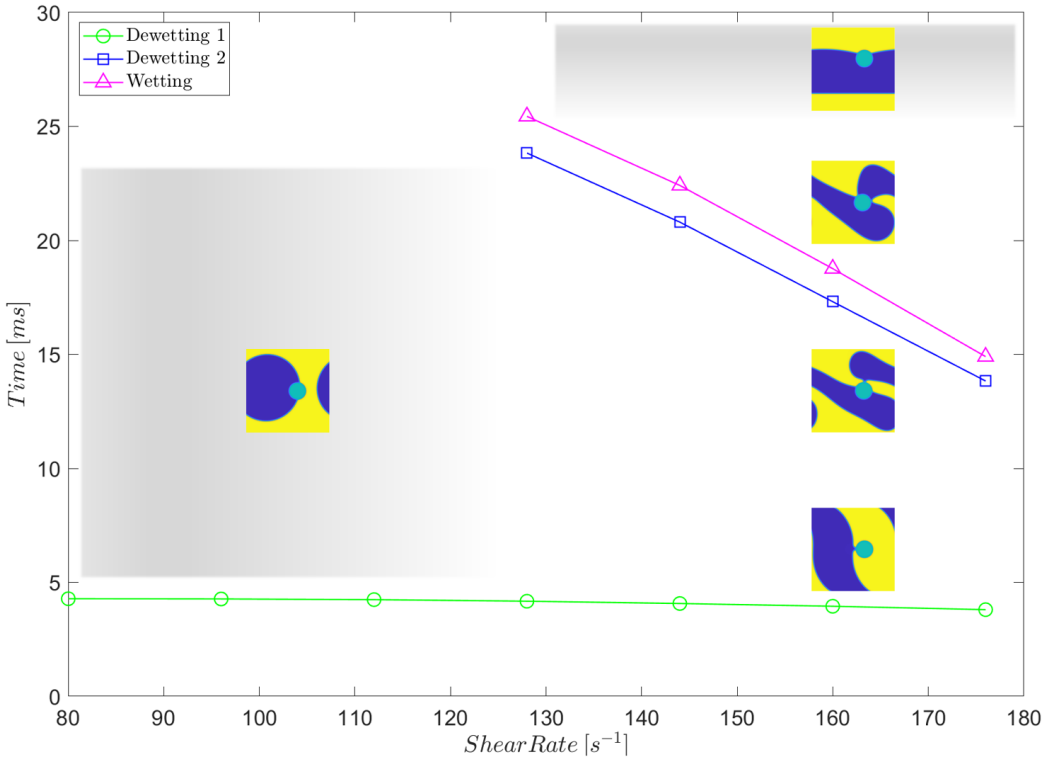

Figure 4.9: Dependence of the expulsion process on shear rate when $D = 5$. The initial distance of the particle from the central interface is $4.5\,nm$ in all simulations, and the system is sheared at various rates. The time to each of the stages of expulsion (dewetting 1, dewetting 2, wetting and expulsion) is determined from snapshots of the system.

The trend at higher shear rates is for the particle to reach a steady state in which it adheres to one of the horizontal interfaces between the two phases in the fully sheared system. The one exception to this occurs when $\dot{\gamma} = 160\,s^{-1}$, when the particle is expelled from its non-preferred phase in approximately $19\,ms$. Note that this occurs almost simultaneously with the wetting of the particle's surface by its preferred phase, which is the penultimate stage of the expulsion process. For the sake of clarity, this data point is not plotted in figure 4.9. A simulation at the higher shear rate of $\dot{\gamma} = 176\,s^{-1}$ shows the particle reverting to its previous behaviour and reaching a steady state in which it adheres to a horizontal interface between the two phases. This result is noted in table 4.6 and, for clarity, is plotted in figure 4.9. We return to these results towards the end of this section.

Turning now to the $D = 2$ intermediate case, inspection of figure 4.8 reveals its similarity with the corresponding plot for the Rouse regime (figure 3.13). In both sets of results, the steady state at lower shear rates is that in which

the particle adheres to a droplet of its preferred phase, within a matrix of the non-preferred phase. At higher shear rates, $\dot{\gamma} \geq 1.75 \times 10^3\, s^{-1}$ when $D = 2$, both the second dewetting time and the wetting time decrease almost linearly as the shear rate increases, just as they do in the Rouse regime. This reflects the fact that the system is being sheared at a constant rate. In addition, the difference between the second dewetting time and the dewetting time, when $D = 2$ is almost constant ($\sim 100\,\mu s$), a regularity that survives the apparent unpredictability of the breaking of the central interface, just as it does in the Rouse regime.

However, the most striking similarity occurs at the highest shear rate used in both sets of simulations, when expulsion of the particle into its preferred phase occurs almost simultaneously with the wetting of the particle. Thus, in both figure 4.8 and figure 3.13, the data points representing these distinct events almost coincide. Although time constraints precluded running a simulation with $D = 2$ and $\tilde{\dot{\gamma}} = 0.0019$, the overall similarity these two figures suggests that the onset of the near collapse of these two events into each other when $D = 2$ is just as precipitous as it is in the Rouse regime.

The expulsion behaviour in the system when $D = 5$ contrasts sharply with the expulsion behaviour when $D = 2$. Looking at figure 4.9, it is obvious that the behaviour it represents is much closer to that of the highly entangled regime, when $D = 10$, than it is to the behaviour of the system in the Rouse regime. In particular, the key result of the highly entangled regime - that the particle is not expelled into its preferred phase at any of the shear rates considered - is replicated in the moderately entangled system when $D = 5$. Beyond this key result, the overall form of figure 4.9 closely resembles that of figure 4.4. In both cases, lower shear rates result in the droplet steady state, and higher shear rates result in the steady state in which the particle adheres to one of the horizontal interfaces between the liquid phases, in the fully sheared system. Likewise, and in common with the results in the Rouse regime and the moderately entangled regime when $D = 2$ there is an almost linear decrease in both the second dewetting time and the wetting time, as the shear rate increases. And, again, the difference between these two times is almost constant: $\sim 1.5\,ms$, in this case. The only significant difference with the $D = 10$ case is that, as noted above, the particle *is* fully expelled into its preferred phase at the higher physical shear rate corresponding with a dimensionless shear rate of $\tilde{\dot{\gamma}} = 0.002$.

To summarise so far, there is a contrast between the expulsion behaviour of the two cases in the intermediately entangled regime we have considered:

when $D = 2$, the behaviour closely resembles that in the Rouse regime; when $D = 5$, the behaviour closely resembles that in the highly entangled regime in which $D = 10$. The implication is that there is a transition point somewhere between these two intermediate values of D, where the expulsion behaviour changes. The most important aspect of this change in behaviour is that the particle is not expelled into its preferred phase at the higher shear rates considered. Simulations are time consuming and constrain the size of the relevant parameter space we can explore, so it has not been possible to identify the exact value of D at which this transition occurs, or to clarify the manner in which the transition occurs (for example, is it a gradual or a sudden change, as D varies).

However, the anomalous result highlighted earlier might offer a clue about when this transition occurs. Recall that when $D = 5$ and $\dot{\gamma} = 160\,s^{-1}$, the particle is fully expelled into its preferred phase, contrary to what we would expect, given the close similarity of the $D = 5$ case with the highly entangled regime, in all other aspects. Moreover, the expulsion of the particle at this shear rate is almost simultaneous with its wetting. This is precisely the behaviour we observe at the higher shear rate in both the Rouse regime and the moderately entangled regime when $D = 2$. This suggests that the transition between the two kinds of expulsion behaviour may occur when $D \lesssim 5$. Likewise, the fact that complete expulsion either does or does not occur as we vary D suggests that the transition in the behaviour of the system might occur suddenly, across a narrow range of values of D, but this can only be a speculative conclusion, given the limited region of parameter space considered.

Finally, although the nature of the simulations, and the way we plot the results, encourages us to directly compare the various regimes, we must not forget that changing the effective diffusion coefficient, D, changes the *physical* shear rates associated with the range of dimensionless shear rates used ($\tilde{\dot{\gamma}} = 0.001$ to $\tilde{\dot{\gamma}} = 0.002$). Thus, the simplest, and probably correct, conclusion to draw from these results is that higher shear rates of $\sim 10^3\,s^{-1} - 10^4\,s^{-1}$ are needed to fully expel the particle into its preferred phase, This is, perhaps, an unsurprising conclusion, but it is pleasing to see it so clearly demonstrated in our model.

For completeness, we conclude this section with plots of the evolution of the mean free energy density in the system up to, and just after, the first dewetting point, when $D = 2$ and $D = 5$ (figures 4.10 and 4.11, respectively).

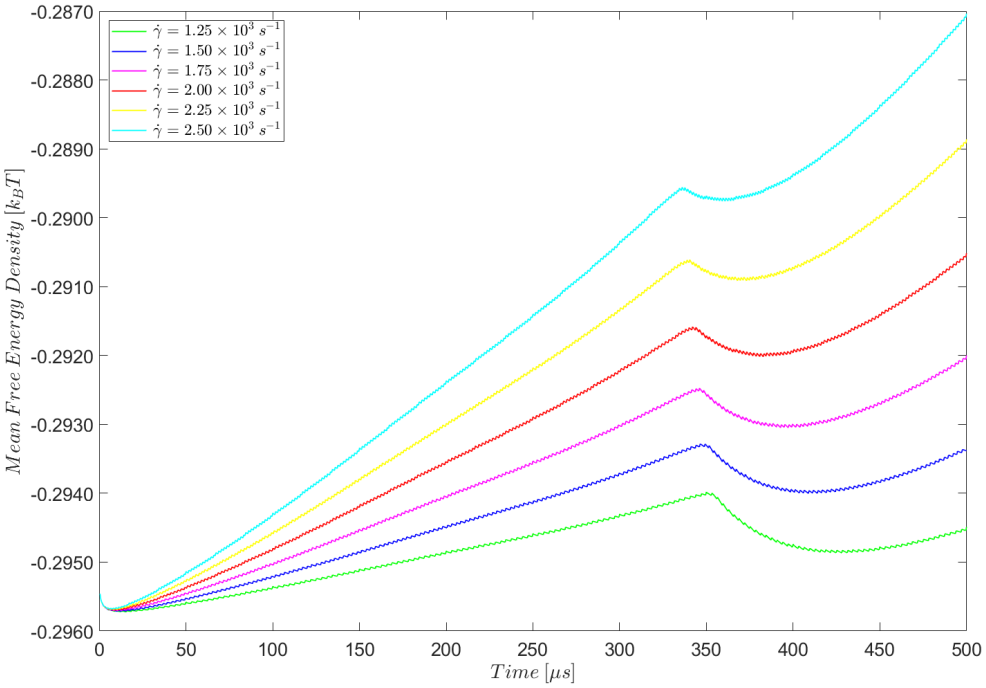

Figure 4.10: Evolution of mean free energy density under shear up to, and just beyond, the first dewetting point for $\dot{\gamma} = 1.25 \times 10^3\, s^{-1}$ to $\dot{\gamma} = 2.50 \times 10^3\, s^{-1}$, and $D = 2$.

Both plots are very similar to figure 4.5, confirming that the mean free energy is essentially independent of the effective diffusion coefficient, as we expect, given the underlying mathematical model. As before, and as in the Rouse regime, the initial mean free energy density is approximately $-0.2955\, k_BT$, and this rapidly decreases in the early stages of each simulation as the central interface equilibriates. This is followed by a period of steadily increasing mean free energy density as the applied shear increases the extent of the central interface. At dewetting, this increase in the mean free energy density is momentarily reversed, before it resumes again as the the shearing of the system continues. There are small variations (compared with the Rouse regime and the highly entangled regime) in the range of free energy densities at which dewetting occurs. Besides observing that that these must ultimately depend on the geometry of the central interface - its length and the variations in its local curvature), we make no attempt to account for these differences here.

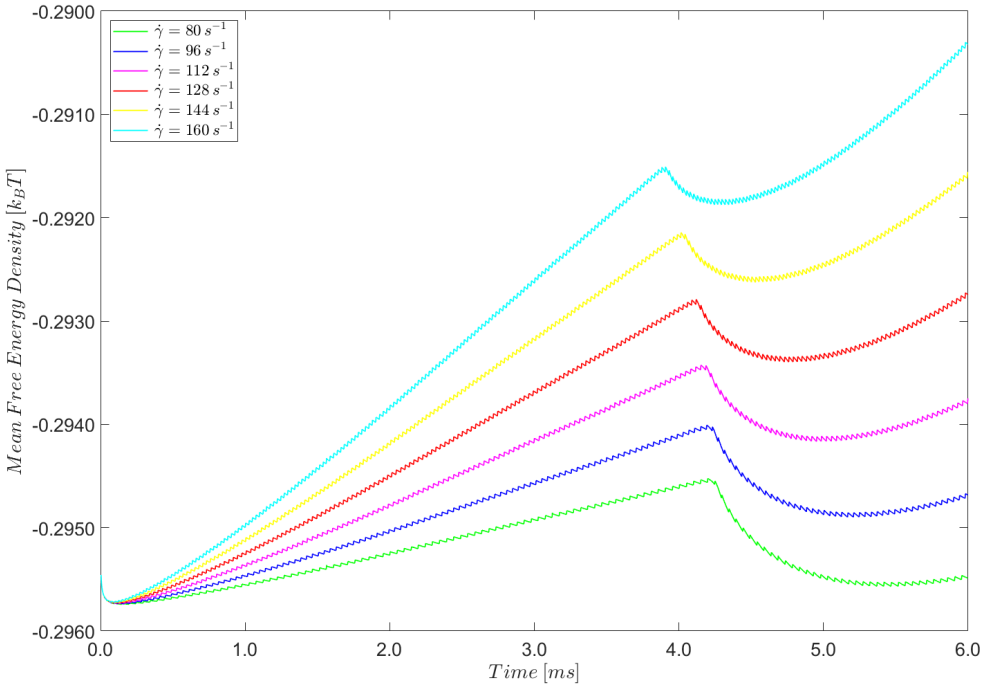

Figure 4.11: Evolution of mean free energy density under shear up to, and just beyond, the first dewetting point for $\dot{\gamma} = 80\,s^{-1}$ to $\dot{\gamma} = 160\,s^{-1}$, and $D = 5$.

4.6 The Geometry of Dewetting

In this section we consider, in greater depth, the mechanisms that might account for the complete set of simulation results in the strongly segregated regime, for all values of the effective diffusion coefficient, D. We focus on the first dewetting results, because these are quite regular, and free of the potentially unpredictable influence of the breaking of the central interface. Although the breaking of the central interface does not completely erase regularities in the simulation results (for example, the linear relationship between both the second dewetting time and the wetting time, and the shear rate is preserved, across a range of shear rates), it does introduce complications that we may avoid by concentrating on an earlier stage in the evolution of the system under shear.

Direct comparison of the first dewetting times is difficult because, within the range of dimensionless shear rates we are interested in, those times vary with D^3, and therefore cover a wide range of physical time scales. For this reason, it is more productive, and convenient, to consider the shear strain within the system at the first dewetting point, γ, where $\gamma = \dot{\gamma} \times t$. This is a dimensionless

quantity and is a simple measure of how far the central interface between the two phases has moved at any given time, thus facilitating the comparison of results over a wide range of physical time scales. This marks a shift from a temporal perspective (how long does dewetting take?) to a spatial perspective (what is the geometry of the system at the dewetting point?). Therefore, our intention is to produce a master plot of the first dewetting results obtained so far, with the shear strain at dewetting plotted against the initial distance of the particle from the central interface, for the range of effective diffusion coefficients, D, used in the simulations. We will show this data for the upper and lower bounds of the range of dimensionless shear rates used in our simulations: $\tilde{\dot{\gamma}} = 0.002$ and $\tilde{\dot{\gamma}} = 0.001$, respectively.

Before presenting this master plot, it is helpful to introduce a simple (even naive) geometrical model of the dewetting process. The model is geometrical in the sense that it takes no account of the physical mechanisms involved in dewetting, and ignores other physically realistic aspects of the behaviour of our system. In particular, this model makes three key assumptions:

Assumption 1: The particle is immobile. It does not move under the influence of hydrodynamic flow, as the system is sheared; nor is it subject to Van der Waals forces, when the central interface is near.

Assumption 2: The central interface shears linearly and, in any given small increment of time, instantaneously. That is, if the interface is initially a vertical line through the centre of the system, at a small interval of time later, it remains perfectly straight, but at a slight incline, having pivoted about the central point of the system. At 100% shear ($\gamma = 1.00$), the interface is a straight diagonal line, between opposite corners of the system.

Assumption 3: Dewetting occurs when the interface between the two phases in the system is tangential to the surface of the particle, and not before.

In addition to these, there are further assumptions - for example, that all interfaces are perfectly sharp - but assumptions 1 to 3 are most important in what follows. Figure 4.12 shows how this simple geometrical model is supposed to work.

The centre of the system, a square box of size $2L$ is at the point O, and the particle, centred at P and of radius r is initially positioned at a distance d from the central interface. At the dewetting point, the central interface is tangential to the surface of the particle, having shifted a distance S along

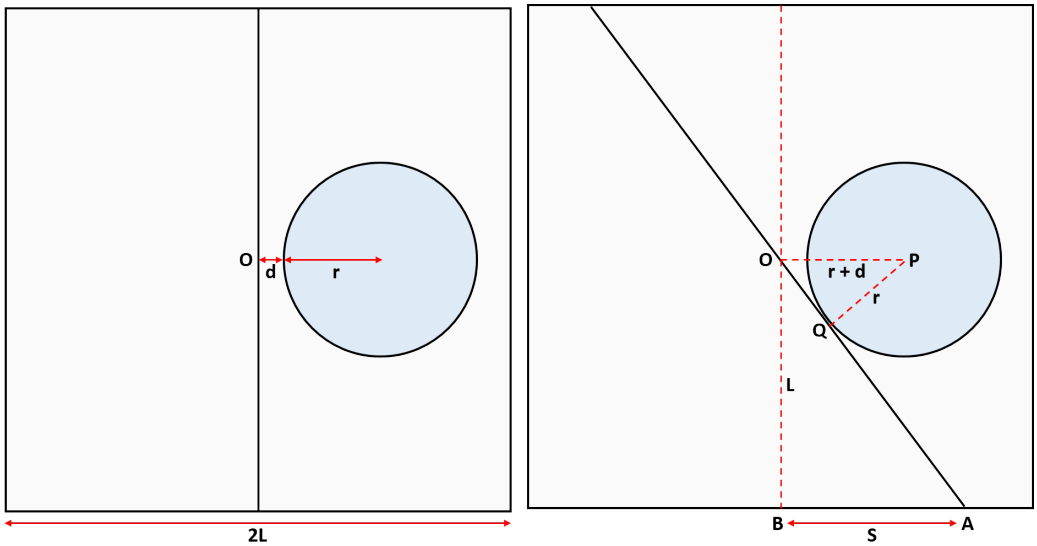

Figure 4.12: A simple geometrical model of dewetting, based on three key assumptions described in the main text. The initial configuration of the system is shown in (a). Dewetting, shown in (b), occurs when the central interface is sheared such that it is tangential to the surface of the particle.

the edge of the system. The shear strain at the dewetting point is $\gamma = \frac{S}{L}$, which it is straightforward to express in terms of known parameters. From the known properties of circles and tangent lines, we deduce that triangles OAB and OPQ are similar. This implies that $\gamma = \frac{S}{L}$ is equal to the ratio of the lengths of the lines OQ and PQ. Application of the Pythagorean theorem then gives the expression we require:

$$\gamma_{dewet} = \frac{S}{L} = \frac{1}{r}\sqrt{(r+d)^2 - r^2} \tag{4.1}$$

As a quick reality check, we note that, when $d = 0$, $\gamma_{dewet} = 0$, as expected, since the central interface is tangential to the particle from the outset, before any shear is applied. We also note that this expression does not depend on either the shear rate or the effective diffusion coefficient, D but, for a given particle size, varies only with the particle's initial distance from the central interface. In other words, if our simulation results are consistent with this geometrical model, all of the associated data points should lie on a single curve.

Figure 4.13 is the master plot we described earlier in this section, with the

theoretical prediction of our model added (the black dotted line).

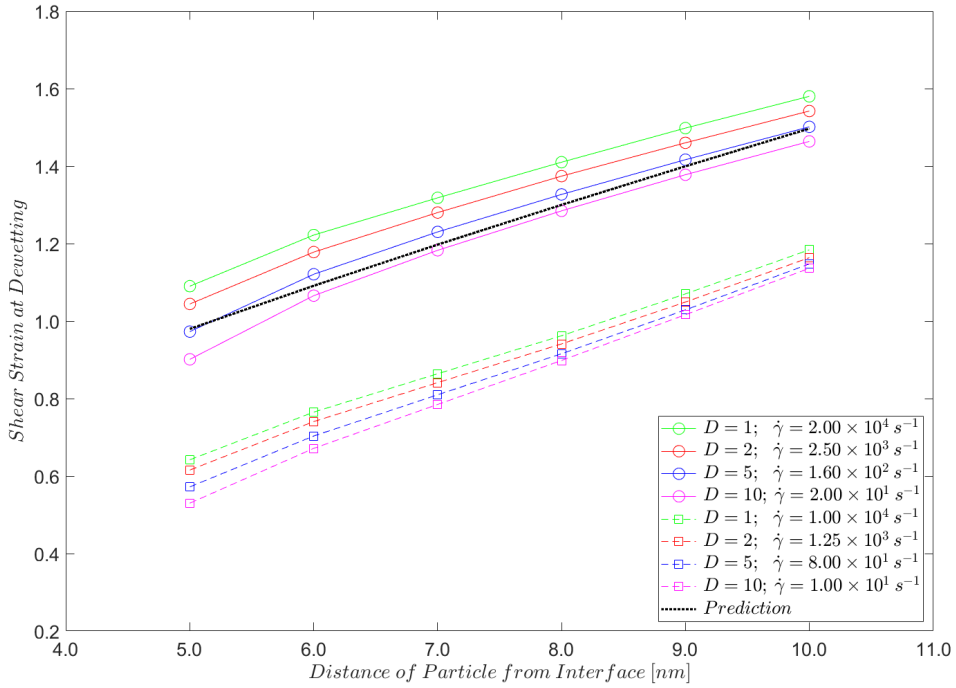

Figure 4.13: Dewetting master plot showing the shear strain at which dewetting occurs, as the distance of the particle from the central interface varies. Shown are the data points when $D = 1$, $D = 2$, $D = 5$ and $D = 10$. The two bands represent the upper and lower ends of the range of dimensionless shear rates used in the simulations ($\tilde{\dot{\gamma}} = 0.002$ and $\tilde{\dot{\gamma}} = 0.001$). The physical value of the shear rate varies, according to the value of the effective diffusion coefficient, D. The predicted values, shown as a black, dotted line, are those of the simple geometrical model described in the text and represented in figure 4.12.

It is immediately obvious that the results of our simulations do not all lie on the single curve implied by our simple geometrical model. Given the complete absence of realistic physics in the model, this is not so surprising. What is surprising is that our results fall clearly into an upper band and a lower band, corresponding with dimensionless shear rates of $\tilde{\dot{\gamma}} = 0.002$ and $\tilde{\dot{\gamma}} = 0.001$, respectively. The data from simulations that use intermediate dimensionless shear rates is not plotted, for reasons of clarity, but we would expect to see a separate band of results for each of these intermediate values. Within each band, individual curves refer to the value of the effective diffusion coefficient, D, used in the simulations. Thus, each band includes four distinct curves, corresponding with the four values of D (1 in the Rouse regime, 10 in the highly entangled regime, and 2 or 5 in the intermediate regime). Interestingly, for any given value of the dimensionless shear rate (i.e. within a given band) and initial distance of the particle from the central interface, the shear strain

at dewetting *decreases* as D increases. The other feature of note in figure 4.13 is that all of the curves are approximately linear. This reflects the fact that the shear rate is constant, and that, in the range of values of d shown, the applied shear, and its associated hydrodynamic effect, dominates the rapid diffusive mechanism, as far as dewetting is concerned.

We begin to make sense of these results by reminding ourselves that all three of the key assumptions underpinning the simple geometrical model are physically unrealistic. For example, the first assumption does not hold because, in our simulations, the particle *is* free to move, under the influence of hydrodynamic forces,as the shear is applied to the system. Figures 4.14 and 4.15 demonstrate that the particle does indeed move.

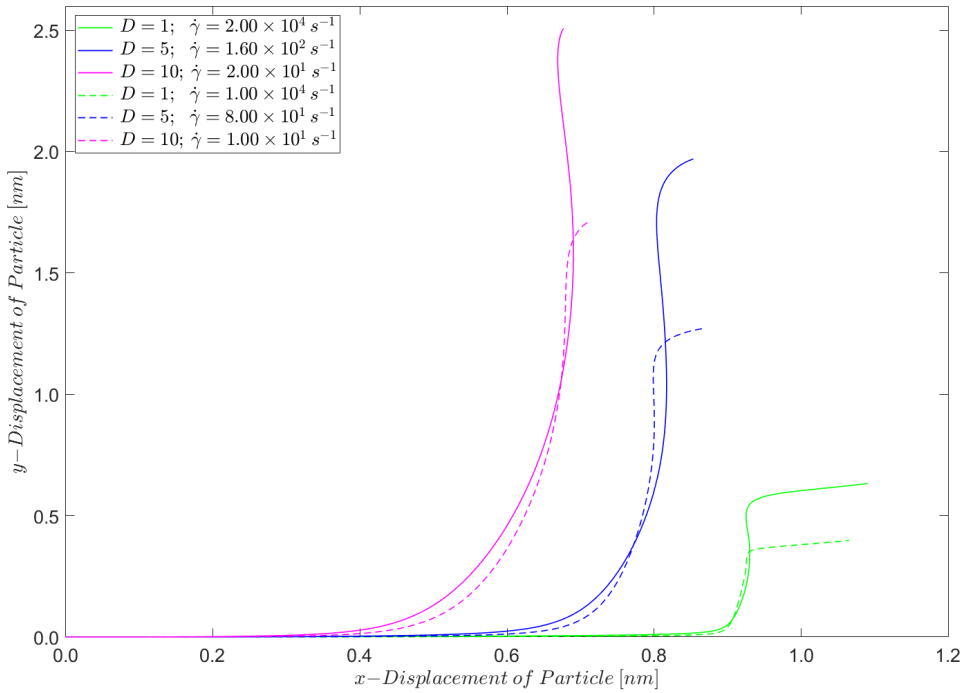

Figure 4.14: Displacement of the particle, relative to its initial position ($d = 5.0\,nm$ from the central interface between the phases) up to the point of first dewetting. The particle trajectory is shown for $D = 1$, $D = 5$ and $D = 10$, and for the the upper and lower end of the range of dimensionless shear rates used in the simulations ($\tilde{\dot{\gamma}} = 0.002$ and $\tilde{\dot{\gamma}} = 0.001$). The physical value of the shear rate varies, according to the value of the effective diffusion coefficient, D.

These figures show the spatial trajectory of the particle as the system is sheared, from its starting position, up to the point at which dewetting occurs, for various combinations of D and $\dot{\gamma}$. Figure 4.14 assumes that the initial distance of the particle from the central interface is $d = 5.0\,nm$, while figure

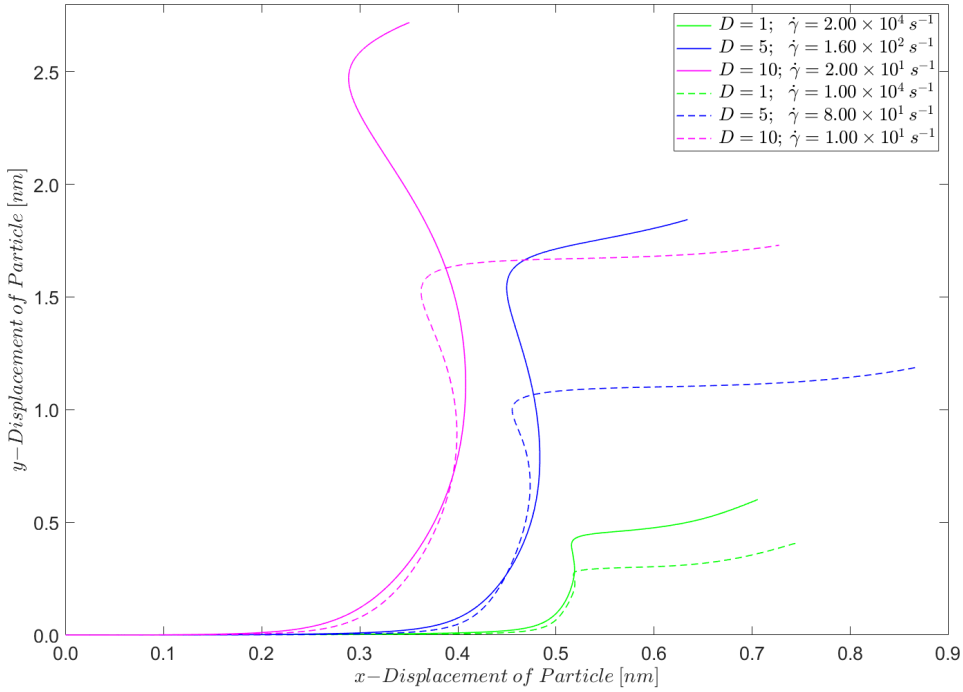

Figure 4.15: Displacement of the particle, relative to its initial position ($d = 10.0\,nm$ from the central interface between the phases) up to the point of first dewetting. The particle trajectory is shown for $D = 1$, $D = 5$ and $D = 10$, and for the the upper and lower end of the range of dimensionless shear rates used in the simulations ($\tilde{\dot{\gamma}} = 0.002$ and $\tilde{\dot{\gamma}} = 0.001$). The physical value of the shear rate varies, according to the value of the effective diffusion coefficient, D.

4.15 assumes an initial distance of $d = 10.0\,nm$. In both figures, we omit the case when $D = 2$, for visual clarity. As in figure 4.13, dashed lines represent a lower dimensionless shear rate of $\tilde{\dot{\gamma}} = 0.001$ and solid lines represent the higher dimensionless shear rate of $\tilde{\dot{\gamma}} = 0.002$. The colour coding represents different values of the effective diffusion coefficient, D.

We make several broad observations about the particle trajectories, as represented in figures 4.14 and 4.15. Firstly, in all cases, at the dewetting point, the particle is displaced in the positive x and the positive y direction, relative to its initial position. From figure 4.12, and the snapshots of the system under shear throughout this chapter, this is consistent with the the particle being subject to the hydrodynamic forces set in motion by the shearing of the central interface between the two phases.

Secondly, noting the differing scales on the x and y axes of figures 4.14 and 4.15, the movement of the particle in the y-direction is significantly greater

than the movement in the x-direction in nearly all cases. Movement in the x-direction is typically $\sim 0.5\,nm$, while movement in the y-direction ranges from $\sim 0.5\,nm$ to $\sim 2.5\,nm$. This suggests that the shear-induced flow in the vicinity of the surface of the particle is, predominantly, in the y-direction, as might be expected since, relative to a point on the lower surface of the particle, the central interface rises upwards, as the system is sheared. This hypothesis is supported by the fact that, in all cases, an initial period of gradual movement in the positive x-direction, gives way to gradual movement in the positive y-direction as the dewetting point is approached. In the early stages of shear, the central interface has not yet reached a point on the edge of the system immediately below the bottom surface of the particle, even as the horizontal distance between the lower half of the central interface and the surface of the particle gradually decreases.

It is possible that this tendency is accentuated by the fact that the initial state of the system has mirror symmetry with respect to the x-axis, but lacks mirror symmetry with respect to the y-axis, due to the addition of a second interface between the two liquid phases near the left hand side of the system to compensate for the volume of the non-preferred phase displaced by the particle on the right hand side of the central interface. However, it is not possible to quantify the size of any such effect which, in any case is likely to be small, since the symmetry of the system is broken far away from the particle, and the flows that influence it. Other factors that might influence the particle's trajectory include the spatial discretisation of the system, necessary to solve the model computationally, and the rapid equilibration of the central interface in the very early stages of each simulation. However, both of these effects are likely to be minor, if they exist at all, and we view the simple geometrical explanation of the shape of the particle's trajectory, set out in the previous paragraph, as essentially correct.

Our third, and final, broad observation is that the particle does not move *much* in any scenario. As previously noted, the maximum displacement in the y-direction is $\sim 2.5\,nm$, while its displacement in the x-direction is $\sim 0.5\,nm$. This is an important point, to which we return after describing the results shown in figures 4.14 and 4.15 in greater detail.

Firstly, note that, for any given value of the effective diffusion coefficient, D, there is less movement in the y-direction, prior to dewetting, at the lower shear rate, than there is at the higher shear rate. However, the movement in the x-direction is roughly the same. However, this difference in the displacement in the y-direction is never great, typically being of the order of

$1.0\,nm$.

In contrast, for any given choice of the two dimensionless shear rates represented, the higher the value of D, the less movement in the x-direction there is, before the particle starts to move in the y-direction, as the dewetting point approaches. In general, higher values of D result in less movement in the x-direction and more movement in the y-direction, prior to dewetting, than lower values of D. A final point to note is that, for higher values of D, the transition between motion in the x-direction and motion in the y-direction is more gradual (the particle's trajectory curves more smoothly) than it is for lower values of D. It is likely that this reflects the slower dynamics of the system, as the effective diffusion coefficient, D, increases.

There are a few interesting points of difference between figure 4.14 and 4.15. For example, the latter figure is harder to interpret because there is greater overlap between the curves associated with different values of D. The physical explanation for this is not clear, but it correlates with the closer spacing between points in both bands of figure 4.13, when $d = 10.0\,nm$, in comparison with the spacing between points when $d = 5.0\,nm$. Another difference is that there is generally less movement of the particle in the x-direction in figure 4.15, where $d = 10.0\,nm$ than there is in figure 4.14, where $d = 5.0\,nm$, even though the movement of the particle in the y-direction is broadly comparable in the two figures. Finally, an intriguing feature of figure 4.15 is the long "tails" of the particle trajectories, compared with those in figure 4.14, even though the end of every trajectory represented in these figures corresponds with the same point, physically speaking - the point at which the preferred phase first makes contact with the particle's surface. However, since these observations play no role in what follows, we do not explore them further.

What bearing does all of this have on the features of the master dewetting plot (figure 4.13) we described earlier? The main point is that relaxing the first key assumption of our simplified geometrical model, in recognition of the physical reality that the particle moves as the system is sheared, opens up the possibility that at least some of our simulation results might deviate from the curve predicted by the model. If the particle moves, and the degree of movement varies with both D and the shear rate, this must surely be reflected in the value of the shear strain when dewetting occurs. Although this is correct, neither the magnitude, nor the direction of the particle's movement is enough to account for the main features of figure 4.13. Firstly, the displacement of the particle at the dewetting point, relative to its initial position is not great, rarely exceeding $\sim 2.5\,nm$ in the results shown in figures

4.14 and 4.15. In addition, for any given initial displacement of the particle from the central interface, and effective diffusion coefficient, D, doubling the dimensionless shear rate from $\tilde{\dot{\gamma}} = 0.001$ to $\tilde{\dot{\gamma}} = 0.002$ has little effect on the final displacement of the particle, the difference being $\sim 1.0\,nm$ at most. Taken together, these two observations mean that the movement of the particle as the system is sheared cannot account for the two bands of curves seen in figure 4.13. The separation of these two bands is too great to be attributable to the relatively small movements of the particle.

This leaves open the possibility that the movement of the particle under shear might account for the separation of curves (corresponding with different values of D) *within* the bands (corresponding with different values of the dimensionless shear rate) shown in figure 4.13. However, a plausible account of how this separation within a band *might* occur cannot account for the ordering in which the curves *do* occur in each band. The plausible account is that the particle moves under the influence of shear, so the more the particle moves, the greater the shear strain at the dewetting point will be. Hence, for a given initial distance, d from the central interface, and dimensionless shear rate, different values of D will result in different shear strains at dewetting, and we will observe a band of curves on the master plot, with each curve in the band corresponding with a different value of D. The problem is that figures 4.14 and 4.15 show that, other parameters being equal, increasing the effective diffusion coefficient, D, *increases* the displacement of the particle relative to its initial position, when dewetting occurs. Thus increasing D should increase the shear strain at the dewetting point. This is the opposite of what we observe in the master plot where, for a given value of d, and dimensionless shear rate, increasing D *decreases* the shear strain at the dewetting point - data points are "stacked" vertically, with the lowest point corresponding with the highest value of D.

In summary, it is important to acknowledge that the particle is free to move, and that the extent of its movement is influenced by various parameters of the model. However, the movement of the particle is too limited to account for the two bands seen in the master plot, and the relationship between D and the displacement of the particle points in the wrong direction, as far as the ordering of the dewetting curves within each band is concerned.

Perhaps we will make more progress by scrutinising the second key assumption of our geometrical model: does the central interface really deform in a perfectly linear fashion when shear is applied to the system? The simplest way to answer this question is to look at a specific example (figure 4.16).

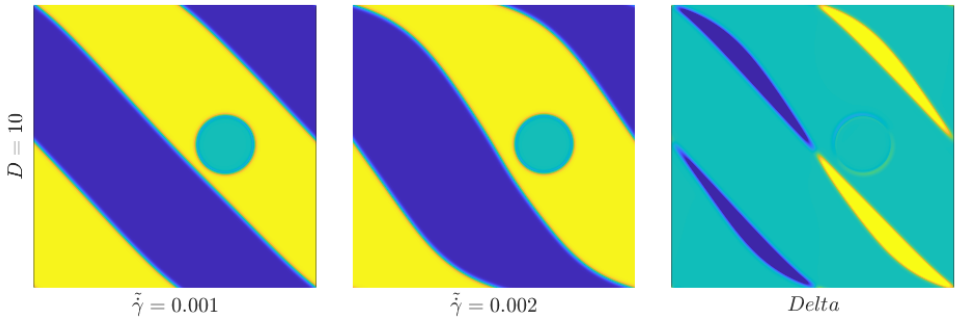

Figure 4.16: The state of the system at 100% shear ($\gamma = 1.00$) when the dimensionless shear rate is $\tilde{\dot{\gamma}} = 0.001$ and $\tilde{\dot{\gamma}} = 0.002$. In both cases, $D = 10$ and the initial distance of the particle from the central interface is $d = 10.0\,nm$. The third image represents the difference in the order parameter at every point in the system (the "delta" of the first two images).

Figure 4.16 shows two snapshots of a system where the shear strain $\gamma = 1.00$. We are in the highly entangled regime ($D = 10$) and, in both cases, the particle is located at $d = 10.0\,nm$ from the central interface. The only difference is the rate at which shear is applied: $\tilde{\dot{\gamma}} = 0.001$ in the first snapshot, and $\tilde{\dot{\gamma}} = 0.002$ in the second (corresponding with physical shear rates of $\dot{\gamma} = 10\,s^{-1}$ and $\dot{\gamma} = 20\,s^{-1}$, respectively).

It is clear, by inspection alone, that the central interface has deformed very differently under the two shear rates. In particular, the central interface at the lower shear rate is more linear, and closer to what we would expect if the simple geometrical model were correct. In contrast, at the higher shear rate, there is noticeable curvature to the central interface and therefore significant deviation from the geometrical model. The most likely explanation of this difference is that, at the higher shear rate, the interior of the system takes longer to "catch up" with the edge of the system as it is sheared. That is, the displacement of a layer of fluid lags further behind the movement at the edge, the closer to the centre of the system it is. Ultimately, this physical feature is responsible for the difficulty of sustaining dimensionless shear rates much greater than $\tilde{\dot{\gamma}} = 0.002$ in our simulations. If the edge of the system is sheared at a rate much greater than this, it becomes unstable. This difficulty becomes acute in the weak segregation regime, which we consider in the next chapter.

This visual impression is confirmed by the third image in figure 4.16, which represents the difference (or "delta") in the order parameter at every point in

the system, when the two system snapshots are compared. The third image uses the same colour scheme as is used throughout this thesis, so it is not surprising that most points in the system are coloured cyan, signifying that the system with the higher shear rate is almost identical to the system with the lower shear rate, at that point. The narrow yellow segment that extends from the centre of the system to the bottom-right corner implies that there is an excess of the non-preferred phase in this region of the system with the higher shear rate, compared with the system with the lower shear rate (and similarly, for the thin blue segment that extends from the centre of the system to the top-left corner). In other words, at the higher shear rate, the particle is further away from its preferred phase, than it is at the lower shear rate, even when the shear strain and all other parameters are identical.

All of the above implies that the shear strain at dewetting is higher in the system with the higher shear rate, than it is in the system with the lower shear rate. Furthermore, this is not a small effect - the curvature of the central interface at the higher shear rate deviates significantly from near-linear central interface at the lower shear rate. The natural conclusion, which we believe to be correct, is that this effect accounts for the appearance of two bands in the master dewetting plot (figure 4.13), one for each of the dimensionless shear rates represented. In particular, the band of curves associated with the higher dimensionless shear rate of $\tilde{\dot{\gamma}} = 0.002$ occupies a higher range along the shear strain axis than does the band associated with the lower dimensionless shear rate of $\tilde{\dot{\gamma}} = 0.001$, just as we would expect from the deformation of the central interface at the higher shear rate. Note that, although, for simplicity, we have based this conclusion on just one point of comparison, similar comparisons show the same pattern seen in figure 4.16.

We can use similar reasoning to account for the order of the individual dewetting curves *within* each band. Now, we wish to compare the state of the system at 100% shear (for consistency) with different values of the effective diffusion coefficient, D, while holding all other parameters, including the shear rate, constant. Let us compare the Rouse regime ($D = 1$) with the highly entangled regime ($D = 10$), as this ought to give us the greatest contrast. As before, the initial distance of the particle from the central interface is $d = 10.0\,nm$ in all cases. Figures 4.17 and 4.18 show the results of this comparison when $\tilde{\dot{\gamma}} = 0.002$ and $\tilde{\dot{\gamma}} = 0.001$, respectively.

The colour scheme in these images, and its interpretation, is as before. Thus, in figure 4.17, the narrow blue band that extends from the centre of the system to its bottom-right corner represents an excess of the preferred phase

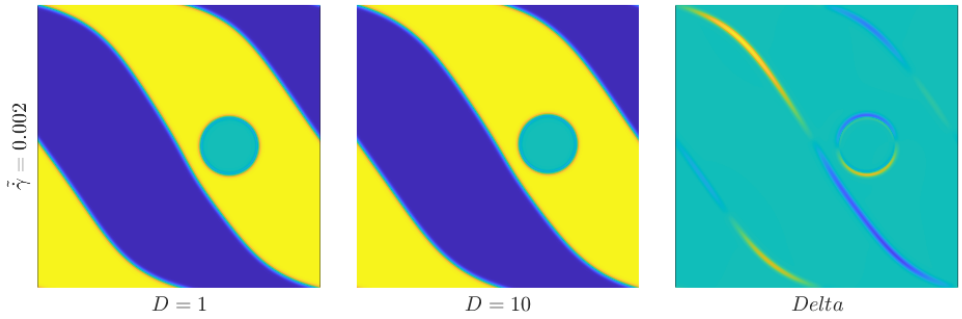

Figure 4.17: The state of the system at 100% shear ($\gamma = 1.00$) when the effective diffusion coefficient is $D = 1$ and $D = 10$. In both cases the dimensionless shear rate is $\tilde{\dot{\gamma}} = 0.002$, and the initial distance of the particle from the central interface is $d = 10.0\,nm$. The third image represents the difference in the order parameter at every point in the system (the "delta" of the first two images).

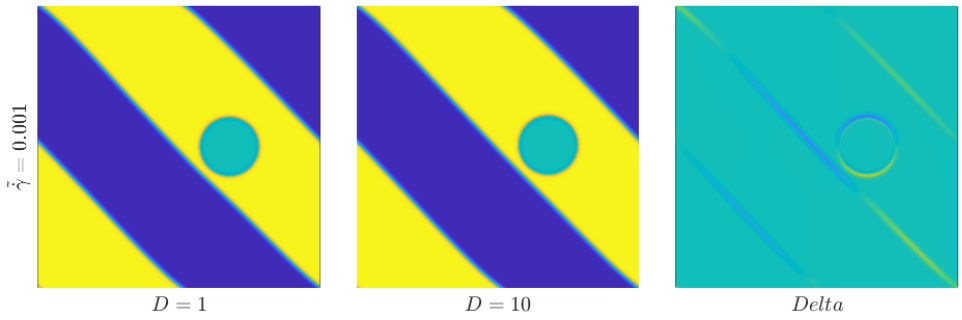

Figure 4.18: The state of the system at 100% shear ($\gamma = 1.00$) when the effective diffusion coefficient is $D = 1$ and $D = 10$. In both cases the dimensionless shear rate is $\tilde{\dot{\gamma}} = 0.001$, and the initial distance of the particle from the central interface is $d = 10.0\,nm$. The third image represents the difference in the order parameter at every point in the system (the "delta" of the first two images).

in that region of the highly entangled system, compared with the the system in the Rouse regime. In other words, when $D = 10$, the particle is closer to its preferred phase than it is when $D = 1$, even though the shear strain is identical, and all other parameters, including the shear rate are held constant. The physical reason for this is not entirely clear, but we speculate that it is a mark of the slower dynamics in the system with the higher effective diffusion coefficient: for any given dimensionless shear rate, a higher value of D implies a system that is slower to reach local equilibrium in the vicinity of the central

interface, as it deforms under the applied shear. The effect is a subtle one, however. Note the advantage of computing the delta of the two snapshots in this figure: it exposes a difference that is not nearly as obvious as the difference between the snapshots in figure 4.16.

Now, by similar reasoning to that used previously, this implies that the shear strain at dewetting ought to be *lower* in the system with the higher value of D, than in the system with the lower value. Referring back to figure 4.13, we see that this is indeed consistent with the ordering of individual dewetting curves within each band of curves. Comparing figure 4.17 with figure 4.16, this is a relatively small effect. However, logically, it must be more than enough to counter the effect of particle movement on the strain at the dewetting point, since the latter tends to order the dewetting curves within a band in the opposite (incorrect) direction.

Identical logic yields the same conclusion when applied to figure 4.18. The only difference is that the effect is weaker still, as shown by the relative faintness of the blue and yellow regions of the system in the final image, compared with figure 4.17. In physical terms, there is simply not much difference between the two systems shown in figure 4.18 though, as before, what difference there is favours dewetting at a lower shear strain in the system with the higher effective diffusion coefficient. This is consistent with our master plot where individual dewetting curves in the band corresponding with a dimensionless shear rate of $\tilde{\dot{\gamma}} = 0.001$ are much more closely spaced than the curves in the band corresponding with the higher dimensionless shear rate.

So far, we have accounted for both the existence of two distinct bands of dewetting curves in the master plot, and the ordering and spacing of individual dewetting curves within each band. The only puzzle that remains is the position of the curve representing the predictions of our geometrical model. The assumptions of the model - especially the second key assumption, that the shearing of the central interface is perfectly linear - suggest that the strain at dewetting ought to track the results represented by the lower band of dewetting curves. This is because the dewetting curves in the lower band correspond with the lower dimensionsless shear rate, $\tilde{\dot{\gamma}} = 0.001$, at which the shearing of the central interface is almost linear, in close agreement with the behaviour of the geometrical model. However, the theoretical curve predicted by the model lies within the band of dewetting curves corresponding with the higher dimensionsless shear rate, $\tilde{\dot{\gamma}} = 0.002$, contrary to what we might expect.

The solution to this difficulty is to abandon the third key assumption of the geometrical model, that dewetting occurs when the central interface is just tangential to the surface of the particle. This is unphysical because we know that, as the central interface approaches the surface of the particle, and $d < d_c$, the rapid diffusive mechanism becomes increasingly important, and that this leads to dewetting in time scales that are much shorter than the timescales over which the central interface is sheared. To capture this effect in the geometrical model, we introduce a further length scale, $e < d_c$, at which dewetting is almost instantaneous, in comparison with the time it takes to shear the system from its initial configuration the point where the shortest distance from the surface of the particle to the central interface is e. The required modification to the geometrical model is straightforward (figure 4.19).

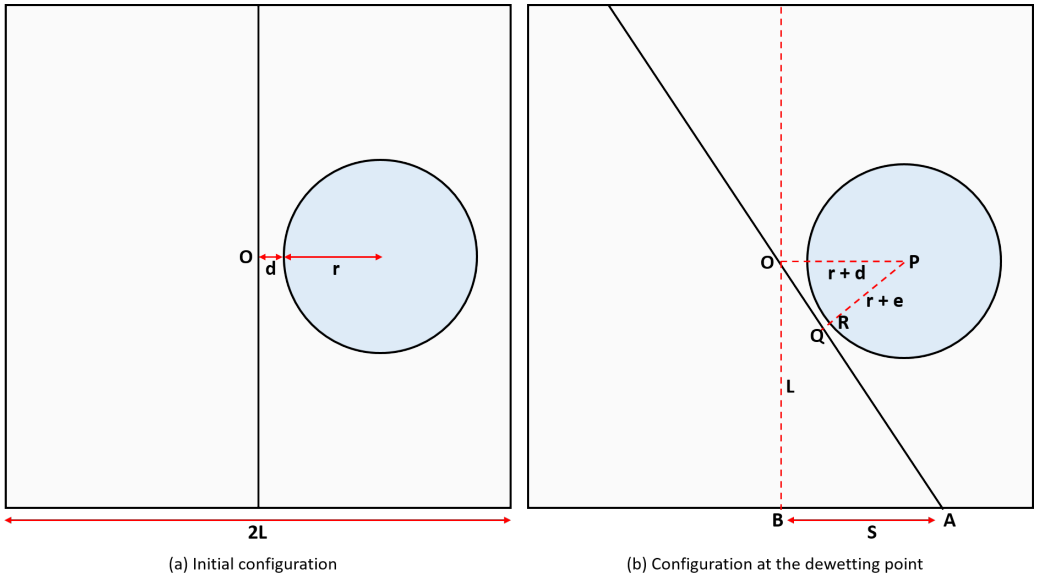

Figure 4.19: A revised geometrical model of dewetting, based on two of the three key assumptions described earlier in this section. The initial configuration of the system is shown in (a). In the revised model, dewetting, shown in (b), occurs when the central interface is sheared such that it is a distance $e < d_c$ from the surface of the particle.

The expression for the shear strain at the dewetting point becomes:

$$\gamma_{dewet} = \frac{S}{L} = \frac{1}{r+e}\sqrt{(r+d)^2 - (r+e)^2} \tag{4.2}$$

There is some discretion in the choice of the parameter e - any value that is sufficiently low that dewetting occurs very rapidly is defensible. Looking

back at various dewetting curves, such as those shown in figure 4.1, a value of $e = 2.5\,nm$ looks to be overly conservative, so we make the somewhat arbitrary choice of $e = 3.0\,nm$. Figure 4.20 reproduces the master plot of figure 4.13 with the predictions of the original model replaced by those of the revised model.

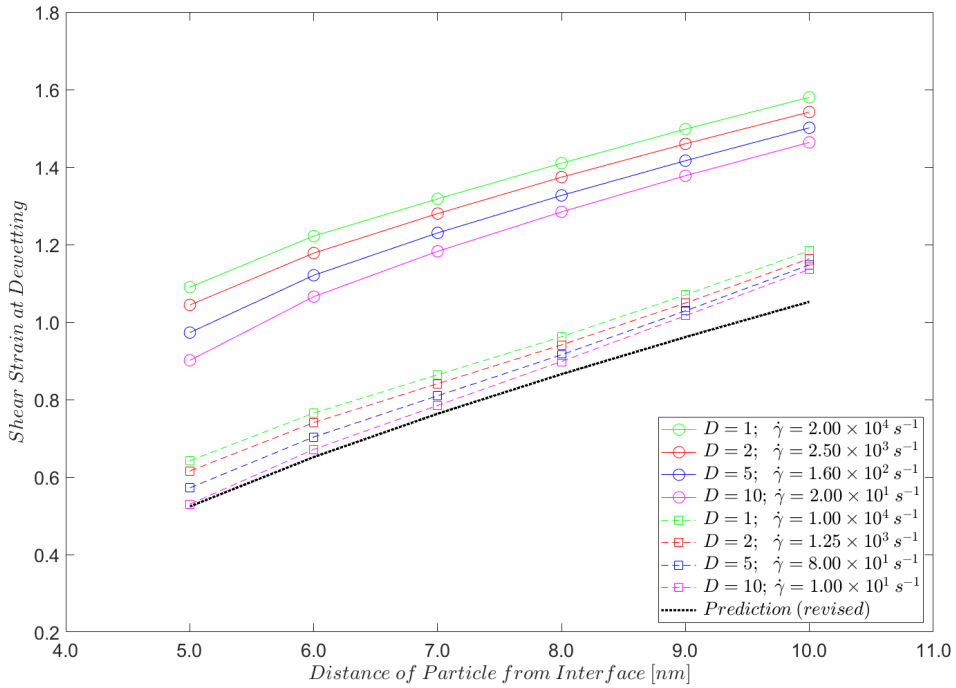

Figure 4.20: Dewetting master plot showing the shear strain at which dewetting occurs, as the distance of the particle from the central interface varies. Shown are the data points when $D = 1$, $D = 2$, $D = 5$ and $D = 10$. The two bands represent the upper and lower ends of the range of dimensionless shear rates used in the simulations ($\tilde{\dot{\gamma}} = 0.002$ and $\tilde{\dot{\gamma}} = 0.001$). The physical value of the shear rate varies, according to the value of the effective diffusion coefficient, D. The predicted values, shown as a black, dotted line, are those of the revised geometrical model described in the main text and represented in figure 4.19.

The predictions of the revised geometrical model now align closely with our simulation results when the dimensionless shear rate is $\tilde{\dot{\gamma}} = 0.001$, consistent with the fact that the shearing of the central interface is almost linear at the lower shear rate, resulting in lower shear strain at the dewetting point. Moreover, the predicted shear strain at dewetting is slightly lower than it is in any of our simulations. This reflects the fact that even the revised geometrical model represents a highly idealised system in which the shear strain at the dewetting point is likely to be minimised. Any deviations from this ideal behaviour, including those that result from features represented

in our physical model and its computational implementation, will tend to increase the shear strain at the dewetting point, relative to that predicted by the geometrical model.

4.7 Summary

In the highly entangled systems ($D = 10$), the dynamics of the system are slow, with dewetting and wetting times $\sim D^3 = 1000$ times greater than in the corresponding simulations in the Rouse regime. One effect of this slowing down in the dynamics is that the particle is no longer be expelled into its preferred phase through the application of shear to the system. This is probably due to the fact that the higher value of D implies a lower range of sustainable shear rates. Thus our results are consistent with the physical intuition that higher shear rates are more effective at promoting the migration of the particle from its non-preferred phase to its preferred phase.

In the intermediate cases ($D = 5$ and $D = 2$), we see evidence of a transition between the Rouse regime and the highly entangled regime. The former case resembles the highly entangled regime in that, with one significant exception, the particle is not expelled into its preferred phase under shear. We interpret the exception, when $\dot{\gamma} = 160\, s^{-1}$, as a sign that the system is close to transitioning to behaviour more reminiscent of the Rouse regime. The simulation results for the intermediate case when $D = 2$ support this conclusion. Now, the application of shear *can* expel the particle into its preferred phase, across a range of shear rates. In this respect, this case resembles a system in the Rouse regime. In both intermediate cases, the dewetting and wetting times scale roughly according to D^3, as expected, given the relationships between the dimensionless quantities used in the model.

Finally, we invoke a simple geometrical model, based on three key assumptions, to shed light on a subset of our results, in which the shear rate is the main factor that determines when dewetting occurs. These results may be represented on a master plot of the shear strain at dewetting against the initial distance of the particle from the interface (figure 4.13). The appearance, in this plot, of a distinct band of curves for each dimensionless shear rate is explained by the non-linear shearing of the central interface at higher shear rates, contrary to assumption 2 of the simple geometrical model. More subtle variations in the deformation of the interface, as it is sheared, account for the ordering of curves within each band. Modification of assumption 3,

by the introduction of a small distance, e, between the central interface and the surface of the particle, at which dewetting occurs almost instantaneously, brings the predictions of our geometrical model into line with the simulation results at the lower dimensionless shear rate, at which the shearing of the central interface is almost linear. In comparison, relaxing assumption 1 of the geometrical model, and allowing the particle to move under the influence of hydrodynamic forces, has relatively little explanatory value. The shear strain at the dewetting point is the result of the interplay between all of these factors, with the nature of the deformation of the central interface as it is sheared being the dominant influence.

Chapter 5

Weakly Segregated Systems

5.1 Introduction

In this chapter, we turn to the weakly segregated regime, in which the strength of the interaction between monomers is much lower than it is when strong segregation is present. The effect of this reduction is to lower the mean free energy density in the system as a whole. In particular, it lowers the interfacial energy between the two liquid phases at the centre of the system. The effect of this is to broaden the interface and to make it more "fragile", so it becomes harder to shear without breaking. A further effect is to slow down the dynamics of wetting and dewetting, since there is less energy to drive the hydrodynamic flows that are necessary for these processes to occur. All these effects - the broader, more fragile interface, and the slower dynamics - create difficulties when we attempt to simulate systems where the two liquid phases are weakly segregated.

Our aim in this chapter is to compare and contrast the behaviour of weakly and strongly segregated systems, with and without shear, and to thereby begin to construct a map of the phenomenology of this particular region of the parameter space of our model.

The chapter begins with a brief review of the required parameter settings before an initial attempt is made to explore the weakly segregated regime. To do this, we choose a value of the Flory-Huggins parameter, $\chi = 2.1$, close to the critical value, $\chi_c = 2.0$ in our model. The purpose of the section is to illustrate the difficulty of simulating weakly segregated systems, and

its conclusion is broadly negative: to obtain satisfactory results, we need to consider less weakly segregated systems.

The following section presents the results of simulations in which $\chi = 2.5$. Although there is no established convention, we consider this to be at the upper end of the weakly segregated regime. Nevertheless, the segregation between the liquid phases is weak enough for the dewetting behaviour of the system, and its behaviour under shear, to differ markedly from the behaviour of the strongly segregated systems we have examined so far. These differences may have useful consequences for tailoring microstructure during the processing of polymer blends containing nanoparticles. The benefit of this approach is that it enables us to run a complete set of simulations, comparable to those already performed in the strongly-segregated regime, for several values of the D parameter. However, due to time constraints, we consider only the case of $D = 1$ (Rouse regime), and the moderately entangled case in which $D = 2$.

In the final section of this chapter, we return to the geometrical considerations of section 4.6. In particular, we consider how well our simple and modified geometrical models of dewetting fit with dewetting results from the weakly segregated regime. Despite a relative lack of data, compared with the results obtained in the strongly segregated regime, we observe several notable differences in the dewetting behaviour, under shear, of weakly segregated systems.

5.2 Parameter Settings and Initial Conditions

Recall that, in our model, the critical point for the blend occurs when the Flory-Huggins interaction parameter, $\chi = 2.0$. All the simulations so far take place in the strongly segregated regime, with $\chi = 4.0$, and equilibrium values of the order parameter of $\psi_{eq} = \pm 0.9562$. Also, recall that the 10th order polynomial approximation of the Flory-Huggins free energy density is not reliable when $\chi \lesssim 2.05$. Figure 5.1 shows how the absolute value of the order parameter at equilibrium changes, as the Flory-Huggins interaction parameter is varied.

Let us define strong segregation, in our model, as applying to any system in which the equilibrium value of the order parameter is $|\psi_{eq}| \gtrsim 0.90$ ($\chi \gtrsim 3.3$), while weak segregation refers to systems in which $|\psi_{eq}| \lesssim 0.75$ ($\chi \lesssim 2.6$),

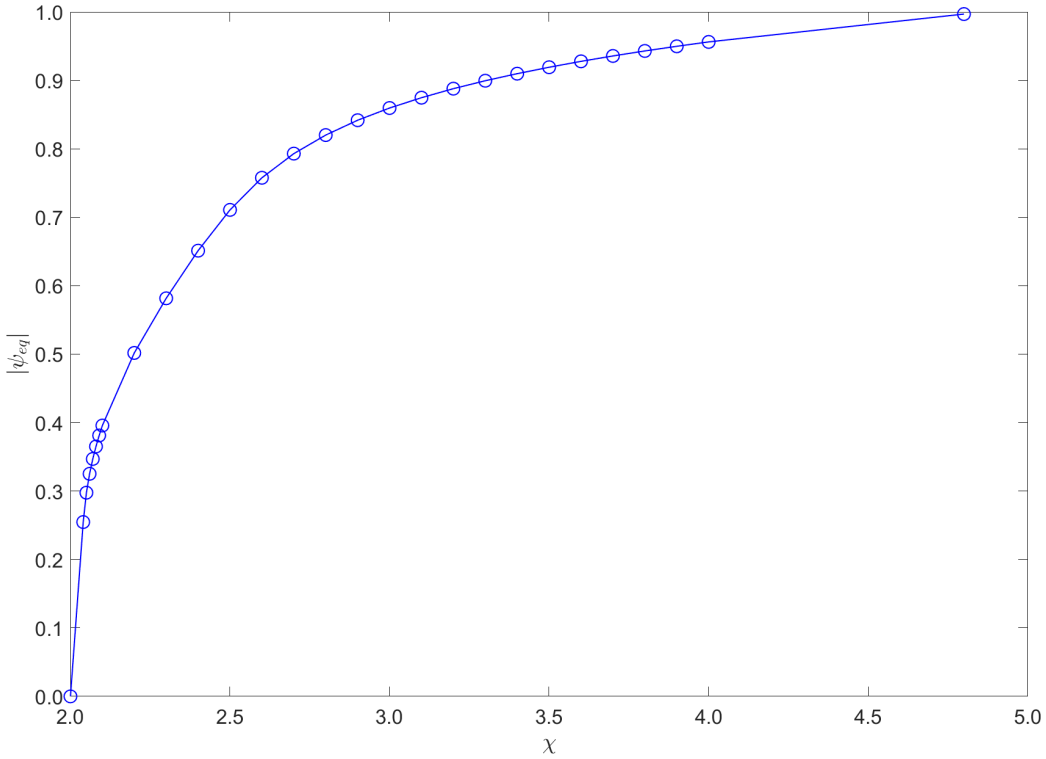

Figure 5.1: Absolute value of the order parameter at equilibrium, $|\psi_{eq}|$, plotted against the Flory-Huggins interaction parameter, χ. Note that the critical point occurs when $\chi = \chi_C = 2.0$, and that our tenth order polynomial approximation of the Flory-Huggins free energy density is unreliable when $\chi \lesssim 2.05$.

with any value in between corresponding to a system in which there is an intermediate degree of segregation.

This gives us a wide range of values of χ to choose from, when thinking about weakly segregated systems, but let us begin, somewhat arbitrarily, by taking $\chi = 2.1$. This is close to the point at which our numerical approximation for the Flory-Huggins free energy density falters, and is unambiguously at the lower end of the range of values of χ that give meaningful results in our model. A value of $\chi = 2.1$ implies equilibrium values of the order parameter, $\psi_{eq} = \pm 0.3957$ (corresponding to polymer volume fractions in the two liquid phases of approximately 0.7 and 0.3). This might appear to be overly conservative, since the phases remain quite distinct. However, the segregation between the phases is already weak enough to cause significant issues in our simulations, as we will see in the next section.

Almost all other parameters remain unchanged. In particular, we operate ini-

tially in the Rouse regime, where $D = 1$, although this condition is relaxed later, when we consider a system that is both weakly segregated ($\chi = 2.5$) and moderately entangled ($D = 2$). Because D is unchanged, for now, the finite difference method used to solve the equations of motion operates with the same dimensionless time step, $\tilde{\Delta t} = 0.001$, as in chapter 3, corresponding with a physical time step of $\Delta t = 10^{-10}\, s$. Similarly, the correspondence between dimensionless and physical shear rates is unchanged with a dimensionless shear rate of $\tilde{\dot{\gamma}} = 0.001$ implying a physical shear rate of $\dot{\gamma} = 1.0 \times 10^4\, s^{-1}$. It turns out that we must use a lower range of shear rates in simulations of weakly segregated systems, because the central interface between the two liquid phases is more likely to break at higher rates. However, the physical shear rate varies linearly with the dimensionless shear rate, for any given value of D, and is easy to determine, from the above reference value.

The exception to the general rule that all parameters, apart from χ, remain unchanged is the wetting parameter, W. This is changed to bring the strength of the interaction between the liquid phases and the surface of the particle approximately into line with the strength of the interaction between monomers. There is nothing intrinsically unphysical about a system in which W is significantly less than or significantly greater than χ, and some systems that satisfy this description might be of theoretical and practical interest. However, for simplicity, we always set $W = \chi$ in our simulations of weakly segregated systems, just as in the strongly segregated regime we put $W = \chi = 4.0$. Later, we will see that decreasing χ from 4.0 to 2.1 has a significant (orders of magnitude) effect on the mean free energy density of the system, so insisting that $W = \chi$ is prudent, and likely to avoid any complications that might arise from too great a disparity in the strengths of the various interactions in the system.

One final point concerns the initial condition of the system: at the start of the simulations in the weakly segregated regime, the width of the interface between the two liquid phases is arbitrarily set to be $\sim 1\, nm$, consistent with the approach taken in the strongly segregated regime. However, a narrow interfacial region is expected in a strongly segregated system, whereas it is less physically realistic in a weakly segregated system, where the interface will be both broader and more diffuse at equilibrium. Physically, starting the simulation of a weakly segregated system at this point corresponds with driving the system closer to its critical point, from a point in phase space that is some distance away. Practically, this might be achieved by means of a rapid increase in the temperature. In principle, we could approximate the width, at equilibrium, of the interface in the weakly segregated system,

and start the simulation from that point. In practice, the broadening of the interface, as it equilibrates, occurs rapidly, due to the short characteristic time scale of the diffusive mechanism involved. This is true in both the strongly segregated regime and the weakly segregated regime, so we start all our simulations with a narrow interfacial region, of width $\sim 1\,nm$ for the sake of consistency and convenience.

5.3 Dewetting: Methodological Challenges

The purpose of this section is to describe some of the methodological difficulties that arise in attempts to simulate dewetting in a weakly segregated system, in which $\chi = 2.1$ and $\psi_{eq} = \pm 0.3957$. Ultimately, these difficulties necessitate the use of a higher value of χ in the remainder of the chapter. As usual, we proceed by attempting to determine the critical film thickness, beyond which dewetting no longer occurs in a quiescent system. We do this by starting the particle in its non-favoured phase, $\sim 2.5\,nm$ from the central interface. We then increase the initial distance of the particle from the central interface in small increments, until dewetting is no longer observed.

As soon as we attempt to reproduce this earlier approach to determining the critical film thickness, the lower energy and slower dynamics in the weakly segregated system raises a methodological issue. In the strongly segregated systems we have studied, the process of dewetting is extremely rapid, due to the high energy of the interface between the two liquid phases. Thus, our choice of *when* the dewetting point occurs is of little consequence to any trends in the observed behaviour of the system. However, when we inspect snapshots of the dewetting process in a weakly segregated system, we are compelled to be more precise about when dewetting occurs. Figure 5.2 illustrates this point.

Careful inspection of figure 5.2 reveals that there are at least three points at which dewetting might be said to occur. The first possibility is that dewetting occurs as soon as the central interface between the two liquid phases shows any sign of being breached. A second option is that the dewetting point occurs at the later time, at which *none* of the non-preferred polymer makes contact with the particle (or, equivalently, the order parameter, ψ, close to the surface of the particle is zero). The third and final option is that dewetting occurs when the preferred polymer first makes contact with the surface of the particle. Of these options, the third is probably the most intu-

Figure 5.2: Stages of dewetting in a weakly segregated system ($\chi = 2.1$): stage A is the initial breach of the interface between the two liquid phases; stage B is the point at which the non-preferred phase no longer makes contact with the particle; and stage C is the initial contact of the preferred phase with the particle. The initial distance of the particle from the central interface is $d = 4.5\,nm$ and the effective diffusion coefficient is $D = 1$ (Rouse regime).

itive and is the one we have used to determine the dewetting time in strongly segregated systems (see section 3.9). However, in the strongly segregated regime, the choice is not critical, because all three stages of dewetting occur in rapid succession. In comparison, the dewetting process occurs much more slowly in a weakly segregated system (figure 5.3).

If we take the duration of the dewetting process to be the time interval between stage A and stage C then, in the example shown in figure 5.3, the process takes $25.5\,\mu s$ in the weakly segregated system, and $0.9\,\mu s$ in the strongly segregated system. Thus the duration of the dewetting process is more than twenty times longer in the weakly segregated system.

This nicely illustrates the slower dynamics of the weakly segregated regime. This is a general feature of such systems, and it raises another practical difficulty when we try to study their dewetting behaviour: the dynamics of the system are so slow that the computation time required for the simulations starts to become prohibitive. This is especially the case, if we insist on defining dewetting as the point at which the preferred phase first makes contact with the surface of the particle, since this is the latest stage of the dewetting process. The difficulty here is compounded by the diffuse nature of the central interface in weakly segregated systems, which makes it hard to be certain that the final stage of dewetting has occurred. In short, when the Flory-Huggins interaction parameter, $\chi = 2.1$, dewetting data takes a long time to collect and is inherently unreliable. These difficulties are apparent in

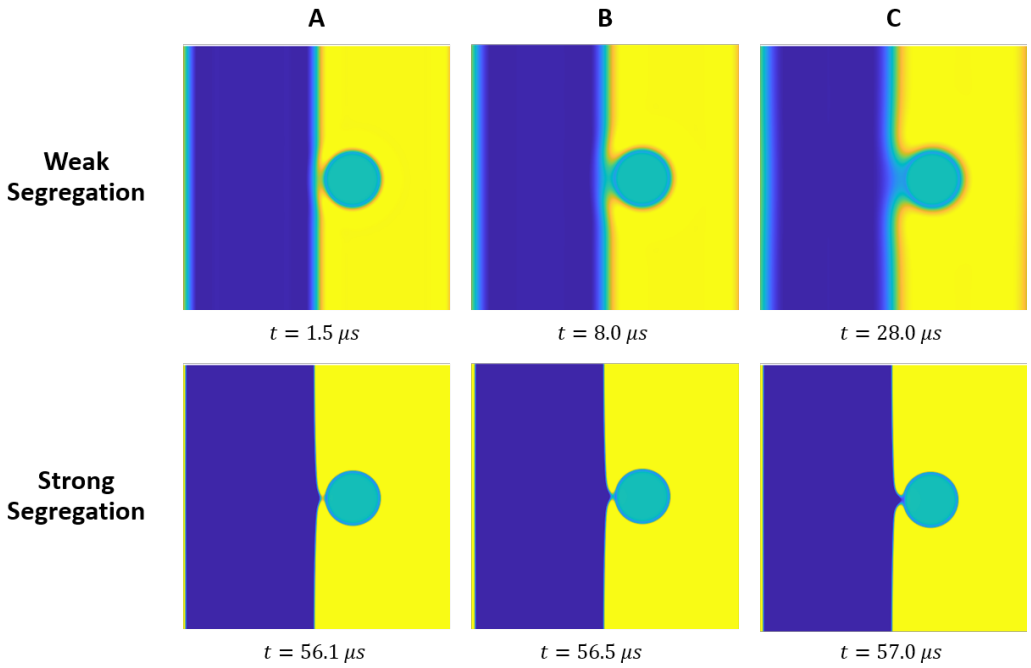

Figure 5.3: Comparison of the dynamics of dewetting in the strong ($\chi = 4.0$) and weak ($\chi = 2.1$) segregation regimes. The dewetting period, as measured by the time interval between stage A and stage C of the dewetting process, occurs much more rapidly in the strongly segregated system (approximately 20× faster than in the weakly segregated system).

table 5.1 and figure 5.4, which present the results of one attempt to determine the critical film thickness in this weakly segregated system.

Although the data plotted in figure 5.4 is clearly flawed, and is hard to directly compare with previous plots of dewetting time against the initial distance of the particle from the central interface, we can make a few observations. Firstly, we see the start of the divergence in the dewetting time that is characteristic of the existence of a critical film thickness: each increase of $\sim 3\,nm$ in the initial distance of the particle from the central interface approximately doubles the dewetting time. Secondly, the dewetting time when the particle is initially $2.5\,nm$ from the central interface between the two liquid phases is approximately ten times greater than in the strongly segregated regime ($9.0\,\mu s$, compared with $1.0\,\mu s$). This is consistent with the slower dynamics we have already observed in the weakly segregated regime.

It is interesting that, at an initial distance of $4.5\,nm$ from the central interface, this situation is reversed: the dewetting time in the weakly segregated

Distance [nm]	Dewetting Time [μs]	Comment
2.5	9.0	
4.5	28.0	
5.0	34.0	
6.0	50.4	estimate
7.0	-	not used
9.0	108.6	estimate
10.0	157.4	estimate
12.0	225.8	estimate
14.0	421.2	estimate

Table 5.1: Variation of the stage C dewetting time with the initial distance of the particle from the central interface in a quiescent, weakly segregated system ($\chi = 2.1$). Due to the difficulty of determining when stage C dewetting has occurred, most times are rough estimates. The result of the simulation when $d = 7.0\,nm$ is too unreliable to use.

system is approximately half the dewetting time in the strongly segregated system ($28.4\,\mu s$, compared with $57.4\,\mu s$). This might reflect an error in the measurement of the dewetting time, due to the uncertainty introduced by the diffuse interface associated with the weakly segregated regime. But it might also reflect the fact that, at $4.5\,nm$ from the central interface, we are close to the critical film thickness in the strongly segregated system, so dewetting is highly retarded at this point. On the other hand, the results of the simulations in the weakly segregated regime indicate that the particle continues to dewet, even when the initial distance of the particle from the central interface is much greater than $4.5\,nm$. Therefore, we are not close to the critical film thickness of the weakly segregated system at this point, and dewetting can occur relatively quickly, via the usual diffusive mechanism.

Given the issues identified so far, further progress is not possible. An alternative approach to obtaining usable data in the weakly segregated regime is to focus on an earlier stage of the dewetting process - specifically, stage A, the point at which the interface between the two liquid phases is first breached. This cuts down the simulation time needed and produces clearer, less uncertain, results (table 5.2 and figure 5.5). On this occasion, our plot of the dewetting time includes error bars that reflect the difficulty of determining the precise time at which stage A dewetting occurs.

As before, the divergence in the dewetting time as the critical film thickness is approached is apparent, but now the curve is free of the kinks, attributed

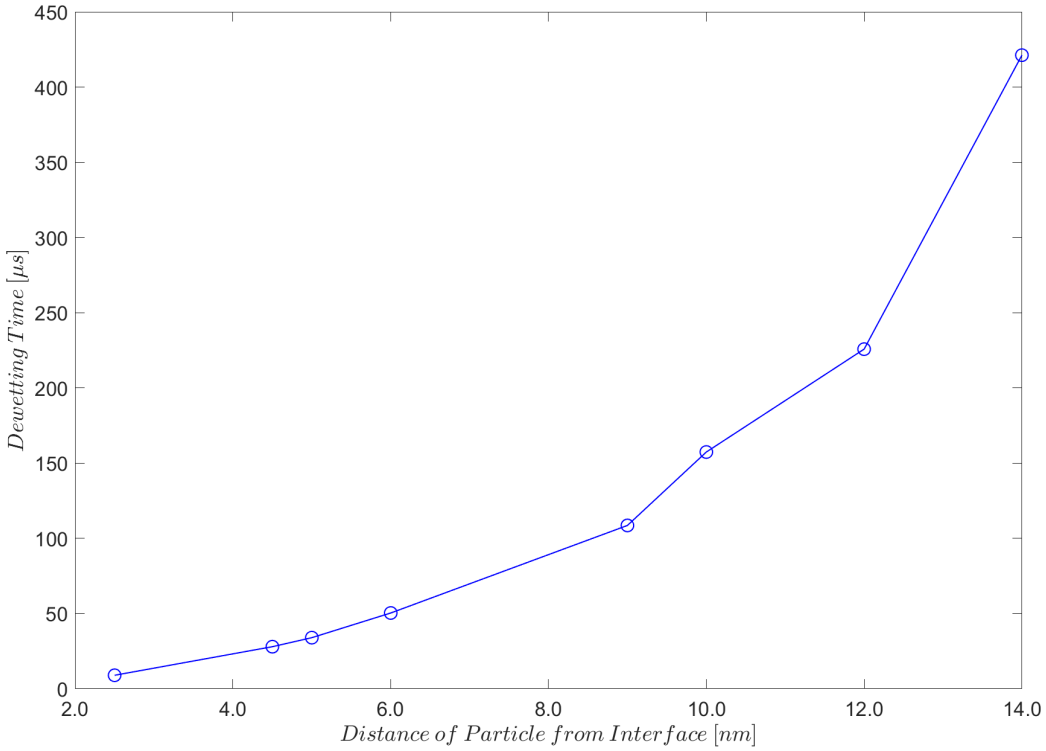

Figure 5.4: Dependence of the stage C dewetting time on the initial distance of the particle from the central interface, in a weakly segregated system ($\chi = 2.1$), showing the beginning of the divergence in dewetting time as the critical film thickness is approached. Note that the data is flawed due to the difficulty of determining when dewetting occurs with a diffuse central interface.

to unreliable data, in figure 5.4. Comparing the new dewetting times with the corresponding times for stage C dewetting (table 5.1), we note that they are generally much shorter, as we would expect. For example, at a starting distance of $d = 12\,nm$ from the central interface, stage C dewetting takes approximately twice as long as stage A dewetting ($225.8\,\mu s$, compared with $91.5\,\mu s$). The effect is even more obvious when the particle starts closer to the interface between the two liquid phases: when the initial distance of the particle from the central interface is $d = 5\,nm$, stage C of the dewetting process occurs after $34.0\,\mu s$, while stage A occurs after just $2.0\,\mu s$.

The drawback of redefining the dewetting point in this way is that it is no longer possible to directly compare dewetting times in the strongly and weakly segregated regimes. Additionally, although focusing on the earliest stage of dewetting saves computation time, the simulations remain resource intensive. This is exacerbated by the fact that the critical film thickness in the

Distance [nm]	Dewetting Time [μs]	Uncertainty [μs]
2.5	0.1	$\pm$ 0.2
4.5	1.2	$\pm$ 0.9
5.0	2.0	$\pm$ 1.2
6.0	4.0	$\pm$ 0.8
7.0	7.7	$\pm$ 1.4
9.0	21.5	$\pm$ 3.0
10.0	38.7	$\pm$ 7.4
12.0	91.5	$\pm$ 17.0
14.0	207.0	$\pm$ 14.0

Table 5.2: Variation of the stage A dewetting time with the initial distance of the particle from the central interface in a quiescent, weakly segregated system ($\chi = 2.1$). The stage A dewetting time is easier to determine than the stage C dewetting time due, in part, to the reduction in the computation time required to reach this point in the dewetting process.

weakly segregated regime is clearly much greater than $\sim 5\,nm$, its value in the strongly segregated regime. This leads to ever greater simulation times, as the distance of the particle from the central interface is increased. Note that table 5.2 and figure 5.5 show dewetting occurring even when $d = 14.0\,nm$, more than twice the value of the critical film thickness in the strongly segregated regime. It is not clear from this data how much further the particle needs to be from the central interface, at the start of the simulation, to prevent dewetting from occurring.

This brings us to a further methodological difficulty in simulating the behaviour of a weakly segregated system. This difficulty is a consequence of the periodic boundary conditions used in our simulations, and is best illustrated with a diagram (figure 5.6).

Recall that, in order to compensate for the volume of the non-preferred phase displaced by the particle in its initial position, we introduce a second "dummy" interface between the two liquid phases at the left edge of the system. This, combined with periodic boundary conditions, means that, as the initial distance of the particle from the central interface increases, it moves *closer* to the second interface near the opposite edge of the system. For example, if the particle starts at $d = 14\,nm$ from the central interface, periodic boundary conditions imply that it is $d' = 27\,nm$ from the additional interface at the left edge of the system. And, to take a more salient example, if the particle is initially located at $d = 20\,nm$ from the central interface, it is

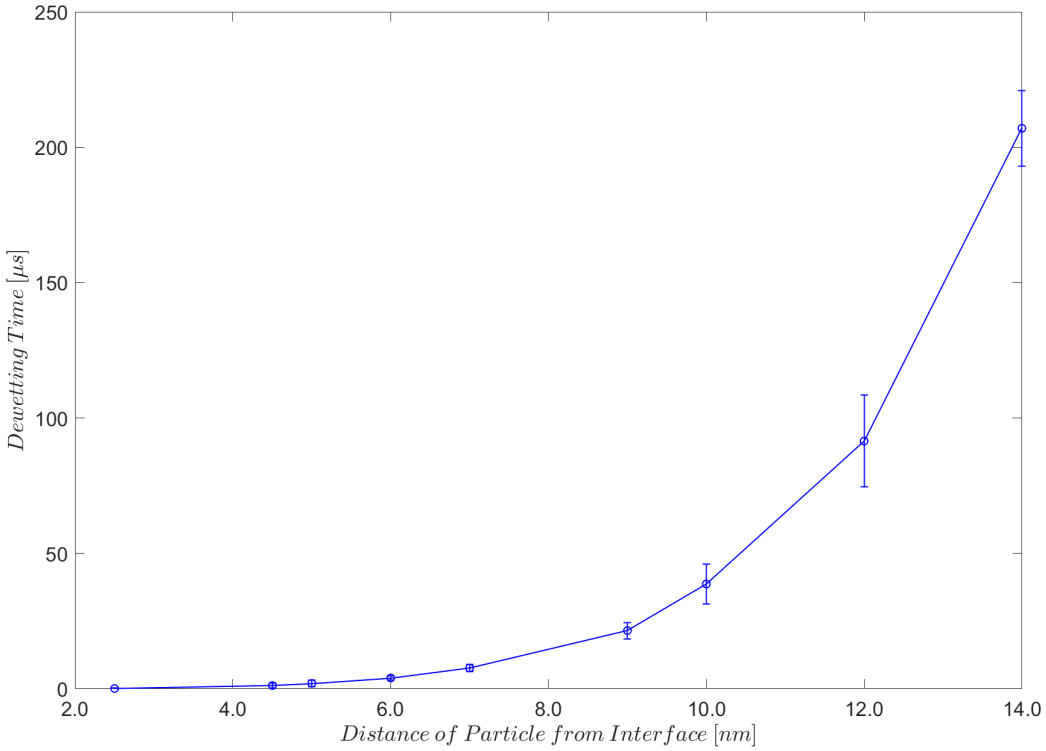

Figure 5.5: Stage A dewetting time against the initial distance of the particle from the central interface in a quiescent, weakly segregated system ($\chi = 2.1$). Although the stage A dewetting time is easier to determine than the stage C dewetting time, comparison with dewetting in the strong segregation regime is more difficult, due to the use of a different operational definition of dewetting.

just $d' = 21\,nm$ - virtually equidistant - from the second interface. This raises the possibility, and even the likelihood, that the second interface between the two liquid phases will start to exert a significant influence on the particle, confounding any attempt to accurately determine the dewetting time, and the critical film thickness. Although we do not reach this point in our simulations of the weakly segregated regime, when $\chi = 2.1$, we know that the critical film thickness is greater than $14\,nm$ and there is no indication that the critical film thickness will be reached any time soon.

An obvious solution to this difficulty is to increase the system size, but this significantly increases the computation time needed to complete each simulation. A less obvious option is to decrease the particle size, which has the additional advantage of decreasing the computation time required for any given initial distance of the particle from the central interface. The result of one such simulation is shown in figure 5.7.

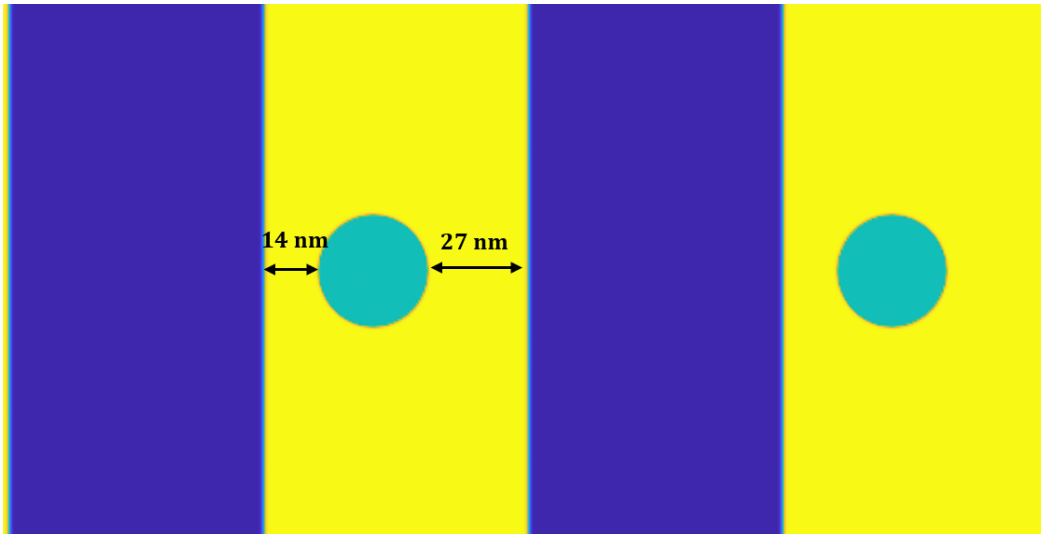

Figure 5.6: A potential effect of periodic boundary conditions on dewetting dynamics. The right-hand side of the figure is the continuation of the left-hand side. When the particle is, for example, 14 nm from the central interface, the periodic boundary conditions entail that it is 27 nm from the additional interface near the left edge of the system. As the former distance increases, the latter will decrease. Note that, for clarity these images show the initial state of a simulation in the Rouse regime.

Inspecting figure 5.7, it appears that the size of the particle does not significantly change the physical dewetting time, though, the computation time needed to reach the final state shown in each row of figure 5.7 is reduced from ~ 80 hours to ~ 70 hours a small, yet worthwhile saving. However, although the dynamics of dewetting do not appear to be significantly affected by the reduction in the radius of the particle, we cannot be certain that there is no effect whatsoever. The application of constant shear to the system, to promote the migration of the particle from one phase to the other, introduces further opportunities for the radius of the particle to influence the outcome of the simulation. In particular, the second dewetting that usually follows the breaking of the central interface under shear stress is sensitive to the position of the surface of the particle relative to the broken interface, as it retracts. This, in turn, will depend on the radius of the particle. Put simply, based on the results of our previous simulations, there is a greater chance that the smaller particle will miss the second dewetting point entirely, leading to a steady state in which the particle adheres to a droplet of the preferred phase, surrounded by the non-preferred phase. In short, although there is a small reduction in the computation time needed when a smaller particle is used, this is meagre compensation for losing direct comparability of results in the weakly separated regime, with our previous results in the strongly segregated

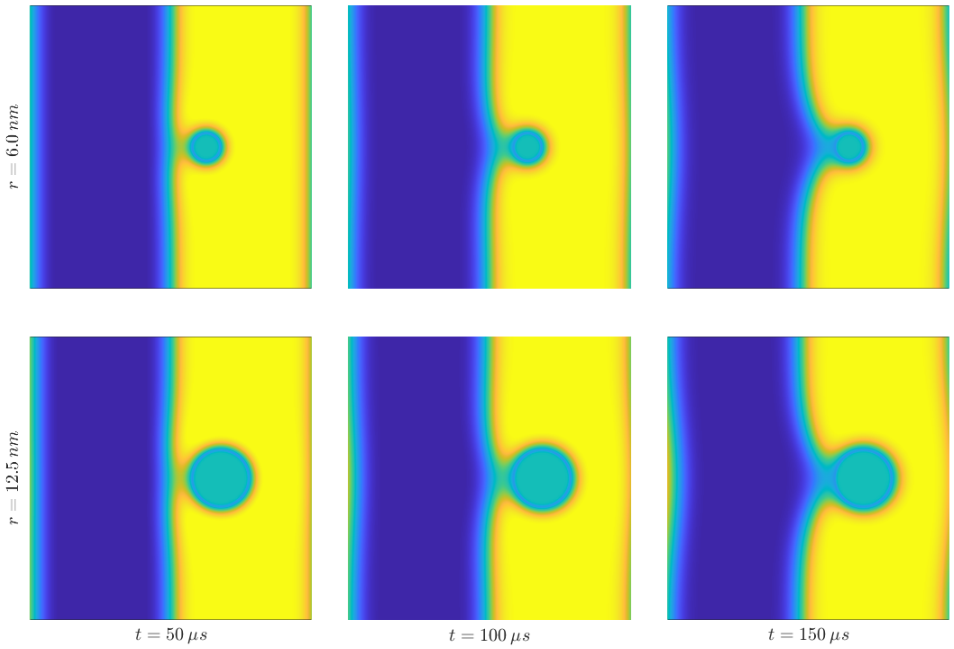

Figure 5.7: Dewetting in a weakly segregated system ($\chi = 2.1$) with a particle of radius $r = 6.0\,nm$ compared with a particle of default radius $r = 12.5\,nm$. In both cases, snapshots are taken at $50\,\mu s$, $100\,\mu s$ and $150\,\mu s$, and the initial distance of the particle from the central interface is $d = 5.0\,nm$.

regime.

The application of shear to a weakly segregated system introduces one final methodological difficulty. The low energy of the central interface, compared with the central interface in a strongly segregated system, means that it is delicate. A consequence of this is that the central interface in a weakly segregated system is unable to sustain the shear rates studied in strongly segregated systems which, in the Rouse regime, ranged, roughly, from $\dot{\gamma} = 1.0 \times 10^4\,s^{-1}$ to $\dot{\gamma} = 2.0 \times 10^4\,s^{-1}$. Figure 5.8 illustrates the effect of applying a shear rates at the upper and lower end of this range to a weakly segregated system:

At the higher of the two shear rates, especially, the interface is not sheared smoothly and becomes detached from the top and bottom edges of the system in an unpredictable way. This problem persists even when we apply a lower shear rate to the system of $\dot{\gamma} = 5.0 \times 10^3\,s^{-1}$ (figure 5.9).

In this simulation we note that the dewetting time scale is largely determined

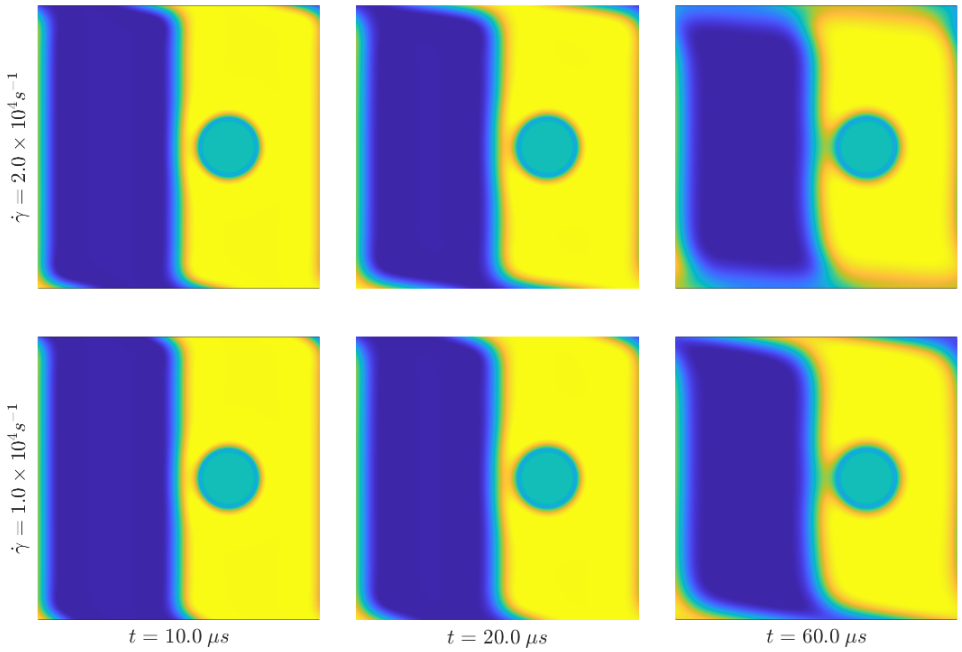

Figure 5.8: Dewetting in a weakly segregated system ($\chi = 2.1$) at two higher shear rates. Note the fragility of the interface and its detachment from the top and bottom edges as the shear strain increases, especially when $\dot{\gamma} = 2.0 \times 10^4\, s^{-1}$.

by diffusive effects (the applied shear has had little effect on the location of the middle section of the central interface, when dewetting begins). More to the point, while the central interface appears to shear quite smoothly at first, it eventually becomes less stable, especially after dewetting has occurred. We could experiment with even lower shear rates to maintain the stability of the central interface, but then the combination of a low shear rate, and gradually increasing the distance of the particle from the central interface, implies prohibitively long simulation times.

To summarise the discussion of this section, in the weakly segregated regime, when the Flory-Huggins interaction parameter, $\chi = 2.1$, the interface between the two liquid phases is diffuse and delicate. This makes accurate determination of the dewetting time difficult and time-consuming, even if we modify our operational definition of dewetting. In addition, the critical film thickness is greater than it is in the strongly segregated regime, which raises the possibility that periodic boundary conditions, combined with the additional interface at the edge of the system, will confound our measurements. Using a smaller particle gains little, and compromises our ability to compare results in the weakly segregated regime with those from earlier simulations.

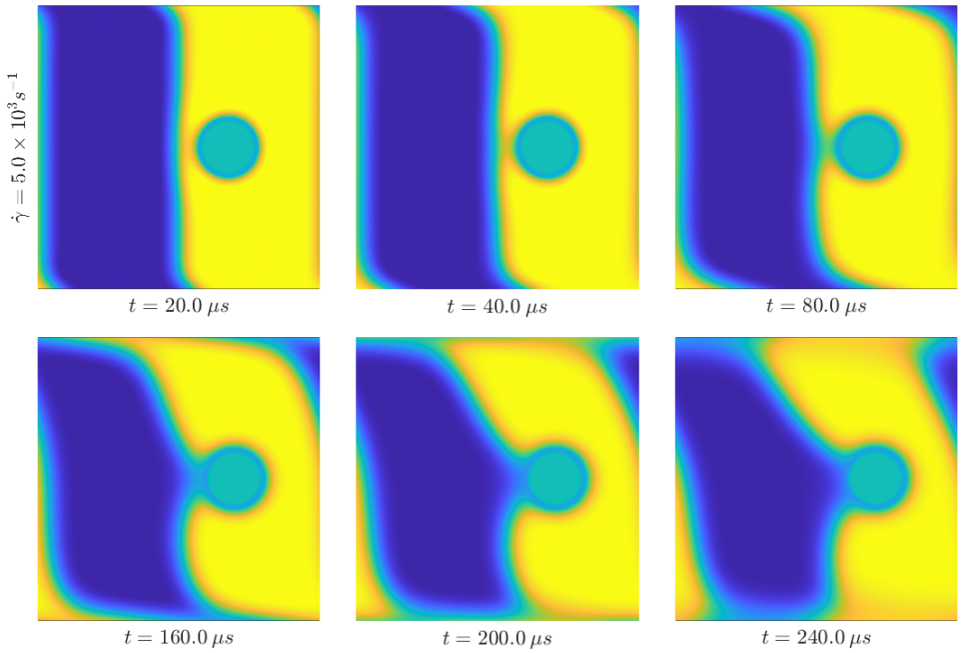

Figure 5.9: Dewetting in a weakly segregated system ($\chi = 2.1$) at a shear rate of $\dot{\gamma} = 5.0 \times 10^3\, s^{-1}$. The shearing of the interface is initially quite smooth, but becomes more less regular with the onset of dewetting, due to the fragility of the low energy interface.

Finally, attempts to apply higher shear rates on the fragile interface cause it to become unstable, while lower shear rates add to the computational burden.

For all of these reasons, we take a pragmatic approach and work with a value of the Flory-Huggins parameter, χ, at the upper end of the range of values we associate with the weakly segregated regime, in the remainder of this chapter.

5.4 Dewetting in Weakly Segregated Systems

In this section we present the results of dewetting simulations in the weakly segregated regime, when the Flory-Huggins parameter, $\chi = 2.5$, and the equilibrium value of the order parameter is $\psi_{eq} = \pm 0.7108$. This is at the upper end of the range of values we use to mark the weakly segregated regime, while still being significantly lower than the equilibrium value of $\psi_{eq} = \pm 0.9562$ when $\chi = 4.0$, which we take to be representative of the

strongly segregated regime. Importantly, it is now possible to obtain usable data from our simulations, and we can revert to our original conception of the dewetting point, as the moment when the preferred phase first makes contact with the surface of the particle, thereby enabling like for like comparison with results in the strongly segregated regime. In addition to results in the Rouse regime ($D = 1$), we present a set of results for a moderately entangled system, in which $D = 2$. The aim is to see how far the behaviour of a weakly segregated, entangled system deviates from the behaviour of the strongly segregated system in the Rouse regime, with which we began our investigations.

As always, we begin by determining the critical film thickness. We proceed by varying the distance of the particle from the central interface between the two liquid phases, in a quiescent system, until dewetting no longer occurs. Since increasing the Flory-Huggins interaction parameter to $\chi = 2.5$ enables us to determine the stage C dewetting time with some accuracy, we now refer simply to the "dewetting time", consistent with the terminology used in previous chapters, and drop the use of error bars, since any uncertainty in the dewetting time is small, compared with the range of dewetting times we observe.

We then determine the dewetting time at two different shear rates, as the distance of the particle from the central interface is increased beyond the critical film thickness, so that shear must be applied to promote dewetting. The shear rates used are lower than those used in simulations of the strongly segregated regime because the central interface between the two liquid phases remains delicate, despite the increase from $\chi = 2.1$ to $\chi = 2.5$. Table 5.3 and figure 5.10 show the results in the Rouse regime, while table 5.4 and figure 5.11 show the corresponding results in the moderately entangled regime, when $D = 2$.

Note that, figures 5.10 and 5.11 omit the data point when the initial distance of the particle from the central interface is $d = 9.0\,nm$ because the dewetting time is so great that it would distort the rest of the plot. The divergence in the dewetting time of the quiescent system at this point is so marked we may immediately conclude that the critical film thickness in this weakly segregated system is $d_c \sim 9\,nm$, approximately twice its value in the strongly segregated systems we have studied.

Before comparing these results directly with those in the strongly segregated regime, we first note that the relationship between dewetting times in the

Distance [nm]	Dewetting Time [μs]		
	$\dot{\gamma} = 0$ [$\times 10^3\, s^{-1}$]	$\dot{\gamma} = 2.0$ [$\times 10^3\, s^{-1}$]	$\dot{\gamma} = 8.0$ [$\times 10^3\, s^{-1}$]
4.0	9.0	8.0	8.0
5.0	15.0	15.0	15.0
6.0	25.0	26.0	27.0
7.0	46.0	49.0	49.0
8.0	95.0	96.0	94.0
8.5	151.0	141.0	119.0
9.0	1947.0	204.0	133.0
10.0	-	302.0	151.0
11.0	-	361.0	165.0
12.0	-	405.0	176.0
13.0	-	446.0	187.0
14.0	-	485.0	197.0
15.0	-	522.0	208.0

Table 5.3: Dewetting time in a weakly segregated ($\chi = 2.5$), quiescent system and at a constant shear rate of $\dot{\gamma} = 2.0 \times 10^3\, s^{-1}$ and $\dot{\gamma} = 8.0 \times 10^3\, s^{-1}$ as the distance of the particle from the interface varies from $d = 4.0\, nm$ to $d = 15.0\, nm$.

Distance [nm]	Dewetting Time [μs]		
	$\dot{\gamma} = 0$ [$\times 10^3\, s^{-1}$]	$\dot{\gamma} = 0.25$ [$\times 10^3\, s^{-1}$]	$\dot{\gamma} = 1.00$ [$\times 10^3\, s^{-1}$]
4.0	56	56	56
5.0	90	92	92
6.0	160	160	160
7.0	296	300	300
8.0	628	628	628
8.5	1044	1000	864
9.0	6920	1540	992
10.0	-	2312	1140
11.0	-	2768	1244
12.0	-	3132	1336
13.0	-	3460	1420
14.0	-	3764	1500
15.0	-	4060	1580

Table 5.4: Dewetting time in a weakly segregated, moderately entangled ($\chi = 2.5$, $D = 2$), quiescent system, and at a constant shear rate of $\dot{\gamma} = 0.25 \times 10^3\, s^{-1}$ and $\dot{\gamma} = 1.00 \times 10^3\, s^{-1}$ as the distance of the particle from the interface varies from $d = 4.0\, nm$ to $d = 15.0\, nm$.

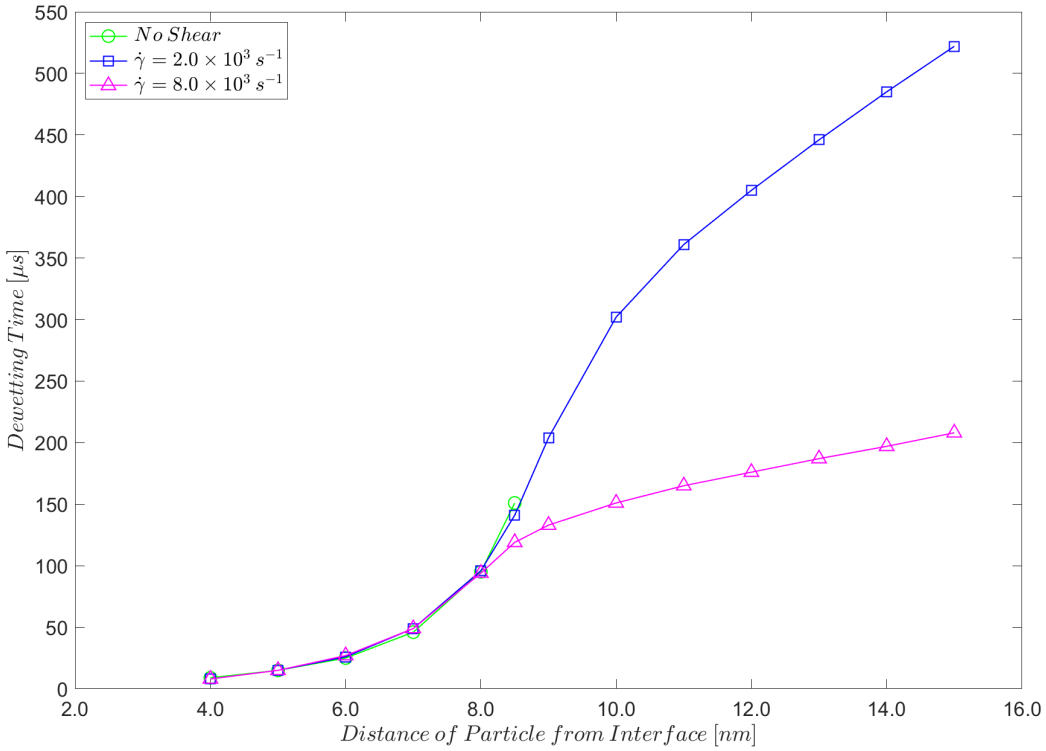

Figure 5.10: Dewetting time against the initial distance of the particle from the central interface in a weakly segregated system ($\chi = 2.5$) in the Rouse regime, in a quiescent state, and at two shear rates ($\dot{\gamma} = 2.0 \times 10^3\, s^{-1}$ and $\dot{\gamma} = 8.0 \times 10^3\, s^{-1}$). Note that the long dewetting time in the quiescent system when $d = 9.0\, nm$ has been omitted to improve resolution in the y-direction.

Rouse regime ($D = 1$) and in the moderately entangled regime ($D = 2$), when the system is weakly segregated, parallels what we observe when D is varied in the strongly segregated regime. In particular, all other parameters being equal, the dewetting time scales roughly with D^3, especially in the near-linear region of each dewetting curve, where the shear rate is the main determinant of the dewetting time. This is most apparent when the initial distance of the particle from the central interface is high, and the system is sheared. For example, when $d = 15.0\, nm$, the dewetting time in the Rouse regime, at the higher shear rate is approximately $200\, \mu s$, compared with a dewetting time of approximately $1600\, \mu s$ in the moderately entangled regime at the higher shear rate. The factor of $D^3 = 2^3 = 8$ between these two times reflects the fact that the same dimensionless shear rate implies a physical shear rate in the Rouse regime that is eight times the physical shear rate in the moderately entangled regime.

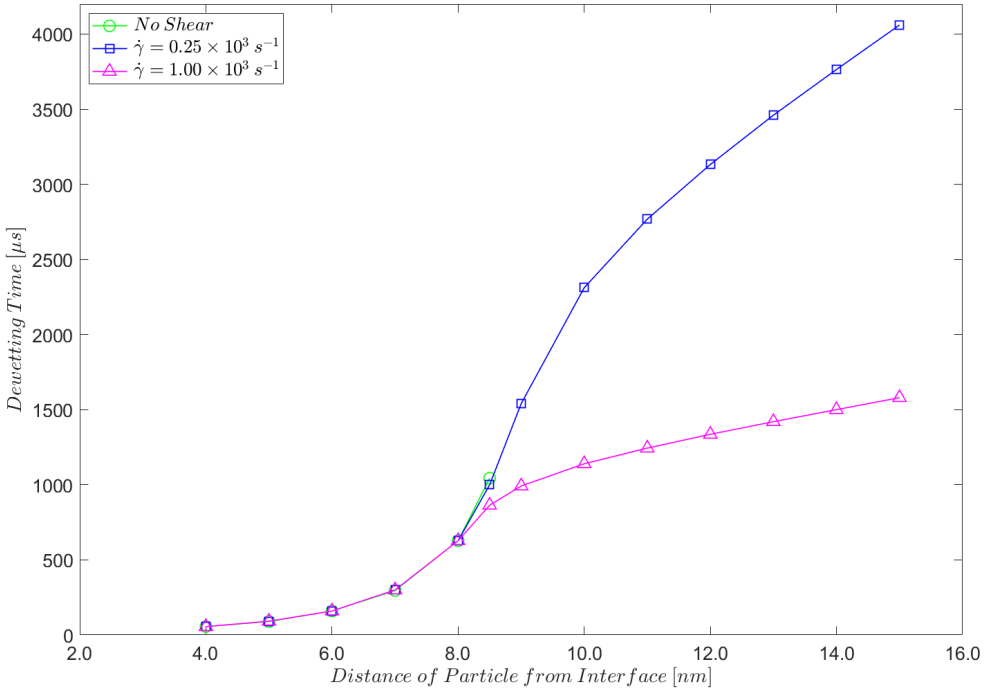

Figure 5.11: Dewetting time against the initial distance of the particle from the central interface in a weakly segregated, moderately entangled system ($\chi = 2.5$; $D = 2$), in a quiescent state, and at two shear rates ($\dot{\gamma} = 0.25 \times 10^3\, s^{-1}$ and $\dot{\gamma} = 1.00 \times 10^3\, s^{-1}$). Note that the long dewetting time in the quiescent system when $d = 9.0\, nm$ has been omitted to preserve a sensible vertical scale.

As usual, the results are less clear cut when the system is quiescent and/or the initial distance of the particle from the central interface is significantly less than the critical film thickness of $d_c \sim 9.0\, nm$. Having discussed this at some length in the previous chapter, we make no further comment here, other than to observe that, when these conditions apply, dewetting times in the moderately entangled regime tend to be lower than what would be predicted if they scaled with D^3. This is due to diffusive effects, which play a significant role when $d < d_c$, especially in weakly segregated systems.

Turning to a more direct comparison with the results in the strongly segregated regime, the most obvious point is that the dewetting curves have a broadly similar shape, regardless of the value of the Flory-Huggins interaction parameter, χ. In both regimes, for each curve plotted, there is a region in which the initial distance of the particle from the central interface is less than the critical film thickness, d_c, where diffusive effects dominate the dynamics of the system. Similarly, all curves have a region in which $d > d_c$ where the hydrodynamic effects of applying shear to the system are apparent. In the

latter region, the dewetting time increases approximately linearly with the initial distance of the particle from the central interface, because the system is sheared at a constant rate. Between these two regions, in every case, there is a transition zone, at around $d = d_c$.

The most interesting *difference* between the dewetting curves in the weakly and strongly segregated regimes is the rapidity at which this transition from the diffusive to the hydrodynamic regime occurs. In the strongly segregated regime, the transition is quite rapid, as shown in figures 3.8 (Rouse regime) and figure 4.6 (moderately entangled regime, with $D = 2$) by the large increase in the dewetting time, when the distance of the particle from the central interface increases from $4.0\,nm$ to $4.5\,nm$, just before the dewetting time diverges in the quiescent system. This is the case at both the higher and the lower shear rates used in these simulations. In contrast, the transition from the diffusive to the hydrodynamic regime in the weakly segregated system is notably more gradual, as shown by the relatively smooth plots of the dewetting time against the initial distance of the particle from the central interface in figures 5.10 and 5.11. Note, especially the smoothness of the dewetting curves in the vicinity of $d = d_c \sim 9.0\,nm$, when the dewetting time diverges in the quiescent system, and that the transition is gradual at both of the shear rates used in these simulations. We attribute this difference in the rapidity of the transition from the diffusive to the hydrodynamic regime to the greater effectiveness of the diffusive mechanism in weakly segregated systems. This, in turn, is due to the increase in the critical film thickness (so diffusive mechanisms have more time to influence the dynamics), and the broader central interface between the two liquid phases, in a weakly segregated system.

The increase in the critical film thickness makes further detailed comparison of the dewetting time in a *quiescent* system in the weakly and strongly segregated regime difficult, because there is little overlap in the range of d, the initial distance of the particle from the central interface, at which dewetting occurs. However, we note that, when $d = 4.0\,nm$ the dewetting time is $10.4\,\mu s$ in the strongly segregated system, and $9.0\,\mu s$. Although, in theory, the dynamics ought to be slower in the weakly segregated system, the initial distance of the particle from the central interface is much closer to the critical film thickness of the strongly segregated system, so we would expect dewetting to be significantly retarded in this case. This is similar to what we observed in the much more weakly segregated system, where $\chi = 2.1$, and supports the hypothesis that, in both cases, the more rapid dewetting (compared with the strongly segregated system) is due to a real physical effect,

rather than uncertainty in the measurement of the dewetting time.

Similarly, direct comparison, between the two regimes, of the dewetting time *under shear* is not straightforward because the shear rates used differ. This is a matter of necessity, as the central interface in the weakly segregated regime is too delicate to sustain the higher shear rates used to study the strongly segregated regime. However, the higher shear rate used in our simulations of weakly segregated systems is just 20% lower than the lower shear rate used in simulations of strongly segregated systems, so we can gain some impression of how the dynamics compare by considering initial distances, d, that are common to both sets of simulations. For example, in the strongly segregated regime, with a shear rate of $\dot{\gamma} = 1.0 \times 10^4\, s^{-1}$, we observe dewetting times of $96.2\,\mu s$, $107.0\,\mu s$, and $118.4\,\mu s$ respectively when the initial distance of the particle from the central interface is $8.0\,nm$, $9.0\,nm$, and $10.0\,nm$. in the weakly segregated system, with a slightly lower shear rate of $\dot{\gamma} = 8.0 \times 10^3\, s^{-1}$ respectively, the corresponding dewetting times are $94.0\,\mu s$, $133.0\,\mu s$, and $151.0\,\mu s$. So, as the initial distance of the particle from the central interface increases, the dewetting time in the weakly segregated system begins to exceed the dewetting time in the strongly segregated system, to a degree that may be hard to account for solely in terms of the lower shear rate in the latter.

However, the above comparison is confounded by the fact that the range of values of d considered is clearly above the critical film thickness, $d_c \sim 5.0\,nm$ in the strongly segregated regime, while it includes the critical film thickness, $d_c \sim 9.0\,nm$ in the weakly segregated regime. Therefore, let us compare values of the dewetting time in the linear section of the dewetting curves, well above the point at which the transition from the diffusive to the hydrodynamic regime occurs. For example, in a strongly segregated system in the Rouse regime, at $d = 8.0\,nm \sim 1.6\,d_c$, the dewetting times are $96.2\,\mu s$ and $72.5\,\mu s$ respectively, at the lower and higher shear rates. That is, the ratio of the two dewetting times, at this point, is approximately 0.75, when the shear rate doubles. In a weakly segregated system in the Rouse regime, at $d = 14.4\,nm \sim 1.6\,d_c$, we estimate the corresponding dewetting times to be $499.8\,\mu s$ and $201.4\,\mu s$ (interpolating linearly, between known data points). So, the ratio of the two dewetting times, at this point, is approximately 0.40, when the shear rate quadruples. This is close to, but not exactly, half the corresponding ratio at this point in the strongly segregated regime, indicating that mechanisms other than the ratio of the two shear rates influence the dewetting times. We believe this to be yet another effect of the wider, more diffuse, interface that is characteristic of the weakly segregated regime.

5.5 Expulsion in Weakly Segregated Systems

As in previous chapters, we now consider the long term behaviour of the particle as the system is sheared and, in particular, its eventual steady state: is the particle completely expelled from the non-preferred phase; does it adhere to a droplet of the preferred phase, or to the interface between the two liquid phases; or does it reach some other steady state? In these simulations, we vary the shear rate from $\dot{\gamma} = 0.1 \times 10^4\, s^{-1}$ to $\dot{\gamma} = 1.0 \times 10^4\, s^{-1}$, in recognition of the fragility of the interface between the two liquid phases, compared with the strong segregation regime. Although the central interface is more robust than it is when $\chi = 2.1$, shear rates much greater than the upper end of this range create instability, similar to that observed in figure 5.8. As in the strongly segregated regime, the initial distance of the particle from the central interface is the same in all simulations, and is just less than the critical film thickness; thus, we choose $d = 8.5\, nm$ in all cases. As in the previous section, we run simulations in both the Rouse regime, and in the moderately entangled regime, when $D = 2$.

Before presenting the results of these simulations in detail, we note that a previously unobserved steady state occurs at some shear rates, in both the Rouse regime and the moderately entangled regime. In this steady state, the particle is caught in the middle of the system, apparently adhering to the rightmost edge of one droplet of the preferred phase, and the leftmost edge of another. In fact, periodic boundary conditions imply that this is the *same* droplet so, strictly speaking, this represents an unphysical state in which the particle is in two places at the the same time (the left and right edge of the droplet). Of course, in a real physical system, a particle might adhere to two *different* droplets at the same time, but it is not clear that this could ever be a stable steady state, as the two droplets will tend to coalesce, as the system evolves, especially if shear is being applied. For these reasons, this new steady state is best seen as a special case of the one observed in previous simulations, in which the particle adheres to a droplet of its preferred phase. However, for clarity, we show this steady state as a distinct alternative in what follows. Figure 5.12 summarises the full set of alternative steady states available to a weakly segregated system, for the range of shear rates we have investigated. It is worth noting that the labelling of these states reflects the order in which they occurred in our simulations. In terms of the expulsion process, the correct ordering is A1, A3 and A2, corresponding to steady states in which the expulsion process is arrested after the first dewetting, the second dewetting, and the first wetting, respectively.

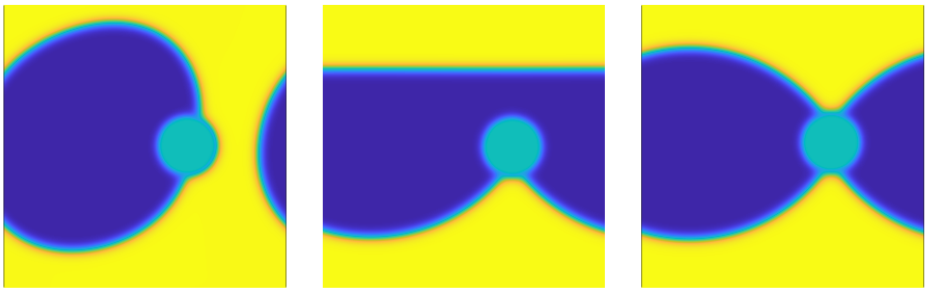

Figure 5.12: Alternative steady states when a weakly segregated system ($\chi = 2.5$) is sheared. In steady state A1 ($\dot{\gamma} = 1.0 \times 10^3\, s^{-1}$), the particle adheres to a droplet of its preferred phase in a matrix of the non-preferred phase. In steady state A2 ($\dot{\gamma} = 4.0 \times 10^3\, s^{-1}$), the particle remains attached to the now horizontal interface between the two phases. And in steady state A3 ($\dot{\gamma} = 5.0 \times 10^3\, s^{-1}$), which is not observed in simulations of the strongly segregated regime, the particle appears to adhere to two droplets of the non-preferred phase, one to its left and one to its right. In all simulations, the initial distance of the particle from the central interface is $d = 8.5\, nm$, and $D = 1$ (Rouse regime).

The results of the Rouse regime simulations are summarised in table 5.5 and plotted in figure 5.13, while the results of simulations in the moderately entangled regime ($D = 2$) are shown in table 5.6 and figure 5.14.

Shear Rate $[\times 10^3\, s^{-1}]$	Dewetting 1 $[ms]$	Dewetting 2 $[ms]$	Wetting $[ms]$	Expulsion $[ms]$
0.0	0.151	-	-	-
1.0	0.148	A1	A1	A1
2.0	0.141	1.023	1.103	1.127
3.0	0.135	0.723	0.789	0.800
4.0	0.130	0.575	0.784	A2
5.0	0.126	0.473	A3	A3
6.0	0.123	0.393	A3	A3
8.0	0.119	0.281	0.505	A2
10.0	0.116	A1	A1	A1

Table 5.5: Summary of times to the various stages of expulsion at a range of shear rates in a weakly segregated system ($\chi = 2.5$), in the Rouse regime ($D = 1$). A1, A2 and A3 denote alternative steady states where the particle is not fully expelled from the non-preferred phase (see figure 5.12). At shear rates of $\dot{\gamma} \gtrsim 12.0 \times 10^3\, s^{-1}$ the interface between the two liquid phases starts to become unstable under shear.

Comparing figures 5.13 and 5.14 with figures 3.13 and 4.8, the most striking

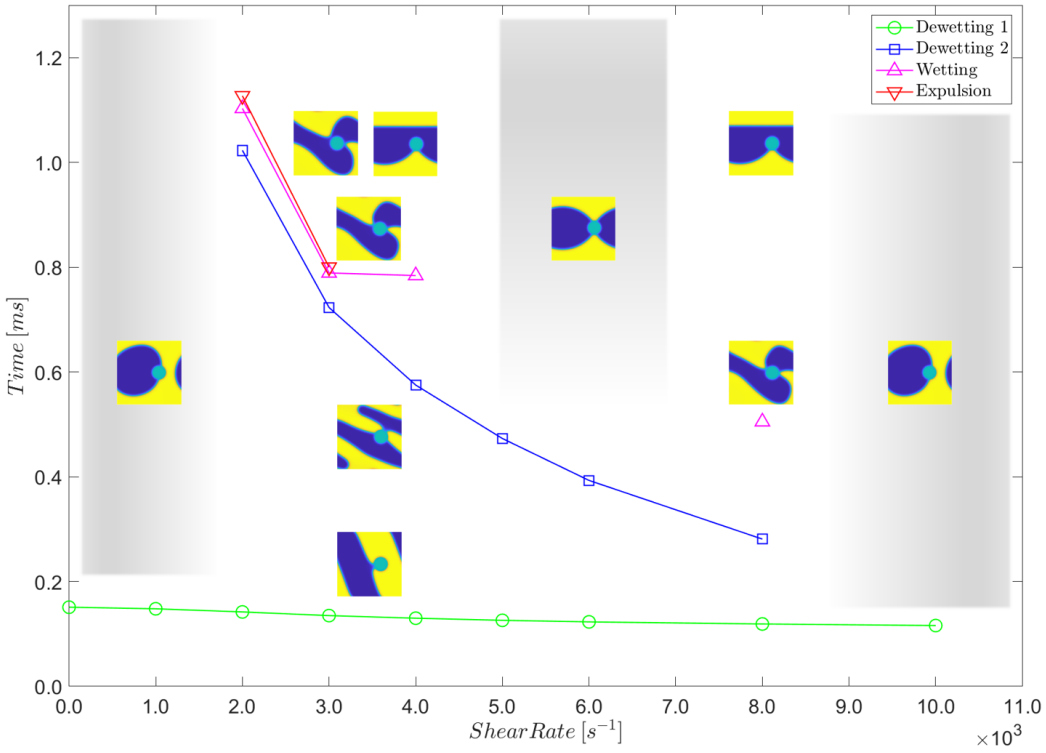

Figure 5.13: Stages of the expulsion process in a weakly segregated system ($\chi = 2.5$) at constant shear rates from $\dot{\gamma} = 1.0 \times 10^3\, s^{-1}$ to $\dot{\gamma} = 1.0 \times 10^4\, s^{-1}$. In all simulations, $D = 1$ and the initial distance of the particle from the central interface is $d = 8.5\, nm$.

Shear Rate $[\times 10^3\, s^{-1}]$	Dewetting 1 $[ms]$	Dewetting 2 $[ms]$	Wetting $[ms]$	Expulsion $[ms]$
0.0	1.044	-	-	-
0.125	1.036	15.48	16.00	16.16
0.250	1.000	A1	A1	A1
0.375	0.968	5.836	6.308	6.344
0.500	0.932	4.508	5.220	A2
0.625	0.904	3.672	A3	A3
0.750	0.884	3.044	3.684	A2
1.000	0.864	2.120	A3	A3
1.250	0.836	A1	A1	A1

Table 5.6: Summary of times to the various stages of expulsion at a range of shear rates in a weakly segregated system ($\chi = 2.5$), with moderate entanglement ($D = 2$). A1, A2 and A3 denote alternative steady states where the particle is not fully expelled from the non-preferred phase (see figure 5.12). Note that at shear rates of $\dot{\gamma} \gtrsim 12.0 \times 10^3\, s^{-1}$ the interface between the two liquid phases starts to become unstable under shear.

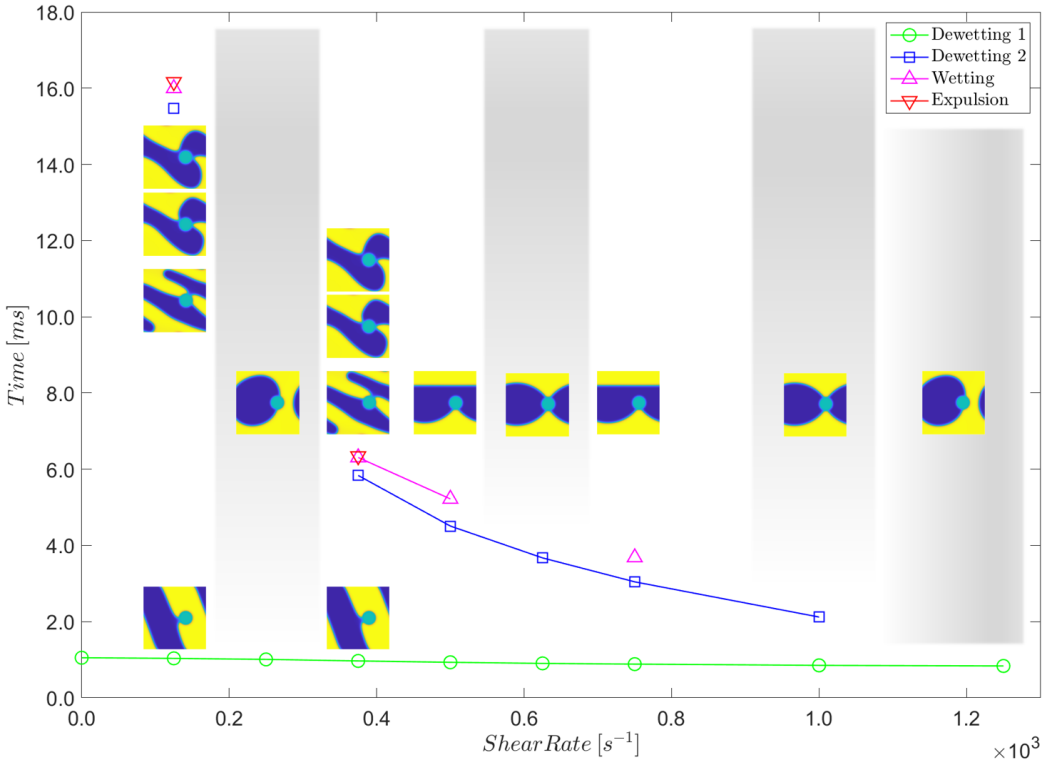

Figure 5.14: Stages of the expulsion process in a weakly segregated system ($\chi = 2.5$) at constant shear rates from $\dot{\gamma} = 0.25 \times 10^3\, s^{-1}$ to $\dot{\gamma} = 1.25 \times 10^3\, s^{-1}$. In all simulations, $D = 2$ and the initial distance of the particle from the central interface is $d = 8.5\, nm$.

difference is the complexity of the behaviour of the sheared system in the weakly segregated regime. Compared with the strongly segregated regime, we observe both a greater range of steady states, and less predictability in the steady state the system reaches. Regardless of the value of D, there are relatively few regions, in figures 5.13 and 5.14, where the same steady state is reached across a range of different shear rates. In contrast, in the strongly segregated regime, the particle is expelled from the non-preferred phase, across a range of higher shear rates, in both the Rouse regime, and the moderately entangled regime, when $D = 2$. We attribute the greater sensitivity of the weakly entangled system to the applied shear rate, and other parameters, to its more diffuse and delicate interface. It is natural to suppose that such an interface will be more sensitive to small changes in the variables and parameters used in the simulation, than will the sharply defined, high energy interface that is characteristic of the strongly segregated regime.

A common feature in both the strongly and weakly segregated regimes ap-

pears to be that increasing the effective diffusion coefficient, D, tends to lead to alternative steady states, in which the particle is not expelled from the non-preferred phase. In the strongly segregated regime, these alternative steady states are seen more frequently when $D = 5$ or $D = 10$ (recall that, in the latter case, we did not observe expulsion of the particle from the non-preferred phase, at any of the applied shear rates). In the weakly segregated regime, we observe alternative steady states (including the new steady state, in which the particle appears to adhere to two particles) even when $D = 2$. For example, at the same dimensionless shear rate of $\tilde{\dot{\gamma}} = 0.0002$, the particle is expelled into its preferred phase in the weakly segregated system in which $D = 1$ (physical shear rate: $\dot{\gamma} = 2.0 \times 10^3\, s^{-1}$), while it adheres to a droplet of its preferred phase in a mildly entangled ($D = 2$) version of the same system (physical shear rate: $\dot{\gamma} = 0.25 \times 10^3\, s^{-1}$). Interestingly, the reverse effect is observed when the dimensionless shear rate is $\tilde{\dot{\gamma}} = 0.0001$. However, broadly speaking, the complete migration of the particle across the central interface, and into its preferred phase, is less commonly observed in the weakly segregated system, when $D = 2$. In addition to being a point of contrast with results in the strongly segregated regime, this again illustrates the sensitivity of the eventual steady state, in a weakly segregated system, to the applied shear, and to the parameters used in the simulation.

Turning to a more detailed inspection of figure 5.13, we note the familiar presence of a first dewetting curve that is almost independent of the shear rate: because the initial distance of the particle from the central interface is just less than the critical film thickness, $d_c \sim 9.0\, nm$), diffusive effects tend to dominate and the applied shear rate has relatively little influence on the dewetting time. The complete migration of the particle from the non-preferred to the preferred phase is a relatively rare event, ocurring only at two of the lowest shear rates ($\dot{\gamma} = 2.0 \times 10^3\, s^{-1}$ and $\dot{\gamma} = 3.0 \times 10^3\, s^{-1}$). Similarly, the wetting of the particle, the penultimate stage of the expulsion process, is quite uncommon, and the particle often reaches one of the alternative steady states instead.

The most interesting contrast with the results from the strongly segregated regime results is seen in the second dewetting curve. Second dewetting does not occur at the upper and lower ends of the range of shear rates used. This is reminiscent of simulation results in the strongly segregated regime, where the steady state in which the particle adheres to a droplet of its preferred phase is common at lower and higher shear rates. However, in the strongly segregated regime, the time to the second dewetting (when it *does* occur) tends to decrease linearly with the shear rate. This is not surprising, since

the shear rate is constant, and we expect a higher shear rate to result in shorter dewetting times. In contrast, the second dewetting curve in figure 5.13 is clearly *not* linear. In fact, the second dewetting time appears to be approximately inversely proportional to the shear rate. We return to this point after reviewing the expulsion results in the weakly segregated system, when $D = 2$.

Finally, although it is not apparent in figure 5.13, at some shear rates, the sequence from first dewetting to final expulsion differs slightly from that in the strong segregation regime. In particular, sometimes, the second dewetting occurs *before* (or very close to the point at which) the central interface breaks. Figure 5.15 shows this alternative dewetting scenario when the shear rate is $\dot{\gamma} = 2.0 \times 10^3\, s^{-1}$.

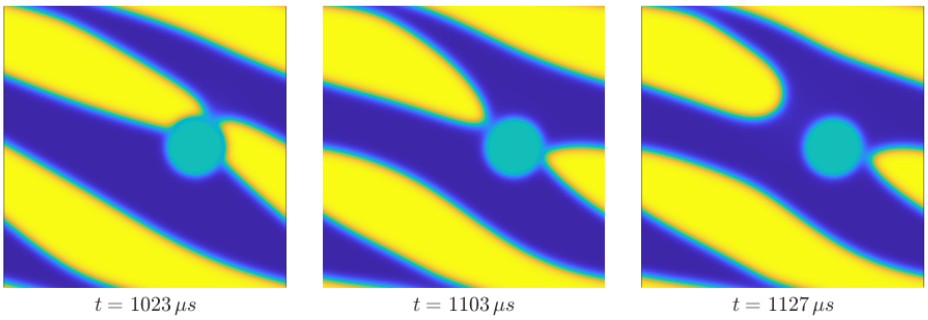

Figure 5.15: An unusual case of second dewetting. This occurs when the shear rate is $\dot{\gamma} = 2.0 \times 10^3\, s^{-1}$ and, as usual, $d = 8.5\,nm$. It differs from the usual case because the second dewetting *precedes* the breaking of the central interface as a result of shear stress. The second and third images show the wetting and expulsion of the particle into its preferred phase, respectively.

We attribute this effect to the greater initial distance of the particle from the central interface in these simulations ($8.5\,nm$, compared with $4.5\,nm$ in simulations of the strongly segregated regime), which means that the particle is closer to the interface between the two liquid phases, *before* it breaks and retracts. It is possible that the more diffuse central interface in the weakly segregated regime also plays a role, but we expect this to be a relatively small effect.

The results in the weakly segregated regime when the effective diffusion coefficient, $D = 2$ (figure 5.14) are similar to the corresponding results in the Rouse regime (figure 5.13). The main difference is that, at most shear rates,

the expulsion process is arrested at an earlier stage, leading to a greater diversity in the steady states reached, and greater fragmentation of the four curves plotted, for each set of simulations. Despite this fragmentation, the approximate inverse proportionality between the second dewetting time and the shear rate appears to survive the transition to the moderately entangled regime.

To probe this relationship further, let us assume a power law of the form, $t_2 = A\dot{\gamma}^n$, where t_2 is the time at which second dewetting occurs, and A and n are numerical constants, the former having appropriate dimensions, and the latter being dimensionless. It is apparent from figures 5.13 and 5.14 that n must be negative, and we assume that, if it were physically possible to sustain an arbitrarily high shear rate, the second dewetting time, t_2, would approach zero (as would all other times associated with the stages of expulsion). Figure 5.16 is a log-log plot of the second dewetting data for the weakly segregated system in both the Rouse regime ($D = 1$) and the moderately entangled regime ($D = 2$).

Note that, here, we treat t_2 (measured in μs) as dimensionless, through implicit multiplication by a quantity of appropriate dimensions (μs^{-1}), and magnitude unity. In a similar fashion, the shear rate, $\dot{\gamma}$, is also treated as a dimensionless quantity.

Figure 5.16 shows that the power law model is an excellent fit in both the Rouse regime, and the moderately entangled regime, with $R^2 > 0.99$ in both cases, meaning that more than 99% of the variation in $ln(t_2)$ can be accounted for by the variation in $ln(\dot{\gamma})$. Moreover, the two lines of best fit are almost identical. This shows that changing the effective diffusion coefficient, D, enables us, among other things, to access a different range of shear rates, while leaving the fundamental dynamics of the system more or less unchanged.

However, the fact that the two lines of best fit don't quite coincide indicates that varying D subtly changes the dynamics of the system. We saw this in the previous chapter, in our discussion of the simple geometrical model of dewetting. There, we discovered that, for any given dimensionless shear rate, changing the value of D subtly affects the way in which the central interface between the two liquid phases deforms, resulting in a lower shear strain at the *first* dewetting point, at higher values of D (figures 4.17 and 4.18). In the master dewetting plot (figure 4.13), this gives rise to a band of dewetting curves (one for each value of D) at each dimensionless shear rate.

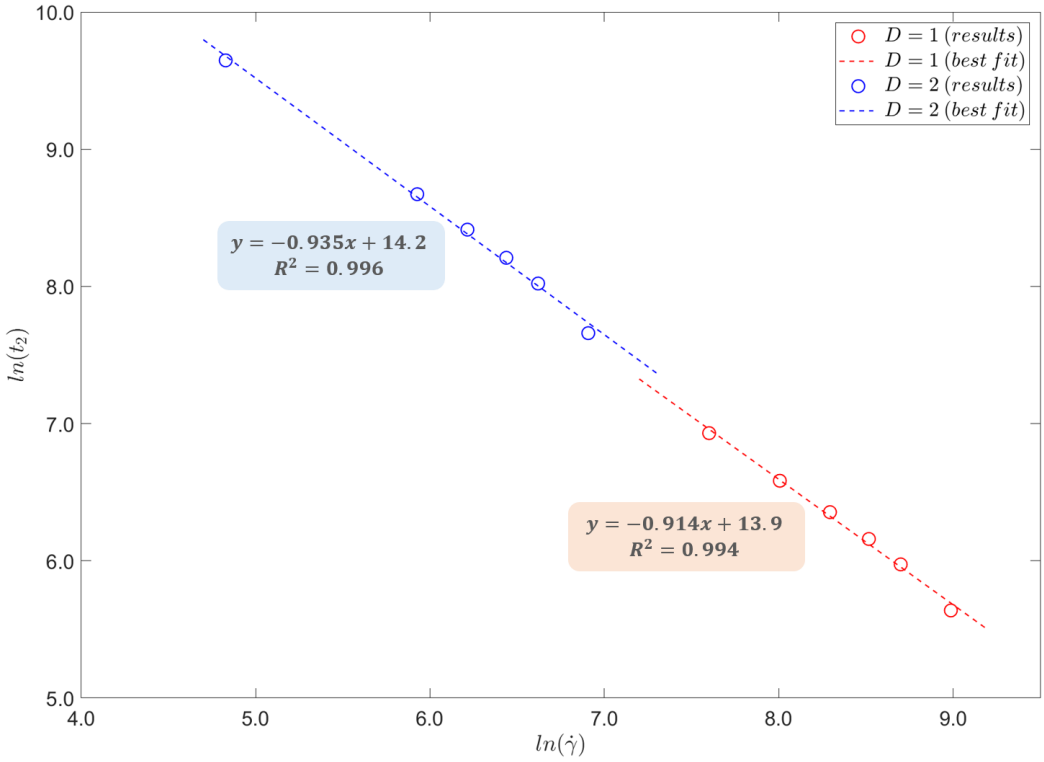

Figure 5.16: Plots of $ln(t_2)$ against $ln(\dot{\gamma})$ in a weakly segregated system, where t_2 is the time at which second dewetting occurs, and both quantities are treated as dimensionless. Plots are shown for both $D = 1$ and $D = 2$, and lines of best fit are marked for each dataset. The lines of best fit indicate a power law relationship between t_2 and $\dot{\gamma}$.

We believe the appearance of two distinct but, similar, lines of best fit in figure 5.16 is an example of the same phenomenon. Taking mean values of the coefficients from these two lines, we may say that the relationship between the second dewetting time and the shear rate is a power law, of the form, $t_2 \approx 1.26\,\dot{\gamma}^{-0.925}$, where, for presentational simplicity, t_2 is now measured in seconds, and appropriate units are implied in the numerical factor on the right hand side. Thus, as suspected, the time at which second dewetting occurs in this weakly segregated system is almost inversely proportional to the applied shear rate.

The reason for this apparent relationship of near-inverse proportionality, and the contrast with near-linear second dewetting curves we observe in the strongly segregated regime is not clear. One hypothesis is that the time at which the central interface breaks, under shear stress, influences the form of the relationship between the second dewetting time and the shear rate (recall that second dewetting usually occurs after the interface breaks). As a matter

of fact, in the weakly segregated regime, this breaking of the central interface tends to occur at a lower shear strain than it does in a strongly segregated system, and the shear strain at breaking depends on the shear rate. Figure 5.17 illustrates this point, contrasting a strongly segregated system in the Rouse regime, with a weakly segregated system, also in the Rouse regime, that is sheared at two different rates.

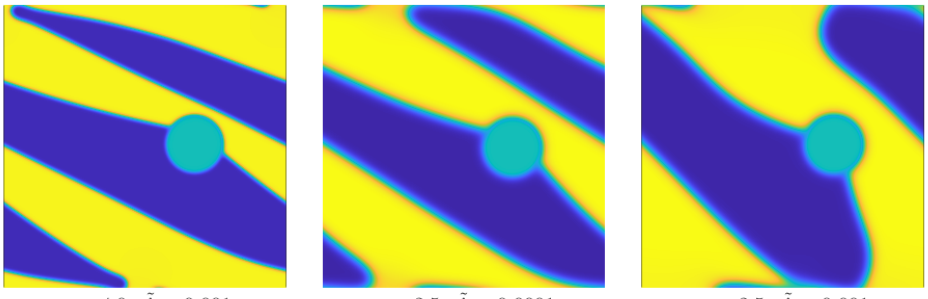

Figure 5.17: Breaking of the central interface in a strongly segregated system ($\chi = 4.0$) and in a weakly segregated system ($\chi = 2.5$) at two different shear rates. The dimensionless shear rates shown correspond with physical shear rates of $\dot{\gamma} = 1.0 \times 10^4\, s^{-1}$, $\dot{\gamma} = 1.0 \times 10^3\, s^{-1}$ and (again) $\dot{\gamma} = 1.0 \times 10^4\, s^{-1}$, respectively. All three simulations take place in the Rouse regime, in which $D = 1$. The initial distance of the particle from the central interface is $d = 9.0\, nm$ in the first image, and $d = 8.5\, nm$ in the second and third images.

The shear strain in the strongly segregated system, just after the central interface breaks is $\gamma \sim 2.5$, while the shear strain in the weakly segregated system is $\gamma \sim 1.7$ at the lower shear rate, and $\gamma \sim 1.6$ at the higher rate. However, it is hard to see how this effect, in itself, could give rise to the relationship we see in figure 5.16.

Another possibility is that this relationship is a mathematical coincidence, but the high R^2 value for both the the Rouse regime data, and the data from the moderately entangled regime, makes it difficult to defend this claim. Nevertheless, this idea is on the right lines, as may be seen by revisiting the second dewetting data from the strongly segregated regime when $D = 1$ and $D = 2$. Figure 5.18 plots this data using the same method as figure 5.16. Although the fit is not quite as good as it is for the same data in the weakly segregated regime, it is clear that a power law, with an exponent of $n \approx -1.2$ is an excellent fit ($R^2 \approx 0.97$) for the second dewetting data in the strongly segregated regime.

On reflection, this is not so surprising. Although there are more confounding

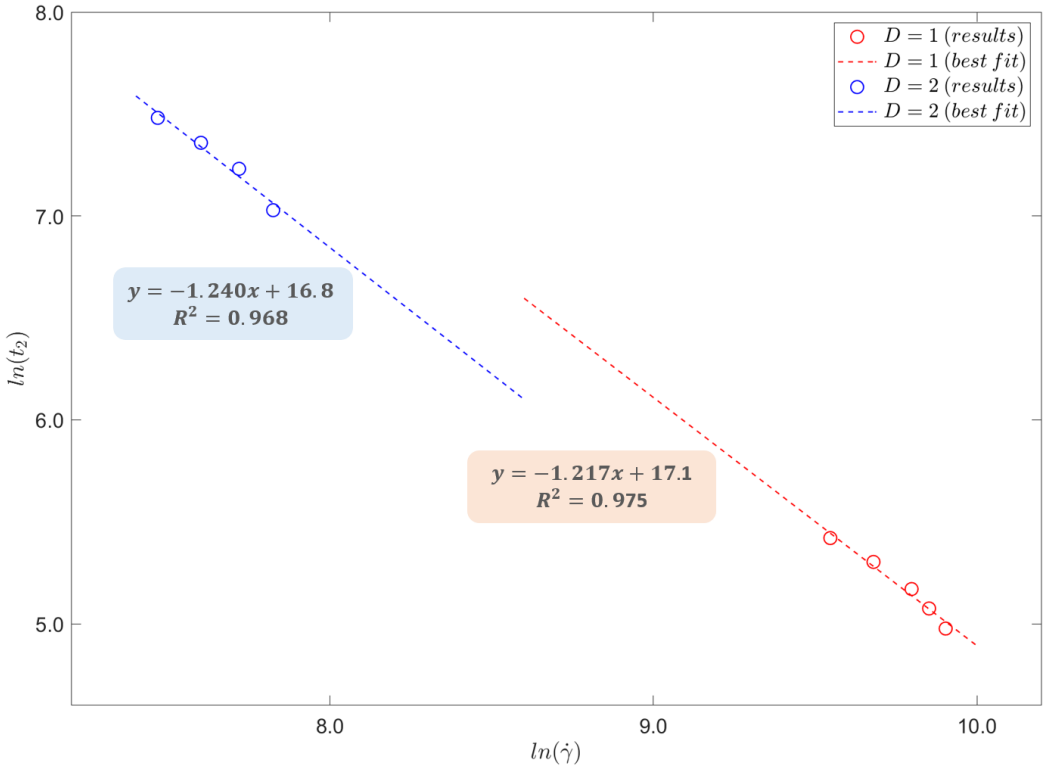

Figure 5.18: Plots of $ln(t_2)$ against $ln(\dot{\gamma})$ in a strongly segregated system, where t_2 is the time at which second dewetting occurs, and both quantities are treated as dimensionless. Plots are shown for both $D = 1$ and $D = 2$, and lines of best fit are marked for each dataset. The lines of best fit indicate a power law relationship between t_2 and $\dot{\gamma}$.

factors - notably, the timing of the breaking of the central interface - these results are reminiscent of the first dewetting results summarised in section 4.6 (which we revisit, in the weakly segregated regime, in section 5.6). The tight banding of the dewetting curves in figures 4.13 and 4.20 indicates that, for a given initial distance, d, of the particle from the central interface, and a given dimensionless shear rate, $\tilde{\dot{\gamma}}$, the shear strain at the first dewetting point is almost constant. Since the shear strain at the first dewetting point is the product of the first dewetting time and the shear rate, this is equivalent to saying that the former is (almost) inversely proportional to the latter. In section 4.6, we saw how this could be explained by a geometrical model, in which the central interface shears linearly, until its distance from the surface of the particle approaches a critical distance, e, when dewetting occurs rapidly, compared with the time scale over which the system is sheared.

The second dewetting results, in both the strongly and weakly segregated regimes, are similar in that they imply the shear strain of the system at the

second dewetting point is almost constant. This then gives rise to the near inverse proportionality between t_2 and $\dot{\gamma}$ we observe in these results. The deviation from inverse proportionality is due to the confounding factors alluded to above. Although we do not attempt this here, it might be possible to construct a model of the second dewetting process, similar to the geometrical model of the first dewetting process, in which the second dewetting times are explained by the linear shearing of the system, up to the breaking of the central interface, after which second dewetting occurs relatively quickly, as the region of the preferred phase retracts and makes contact with the surface of the particle. We believe that such a model could ultimately account for the near inverse proportionality between t_2 and $\dot{\gamma}$. This conclusion highlights the danger of attempting to deduce a mathematical relationship between two variables from a visual inspection of a plot of one against the other: although the second dewetting curves in the strongly segregated regime *look* linear, the underlying logic should lead us to expect a relationship of inverse proportionality. It is an interesting question why the true form of this relationship is so much more apparent in the weakly segregated regime, but we do not pursue this here.

As in previous chapters, we end this section with plots of the mean free energy density, as the system is sheared up to, and just beyond, the first dewetting point. Figures 5.19 and 5.20 show the evolution of the mean free energy density in the weakly segregated system when $D = 1$ and $D = 2$, respectively.

These figures have much in common with the corresponding figures in previous chapters, so we omit the detailed description of the mean free energy density curves here. However, there are some interesting differences. Firstly, the curves are significantly smoother at the dewetting point than are the same curves in strongly segregated systems; in fact, at the lowest shear rate, it is quite hard to discern the point at which the mean free energy decreases, as dewetting occurs. This is another example of the relatively broad, diffuse interface in the weakly segregated system resulting in more gradual dynamics. The second difference is that, at the highest shear rate, there is a further, large decrease in the mean free energy density, *after* the dewetting point, in the weakly segregated system. Examination of the state of the system at this time reveals that this is the point at which the central interface begins to break. This is further confirmation of the fact that the lower energy, more delicate interface in a weakly segregated system tends to break at a lower level of shear strain than its counterpart in a strongly segregated system.

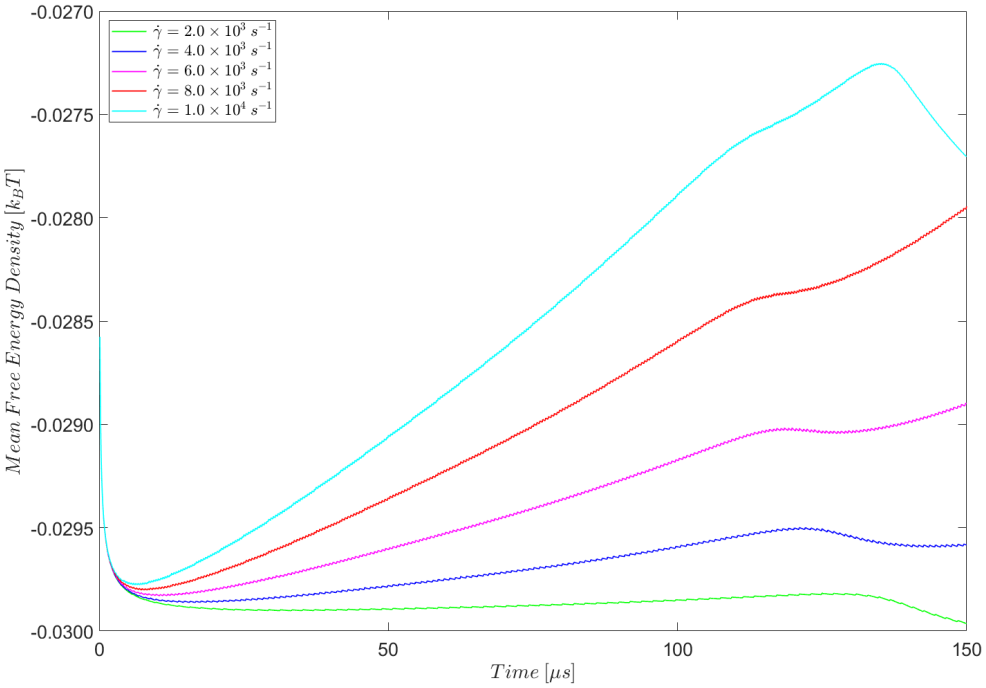

Figure 5.19: Evolution of the mean free energy density under shear in a weakly segregated system up to, and just beyond, the first dewetting point for $\dot{\gamma} = 2.0 \times 10^3\, s^{-1}$ to $\dot{\gamma} = 1.0 \times 10^4\, s^{-1}$. In all cases, $D = 1$ (Rouse regime), $\chi = 2.5$ (weak segregation) and the initial distance of the particle from the central interface is $d = 8.5\, nm$. The sudden decrease in the mean free energy density at the highest shear rate, when $t \approx 135\, \mu s$ is due to the central interface beginning to break under shear stress.

Finally, it is interesting to compare the the mean free energy density in the early stages of the evolution of the system, for all three values of the Flory-Huggins interaction parameter, χ, used in our simulations (figure 5.21).

Note that, when considering the effect of varying the Flory-Huggins interaction parameter, it is the *magnitude* of the mean free energy density that matters. Thus, figure 5.21 appears to show the mean free energy density increasing, at all three values of χ although, physically, the mean free energy density becomes more negative, over time (also, practically, the log scale used requires positive values). Figure 5.21 is interesting because it shows how sensitive the mean free energy density is to changes in the Flory-Huggins interaction parameter. In fact, the absolute value of the mean free energy density increases by roughly an order of magnitude when we increase χ from 2.1 to 2.5, and then increases by another order of magnitude when χ increases from 2.5 to 4.0.

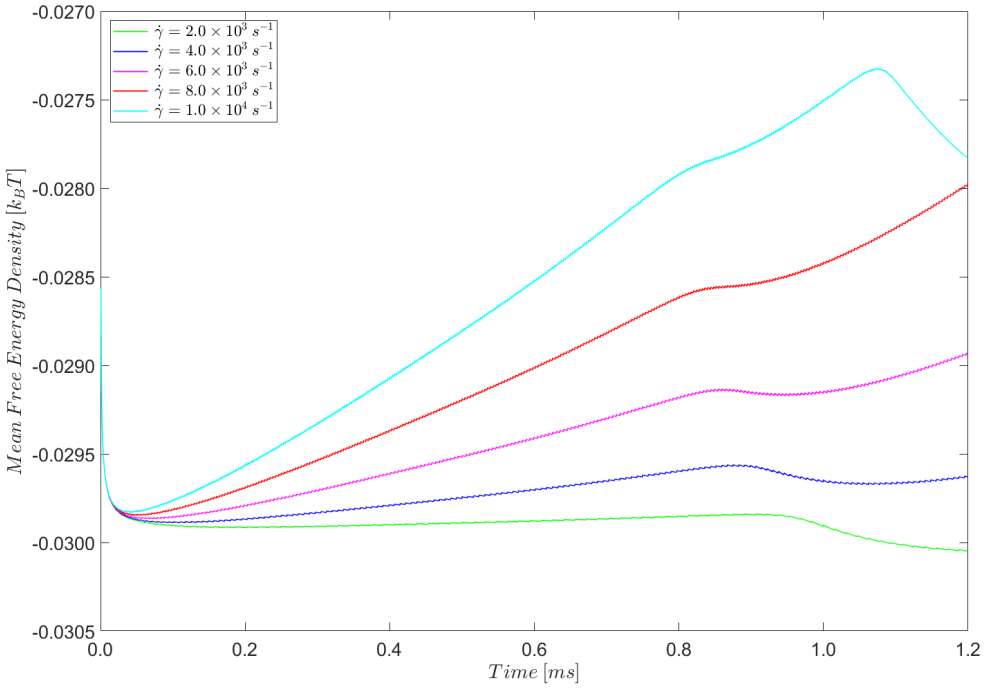

Figure 5.20: Evolution of the mean free energy density under shear in a weakly segregated system up to, and just beyond, the first dewetting point for $\dot{\gamma} = 2.0 \times 10^3\, s^{-1}$ to $\dot{\gamma} = 1.0 \times 10^4\, s^{-1}$. In all cases, $D = 2$ (moderate entanglement), $\chi = 2.5$ (weak segregation) and the initial distance of the particle from the central interface is $d = 8.5\, nm$. The sudden decrease in the mean free energy density at the highest shear rate, when $t \approx 1.1\, ms$ is due to the central interface beginning to break under shear stress.

Therefore, it is not surprising that the particle behaves so differently in a weakly segregate system when the system is sheared. There is much less free energy available for use in the system, compared with an otherwise identical system in the strongly segregated regime. The overall effect is that it becomes more difficult to expel the particle from its non-preferred phase. This effect is compounded by the generally lower shear rates, necessary to ensure that the diffuse and delicate central interface of the weakly segregated system remains stable, as it is sheared.

5.6 The Geometry of Dewetting Revisited

To close this chapter, we revisit the geometrical model of dewetting we introduced to clarify the results of our simulations in the strongly segregated regime. Can this geometrical model shed light on dewetting behaviour in

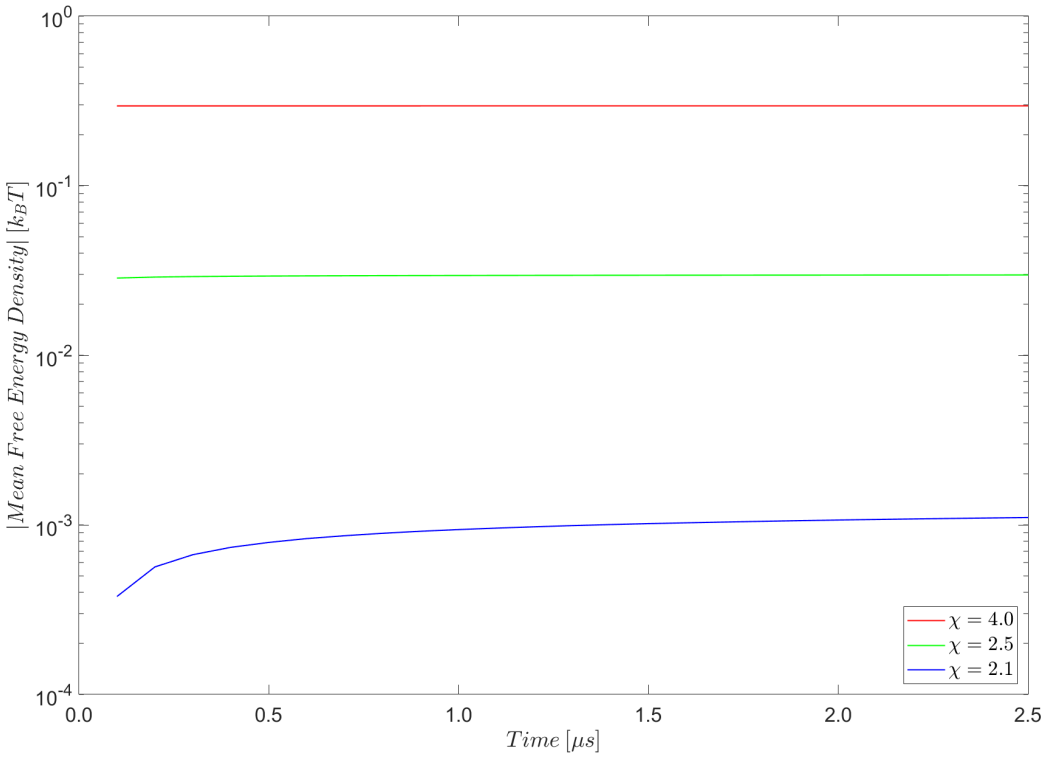

Figure 5.21: Magnitude of the mean free energy density in the early stages of our dewetting simulations, with various values of the Flory-Huggins interaction parameter, χ. In all cases, the system is quiescent and the particle is initially located $d = 5.0\,nm$ from the central interface. Note that the interface equilibrates in all three stages but this is only apparent for the lowest value of $\chi = 2.1$ due to the scaling of the y-axis.

weakly segregated systems?

The data from the weakly segregated regime is relatively limited, since we only have simulation results for two values of the effective diffusion coefficient, D, rather than the four sets of results available in the strongly segregated regime. However, there is enough data to observe many similarities between the two regimes, as the dewetting master plot for the weakly segregated systems we have studied shows (figure 5.22).

As in the previous chapter, we plot the shear strain at the first dewetting point against the initial distance of the particle from the central interface, at two dimensionless shear rates ($\tilde{\dot{\gamma}} = 0.0002$ and $\tilde{\dot{\gamma}} = 0.0008$) and for the two values of D used in the simulations ($D = 1$ and $D = 2$). Figure 5.22 also shows the predictions of the geometrical model. The solid black line is predicted by the naive version of the model, in which dewetting occurs

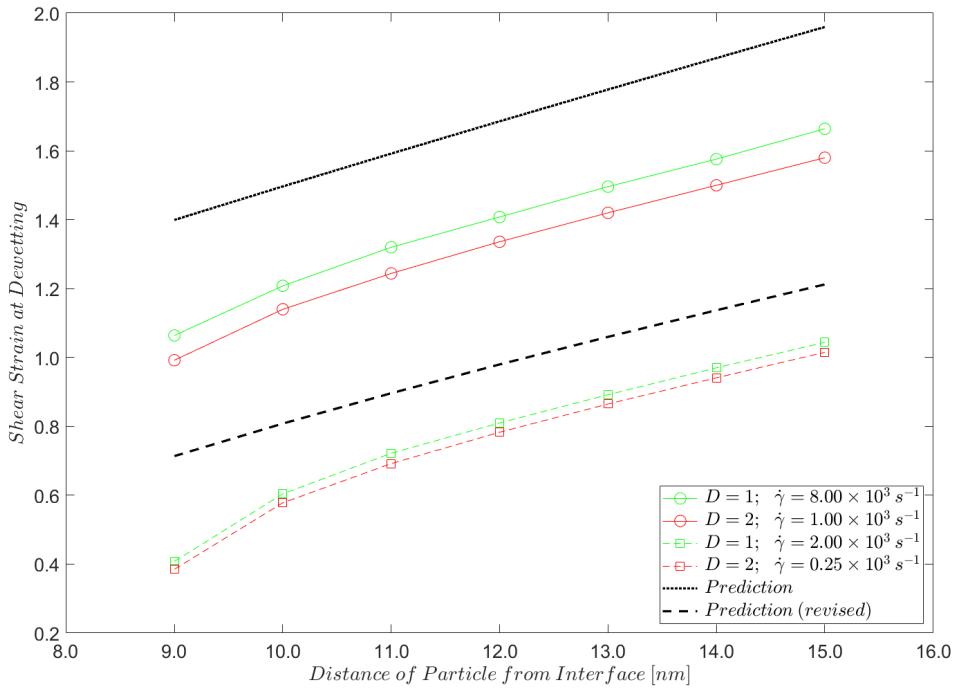

Figure 5.22: Dewetting master plot showing the shear strain at which dewetting occurs, as the distance of the particle from the central interface varies. Shown are the data points when $D = 1$ and $D = 2$. The two bands represent the upper and lower ends of the range of dimensionless shear rates used in the simulations ($\tilde{\dot{\gamma}} = 0.0008$ and $\tilde{\dot{\gamma}} = 0.0002$). The physical value of the shear rate varies, according to the value of the effective diffusion coefficient, D. The predicted values are those of the simple geometrical model described in section 4.6, and represented in figures 4.12 and 4.19. The revised predicted values come from the modified geometrical model, with parameter $e = 5.0\,nm$.

when the sharply defined interface is just tangential to the surface of the particle. The dashed black line is the prediction of the revised model in which dewetting occurs almost instantaneously, compared with the time scale over which the system is sheared, when the distance between the central interface and the surface of the particle is equal to some length scale, e. Based on dewetting curves shown earlier in this chapter (figures 5.10 and 5.11) we have chosen $e = 5.0\,nm$. This already contrasts with the strongly segregated regime in which we set $e = 3.0\,nm$.

It is clear that figure 5.22 shares many features with the dewetting master plot for the strongly segregated regime (figure 4.20). Firstly, there is a distinct band of dewetting curves associated with each value of the dimensionless shear rate used in the simulations. Furthermore, the higher dimensionless shear rate is associated with the higher band: so, for a given initial distance

of the particle from the central interface, dewetting occurs later, as measured by the shear strain of the system, at the higher shear rate. Within each band, the curve corresponding with the lower value of $D = 1$ is higher than the curve corresponding with the higher value of $D = 2$. Despite the limited data sample, this is consistent with the pattern observed in the strongly segregated regime, and we are confident that the full pattern would be repeated, if data for more values of D were available.

To account for these features of the dewetting master plot, we repeat the analysis of the previous chapter, considering each of the three key assumptions of the simple geometrical model in turn:

Assumption 1: The particle is immobile. It does not move under the influence of hydrodynamic, or other forces.

Assumption 2: The central interface shears linearly and, in any given small increment of time, instantaneously.

Assumption 3: Dewetting occurs when the interface between the two phases in the system is tangential to the surface of the particle, and not before.

The first assumption is not true of our simulations, in which the particle is free to move. Figures 5.23 and 5.24 show the extent of this movement when the initial distance of the particle from the central interface is $d = 10.0\,nm$ and $d = 15.0\,nm$, respectively. The trajectory of the particle is shown up to the point of the first dewetting, for various combinations of the dimensionless shear rate and the effective diffusion coefficient used in the simulations.

Figures 5.23 and 5.24 resemble the corresponding figures in the strongly segregated regime, in that they show a general tendency of the particle to move first rightwards, and then upwards, as the the system is sheared, and approaches its first dewetting point. This is consistent with our previous hypothesis that, initially, the particle only "sees" movement of the central interface in the x-direction. It is only when the system is under a certain amount of shear strain that the vertical distance between the central interface and the bottom surface of the particle begins to decrease, pushing it upwards in the y-direction. Further support for this hypothesis comes from the fact that, typically, the movement in the x-direction is greater in figures 5.23 and 5.24, than it is in the figures that illustrate the trajectory of the particle in the strongly segregated regime. This is most likely due to the fact that the initial distance of the particle from the central interface is greater in the

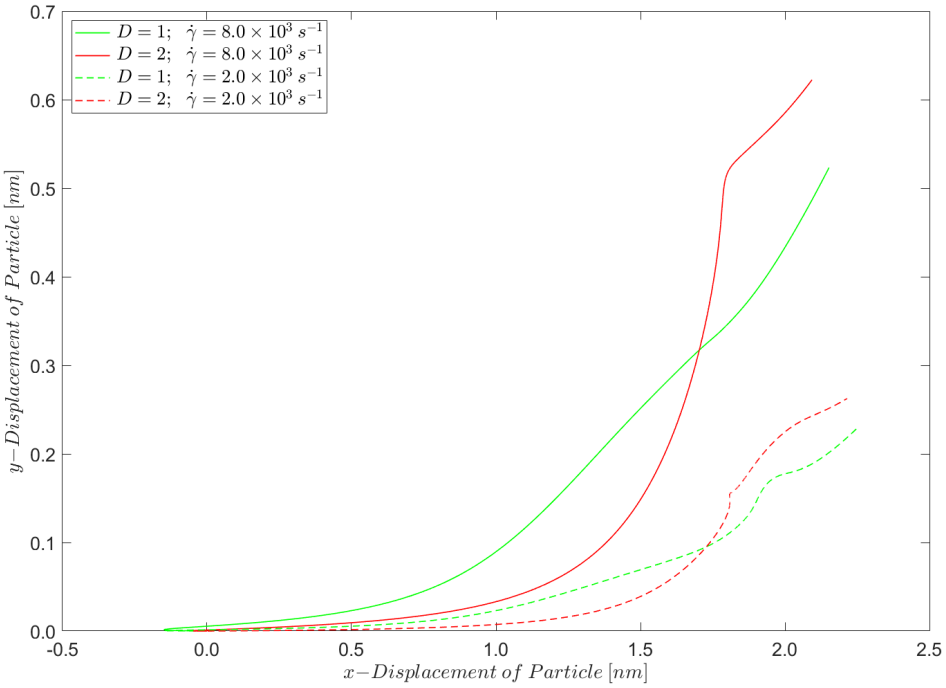

Figure 5.23: Displacement of the particle, relative to its initial position ($d = 10.0\,nm$ from the central interface between the phases) up to the point of first dewetting. The particle trajectory is shown for $D = 1$ and $D = 2$, and for the the upper and lower end of the range of dimensionless shear rates used in the simulations ($\tilde{\dot{\gamma}} = 0.0002$ and $\tilde{\dot{\gamma}} = 0.0008$). The physical value of the shear rate varies, according to the value of the effective diffusion coefficient, D.

simulations we have chosen to represent the weakly segregated regime, so it takes longer for the central interface's influence in the y-direction to be felt by the particle.

A point of contrast with the earlier simulations is that the transition, in the particle's trajectory, from movement in the x-direction, to movement in the y-direction is more gradual in weakly segregated systems, than it is in their strongly segregated counterparts. This might be another effect of the broader, more diffuse central interface that is characteristic of the weakly segregated system; intuitively, the particle will "feel" the approach of such an interface sooner than it would, if the interface were more sharply defined, as it is in the strongly segregated regime. The effect here is similar to the gradual transition from the diffusive to the hydrodynamic regime in the dewetting curves (figures 5.10 and 5.11), and the underlying mechanism is likely to be the same.

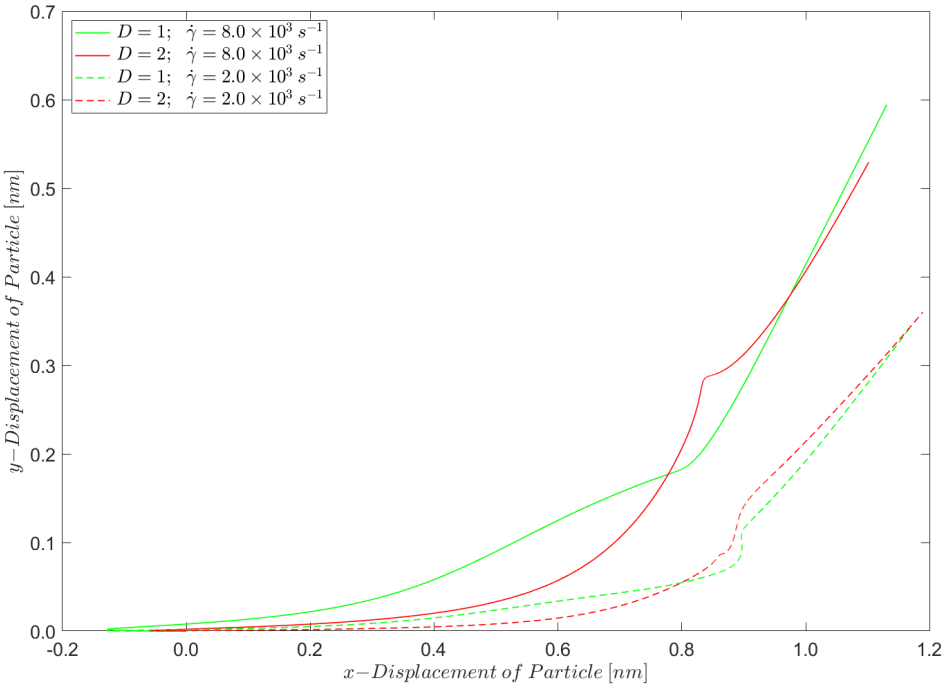

Figure 5.24: Displacement of the particle, relative to its initial position ($d = 15.0\,nm$ from the central interface between the phases) up to the point of first dewetting. The particle trajectory is shown for $D = 1$ and $D = 2$, and for the the upper and lower end of the range of dimensionless shear rates used in the simulations ($\tilde{\dot{\gamma}} = 0.0002$ and $\tilde{\dot{\gamma}} = 0.0008$). The physical value of the shear rate varies, according to the value of the effective diffusion coefficient, D.

Turning to the second key assumption of the geometrical model, that the deformation of the central interface, under shear, is perfectly linear, we see that this is not the case in figure 5.25, which shows the state of the system at 100% shear strain ($\gamma = 1.0$) at the lower and higher shear rates used in our dewetting simulations of a weakly segregated system in the Rouse regime ($D = 1$).

The third image in figure 5.25 shows the difference in the order parameter (the "delta"), at every point in the system. It is clear, by inspection alone, that the deformation of the central interface at the higher shear rate deviates significantly from the perfectly linear form assumed in the geometrical model, and the image of the delta in figure 5.25 merely emphasises the point. Thus, the central interface of our weakly segregated system behaves, at higher shear rates, in the same way as the interface in a strongly segregated system, and the argument used in the previous chapter may be used to explain the existence of two distinct bands of dewetting curves in figure 5.22.

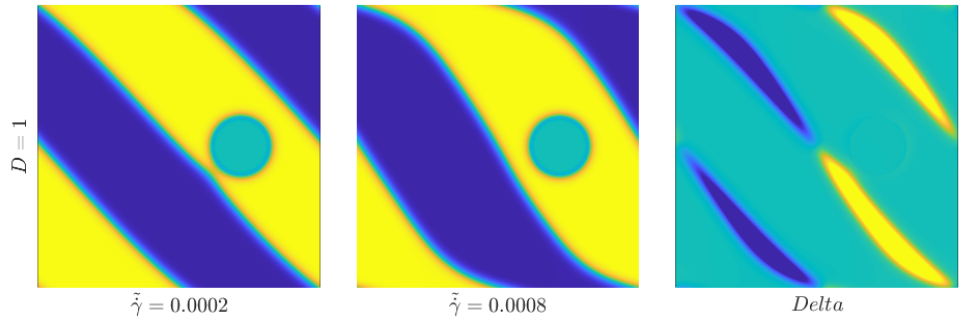

Figure 5.25: The state of the system at 100% shear ($\gamma = 1.00$) when the dimensionless shear rate is $\tilde{\dot{\gamma}} = 0.0002$ and $\tilde{\dot{\gamma}} = 0.0008$. In both cases, $D = 1$ and the initial distance of the particle from the central interface is $d = 15.0\,nm$. The third image represents the difference in the order parameter at every point in the system (the "delta" of the first two images).

Just as in the strongly segregated regime, a similar analysis can account for the *ordering* of dewetting curves, within each band (figures 5.26 and 5.27).

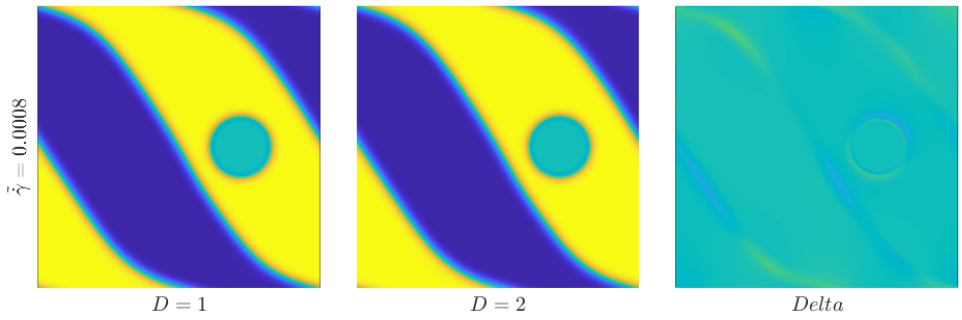

Figure 5.26: The state of the system at 100% shear ($\gamma = 1.00$) when the effective diffusion coefficient is $D = 1$ and $D = 2$. In both cases the dimensionless shear rate is $\tilde{\dot{\gamma}} = 0.0008$, and the initial distance of the particle from the central interface is $d = 15.0\,nm$. The third image represents the difference in the order parameter at every point in the system (the "delta" of the first two images). For clarity, the contrast in the third image has been increased.

Now, we vary the effective diffusion coefficient, D, and observe the delta when the shear strain of $\gamma = 1.0$, at each of the two dimensionless shear rates used in these simulations. Again, the results strongly resemble those in the strongly segregated regime, although the effect is much harder to detect in a weakly segregated system. The relative weakness of the effect,

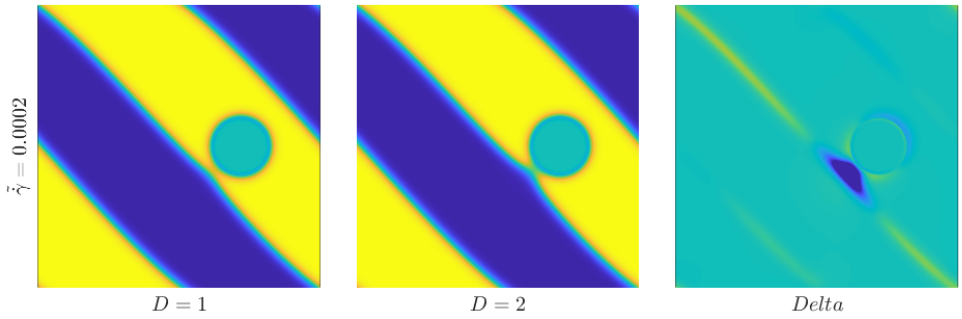

Figure 5.27: The state of the system at 100% shear ($\gamma = 1.00$) when the effective diffusion coefficient is $D = 1$ and $D = 2$. In both cases the dimensionless shear rate is $\tilde{\dot{\gamma}} = 0.0002$, and the initial distance of the particle from the central interface is $d = 15.0\,nm$. The third image represents the difference in the order parameter at every point in the system (the "delta" of the first two images). For clarity, the contrast in the third image has been increased.

in the weakly segregated system, necessitates increasing the contrast in the image of the delta, by compressing the colour scale used in the third image of both figures 5.26 and 5.27. A minor quirk, at the lower dimensionless shear rate, is that a shear strain of $\gamma = 1.0$ coincides with the onset of dewetting. It is clear in figure 5.27 that the dewetting process is slightly more advanced in the moderately entangled system, in which $D = 2$, than it is in the system in the Rouse regime. This is a vivid illustration of the fact, previously observed in the strongly entangled regime, that, at a given dimensionless shear rate, dewetting occurs at lower shear strains, as the degree of entanglement increases.

The third key assumption of the geometrical model is that dewetting occurs when the sheared central interface is just tangential to the surface of the particle. This is inconsistent with the physics of the dewetting process, which tends to occur much sooner (i.e. at lower shear strain) than the naive geometrical model implies. To some degree, figure 5.22 pre-empts this point by already showing the predictions of the revised geometrical model, which incorporates the parameter e, the length scale at which dewetting occurs almost instantaneously. What is striking about figure 5.22 is the amount by which the predictions of the naive geometrical model exceed the actual shear strain at dewetting that we observe in our simulations. This contrasts sharply with the dewetting master plot for the strongly segregated regime, in which the the curve predicted by the naive geometrical model fell within one of the bands of dewetting curves observed in our simulations. As it happens,

this was the incorrect band, but the revised geometrical model corrected this error and predicted a curve that was broadly in line with the simulation results.

The same strategy, of revising the geometrical model by introducing the parameter e is not nearly so successful in the weakly entangled regime. To bring the geometrical model into line with the simulation results, its revised predictions would have to lie in the vicinity of the lower band of dewetting curves shown in figure 5.22, since the lower dimensionless shear rate used in this set of simulations deforms the central interface in a near-linear fashion. Instead, the predictions of the revised geometrical model lie above the lower band of dewetting curves in figure 5.22: in simulations, at lower shear rates, dewetting occurs at significantly lower levels of shear strain than are predicted by even our revised model.

Again, it is likely that the explanation for this effect lies in the broader, more diffuse interface observed in weakly segregated systems. The parameter e, in the revised geometrical model, tries to take account of the width of the central interface between the liquid phases, and it appears to do this adequately when the interface is narrow and sharp, as it is in the strongly segregated regime. However, as the central interface becomes broader and more diffuse, the particle will feel the effect of its approach sooner, even if this effect is quite weak at lower levels of shear strain in the system. The strength of this effect will increase as shear brings the central interface closer to the particle until, eventually, dewetting occurs rapidly, when the distance separating the two is $\sim e = 5.0\,nm$. But the important point is that, in a weakly segregated system, there is a gradual build up to this moment, during which the influence of the broader, diffuse central interface has a cumulative effect. A complete model of this process would describe the physics of the dewetting process in greater depth, and integrate the influence of the broad, diffuse interface over the interval between the start of the simulation and the dewetting point. However, we consider this to be beyond the scope of the present work.

Instead, we consider the simpler question of how the parameter e should be adjusted to bring the predictions of the revised geometrical model into agreement with the simulation results at the lower shear rate. It turns out that a value of $e \approx 7.0\,nm$, gives the best fit with the simulation results (figure 5.28). We may, if we wish, think of this as the effective width, e', of the the central interface in the weakly segregated system when $\chi = 2.5$, and it is reassuring to note that, physically, this is a realistic value [130].

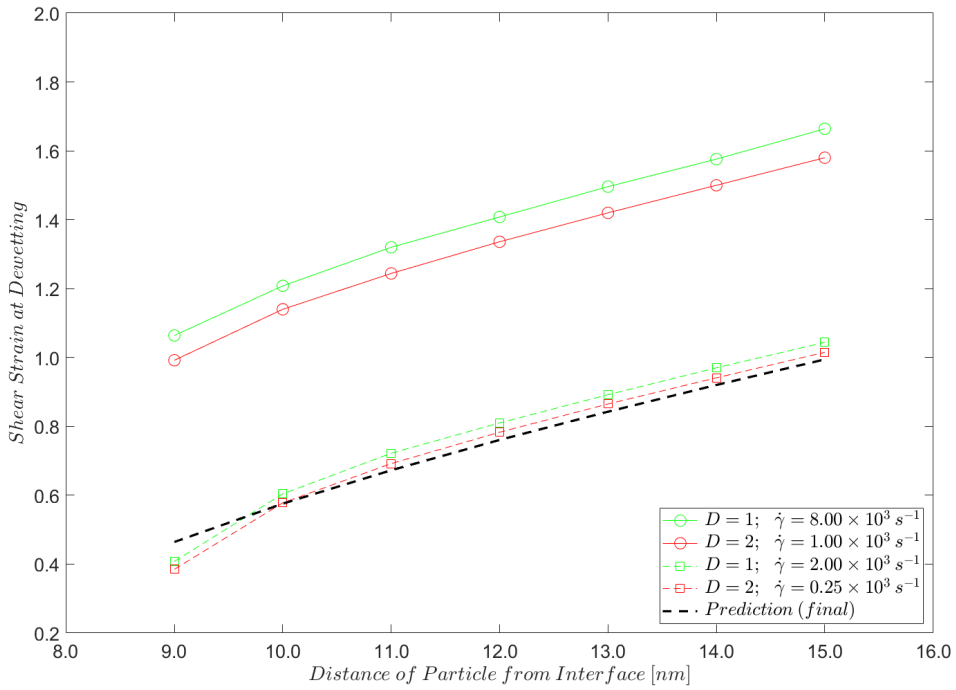

Figure 5.28: Dewetting master plot showing the shear strain at which dewetting occurs, as the distance of the particle from the central interface varies. Shown are the data points when $D = 1$ and $D = 2$. The two bands represent the upper and lower ends of the range of dimensionless shear rates used in the simulations ($\tilde{\dot{\gamma}} = 0.0008$ and $\tilde{\dot{\gamma}} = 0.0002$). The physical value of the shear rate varies, according to the value of the effective diffusion coefficient, D. The predicted values are those of the simple geometrical model described in section 4.6, and represented in figures 4.12 and 4.19, now revised to include an effective interface width of $e' = 7.0\,nm$.

5.7 Summary

We began the chapter with a review of the practical difficulties that arise when we try to simulate the behaviour of a weakly segregated system with $\chi = 2.1$. Most of these stem from the physical nature of such a system. For example, the broad and diffuse interface between the two liquid phases in the system makes it hard to discern the dewetting point, and the low free energy density of the interface makes it delicate, and susceptible to instability at higher shear rates. These physical difficulties are compounded by the use of periodic boundary conditions in the implementation of our model, which risks confounding the results of dewetting simulations as the initial distance of the particle from the central interface increases. This motivates the study of a less weakly segregated system, in which $\chi = 2.5$.

The results of dewetting simulations for this system show many similarities with the corresponding results in the strongly segregated regime. The main difference is that the transition from the regime in which diffusive effects dominate, to the hydrodynamic regime, in which, at a given shear rate, the dewetting time tends to increase linearly with the initial distance of the particle from the central interface is notably more gradual in the weakly segregated regime. We attribute this to the broader, more diffuse interface. Also of note is that the critical film thickness in the weakly segregated regime, when $\chi = 2.5$ is $d_c \sim 9.0\,nm$, almost double its value of $d_c \sim 5.0\,nm$ in the strongly segregated regime with $\chi = 4.0$.

The migration, under shear, of the particle from its non-preferred phase to its preferred phase also shows some similarities with its behaviour in the strongly segregated regime, but there are some important differences. In particular, a new steady state is observed in the weakly segregated regime and, broadly speaking, the eventual steady state of the particle is less predictable, with most of the apparent trends in the behaviour of the particle as the shear rate increases being short-lived. A plausible explanation for this is that the diffuse and delicate nature of the central interface in a weakly segregated system makes the eventual steady state more sensitive to small variations in the shear rate. It is also the case that, for a given value of the effective diffusion coefficient, D, complete expulsion of the particle from its non-preferred phase, occurs less frequently in the weakly segregated regime than it does in strongly segregated systems. Here, we see the net result of several competing factors. Firstly the diffuse interface should favour migration of the particle into its preferred phase, because it presents less of an energy barrier. However, secondly, there is less energy in the system to drive this migration and, thirdly, the delicate interface necessitates the use of lower shear rates, which further limits the energy available to the particle. Our results indicate that, in most cases, the second and third factors prevail over the first.

Finally, we revisited the simple geometrical model of section 4.6, and saw how it may be used to shed light on the results of our simulations in the weakly segregated regime. The argument parallels that in the previous chapter, but it is necessary, at the end, to introduce the concept of the effective interface width, e', to bring the predictions of the revised geometrical model into line with the simulation results.

Chapter 6

Conclusion

6.1 Review of Research

Chapter 1 introduces the idea of a minimal nanocomposite system consisting of a single nanoparticle at, or close to, the interface between two liquid phases. In the remainder of the chapter we assemble the building blocks we need to develop a model of this system, chiefly, the theory of the equilibrium thermodynamics of polymer blends, and the Cahn-Hilliard equation, which describes the dynamics of phase separation in binary systems, including polymer blends, near their critical point. The chapter also presents the fundamental concepts needed to describe the wetting and dewetting behaviour of the minimal nanocomposite system, which we aim to observe in our simulations. Finally, we present a brief survey of experimental and computational work on polymer blends, and binary fluids, undergoing phase separation, when nanoparticles are present, with a view to contextualising the results described in this thesis. Some reflections about the advantages and disadvantages of common computational approaches to the simulation of complex, multi-phase systems lead us to conclude that a model based on continuum fluid mechanics is likely to provide the most transparent insight into the essential physics of the minimal nanocomposite system.

The theoretical underpinnings of our model are laid out in chapter 2. We approach the task indirectly, via some general thoughts about force-free motion, before turning to the question of how to account for the phenomenon of diffusio-osmosis. A common theory, due to Derjaguin [98], is found to be

inconsistent with the contact theorem in colloidal science, which is known to be generally valid. This motivates a different approach to the explanation of diffusio-osmosis, based on the Gibbs free energy of the system, and a virtual work principle. This approach enables us to account for the phenomena of the plug flow of a liquid, within which there is a concentration gradient, in a capillary. The connection with wetting and dewetting is that the interface between the two liquid and vapour phase in a typical wetting situation, may be treated as a special case of inhomogeneous composition, in which the concentration gradient is sharp (in the limit, a delta function), rather than gradual, as it is in the case of diffusio-osmosis. One benefit of this approach to wetting and dewetting is that it delivers a more realistic picture of the forces acting in the small region where the three phases of the system meet, and has the potential to explain phenomenon such as the thin precursor film which, in many cases, accompanies the spreading of a macroscopic droplet on a solid substrate.

The extension of our account of diffusio-osmosis to sharper interfaces in three-phase systems, in which wetting and dewetting occur, is the key insight needed to develop a model that can be applied to a minimal nanocomposite system. The final piece of the puzzle is provided by Araki and Tanaka's fluid particle dynamics method, which makes the management of interfaces between solid and liquid phases tractable, by modelling the solid phase as a highly viscous liquid. By considering the Gibbs free energy of such a system, we derive coupled equations of motion for the evolution of the order parameter field, and the fluid flow within the minimal nanocomposite system. These equations are then solved numerically using a finite difference method, implemented on the CUDA architecture, which enables us to take advantage of the computational efficiency of modern GPUs.

The model is initially applied to the wetting of a stationary particle symmetrically position at the interface between the two liquid phases, thereby illustrating the transition to total wetting as the parameter W is increased. Having validated the model for these relatively straigtforward initial conditions, we examine dewetting behaviour in the minimal nanocomposite system in more depth, varying the initial distance of the particle from the central interface, in a quiescent system, to determine the critical film thickness. Dewetting times in the quiescent system are also compared with dewetting times when the system is sheared at a lower and a higher rate. Where the system is sheared, we also track the evolution of the mean free energy density up to, and just beyond, the dewetting point.

Finally, the model is used to explore the behaviour of a particle close to the central interface, when the system is sheared at a constant rate. In particular, we focus on whether the particle migrates across the interface, into its preferred phase, or whether the process of migration is arrested, and the particle reaches an alternative steady state, in which it remains stuck at the interface. This is a question of some relevance to the fabrication of nanocomposite materials, as discussed in the introduction to this thesis.

The dewetting behaviour of the system, and the question of whether the particle migrates to its preferred phase under shear, are explored in both the Rouse regime, where the effective diffusion coefficient, $D = 1$, and the entangled regime, with various values of D. Similarly, we explore both questions in a strongly segregated system, in which the Flory-Huggins interaction parameter $\chi = 4.0$, and in weakly segregated systems, in which $\chi = 2.1$ and $\chi = 2.5$. Methodological difficulties associated with the lower value of χ are identified, and this motivates our use of the higher value.

In these later chapters, we introduce a simple, purely geometrical model, and use it to guide our thinking about the mechanisms responsible for dewetting under shear. With the addition of a small amount of physical realism, this geometrical model can account for our simulation data on the shear strain of the system at the dewetting point.

6.2 Key Results

Simulations, in the Rouse regime, of the wetting of a particle fixed symmetrically at the interface between the two liquid phases show a range of outcomes, from partial to total wetting. The latter outcome is confirmed by both visual inspection of snapshots of the system, and tracking the evolution of the mean free energy density of the system, as wetting proceeds. We find that total wetting occurs when $W \gtrsim 4.0$, consistent with a simple model that relates the surface tension between the two liquid phases to the Flory-Huggins interaction parameter, χ.

Turning to dewetting, our simulations reproduce the the correct qualitative behaviour, in the form of a ridge of the non-preferred phase that grows as it withdraws from the surface of the particle. This is most clearly seen in the simulation in which the dimensions of the system are quadrupled ($L = 1024$ lattice cells), while scaling the radius of the particle accordingly.

All other dewetting simulations are carried out in a system of size $L = 256$ lattice cells, and show, in the quiescent case, that the critical film thickness is $d_c \sim 5.0\,nm$, which is physically plausible. When the system is sheared at two different rates, and the dewetting time plotted against the initial distance, d, of the particle from the central interface, we see a clear transition from the diffusive regime, which prevails at low values of d, significantly less than d_c, to the hydrodynamic regime, when $d > d_c$. In the latter case, the dewetting time varies almost linearly with d, reflecting the constant shear rate.

Remaining in the Rouse regime, simulation results show that the particle tends to migrate across the phase boundary, and into its preferred phase, at higher shear rates. At lower shear rates, the result is an alternative steady state in which the particle adheres to a droplet of its preferred phase, in a matrix of the non-preferred phase. Although there are some differences in these results when we double the initial distance of the particle from the central interface to $d = 4.5\,nm$ to $d = 9.0\,nm$, the essential conclusions are unchanged. It is worth noting that there is a limit to the rate at which shear may be applied to the system: when the dimensionless shear rate, $\tilde{\dot{\gamma}}$, is significantly greater than 0.002 (equivalent to a physical shear rate of $\dot{\gamma} = 2.0 \times\ 10^4\,s^{-1}$), the interface between the liquid phases does not shear stably at the upper and lower boundaries of the system.

In the entangled regime, regardless of the value of D, we find the critical film thickness in the quiescent system to be $d_c \sim 5.0\,nm$, as it is in the Rouse regime. In addition, the dewetting curves when the system is sheared, exhibit the same transition from the diffusive regime to the hydrodynamic regime, as the initial distance of the particle from the central interface is increased. In the entangled regime, when $D = 10$, the main difference is that the dewetting times are of the order of milliseconds, rather than microseconds, as in the Rouse regime. In the linear part of the dewetting curve, where the shear rate is the main determinant of the dewetting time, there is a factor of ~ 1000 between the two wetting times, other things being equal. This, and similar results when $D = 2$ and $D = 5$, is consistent with the fact that the physical shear rate, $\dot{\gamma} \propto \frac{1}{D^3}$.

The complete expulsion of the particle into its preferred phase is less common in the entangled regime than it is in the Rouse regime, This is especially the case for the higher values of the effective diffusion coefficient ($D = 5$ and $D = 10$) used in our simulations. We noted evidence, in the form of a single anomalous result, of a transition from the highly entangled regime ($D = 10$) to Rouse-like behaviour when $D \simeq 5$. Finally, in these simulations of the

entangled regime, we observe a new steady state in which the particle adheres to the interface between the two liquid phases, even when the system is fully sheared: the complete migration of the particle into its preferred phase is arrested at this penultimate stage.

Combining the simulation results for strongly segregated systems ($\chi = 4.0$) in both the Rouse regime and the entangled regime, we produce a master plot of the shear strain at the first dewetting point, against the intial distance of the particle from the central interface. The plot shows two bands of curves, one for each of the dimensionless shear rates used in our simulations and, within each band, a distinct curve for each value of the effective diffusion coefficient, D.

The simple geometrical model, introduced in section 4.6 is used to account for these features of the dewetting master plot. The presence of two bands of curves is explained by the fact that the central interface between the two liquid phases does not shear linearly at the higher dimensionless shear rate used in the simulations. Thus the shear strain at dewetting exceeds that at the lower shear rate, for any given value of D. The ordering of dewetting curves *within* each band is explained by more subtle differences in the way the central interface deforms, at any given dimensionless shear rate, as D varies. A higher value of D leads to a *lower* value of the shear strain at the dewetting point. We also observe movement of the particle, as the system is sheared, but this effect is small and does not play a significant role in explaining the main features of the dewetting master plot. Finally, in order to bring the predictions of the geometrical model into line with the simulation results, it is necessary to introduce an additional parameter e. Physically, this represents the distance of the sheared interface from the surface of the particle at which dewetting occurs almost instantaneously, compared with the time scale over which the system is sheared. Thus, a *purely* geometrical model of dewetting under shear is shown to be inadequate, but the model can be fixed by the addition of a small amount of physical realism.

Initial attempts to apply our model to a weakly segregated system, in which $\chi = 2.1$, run into methodological difficulties, caused mainly by the diffuse nature of the interface between the liquid phases, and its low energy, and consequent fragility under shear. This motivates the use of a weakly segregated system in which $\chi = 2.5$, which we find to be more tractable. Nevertheless, the interface between the liquid phases remains delicate, even at this higher value of χ, necessitating the use of a lower range of dimensionless shear rates in our simulations.

The shape of the dewetting curves for this system, resemble those for strongly segregated systems, for all values of D, but the transition from the diffusive to the hydrodynamic regime is more gradual due to the enhanced efficiency of the diffusive mechanism at low values of χ. In effect, the particle feels the influence of the diffuse interface sooner, and there is a cumulative effect as the interface approaches the surface of the particle. The more diffuse nature of the interface in the weakly segregated system also accounts for the greater critical film thickness found in the quiescent system ($d_c \sim 9.0\,nm$).

When the weakly segregated system is sheared, the migration of the particle across the phase boundary is less common than it is in the highly segregated system, for a given value of D. In addition, complete migration of the particle into its preferred phase tends to occur at *lower* shear rates in the weakly segregated system, in contrast with the higher shear rates needed in strongly segregated systems. This might be a sign that, for a given value of the Flory Huggins interaction parameter, χ, there is specific range of shear rates which allow the particle to migrate into its preferred phase.

In addition, the steady state of the system, when it is sheared, exhibits more variety - and is therefore less predictable - than is seen in the strongly segregated regime. We attribute this to the lower mean free energy density in the weakly segregated system, making it more sensitive to small changes in the parameter values and initial conditions. In fact, we observe yet another new steady state in the weakly segregated regime - the two droplet formation - although this is an artefact of the use of periodic boundary conditions, and is therefore not physically realistic.

An interesting feature of these simulation results is that the time at which the second dewetting occurs (following the breaking and retraction of the central interface) is almost inversely proportional to the shear rate. The agreement with a power law of the form $t_2 = A\dot{\gamma}^n$, with $A = 1.26$ and $n = -0.925$, is good, and contrasts with the apparently near-linear relationship between the second dewetting time and the shear rate observed in strongly segregated systems. In fact, the near-linear relationship in the strongly segregated regime is something of a coincidence, and the underlying logic of shearing the system at a constant rate should lead us to expect a relationship of approximate inverse proportionality between t_2 and $\dot{\gamma}$. Why this underlying logic is much more apparent in the weakly segregated regime is not understood.

Finally, we revisit the simple geometrical model of the previous chapter. Using similar arguments, we show that it may be used to account for the main

features of the dewetting master plots of simulation results in the weakly segregated regime. However, the natural value of the parameter e, which modifies the simple geometrical model, is no longer enough to align the predictions of the geometrical model with the simulation results. This motivates the introduction of the concept of an effective interface width, somewhat greater than the natural value of e suggested by the dewetting simulations. Physically, this reflects the fact that the interface in the weakly segregated system is more diffuse, influences the particle sooner, and therefore has a cumulative effect, over a longer period of time than in the strongly segregated system, where dewetting occurs almost instantly when $d \sim e$.

For ease of reference, figure 6.1 presents an overview of the final steady state observed in all simulations in which the system is sheared.

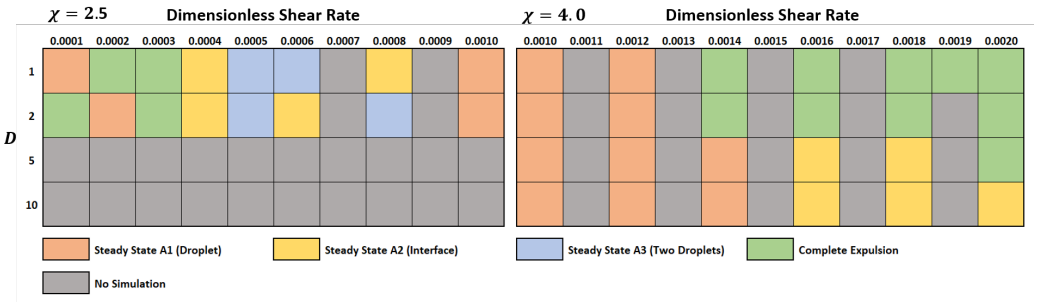

Figure 6.1: Summary of the effect of the shear rate and other parameters on the steady state of the system. In each row, the dimensionless (and physical) shear rate increases from left to right, with the exception of the rightmost cell when $\chi = 2.5$, and the leftmost cell when $\chi = 4.0$, when the shear rates are equal. The effective diffusion coefficient, D, increases from the top of a column to the bottom, implying a *decrease* in the physical shear rate. The colour of a cell indicates the steady state of the system, for that combination of parameters and dimensionless shear rate. The initial distance of the particle from the interface is $d = 8.5\,nm$ when $\chi = 2.5$ and $d = 4.5\,nm$ when $\chi = 4.0$.

The colour coding of the final steady state highlights the relative predictability of the simulation results in the strongly segregated regime, regardless of the value of the effective diffusion coefficient, D, compared with those in the weakly segregated regime.

6.3 Critique and Prospects

Finally, we turn to an appraisal of the work on the minimal nanocomposite system described in this thesis, and offer some thoughts about how it might

be extended to more complex systems.

It is clear that our model of the minimal nanocomposite system could be more physically realistic. Most obviously, it is a two-dimensional model, whereas real nanocomposite systems (even very thin films) are three-dimensional. Generally speaking, a two-dimensional model can recreate much of the essential physics, in many systems, but there is no doubt that exclusively three-dimensional effects exist in some systems, and need to be captured in any realistic model. That said, the *simplicity* of the minimal nanocomposite system is a mitigating factor here, and it is hard to imagine any significant physical effect in three dimensions that does not have an analogue in two. The restriction to two dimensions is likely to be more of a limitation if the model is extended to some of the more complex systems, described later in this section.

Our model of a minimal nanocomposite system also omits some potentially interesting physical mechanisms. For example, the equations of motion it uses do not include terms for thermal noise, which might be expected to have some effect at the length and time scales of interest, vitiating the decision to apply continuum fluid mechanics to the minimal nanocomposite system. This point applies equally to the modified Cahn-Hilliard equation, and to the modified Stokes equation used in our model. While this is an omission, we do not believe it to be a significant one. As discussed in the introduction to the thesis, the broad effect of such terms is to make the system more sensitive to small changes, rendering the relevant boundaries its phase diagram more diffuse. Still, it would be interesting to compare at least some of our simulation results with a corresponding set of results from a noisy system.

A further physical phenomenon that our model does not take into account is the viscoelasticity of many polymers. It might be argued that this is a significant omission, given the novel effects associated with viscoelasticity - for example the formation of a network structure in the *minority* phase, as a dynamically asymmetric blend undergoes spinodal decomposition [25]. However, in a *minimal* nanocomposite system, it is not clear what significantly different qualitative effects we would observe, if our model incorporated viscoelasticity, although we would expect to observe quantitative differences.

Some issues of methodology are worth noting, before we consider how our model might be extended to more complex systems. Firstly, throughout the thesis, we take it that the end result of a simulation - the eventual steady

state - is fully determined by the parameter values and the initial conditions. That is, if we keep the same parameter values and initial conditions, we will always observe the same steady state. To be certain of this, we ought to run duplicates of every single simulation, but this is clearly not feasible, given the time and resource constraints. Despite this limitation, we have some confidence that the results of our simulations represent genuine physical outcomes, that are replicable. The reason is that duplicate simulations were run, whenever we encountered an unexpected result (for example, a data point that was contrary to an apparent trend), and the outcome was always consistent with the first simulation. Although the limited use of duplicate simulations can never be conclusive, we believe it provides enough evidence to be confident in our results.

A second methodological issue concerns the question of initial conditions: in particular, how sensitive is the eventual steady state of the sheared system to the initial distance of the particle from the central interface? The question arises because, for any given set of simulations in which the shear rate is varied, the initial distance of the particle from the interface is held constant, usually just under the critical film thickness, d_c. Yet, it is clear from the second set of simulations with shear in chapter 3, where the initial distance of the particle from the central interface is $d = 9.0\,nm$, that the initial state of the system has some influence on its eventual steady state. The key stage of the entire process is the second dewetting, which occurs after the broken central interface retracts and either makes contact with the particle, or fails to make contact. Which of these happens must depend, to some degree, on the initial position of the particle, with respect to the interface. Although the second set of simulations in chapter 3 resembles the first, there are some differences. We feel that the question of the effect of varying the initial distance of the particle from the central interface on the steady state, when the system is sheared, is under-explored, although this is understandable, given the significant time and resource implications of such an investigation.

Finally, there are some gaps in figure 6.1, where simulations were not carried out, either by design, or due to a lack of time. The gaps in the simulations of strongly segregated systems ($\chi = 4.0$) are all deliberate choices and we do not believe them to be a serious issue: given the overall predictability in the pattern of outcomes, it is reasonable to interpolate the appropriate steady state, where the data is missing. In the weakly segregated regime, the missing simulations when $D = 5$ and $D = 10$, are due to a lack of time. Based on simulation results in the strongly segregated regime, we would expect to see more of steady state $A1$, in which the particle adheres to a droplet of its

preferred phase, as we increase D in the weakly segregated regime, but it would be helpful to have the simulation results to confirm this.

This highlights an issue that has a pervasive presence in this thesis, and in any similar project: given the size of the parameter space, how do we explore it in a principled way, to obtain a representative cross-section of the behaviour of the system? The problem is rendered especially acute by the inevitable constraints on time and resources that attend any research project. Careful planning is needed, combined with a willingness to change one's plans as results become available, but sometimes even that is not enough. That said, we believe that our simulation results represent a rich and interesting cross-section of the totality of possible behaviour in the minimal nanocomposite system, while remaining conscious of the regions of parameter space that remain unexplored due to time constraints.

We now offer some brief thoughts about how our model - or one very similar - might be extended to represent more complex nanocomposite systems. Proceeding cautiously, the obvious first step is to consider a system in which there are two particles close to an interface between two liquid phases. This introduces the additional physical effect of interactions between particles into the model, which may be readily represented by a Lennard-Jones type potential. Several initial configurations are possible in the two-particle case, but figure 6.2 shows the main options.

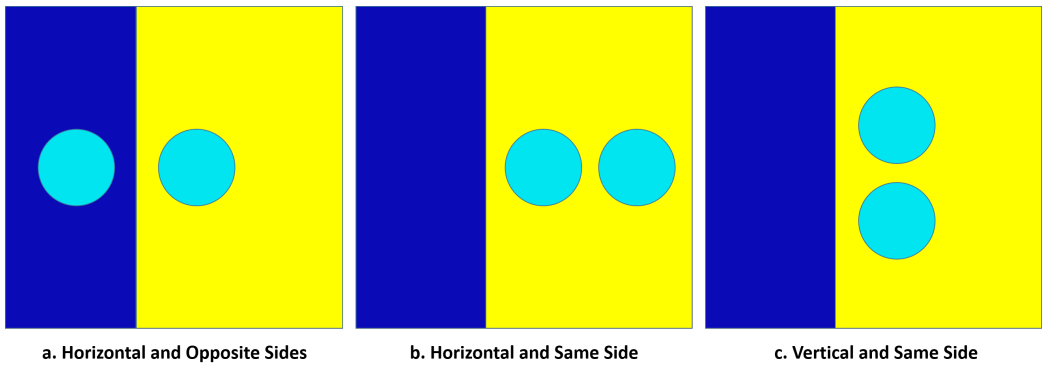

Figure 6.2: Some initial configurations of a simple, two-particle nanocomposite system. In (a), the particles are initially located on the opposite sides of the central interface between the liquid phases. In (b) and (c), the particles are initially located on the the same side, in the non-preferred phase, and aligned either horizontally, or vertically. Clearly, other initial configurations are possible, including ones that break horizontal and vertical symmetry.

Our preference would be to run simulations for the third of these initial states (figure 6.2c), since, intuitively, it ought to be easier to disentangle the

effect of the inter-particle interaction, from the diffusive and hydrodynamic effects in the liquid phases of the system, and to thereby appreciate the interplay between them. The initial distance between the particles becomes an additional variable in the model, further extending the range of parameters and initial conditions that would need to be considered.

The extension from a two-particle system to a many-particle system, more representative of a real nanocomposite, is then a natural one, albeit one with significant implications for the computational resources required. Various choices would need to be made in the modelling of such a system, including the size of the "box", the radius of the particles, and their initial positions. If the intention is to model a real system, it would be natural to either distribute the particles randomly, or to bunch them together at the start of the simulation, as if they had just been added to the polymer blend. At this point, it also becomes natural to begin the simulation with the polymer blend close to its critical point, and to allow it to undergo spinodal decomposition, as occurs in the fabrication of real nanocomposite materials. This would require some quantitative measure of the distribution of particles in the blend, and how it evolves during phase separation, but such measures are available [95]. The equations of motion in our model of the minimal nanocomposite system can readily accommodate this additional complexity

The final extension we might consider is to vary the geometry of the particles in the system from spheres to ellipsoids or nano-rods. This would lead to questions about how the eventual distribution of such particles compares with that of spherical particles in the same system, with the same parameter values and initial conditions, and the effect of varying the aspect ratio of the ellipsoids or rods. Given the anisotropy of the non-spherical particles, rotational motion, and the way in which the particles align along phase boundaries is likely to become a factor of some interest, even though particle movement is generally quite limited in our simulations.

In conclusion, we have described a mathematical framework, consistent with the principles of non-equilibrium thermodynamics, through which we may understand the motion of inhomogeneous fluids near a solid surface. Within this framework, we have constructed a model of a minimal nanocomposite system, and used it to explore the wetting and dewetting dynamics of a nanoparticle close to the interface between two liquid polymer phases. We have also considered whether applying shear to the system promotes the migration of the nanoparticle across the interface between the two liquid phases, into its preferred phase, or whether the particle is arrested at the interface.

A simple geometrical model of dewetting under shear has been shown to be predictive, as long as the purely geometrical perspective is complemented with a modest dose of physical realism.

We have varied the degree of entanglement in the system, represented by the effective diffusion coefficient, D, and the degree of segregation between the liquid polymer phases, represented by the Flory-Huggins interaction parameter, χ, while attempting to account for the similarities and differences observed in the simulation results. There remains much to explore, but the comparative simplicity of our model, grounded in continuum fluid mechanics and the Cahn-Hilliard theory of phase separation, means that it will be quite straightforward to adapt it to describe the behaviour of more complex nanocomposite systems.

References

[1] N. Clarke, N. Gibbions, and D. R. Long. Diffusio-osmosis and wetting on solid surfaces: a unified description based on a virtual work principle. *Soft Matter*, 16(14):3485–3497, 2020.

[2] N. Gibbions, N. Clarke, and D. R. Long. Migration of nanoparticles across a polymer-polymer interface: theory and simulation. *Soft Matter*, 17(31):7294–7310, 2021.

[3] J. Jancar, J. F. Douglas, F. W. Starr, S. K. Kumar, P. Cassagnau, A. J. Lesser, S. S. Sternstein, and M. J. Buehler. Current issues in research on structure-property relationships in polymer nanocomposites. *Polymer*, 51(15):3321–3343, 2010.

[4] P. J. Flory and W. R. Krigbaum. Thermodynamics of high polymer solutions. *Annu. Rev. Phys. Chem.*, 2:383–402, 1951.

[5] M. L. Huggins. Solutions of long chain compounds. *J. Chem. Phys.*, 9(5):440, 1941.

[6] M. Rubinstein and R. H. Colby. *Polymer Physics*. Oxford University Press, Oxford, UK, 2003.

[7] J. E. Mark. *Physical Properties of Polymers Handbook*. AIP Press, New York, 1996.

[8] K. F. Freed. New lattice model for interacting, avoiding polymers with controlled length distribution. *J. Phys. A-Math. Gen.*, 18(5):871–887, 1985.

[9] M. G. Bawendi, K. F. Freed, and U. Mohanty. A lattice model for self-avoiding polymers with controlled length distributions .II. corrections to flory-huggins mean field. *J. Chem. Phys.*, 84(12):7036–7047, 1986.

[10] M. G. Bawendi, K. F. Freed, and U. Mohanty. A lattice field-theory for polymer systems with nearest-neighbor interaction energies. *J. Chem. Phys.*, 87(9):5534–5540, 1987.

[11] J. W. Cahn and J. E. Hilliard. Free energy of a non-uniform system. I. interfacial free energy. *J. Chem. Phys.*, 28:258–267, 1958.

[12] J. W. Cahn. On spinodal decomposition. *Acta Metall. Mater.*, 9(9):795–801, 1961.

[13] J. W. Cahn. Free energy of a nonuniform system .II. thermodynamic basis. *J. Chem. Phys.*, 30(5):1121–1124, 1959.

[14] J. W. Cahn and J. E. Hilliard. Free energy of a nonuniform system .III. nucleation in a 2-component incompressible fluid. *J. Chem. Phys.*, 31(3):688–699, 1959.

[15] J. W. Cahn. Phase separation by spinodal decomposition in isotropic systems. *J. Chem. Phys.*, 42(1):93–99, 1965.

[16] J. W. Cahn. Initial stages of phase separation. *Am. Ceram. Soc. Bull.*, 44(4):307, 1965.

[17] J. W. Cahn. The later stages of spinodal decomposition and the beginnings of particle coarsening. *Acta Metall. Mater.*, 14(12):1685–1692, 1966.

[18] T. C. Lubensky and M. H. Rubin. Critical phenomena in semi-infinite systems .II. mean-field theory. *Phys. Rev. B*, 12(9):3885–3901, 1975.

[19] P. G. de Gennes. Dynamics of fluctuations and spinodal decomposition in polymer blends. *J. Chem. Phys.*, 72:572–579, 1980.

[20] H. E. Cook. Brownian motion in spinodal decomposition. *Acta. Metall. Mater.*, 18(3):297–306, 1970.

[21] T. M. Rogers, K. R. Elder, and R. C. Desai. Numerical study of the late stages of spinodal decomposition. *Phys. Rev. B*, 37(16):9638–9649, 1988.

[22] K. R. Elder, T. M. Rogers, and R. C. Desai. Early stages of spinodal decomposition for the cahn-hilliard-cook model of phase-separation. *Phys. Rev. B*, 38(7):4725–4739, 1988.

[23] G. Brown and A. Chakrabarti. Phase separation dynamics in off-critical polymer blends. *J. Chem. Phys.*, 98(3):2451–2458, 1993.

[24] A. Voit, A. Krekhov, and W. Koehler. Quenching a UCST polymer blend into phase separation by local heating. *Macromolecules*, 40(1):9–11, 2007.

[25] H Tanaka. Viscoelastic phase separation. *J. Phys-Condens. Mat.*, 12(15):R207–R264, 2000.

[26] C. C. Han and A. Z. Akcasu. Phase-decomposition in polymers. *Annu. Rev. Phys. Chem.*, 43:61–90, 1992.

[27] K. Binder. Phase transitions in polymer blends and block copolymer melts: Some recent developments. *Adv. Polym. Sci.*, 112:181–299, 1994.

[28] I. M. Lifshitz and V. V. Slyozov. The kinetics of precipitation from supersaturated solid solutions. *J. Phys. Chem. Solids*, 19(1):35–50, 1961.

[29] N. Kuwahara, H. Sato, and K. Kubota. Kinetics of spinodal decomposition in a polymer mixture. *Phys. Rev. E*, 47(2):1132–1138, 1993.

[30] K. Kawasaki and T. Ohta. Kinetics of fluctuations for systems undergoing phase-transitions - interfacial approach. *Physica A*, 118(1):175–190, 1983.

[31] E. D. Siggia. Late stages of spinodal decomposition in binary-mixtures. *Phys. Rev. A*, 20(2):595–605, 1979.

[32] S. Puri and B. Dunweg. Temporally linear domain growth in the segregation of binary fluids. *Phys. Rev. A*, 45(10):R6977–R6980, 1992.

[33] K. Koga, T. Kawasaki. Spinodal decomposition in binary fluids - effects of hydrodynamic interactions. *Phys. Rev. A*, 44(2):R817–R820, 1991.

[34] K. Koga, T. Kawasaki. Late-stage dynamics of spinodal decomposition in binary fluid mixtures. *Physica A*, 196(3):389–415, 1993.

[35] K. Koga, T. Kawasaki, M. Takenaka, and T. Hashimoto. Late-stage spinodal decomposition in binary fluids - comparison between computer-simulation and experimental results. *Physica A*, 198(3-4):473–492, 1993.

[36] K. Kawasaki and T. Koga. Relaxation and growth of concentration fluctuations in binary fluids and polymer blends. *Physica A*, 201(1-3):115–128, 1993.

[37] Y. C. Chou and W. I. Goldburg. Angular-distribution of light scattered from critically quenched liquid-mixtures. *Phys. Rev. A*, 23(2):858–864, 1981.

[38] N. C. Wong and C. M. Knobler. Light-scattering-studies of phase-separation in isobutyric acid and water mixtures - hydrodynamic effects. *Phys. Rev. A*, 24(6):3205–3211, 1981.

[39] C. M. Knobler and N. C. Wong. Light-scattering-studies of phase-separation in isobutyric acid and water mixtures .II. test of scaling. *J. Phys. Chem.*, 85(14):1972–1976, 1981.

[40] P. G. de Gennes. Wetting: Statics and dynamics. *Rev. Mod. Phys.*, 57(3):827–863, 1985.

[41] P. G. de Gennes, F. Brochard-Wyart, and D. Quéré. *Capillarity and Wetting Phenomena*. Springer, New York, 2004.

[42] M. Geoghegan and G. Krausch. Wetting at polymer surfaces and interfaces. *Prog. Polym. Sci.*, 28:261–302, 2003.

[43] D. Bonn, J. Eggers, J. Indekeu, J. Meunier, and E. Rolley. Wetting and spreading. *Rev. Mod. Phys.*, 81:739–805, 2009.

[44] D. Long, A. Ajdari, and L. Leibler. Static and Dynamic Wetting Properties of Thin Rubber Films. *Langmuir*, 12(21):5221–5230, 1996.

[45] M. Doi. *Soft Matter Physics*. Oxford University Press, Oxford, 2013.

[46] M. N. Popescu, G. Oshanin, S. Dietrich, and A-M. Cazabat. Precursor films in wetting phenomena. *J. Phys. Condens. Mat.*, 24:243102, 2012.

[47] V. M. Starov and M. G. Velarde. Surface forces and wetting phenomena. *J. Phys.: Condens. Matter*, 21(46):464121, 2009.

[48] L. H. Tanner. The spreading of silicone oil drops on horizontal surfaces. *J. Phys. D: Appl. Phys.*, 12:1473, 1979.

[49] A. M. J. Edwards, R. Ledesma-Aguilar, M. I. Newton, C. V. Brown, and G. Mchale. Not spreading in reverse: the dewetting of a liquid film into a single drop. *Science Advances*, 2(9):1–11, 2016.

[50] C. Bollinne, S. Cuenot, B. Nysten, and A. M. Jonas. Spinodal-like dewetting of thermodynamically-stable thin polymer films. *Eur. Phys. J. E*, 12:389–396, 2003.

[51] R. Xie, A. Karim, J. F. Douglas, C. C. Han, and R. A. Weiss. Spinodal Dewetting of Thin Polymer Films. *Phys. Rev. Lett.*, 81:1251–1254, 1998.

[52] D. Gentili, G. Foschi, F. Valle, M. Cavallini, and F. Biscarini. Applications of dewetting in micro and nanotechnology. *Chem. Soc. Rev.*, 41:4430–4443, 2012.

[53] R. Aveyard, B. P. Binks, and J. H. Clint. Emulsions stabilised solely by colloidal particles. *Adv. Colloid Interfac.*, 100(SI):503–546, 2003.

[54] M-A. Chevalier, Y.and Bolzinger. Emulsions stabilized with solid nanoparticles: Pickering emulsions. *Colloid Surface A*, 439(SI):23–34, 2013.

[55] K. Stratford, R. Adhikari, I. Pagonabarraga, J. C. Desplat, and M. E. Cates. Colloidal jamming at interfaces: a route to fluid-bicontinuous gels. *Science*, 309(5744):2198–2201, 2005.

[56] E. M. Herzig, K. A. White, A. B. Schofield, W. C. K. Poon, and P. S. Clegg. Bicontinuous emulsions stabilized solely by colloidal particles. *Nat. Mater.*, 6(12):966–971, 2007.

[57] P. J. Lu, E. Zaccarelli, F. Ciulla, A. B. Schofield, F. Sciortino, and D. A. Weitz. Gelation of particles with short-range attraction. *Nature*, 453(7194):499–503, 2008.

[58] E. Zaccarelli, P. J. Lu, F. Ciulla, D. A. Weitz, and F. Sciortino. Gelation as arrested phase separation in short-ranged attractive colloid-polymer mixtures. *J. Phys. Condens. Mat.*, 20(49):494242, 2008.

[59] M. Reeves, A. T. Brown, A. B. Schofield, M. E. Cates, and J. H. J. Thijssen. Particle-size effects in the formation of bicontinuous pickering emulsions. *Phys. Rev. E*, 92(3):032308, 2015.

[60] M. Reeves, K. Stratford, and J. H. J. Thijssen. Quantitative morphological characterization of bicontinuous pickering emulsions via interfacial curvatures. *Soft Matter*, 12(18):4082–4092, 2016.

[61] N. Hijnen, D. Cai, and P. S. Clegg. Bijels stabilized using rod-like particles. *Soft Matter*, 11(22):4351–4355, 2015.

[62] H. Chung, K. Ohno, T. Fukuda, and R.J. Composto. Self-regulated structures in nanocomposites by directed nanoparticle assembly. *Nano Lett.*, 5(10):1878–1882, 2005.

[63] S. Gam, A. Corlu, H-J. Chung, K. Ohno, M. J. A. Hore, and R. J. Composto. A jamming morphology map of polymer blend nanocomposite films. *Soft Matter*, 7(16):7262–7268, 2011.

[64] L. Li, C. Miesch, P. K. Sudeep, A. C. Balazs, T. Emrick, T. P. Russell, and R. C. Hayward. Kinetically trapped co-continuous polymer morphologies through intraphase gelation of nanoparticles. *Nano Lett.*, 11(5):1997–2003, 2011.

[65] L. Li, C. Miesch, P. K. Sudeep, A. C. Balazs, T. Emrick, T. P. Russell, and R. C. Hayward. Stabilizing co-continuous structures in polymer blends through intra-phase gelation of nanoparticles. *Abstr. Pap. Am. Chem. S.*, 242, 2011.

[66] A. Walther and A. H. E. Mueller. Janus particles: synthesis, self-assembly, physical properties, and applications. *Chem. Rev.*, 113(7):5194–5261, 2013.

[67] T. M. Ruhland, A. H. Groeschel, N. Ballard, T. S. Skelhon, A. Walther, A. H. E. Mueller, and S. A. F. Bon. Influence of janus particle shape on their interfacial behavior at liquid-liquid interfaces. *Langmuir*, 29(5):1388–1394, 2013.

[68] A. Walther, K. Matussek, and A. H. E. Mueller. Engineering nanostructured polymer blends with controlled nanoparticle location using janus particles. *ACS Nano*, 2(6):1167–1178, 2008.

[69] L. Elias, F. Fenouillot, J. C. Majeste, G. Martin, and P. Cassagnau. Migration of nanosilica particles in polymer blends. *J. Polym. Sci. Pol. Phys.*, 46(18):1976–1983, 2008.

[70] M. Du, Q. Wu, M. Zuo, and Q. Zheng. Filler effects on the phase separation behavior of poly (methyl methacrylate)/poly (styrene-co-acrylonitrile) binary polymer blends. *Eur. Polym. J.*, 49(9):2721–2729, 2013.

[71] X. Zhong, Y. Liu, H. Su, G. Zhan, Y. Yu, and W. Gan. Enhanced viscoelastic effect of mesoscopic fillers in phase separation. *Soft Matter*, 7(7):3642–3650, 2011.

[72] J. K. Yeganeh, F. Goharpey, E. Moghimi, G. Petekidis, and R. Foudazi. Manipulating the kinetics and mechanism of phase separation in dynamically asymmetric LCST blends by nanoparticles. *Phys. Chem. Chem. Phys.*, 17(41):27446–27461, 2015.

[73] F. Fenouillot, P. Cassagnau, and J. Majeste. Uneven distribution of nanoparticles in immiscible fluids : Morphology development in polymer blends. *Polymer*, 50(6):1333–1350, 2009.

[74] V. V. Ginzburg. Influence of nanoparticles on miscibility of polymer blends. a simple theory. *Macromolecules*, 38(6):2362–2367, 2005.

[75] M. E. Cates and P. S. Clegg. Bijels: a new class of soft materials. *Soft Matter*, 4(11):2132–2138, 2008.

[76] E. Kim, K. Stratford, R. Adhikari, and M. E. Cates. Arrest of fluid demixing by nanoparticles: A computer simulation study. *Langmuir*, 24(13):6549–6556, 2008.

[77] M. J. A. Hore and M. Laradji. Microphase separation induced by interfacial segregation of isotropic, spherical nanoparticles. *J. Chem. Phys.*, 126(24):244903, 2007.

[78] M. J. A. Hore and M. Laradji. Prospects of nanorods as an emulsifying agent of immiscible blends. *J. Chem. Phys.*, 128(5):054901, 2008.

[79] G. Allegra, G. Raos, and M. Vacatello. Theories and simulations of polymer-based nanocomposites: from chain statistics to reinforcement. *Prog. Polym. Sci.*, 33(7):683–731, 2008.

[80] Q. H. Zeng, A. B. Yu, and G. Q. Lu. Multiscale modeling and simulation of polymer nanocomposites. *Prog. Polym. Sci.*, 33(2):191–269, 2008.

[81] L-T. Yan and X-M. Xie. Computational modeling and simulation of nanoparticle self-assembly in polymeric systems: Structures, properties and external field effects. *Prog. Polym. Sci.*, 38(2):369–405, 2013.

[82] A. Heinecke, W. Eckhardt, M. Horsch, and H-J. Bungartz. *Supercomputing for Molecular Dynamics Simulations: Handling Multi-Trillion Particles in Nanofluidics*. Springer, Berlin, 2015.

[83] D. Raabe. Overview of the lattice boltzmann method for nano- and microscale fluid dynamics in materials science and engineering. *Model. Simul. Mater. Sc.*, 12(6):R13–R46, 2004.

[84] E. Moeendarbary, T. Y. Ng, and M. Zangeneh. Dissipative particle dynamics: Introduction, methodology and complex fluid applications - a review. *Int. J. Appl. Mech.*, 1(4):737–763, 2009.

[85] P. J. Hoogerbrugge and J. M. V. Koelman. Simulating microscopic hydrodynamic phenomena with dissipative particle dynamics. *Europhys. Lett.*, 19(3):155–160, 1992.

[86] P. Espanol and P. Warren. Statistical-Mechanics of Dissipative Particle Dynamics. *Europhys. Lett.*, 30(4):191–196, 1995.

[87] P. Espanol and P. B. Warren. Perspective: Dissipative particle dynamics. *J. Chem. Phys.*, 146(15):150901, 2017.

[88] B. J. Alder and T. E. Wainwright. Decay of velocity autocorrelation function. *Phys. Rev. A*, 1(1):18–21, 1970.

[89] L. D. Landau and E. M. Lifshitz. *Fluid Mechanics*. Elsevier, Amsterdam, 1987.

[90] H. Tanaka and T. Araki. Simulation method of colloidal suspensions with hydrodynamic interactions: fluid particle dynamics. *Phys. Rev. Lett.*, 85:1338, 2000.

[91] T. Araki and H. Tanaka. Dynamic depletion attraction between colloids suspended in a phase-separating binary liquid mixture. *J. Phys. Condens. Mat.*, 20(7):072101, 2008.

[92] T. Araki and S. Fukai. Controlled motion of Janus particles in periodically phase-separating binary fluids. *Soft Matter*, 11(17):3470–9, 2015.

[93] T. Araki and H. Tanaka. Dynamics of Colloidal Particles in Soft Matters. *Prog. Theor. Phys.*, 175:37–46, 2008.

[94] T. Araki and H. Tanaka. Colloidal aggregation in a nematic liquid crystal: Topological arrest of particles by a single-stroke disclination line. *Phys. Rev. Lett.*, 97(12):1–4, 2006.

[95] T. Araki and H. Tanaka. Wetting-induced depletion interaction between particles in a phase-separating liquid mixture. *Phys. Rev. E*, 73(6):1–7, 2006.

[96] T. Araki and H. Tanaka. Nematohydrodynamic effects on the phase separation of a symmetric mixture of an isotropic liquid and a liquid crystal. *Phys. Rev. Lett.*, 93:015702, 2004.

[97] H. Kodama, K. Takeshita, T. Araki, and H. Tanaka. Fluid particle dynamics simulation of charged colloidal suspensions. *J. Phys. Condens. Mat.*, 16:L115, 2004.

[98] B. V. Derjaguin, G. P. Sidorenkov, E. A. Zubaschenkov, and E. V. Kiseleva. Kinetic phenomena in boundary films of liquids. *Kolloidn. Zh.*, 9:335, 1947.

[99] M. Doi and S. F. Edwards. *The Theory of Polymer Dynamics*. Oxford University Press, New York, 1986.

[100] J. L. Anderson. Colloid transport by interfacial forces. *Ann. Rev. Fluid Mech.*, 21:61–99, 1989.

[101] H. A. Stone, A.D. Stroock, and A. Ajdari. Engineering flows in small devices: Microfluidics toward a lab-on-a-chip. *Ann. Rev. Fluid Mech.*, 36:381–411, 2004.

[102] N. Clarke. Effect of shear flow on polymer blends. *Adv. Polym. Sci.*, 183:127–173, 2005.

[103] J. L. Anderson and D. C. Prieve. Diffusiophoresis caused by gradients of strongly adsorbing solutes. *Langmuir*, 7:403–406, 1991.

[104] N. V. Churaev, B. V. Derjaguin, and V. M. Muller. *Surface Forces*. Springer Science, New York, 1987.

[105] A. Ajdari and L. Bocquet. Giant amplification of interfacially driven transport by hydrodynamic slip: Diffusio-osmosis and beyond. *Phys. Rev. Lett.*, 96:186102, 2006.

[106] S. Marbach, H. Yoshida, and L. Bocquet. Osmotic and diffusio-osmotic flow generation at high solute concentration. I. mechanical approaches. *J. Chem. Phys.*, 146:194701, 2017.

[107] D. C. Grahame. The electrical double layer and the theory of electrocapillarity. *Chem. Rev.*, 41:441–501, 1947.

[108] V. A. Parsegian and D. Gingell. On the electrostatic interaction across a sakt solution between two bodies bearing unequal charges. *Biophysical Journal*, 12(1192-1204), 1972.

[109] J. Israelachvili. *Intermolecular and Surface Forces*. Academic Press, London, 1991.

[110] D. Ben-Yaakov, D. Andelman, D. Harries, and R. Podgornik. Beyond standard poisson-boltzmann theory: ion-specific interactions in aqueous solutions. *J. Phys. Condens. Mat.*, 21:424106, 2009.

[111] A. C. Maggs and R. Podgornik. General theory of asymmetric steric interactions in electrostaic double layers. *Soft Matter*, 12(4):1219–1229, 2016.

[112] R. M. Adar and D. Andelman. Osmotic pressure between arbitrarily charged planar surfaces: A revisited approach. *Eur. Phys. J. E*, 41:11, 2018.

[113] M. Doi and A. Onuki. Dynamic coupling between stress and composition in polymer solutions and blends. *J. Phys. II*, 2(8):1631–1656, 1992.

[114] S. R. de Groot and P. Mazur. *Non-Equilibrium Thermodynamics*. Dover, Mineola, 1984.

[115] D. Long, H. A. Stone, and A. Ajdari. *J. Coll. Sci.*, 212:338–349, 1999.

[116] L. D. Landau and Lifshitz E. M. *Electrodynamics of Continuous Media*. Elsevier, Amsterdam, 1984.

[117] L. D. Landau and Lifshitz E. M. *Statistical Physics, part 2*. Pergamon Press, New York, 1981.

[118] F. Julicher and J. Prost. Generic theory of colloidal transport. *Eur. Phys. J. E*, 29:27–36, 2009.

[119] S. A. Safran. *Statistical Thermodynamics of Surfaces, Interfaces and Membranes*. Westview Press, Boulder, USA, 2003.

[120] E. Lauga, M. P. Brenner, and H. A. Stone. *Handbook of Experimental Fluid Dynamics*. Springer, New York, 2005.

[121] J. L. Anderson, M. E. Lowell, and D. C. Prieve. Motion of a particle generated by chemical gradients part 1. non-electrolytes. *J. Fluid Mech.*, 117:107–121, 1982.

[122] E. Ruckenstein. Can phoretic motions be treated as interfacial tension gradient driven phenomena? *J. Colloid Interface Sci.*, 83:77–81, 1981.

[123] V. G. Levich. *Physicochemical Hydrodynamics*. Prentice-Hall, Inc., Englewood Cliffs, N.J., 1962.

[124] Y. Liu, R. Ganti, and D. Frenkel. Pressure gradients fail to predict diffusio-osmosis. *J. Phys. Condens. Matter*, 30:205002, 2018.

[125] D. M. Anderson, G. B. McFadden, and A. A. Wheeler. Diffuse-interface methods in fluid mechanics. *Annu. Rev. Fluid Mech.*, 30:139–165, 1998.

[126] Y. J. Choi and P. D. Anderson. Cahn – Hilliard modeling of particles suspended in two-phase flows. *Int. J. Numer. Meth. Fl.*, 69:995–1015, 2011.

[127] N. O. Jaensson, M. A. Hulsen, and P. D. Anderson. Stokes – Cahn – Hilliard formulations and simulations of two-phase flows with suspended rigid particles. *Computers and Fluids*, 111:1–17, 2015.

[128] N.O. Jaensson, M.A. Hulsen, and P.D. Anderson. A comparison between the XFEM and a boundary-fitted mesh method for the simulation of rigid particles in cahn-hilliard fluids. *Computers and Fluids*, 156:81–96, 2017.

[129] N. O. Jaensson, C. Mitrias, M. A. Hulsen, and P. D. Anderson. Shear-Induced Migration of Rigid Particles near an Interface between a Newtonian and a Viscoelastic Fluid. *Langmuir*, 34:1795–1806, 2018.

[130] R. A. L. Jones and R. W. Richards. *Polymers at Surfaces and Interfaces*. Cambridge University Press, Cambridge, UK, 1999.

[131] E. Helfand and Y. Tagami. Theory of interface between immiscible polymers. *J. Polym. Sci. Pol. Lett.*, 9(10):741–746, 1971.

[132] P. G. de Gennes. Reptation of a polymer chain in the presence of fixed obstacles. *J. Chem. Phys.*, 55(2):4756–4763, 1971.

[133] J. des Cloizeaux. Double reptation vs simple reptation in polymer melts. *Europhys. Lett.*, 5(5):437–442, 1988.

[134] C. Tsenoglou. Molecular-weight polydispersity effects on the viscoelasticity of entangled linear polymers. *Macromolecules*, 24(8):1762–1767, 1991.